

UNIVERSIDAD POLITÉCNICA DE MADRID  
ESCUELA TÉCNICA SUPERIOR DE INGENIEROS DE  
TELECOMUNICACIÓN



MODELING AND DESIGN OF RING OSCILLATORS AND  
THEIR APPLICATION IN RADIATION ENVIRONMENTS

Ph.D. Thesis

Javier Agustín Sáenz  
Ingeniero de Telecomunicación  
M.Sc. in Electrical Engineering  
2016



DEPARTAMENTO DE INGENIERÍA ELECTRÓNICA  
ESCUELA TÉCNICA SUPERIOR DE INGENIEROS DE  
TELECOMUNICACIÓN  
UNIVERSIDAD POLITÉCNICA DE MADRID

MODELING AND DESIGN OF RING OSCILLATORS AND  
THEIR APPLICATION IN RADIATION ENVIRONMENTS

Ph.D. Thesis

Author:

Javier Agustín Sáenz  
Ingeniero de Telecomunicación  
M.Sc. with a major in Electrical Engineering

Advisor:

María Luisa López Vallejo  
Catedrática de Universidad  
Dpto. de Ingeniería Electrónica  
Universidad Politécnica de Madrid

2016



PH.D. THESIS: Modeling and Design of Ring Oscillators and their Application in Radiation Environments

AUTHOR: Javier Agustín Sáenz

ADVISOR: María Luisa López Vallejo

El tribunal nombrado para juzgar la Tesis arriba indicada, compuesto por los siguientes doctores:

PRESIDENTE:

VOCALES:

SECRETARIO:

acuerdan otorgarle la calificación de:

Madrid, September 30, 2016

El Secretario del Tribunal



*“The man never knows  
what he’s capable of  
until you try.”*

—Charles Dickens—



---

## Abstract

Humanity has always looked to the sky; first with mystery, later with curiosity. That curiosity led us to the desire of exploration of the unknown worlds. Although it was not immediate, as our limitations tend to keep us with our feet on the ground, we developed the necessary technology to see our dreams came true. This technology has seen its maximum development during the last half century lying on the evolution of electronic systems.

As happens with other implicated sciences, overcoming the challenges presented by electronics along this path has not been a bed of roses. Many problems appeared from the beginning of the application of the well-known and tested technologies to an environment different from ground level. Then, we noticed that the composition of environments could affect the reliability of electronic systems and therefore special attention was required to design systems able to operate in those harsh environments. The radiation particles presented out of the atmosphere were considered the source of unreliability. A new subfield of study was opened within the field of electronics: characterization of radiation environments and their effects in electronic systems.

Attending to the time of exposure, radiation effects are usually classified into long-term effects and single event effects. Long-term effects are generated by the degradation of electronic devices as a consequence of the exposition to radiation. And single event effects refer to a group of effects provoked by the impact of a single particle. The final outcome of this hit in the system depends on many variables such as: shielding, technology or design. To palliate these effects and improve reliability, two approaches have been developed: Radiation Hardening by Process (RHBP) and Radiation Hardening by Design (RHBD).

At the same time the space exploration was relying on electronic systems, the evolution of semiconductor industry has been “forced” to follow the Moore’s law: “The number of transistors in an Integrated Circuit doubles approximately every two years”. This tendency has led to manufacture transistors with feature sizes as small as tens of nanometers. As a consequence, Moore’s law has been fulfilled and the achievements of modern electronic

systems have been translated into amazing advances unimaginable a few years ago. However, the shrinking technology has been also accompanied by new challenges. One of these challenges is the interaction of radiation particles even at ground level while previously it was completely negligible.

Therefore, redesigning conventional circuits used so far may be necessary to avoid the pernicious effects of radiation interaction not only for space exploration but for every application. Taking in mind this final goal, this thesis focuses on studying and improving one the most implemented circuits in recent electronic systems, the ring oscillator, using RHBD techniques. Ring oscillators are very robust and the requirements of oscillation are easily fulfilled. Both features have made them suitable for many applications, for instance, digital clocks, PLLs, DLLs or test structures. Hence, the improvement of this circuit is potentially very important because all of these applications can benefit from these improvement as long as new applications can start using them. Once the effects of radiation in ring oscillators have been analyzed, this thesis provides four main contributions.

First, we designed a Total Ionization Dose sensor that takes advantage of cumulative effects. It presents the following advantages: it is a self-timed digital sensor with a configurable sensitivity whose interface allows its integration in a multidisciplinary network. We designed, implemented and manufactured the sensor in a  $0.35\text{ }\mu\text{m}$  commercial technology. It was characterized in terms of radiation, up to 575 krad, and temperature, from 0 to  $50^{\circ}\text{C}$ . The sensor has an area of  $0.047\text{ mm}^2$  and an energy per conversion of 463 pJ.

Second, we propose a Single Event Transient tolerant ring oscillator which can be designed without area overhead. To achieve this goal, we force the masking of the radiation induced currents by configuring the duty cycle of ring oscillators. This configuration is based on the asymmetric design of odd and even stages of the ring oscillator. The validation of our proposal has been carried out through simulation and emulation methods.

Third, we present two models in order to generalize the variation of the output duty cycle: the first model is based on the layout design and the second model establishes a relation between the output duty cycle and different bias voltage schemes. These models are validated with a 40 nm commercial technology. All of the previous applications of ring oscillators use as system output a clock signal with a 50% duty cycle. Our work sets the analytical basis for understanding and designing a ring oscillator whose outputs are clock signals with fully-configurable duty cycles different from 50%.

Finally, we applied the previous models to design a Ring Oscillator PUF focused on the variability of the duty cycle instead of the frequency. Using a relative value, such as the duty cycle, the robustness of the PUF is improved. For example, the output shift due to radiation is decreased form 7% to 0.1% and due to temperature from 3% to less than 0.5%. Moreover, the input challenges are multiplied by the number of stages of each ring oscillator.

---

## Resumen

El hombre ha mirado siempre hacia el cielo, primero lo hizo con misterio y más tarde con curiosidad. Y fue esa curiosidad la que sembró la semilla que nos ha llevado a desear explorar nuevos mundos más allá de nuestras fronteras. Sin embargo, ha sido necesario realizar un gran desarrollo tecnológico a lo largo de muchos años para poder comenzar a explorar los mundos más cercanos. Toda esta tecnología ha sido impulsada en la última mitad del siglo XX por la aparición de los sistemas electrónicos.

Al igual que en el resto de las ciencias implicadas en este sueño, el desarrollo de la electrónica no ha sido un camino de rosas, surgiendo muchos problemas desde el inicio de la aplicación de tecnologías maduras en entornos diferentes al presente en la superficie terrestre. Fue entonces, cuando se puso de manifiesto que la composición de los diferentes entornos afectaba directamente a la fiabilidad de los sistemas electrónicos, y en consecuencia, comenzó a tenerse en cuenta a la hora de realizar nuevos diseños destinados a operar en ambientes especialmente hostiles. En particular, la radiación de las partículas presentes fuera de la atmósfera terrestre fueron consideradas una importante fuente de fallos. Debido a la importancia de estos resultados, surgió un nuevo campo de investigación dentro de la electrónica que fue: la caracterización de entornos de radiación y sus efectos en sistemas electrónicos.

Los efectos producidos por la radiación, son normalmente clasificados dependiendo del tiempo de exposición a la misma en: efectos a largo plazo y efectos puntuales. Los efectos a largo plazo son generados por la degradación de los dispositivos electrónicos como consecuencia de la exposición. Mientras que los efectos puntuales son producidos por el impacto de una sola partícula. El resultado final de este impacto depende de muchas variables, como por ejemplo, de la protección, la tecnología o el diseño de cada circuito. Para paliar estos efectos y mejorar así la fiabilidad, se han desarrollado dos metodologías diferentes: endurecimiento por proceso (RHBP) y endurecimiento por diseño (RHBD).

Al mismo tiempo que la exploración del espacio dependía del desarrollo de la electrónica,

la evolución de la industria de semiconductores ha sido “forzada” a seguir la famosa ley de Moore: “El número de transistores en un circuito integrado se dobla cada dos años aproximadamente”. Esta tendencia ha llevado a desarrollar transistores cada vez más pequeños hasta llegar a los tamaños actuales de pocas decenas de nanómetros. Sin embargo, este escalado de la tecnología también ha venido acompañado de nuevos retos, y uno de ellos es la aparición de efectos producidos por la radiación de partículas incluso en la superficie terrestre, donde antes estos efectos eran totalmente inapreciables.

Por lo tanto, rediseñar los sistemas para evitar estos efectos perniciosos se ha convertido en algo totalmente obligatorio no solo para aquellos sistemas que van a operar en entornos hostiles sino para todos los sistemas. Siendo este el objetivo final, esta Tesis se centra en el estudio y mejora de uno de los circuitos más utilizados a lo largo de la historia, el oscilador en anillo. Los osciladores en anillo son osciladores muy robustos y que oscilan en casi cualquier circunstancia. Ambas características los han convertido en unos dispositivos muy versátiles que se implementan en aplicaciones muy heterogéneas: estructuras de test, PLLs, DLLs o relojes. Así, mejorar el diseño de este dispositivo supone una mejora potencial en cada una de las aplicaciones finales que lo utilizan. En esta Tesis, utilizamos los efectos producidos por la radiación en los osciladores en anillo para llevar a cabo esta tarea.

Primero, hemos diseñado un sensor de Dosis Total Absorbida que se beneficia de los efectos producidos por la acumulación de carga. Este sensor presenta las siguientes características: es autotemporizado, tiene una sensibilidad configurable, es digital y su interfaz permite integrarlo en una red de sensores multidisciplinar. Hemos diseñado, implementado y fabricado el sensor en una tecnología comercial de  $0,35\text{ }\mu\text{m}$ . Y lo hemos medido y caracterizado en términos de radiación hasta 575 krad y de temperatura dese 0 a 50 °C. El sensor ocupa un área de  $0,0047\text{ mm}^2$  y consume 463 pJ por medida.

Segundo, hemos propuesto un oscilador en anillo tolerante a efectos puntuales transitorios (SETs) sin penalización de área. Para ello, hemos enmascarado las corrientes inducidas por la radiación mediante la configuración del ciclo de trabajo de la señal de salida del oscilador. Esta configuración se basa en la implementación de etapas asimétricas. La validación de nuestra propuesta se realizó mediante métodos de simulación y emulación.

Tercero, hemos desarrollado dos modelos que generalizan el método de configuración del ciclo de trabajo del oscilador en anillo. El primero de estos modelos se basa en el diseño del trazado de cada uno de los transistores, y el segundo se basa en utilizar diferentes esquemas de alimentación. Estos modelos han sido validados con simulaciones de una tecnología comercial de 40 nm.

Por último, hemos aplicado los modelos desarrollados para implementar un PUF basado en osciladores en anillo. Estos sistemas son sistemas de seguridad *hardware* que requieren una gran fiabilidad. Para aumentar la fiabilidad de los sistemas actuales, hemos propuesto medir el ciclo de trabajo en lugar de la frecuencia de salida, consiguiendo mejoras de más del 20% en el peor de los casos.

---

## Agradecimientos

Este documento simboliza una marca en el camino. Una marca para no olvidar lo que estos años han aportado a mi vida. Porque una tesis no es sólo el fruto de la investigación que se ha llevado a cabo. También es todo el proceso que ha llevado a la consecución de esos resultados. Lo que ahora veo al mirar hacia adelante, es un sendero más llano del que pensaba que tenía cuando comencé este último tramo. Y no porque crea que haya sido fácil, más bien porque aquellos con los que compartes el camino aligeran la carga. Porque al final, los senderos son para compartirlos y cada cruce que se presente hay que aprovecharlo.

Puede que las personas a las que agradezca su apoyo no crean que se lo merecen, u otras que crean que merecen estar aquí no lo están. Pero tanto unas como otras os merecéis estar en estas líneas y os lo agradezco.

Por supuesto, esta tesis no habría podido ser posible sin la guía de mi tutora y directora de tesis Marisa Lopez Vallejo, quien me ha llevado por las sendas de la investigación y la docencia desde el primer día que empecé a trabajar con ella. Y todas las personas con las que he compartido algún tiempo como miembros del grupo de Laboratorio de Sistemas Integrados, desde el director, Carlos López Barrio, a todos los investigadores: Miguel Ángel, Pablos, Hernán, Carlos y Fer. Mención especial merece este último por aguantarme cada día durante 5 años con todo lo que ello conlleva.

Quiero agradecer también a la Universidad Politécnica de Madrid, por el afán investigador de la institución, el cual empuja a los miembros que formamos parte de ella a intentar mejorar la sociedad con nuestras humildes contribuciones. Gracias también a todo el personal de administración que consigue que nuestro único foco esté puesto en la investigación.

Gracias a ARQUIMEA por su colaboración y experiencia en la fabricación de los dispositivos que hemos realizado en esta Tesis enmarcados en el desarrollo del proyecto RAD-HARQ.

## Agradecimientos

---

Quiero expresar mi agradecimiento al Profesor Lloyd W. Massengil (Vanderbilt University, Nashville, TN) y al Profesor Tomás Palacios (Massachusetts Institute of Technology, Boston) por darme la oportunidad de haber participado temporalmente en sus respectivos grupos de investigación y haberme permitido ampliar mi conocimiento con experiencias en grupos con gran reconocimiento internacional. Asimismo, al Consejo Social de la Universidad Politécnica de Madrid por realizar un gran trabajo promoviendo la movilidad de los investigadores.

Parte de esta tesis, es de mi familia, mis padres y hermanos, de los que siempre he tenido su apoyo en todo lo que he hecho y decidido en mi vida.

Y otra parte es de mi segunda familia, aquellos con los que he compartido mi vida desde que llegué a Madrid. A Adri, mi “hermano”, Y a Mario, el responsable de “levantarme” cada mañana para avanzar con la tesis y “porque nuestras idas y venidas de la Escuela arreglando el mundo son una parte muy importante de estos años de doctorado”.

Y por último, y más importante, a Bárbara, por estar ahí. Porque la felicidad no es cosa de uno. Y si he tenido una ilusión fuera de la tesis, esa eres tú.

Arnedo, Enero 2017



JAVIER AGUSTÍN  
SÁENZ

Javier Agustín Sáenz

---

# Contents

<b>List of Figures</b>	<b>x</b>
<b>List of Tables</b>	<b>xvi</b>
<b>Acronyms</b>	<b>xix</b>
<b>1 Introduction</b>	<b>1</b>
1.1 Motivation of this Thesis . . . . .	4
1.2 Thesis Organization . . . . .	5
1.3 Contributions of this Thesis . . . . .	7
1.4 Publications . . . . .	8
<b>2 Foundations</b>	<b>9</b>
2.1 Ring Oscillators . . . . .	10
2.1.1 Theory of oscillators . . . . .	10
2.1.2 Types of oscillators . . . . .	12
2.1.3 Ring Oscillators . . . . .	14
2.1.4 Frequency of ring oscillators . . . . .	15
2.2 Radiation Effects in Electronics . . . . .	19
2.2.1 Radiation Units . . . . .	19
2.2.2 Environments . . . . .	20
2.2.3 Radiation Effects . . . . .	25
2.2.4 Mitigation Techniques . . . . .	27
2.3 Ring oscillators in radiation environments . . . . .	34

<b>3 Total Ionization Dose Sensor</b>	<b>37</b>
3.1 Introduction . . . . .	38
3.2 Total Ionization Dose . . . . .	39
3.2.1 Effect of TID on MOS Performance . . . . .	41
3.2.2 RADFETs . . . . .	43
3.3 Sensor Design . . . . .	44
3.3.1 Foundations . . . . .	44
3.3.2 Architecture . . . . .	46
3.3.3 Implementation . . . . .	49
3.4 Radiation Test . . . . .	50
3.4.1 Prototype description . . . . .	50
3.4.2 Test procedure . . . . .	51
3.4.3 Radiation Test Results . . . . .	53
3.5 Temperature Test . . . . .	56
3.5.1 Setup . . . . .	56
3.5.2 Temperature Test Results . . . . .	59
3.6 Calibration . . . . .	60
3.7 Discussion . . . . .	61
3.8 Conclusions . . . . .	63
3.9 Related Publications . . . . .	64
<b>4 Efficient Mitigation of SET Induced Harmonic Error</b>	<b>65</b>
4.1 Introduction . . . . .	66
4.2 Single Event Transients in Electronics . . . . .	67
4.2.1 Introduction . . . . .	67
4.2.2 Testing . . . . .	70
4.2.3 SET Modeling . . . . .	72
4.3 SET Induced Harmonic Errors in Ring Oscillators . . . . .	73
4.4 Proposed Solution . . . . .	76
4.5 SET Induced Harmonic Error Mitigation . . . . .	80
4.6 Implemented Test Circuits . . . . .	82
4.7 Electrical Validation . . . . .	85
4.7.1 Test Set Up . . . . .	86
4.7.2 Experimental Results . . . . .	87
4.7.3 Comments on the third harmonic oscillation . . . . .	89
4.8 Conclusions . . . . .	91
4.9 Related Publications . . . . .	91

## Contents

---

<b>5 Analytical Model of the Duty Cycle in Ring Oscillators</b>	<b>93</b>
5.1 Introduction . . . . .	94
5.2 Model Analysis . . . . .	95
5.2.1 CMOS Inverter . . . . .	95
5.2.2 Ring Oscillator . . . . .	97
5.3 Duty Cycle Configuration Models . . . . .	100
5.3.1 Hard duty cycle configuration . . . . .	100
5.3.2 Soft duty cycle configuration . . . . .	104
5.4 Models Validation . . . . .	108
5.4.1 Hard Configuration Validation . . . . .	109
5.4.2 Soft Configuration Validation . . . . .	112
5.4.3 Transistor Mismatch . . . . .	112
5.5 Jitter and Phase Noise . . . . .	115
5.6 Discussion . . . . .	118
5.7 Conclusions . . . . .	119
5.8 Related Publications . . . . .	119
<b>6 Application of the Duty Cycle Ring Oscillator Model to Improve PUF Reliability</b>	<b>121</b>
6.1 Introduction . . . . .	122
6.2 Related Work . . . . .	124
6.2.1 PUF Foundations . . . . .	124
6.2.2 Types of PUF . . . . .	127
6.3 Ring Oscillator PUF . . . . .	129
6.4 Duty Cylce PUF Proposal . . . . .	131
6.4.1 Duty Cycle PUF Exploration . . . . .	131
6.4.2 Architecture . . . . .	136
6.5 Simulation Results . . . . .	138
6.5.1 Randomness . . . . .	139
6.5.2 Reliability . . . . .	139
6.5.3 Robustness . . . . .	142
6.6 Proof of concept . . . . .	143
6.7 Conclusions . . . . .	144
6.8 Related Publications . . . . .	145
<b>7 Conclusions and Future Work</b>	<b>147</b>
7.1 Future Work . . . . .	152
<b>References</b>	<b>155</b>



---

# List of Figures

1.1	Historic of published paper involving ring oscillator use and indexed in <a href="https://scholar.google.com">https://scholar.google.com</a> . . . . .	4
1.2	Diagram of the thesis organization and the contents of each chapter. . . . .	6
2.1	Feedback model of oscillators using linear analysis. . . . .	11
2.2	Schematic of LC-based ( <i>tank</i> ) Colpitts oscillator (a) and its equivalent Colpitts oscillator using a crystal. . . . .	13
2.3	Schematic of a phase-shift RC oscillator (a) and a Wien oscillator (b). . . . .	14
2.4	3-stage ring oscillator with inverter gates. . . . .	14
2.5	3-stage ring oscillator with CMOS inverter gates. . . . .	16
2.6	Simulated Voltage Transfer Characteristic (a) and voltage gain (b) of CMOS inverter [RCN02]. . . . .	16
2.7	Model of ring oscillators for Linear Analysis. . . . .	17
2.8	(a) Digital inverter symbol with parasitic capacitor $C_p$ and (b) proposed nonlinear model [ES08]. . . . .	18
2.9	Radiation space environment and sources (source JPL nasa.gov). . . . .	21
2.10	Sketch of the Van Allen belts as a result of solar particles interaction with Earth's magnetosphere (source JPL nasa.gov). . . . .	23
2.11	Cascade interactions of cosmic particles with the atoms of the atmosphere. . . . .	24
2.12	Classification of Radiation Effects in Electronics. . . . .	28
2.13	Triple Modular Redundancy scheme used for SEE tolerant Flip-Flops. . . . .	31
2.14	Classification of Radiation Effects mitigation strategies. . . . .	33
3.1	Band diagram of a MOS capacitor with a positive gate bias [Win89]. . . . .	40
3.2	Schematic of n-channel MOSFET illustrating radiation-induced charging of the gate oxide: (a) normal operation and (b) post-irradiation [OM03a]. . . . .	41

---

3.3	Threshold voltage shifts and subthreshold swing changes for nMOS and pMOS transistors are shown relative to the preirradiation curves [Lac08]. . . . .	42
3.4	RADFETs used in [HSGMP14] as discrete components. . . . .	43
3.5	Radiation results in [LOM <sup>+</sup> 01] for 0.35 µm TSMC CMOS technology. . . . .	45
3.6	Self-timed sensor scheme with its three main blocks. . . . .	46
3.7	Timing diagram of the sensor signals and their predicted behavior. . . . .	47
3.8	Radiation Sensor simulations for different values of sensitivity. . . . .	48
3.9	Layout of ELT used for TID hardening. . . . .	49
3.10	Layout of the TID proposed sensor. It is physically divided into two different parts, the unhardened and sensitive area (top) and the radiation hardened control (bottom). . . . .	50
3.11	Test set up for <sup>60</sup> Co radiation test at CIEMAT. . . . .	52
3.12	Diagram of measurement process. . . . .	54
3.13	Radiation results for every DUT at different doses. . . . .	55
3.14	Radiation Sensor Sensitive comparison between simulation (line) and measurements (dots). . . . .	55
3.15	Delay time vs annealing time in DUT2. Test results, fitting curve and the fitting errors. . . . .	56
3.16	Oscilloscope measurements of the temperature tests. . . . .	58
3.17	Temperature transfer function for our sensor design and its associated errors. . . . .	58
3.18	Sensor response variation and its errors due to accelerated annealing at 50 °C. . . . .	59
3.19	Representation of Equation 3.11 for DUT2 with measured data. . . . .	60
3.20	Conversion process from delay to TID value. . . . .	61
3.21	Scheme of the proposed radiation self-recovery system. . . . .	62
4.1	Charge generation and collection phases in a reverse-biased junction and the resultant current pulse caused by the passage of a high-energy ion [Bau05a]. . . . .	68
4.2	Logical Masking (a and c) and propagation (b and d) of SET by NAND and NOR gates. . . . .	69
4.3	Electrical masking of SET due to the propagation delay of combinational gates. . . . .	70
4.4	The temporal masking of Single Event Transients (SETs) depends on the vulnerability window of registers. . . . .	70
4.5	Plateau effect presented in [DWB <sup>+</sup> 07] as a consequence of SETs in technologies under 100 nm. . . . .	74
4.6	SET impact in a ring oscillator and the potential 3rd (a) and 5th (a) induced harmonic oscillations. . . . .	74
4.7	SET pulse parameters defined in [C <sup>+</sup> 14] for Induced Harmonic Errors characterization. . . . .	76

## List of Figures

---

4.8	Proposed asymmetric solution for Harmonic Error Mitigation in ring oscillators. . . . .	77
4.9	Internal nodes (3, 5, 8, 13) of a 15-stage ring oscillator where different duty cycles are observed. . . . .	79
4.10	99-stage ring oscillator duty cycle distribution for different $\gamma$ ratios. Dotted lines are theoretical results and solid lines are simulation results. . . . .	79
4.11	15-stage RO internal nodes (4, 6, 8, 10 and 12) with an injected SET at node 4 and its mitigation thanks to the proposed asymmetry. . . . .	80
4.12	SET propagation within the ring oscillator nodes. Dashed-lines are the edges induced by a SET. . . . .	81
4.13	Nodes propagated of a $SET_{pwmax}$ with respect to $\gamma$ ratio in a 99-stage RO. . . . .	82
4.14	Schematic of the ring oscillator used for SET emulation in electrical validation. . . . .	83
4.15	Schematic of the ring oscillator used for SET emulation in electrical validation based on voltage controlled asymmetry. . . . .	84
4.16	Output waveform of the third harmonic removal in the simulation of the <i>voltage-controlled</i> test circuit validation. . . . .	85
4.17	Layout of the two different manufactured test circuits with their inputs and outputs. (top) layout-based. (bottom) voltage-controlled. . . . .	86
4.18	Set Up used for the validation tests of our new ring oscillator design. . . . .	87
4.19	Waveform captures of the different scenarios occurred during emulated SET injection in electrical validation depending on the test circuit and its configuration. Start of oscillation (left). Steady oscillation (right). . . . .	88
4.20	Representation of the measured frequencies of the <i>voltage-controlled</i> design with respect to the input voltages. (a) behavior without SET emulation. (b) frequency at the start of the oscillation. (c) frequency at steady oscillation. . . . .	89
4.21	Output measurements and their FFTs for a SET-free output (a) and an induced third harmonic error ring oscillator (b). . . . .	90
5.1	Ring Oscillator notation. W (transistor width), L (transistor channel length), $C_i$ (node $i$ capacitance), and $Vdd_i$ (bias voltage of inverter $i$ ). . . . .	98
5.2	Internal nodes of a balanced 5-stage ring oscillator and the times in which the period, $T$ is divided. . . . .	99
5.3	Ring Oscillator with asymmetric odd and even nodes (smaller transistors means narrower channel). . . . .	103
5.4	Transistor size distribution in four different examples of <i>hard</i> duty cycle configuration. . . . .	104
5.5	Theoretical duty cycle distribution for the four different cases of study at every internal node of a 51-stage ring oscillator. . . . .	105

---

5.6	Schematic of a ring oscillator to independently control each inverter gate bias voltage. . . . .	105
5.7	Examples of Vddi distributions of the <i>soft</i> duty cycle configuration. . . . .	107
5.8	Theoretical duty cycle distribution in the 6 different cases of soft configuration study. . . . .	108
5.9	Ring Oscillator with NAND gate to enable the oscillation. . . . .	108
5.10	Internal nodes of a 51-stage ring oscillator where different duty cycle are observed. . . . .	109
5.11	51-stage ring oscillator duty cycle distribution for different $\varphi$ values. Solid lines are simulation results and dashed lines are theoretical values. . . . .	110
5.12	Duty cycle of a K-ratio distribution for ring oscillators with different number of stages. . . . .	110
5.13	Duty cycle for the linear distribution example. Solid lines are simulation results and dashed lines are theoretical values. . . . .	111
5.14	Duty cycle for the triangular distribution case. Solid lines are simulation results and dashed lines are theoretical values. . . . .	111
5.15	51-stage ring oscillator duty cycle distribution for different $\eta$ values. Solid lines are simulation results and dashed lines are theoretical values. . . . .	112
5.16	Duty cycle for the double-triangular distribution case. Solid lines are simulation results and dashed lines are theoretical values. . . . .	113
5.17	Mismatch variability of a 15-stage ring oscillator with $\varphi = 1$ (top left), 2 (top right), 4 (bottom left) and 10 (bottom right). . . . .	113
5.18	Mismatch variability of an N-stage ring oscillator with $\varphi = 4$ and $N=3$ (top left), 5 (top right), 15 (bottom left) and 45 (bottom right). . . . .	114
5.19	Phase noise of a <b>k-Ratio</b> CMOS ring oscillator measured at 1MHz for different $\varphi$ (greater $\varphi$ produces lower $fo$ ) and N. . . . .	117
6.1	PUF basic operation as a CRP pair system and its ideal operation. . . . .	124
6.2	Conventional RO PUF architecture based on frequency variability [MS09]. . . . .	129
6.3	PUF error source as a consequence of different sensitivities to temperature. . . . .	133
6.4	Mismatch variability of a 15-stage ring oscillator with $\varphi = 1$ (top left), 2 (top right), 4 (bottom left) and 10 (bottom right). . . . .	135
6.5	Mismatch variability of an N-stage ring oscillator with $\varphi = 4$ and $N=3$ (top left), 5 (top right), 15 (bottom left) and 45 (bottom right). . . . .	135
6.6	DC-PUF proposed architecture with (N,n) CRPs. . . . .	136
6.7	Response generator blocks: a) DC2V converter [VAFK14], b) Sense amplifier [WH11]. . . . .	137
6.8	Simulation Set-Up for the characterization of the RO-PUF and the DC-PUF. . . . .	138
6.9	Randomness of the RO-PUF and the DC-PUF implemented in simulations. . . . .	140

## List of Figures

---

6.10	Temperature results of simulations carried out to characterize the reliability of RO-PUFs and DC-PUFs. . . . .	141
6.11	Reliability of RO-PUF and DC-PUF for temperature, bias voltage and radiation dose variation. . . . .	142
6.12	Diagram of the implemented test architecture for DC-PUF exploration. . .	143
6.13	Layout of the fabricated proof of concept for the duty cycle exploration. . .	144



---

## List of Tables

2.1	Comparison of the different technologies implemented for radiation systems.	34
3.1	Total Ionization Dose Sensor features. . . . .	51
3.2	Radiation test plan. . . . .	53
3.3	Board Power Consumption. . . . .	56
3.4	Temperature test plan. . . . .	57
4.1	Guidelines ans Standards for SEEs testing. . . . .	71
4.2	5-Stage ring oscillator duty-cycle distribution. . . . .	78
6.1	Classification of previous works according to different features. . . . .	128



---

## Acronyms

<b>ADC</b>	Analog-to-Digital Converter
<b>ASIC</b>	Application-Specific Integrated Circuit
<b>CMOS</b>	Complementary Metal-Oxide-Semiconductor
<b>CME</b>	Coronal Mass Ejections
<b>COTS</b>	Commercial Off-The-Shelf
<b>CRP</b>	Challenge Response Pair
<b>DC-PUF</b>	Duty Cycle PUF
<b>DDE</b>	Displacement Damage Effect
<b>DICE</b>	Dual Interlocked Cell
<b>DLL</b>	Dual Delay-Locked Loop
<b>DRAM</b>	Dynamic Random Access Memory
<b>DSET</b>	Digital Single Event Transient
<b>DSP</b>	Digital Signal Processor
<b>DUT</b>	Device Under Test
<b>EDAC</b>	Error Detection And Correction
<b>ELT</b>	Enclosed Layout Transistor
<b>FFT</b>	Fast Fourier Transform

<b>FPGA</b>	Field Programmable Gate Array
<b>GCR</b>	Galactic Cosmic Ray
<b>HCI</b>	Hot Carrier Injection
<b>HD</b>	Hamming Distance
<b>IC</b>	Integrated Circuit
<b>ITRS</b>	International Technology Roadmap for Semiconductors
<b>LET</b>	Linear Energy Transfer
<b>LHC</b>	Large Hadron Collider
<b>LOCOS</b>	LOCal Oxidation of Silicon
<b>MBU</b>	Multiple Bit Upset
<b>MOSFET</b>	Metal-Oxide-Semiconductor Field-Effect Transistors
<b>NBTI</b>	Negative-Bias Temperature Instability
<b>NVM</b>	Non-Volatile Memory
<b>PLL</b>	Phase-Locked-Loop
<b>PSD</b>	Power Spectral Density
<b>PUF</b>	Physically Unclonable Function
<b>PVT</b>	Process Voltage Temperature
<b>PWM</b>	Pulse Width Modulator
<b>RADFET</b>	RADIation-sensing Field-Effect Transistor
<b>RHBD</b>	Radiation Hardening By Design
<b>RHBP</b>	Radiation Hardening By Process
<b>RO-PUF</b>	Ring Oscillator PUF
<b>SAA</b>	South Atlantic Anomaly
<b>SEB</b>	Single Event Burnout

## Acronyms

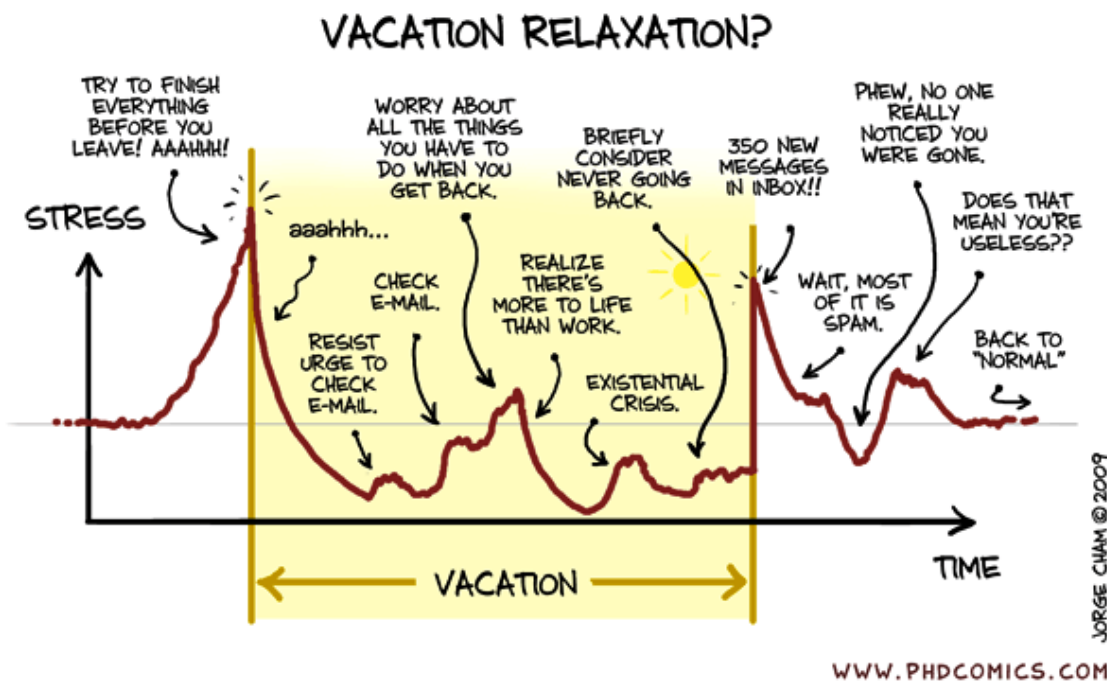
---

<b>SEE</b>	Single Event Effect
<b>SEFI</b>	Single Event Functional Interrupt
<b>SEGR</b>	Single Event Gate Rupture
<b>SEL</b>	Single Event Latchup
<b>SER</b>	Single Event Rate
<b>SET</b>	Single Event Transient
<b>SEU</b>	Single Event Upset
<b>SI</b>	International System
<b>SOI</b>	Silicon on Insulator
<b>SRAM</b>	Static Random Access Memory
<b>STI</b>	Silicon Trench Isolation
<b>TDC</b>	Time-to-Digital Converter
<b>TID</b>	Total Ionization Dose
<b>TMR</b>	Triple Modular Redundancy
<b>TTMR</b>	Time-Triple Modular Redundancy
<b>VCO</b>	Voltage-Controlled Oscillators



# Chapter 1

## Introduction



# Chapter 1

---

## Introduction

Since the beginning of semiconductor electronic industry, the study of circuit reliability has been a hot topic not only for academia, but also for industry. The reliability of circuits depends on many different sources. Some of them can be controlled, such as fabrication process or circuit designs for reliability, but many others are dependent on external conditions that must be dealt with [RCW14].

The 2015 International Technology Roadmap for Semiconductors (ITRS) points out the radiation environment as one of the important uncontrollable sources. The presence of ionizing radiation may be a significant threat to the correct operation of electronic devices [BG15]. The fundamental consequence of ionizing radiation is the deposition of energy in the target material. As a result, radiation can cause a variety of effects which are usually categorized into two different groups: cumulative effects and Single Event Effects (SEEs). Cumulative effects cause the progressive drift in electronic device parameters due to the degradation of insulators and semiconductor materials. On the other hand, SEEs are instant effects produced by the interaction of a single particle with sensitive regions of electronic circuits.

The understanding of radiation effects and the development of different techniques to avoid their consequences have significantly evolved through the last decades. In the 60s [Con94], bipolar devices dominated the semiconductor industry. Throughout this decade, the number of transistors per Integrated Circuit (IC) grew from a few tens to a few hundreds. During this period, the political atmosphere (the Cold War, the threat of nuclear weapons or the beginning of the space exploration with the Sputnik in orbit and the man on the moon) set the perfect scenario for an increasing interest in radiation effects on materials for defense, space and nuclear applications. Wallmark and Marcus [WM62] predicted the occurrence of SEEs in 1962. Hughes and Giroux [HG64] authored the first paper on the Total Ionization Dose (TID) effect on MOSFETs in 1964. And many other works were published trying to explain the different radiation effects and the physical mechanisms that produced them.

The 1970s were very active and productive years in terms of research and development on radiation effects. The complexity and capabilities of integrated circuits increased significantly during this decade. The observation of new effects in the much more complex circuits enhanced the effort to understand the basic mechanisms of ionizing radiation effects

---

on MOS devices. In 1975, Binder et al. [BSH75] published the first observation of a Single Event Upset (SEU) in digital circuits on satellites. And in 1979, May and Wood [MW78] explained the soft errors in DRAMs at ground level based on the alpha particles emitted by the uranium present in packaging materials.

In the early 1980s, the research on SEUs continued to increase, tremendous progress was made in understanding the basic mechanisms of charge build-up and charge trapping in device dielectrics and a clearer physical picture of the effects of TID on the dielectric films began to emerge [MO87]. The band diagram of an MOS capacitor with a positive gate bias was postulated and nowadays it continues to be useful for the understanding of the radiation-induced charge generation and transport processes. The earliest paper from the radiation effects community on Digital Single Event Transients (DSETs) was published in 1983 by Diehl et al. [DCHB83], one decade after the first paper reporting in-flight observation of SEUs in memories. Near the end of the 80s, a paper by Hass et al. [HTG89] described the design of a radiation-hardened microprocessor in a  $2\text{ }\mu\text{m}$  technology.

The 1990s saw two major developments that continued to increase the importance of SEEs. One was the dramatic decrease in the number of manufacturers offering radiation-hardened digital ICs. This led to the increased usage of commercial electronics in space-crafts. The second development was the continuous advance in fabrication technologies towards smaller IC feature sizes, higher speeds and more complex circuitry. These advances typically increased sensitivity to SEE, even to the point of terrestrial errors in a benign environment, and they also led to new failure mechanisms. By the mid 1990s, the study of total dose effects in MOSFETs began to shift. The relevant questions were related to the properties of ultrathin gate oxides [SPM<sup>+</sup>97], the effects of field oxide isolation moving from LOCOS to STI [SDDF98], and the increasing use of Silicon on Insulator (SOI) technology [May90] and advanced gate stacks including high-K gate dielectrics. New processes and technologies were bringing new TID challenges.

During the beginning of the 21st century, microprocessor chips passed the billion transistors. The sensitivity to SEUs continued increasing in memories and core logic because of the technology shrinking. Upsets in terrestrial electronics were a serious reliability concern for commercial manufacturers. In fact, SEE vulnerability became a mainstream product reliability metric for the IC industry [Bau05b]. With the progress in process technology and the degree of gate-oxide hardening that came for free in commercial CMOS, the concept of obtaining TID hardening through design was pursued.

In the last few years, the progression of Moore's law is being compromised and new materials and systems are being explored to replace silicon for electronic circuits [CLZ12]. Research on radiation effects is being focused on characterizing the impact of radiation environments in those new materials. Besides the trend to replace silicon, the contributions on new techniques for radiation hardening by design or characterization of smaller silicon transistors have not decreased.

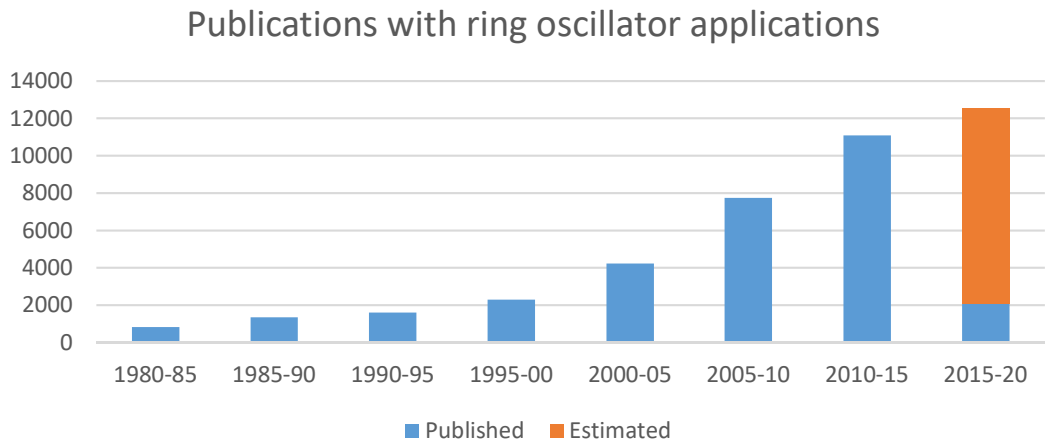


**Figure 1.1:** Historic of published paper involving ring oscillator use and indexed in <https://scholar.google.com>.

The conclusion of the review of historical facts in radiation effects on electronics is that some environments such as space, avionics, high energy physics experiments or biomedical instruments have been always taken into account for electronic design. But the evolution of semiconductor industry has driven space and military vendors to use commercial circuits. And, at the same time, commercial vendors are really concern about radiation effects in the everyday consumer environment due to the errors observed at ground level with modern technologies. As a consequence, the design of actual electronic systems needs to address radiation effects in order to maintain the reliability of circuits at any environment. And the experience acquired in space and military industries can help to solve the new problems of ground level applications.

## 1.1 Motivation of this Thesis

Ring oscillators are one of the most fabricated circuits in electronic systems. Their relevancy can be tracked by the amount of scientific work related to ring oscillators published during the last decades. The historical evolution of these publications is plotted in Figure 1.1. As can be seen, they have increased since the 80's and this tendency seems to carry on. Hence, the impact of an improvement in the design or performance of ring oscillators can potentially benefit a great number of applications which rely on their simplicity and robustness.

Since the appearance of ring oscillators, almost every semiconductor fabrication process includes a small test structure based on a ring oscillator to monitor the quality of each batch. These oscillators are so well-known to digital and analog circuit designers that they have found many different uses beyond the monitoring of the semiconductor

processes. For example, Pulse Width Modulators (PWMs) [PPZM03] are usually used in control applications such as LED lighting or stepper motor driving where ring oscillators play the role of DC-DC converters. Clock generators for digital systems [LKL97] where ring oscillators are the core of the system clocks. Process Voltage Temperature (PVT) sensors [CCSP11] exploit the dependency of the ring oscillator frequency with respect to PVT variations to track the modifications in transistor nominal performance. Time-to-Digital Converters (TDCs) [HKK<sup>+</sup>13] digitize time measurements using the ring oscillator delay chain to integrate analog magnitudes into digital systems. Test systems for aging monitoring [KLR<sup>+</sup>11] measure the ring oscillator frequency variation produced by the degradation during the device lifetime. Phase-Locked-Loops (PLLs) [ESK<sup>+</sup>15] and Dual Delay-Locked Loops (DLLs) [DPMT<sup>+</sup>11] use ring oscillators and their multiphase internal characteristic to correct timing of high-performance digital circuits. Voltage-Controlled Oscillators (VCOs) [EU04] employ current-starved transistors controlled by the gate voltage input to vary the output frequency of the ring oscillator. Physically Unclonable Functions (PUFs) [MS11] make use of PVT variations, what makes frequency slightly different from equally designed ring oscillators, to implement security systems for hardware authentication.

The goal of this thesis is to study the implications of using the widely used ring oscillator circuit in radiation environments and to contribute with new approaches for exploiting the characteristics that have made of this system one of the most implemented circuits. Radiation environments are a perfect scenario to push the ring oscillator to extreme situations and to compromise its reliability. In this thesis we take advantage of the radiation effects in ring oscillators and we address the risks they produce in critical situations. These contributions are not only useful in radiation environments but they improve the traditional ring oscillator based applications.

## 1.2 Thesis Organization

The organization of this thesis is depicted in Figure 1.2. The topic of each chapter and their relationships are organized as follows.

Chapter 2 introduces the general concepts and foundations required for this thesis. It mainly focuses on two different topics. Firstly, ring oscillators are deeply analyzed. This circuit is explored from different approaches. It goes from the most general application of theory of oscillators using signal processing analysis to the explanation of ring oscillator behavior focusing on each individual transistor. Secondly, the effects of radiation environments in electronic systems are reviewed. This part describes the composition and characteristics of these hostile environments and the different types of modifications produced in CMOS circuits. Finally, it also outlines the previous related work on applications

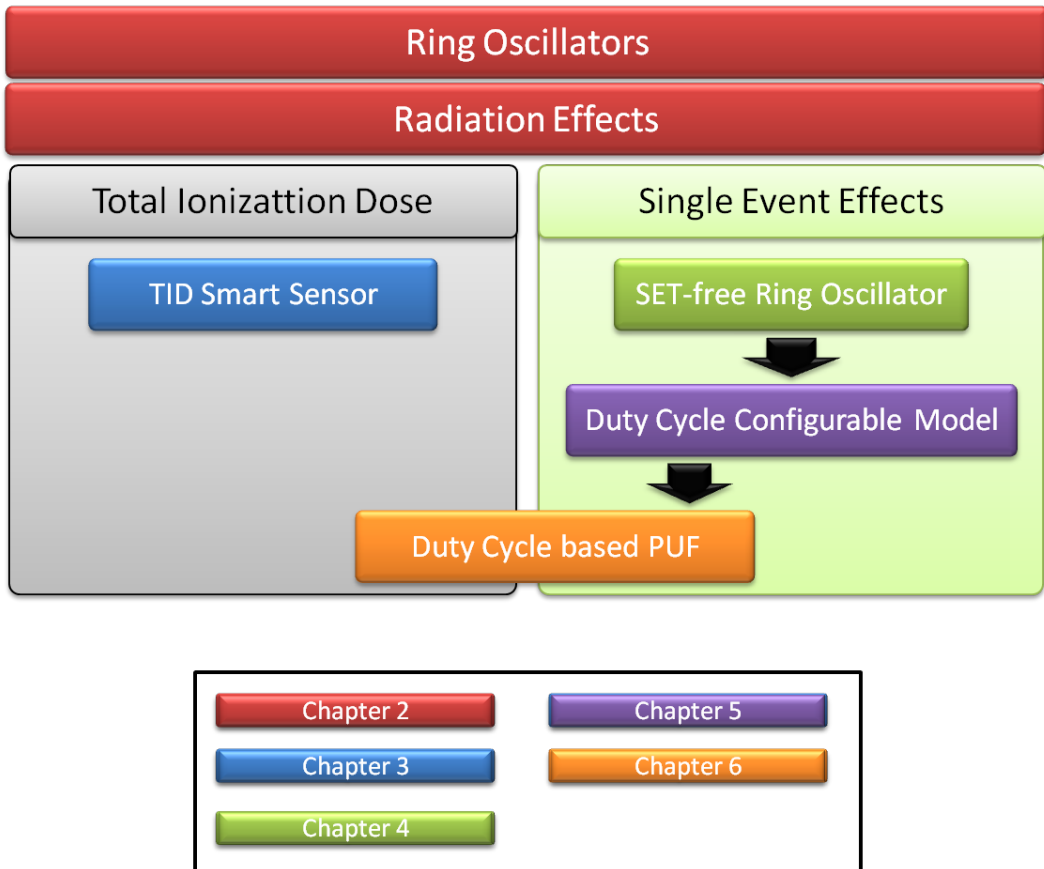


**Figure 1.2:** Diagram of the thesis organization and the contents of each chapter.

of ring oscillators into radiation environments.

Chapter 3 describes the designed prototype of a ring oscillator based Total Ionization Dose Monitor. This chapter introduces the TID effect explaining the physical mechanisms that generate it. The prototype presented in this chapter takes advantage of one of the consequences of TID, the shift of threshold voltages produced by the long exposure to radiation particles. The monitor is analyzed, simulated, manufactured, measured and characterized. The device is also proposed as a smart sensor fully integrable into a multidisciplinary sensor network.

Chapter 4 deals with a problem of SEEs in ring oscillators. The impact of an ionized particle could produce a shift of the fundamental frequency to higher odd harmonics. This problem is presented with previous works, analyzed and addressed using a new design. The proposed solution implements a configurable duty cycle ring oscillator to remove the glitch injected by ionized particles. The proposal has also been fabricated and measured. The characterization is based on an emulated injection of single events in order to avoid the high cost of accelerated radiation tests.

In Chapter 5, the approach of using the duty cycle as an output presented in Chapter 4 is generalized. Then, this chapter explains the basics to design a ring oscillator with fully configurable duty cycle. The generalization is based on an individual analysis of each transistor and the influence of every design parameter (gate length, bias voltage, current-starved circuit, etc.) in the duty cycle of each node within a ring oscillator. As a result, an expression is given in order to determine the duty cycle of each node depending on the ring oscillator design parameters. The generalization allows to apply the new ring oscillator structure to some of the applications that use the ring oscillators as basic devices.

Chapter 6 applies the model developed in Chapter 5 to a specific application, a PUF. The implementation of PUFs using integrated circuits is a recent application that can use ring oscillators as basic structure. This chapter is an example of the potential of using the duty cycle as an output parameter instead of the frequency in ring oscillators based circuits. As PUF circuits are very sensitive to environmental variations, its exposure to radiation particles is a very suitable test for validating our duty cycle proposal.

Finally, in Chapter 7 the conclusions of this thesis are drawn and future research lines are presented.

### 1.3 Contributions of this Thesis

Attending to the topics addressed in this Chapter, the key contributions of this thesis are focused on improving the design of ring oscillators and their applications within radiation environments. The outline of these contributions is:

- Taking advantage of ring oscillator behavior in a radiation environment to be able to monitor the circuit absorbed dose. A built-in monitor has been implemented in order to monitor the actual absorbed dose instead of the exposed dose as traditional TID sensors.
- Solving the Harmonic Problem of ring oscillators produced by the impact of single ionized particles. The solution is based on using an asymmetric design that configures the duty cycle of ring oscillator nodes.
- Development of an analytical model that defines the duty cycle of ring oscillator nodes. This model changes the common view of ring oscillator outputs. So far, just the frequency of the output has been taken into account but this proposal explores the use of the duty cycle instead.
- Application of the configurable duty cycle ring oscillator to the implementation of a very sensitive system to radiation effects, a Physically Unclonable Function architecture. The duty cycle is a very robust parameter that allows to improve the features of previous ring oscillator based PUFs.

## 1.4 Publications

The contributions previously outlined and the results of this thesis have been published in the following international conferences and journals:

### Papers in JCR indexed journals

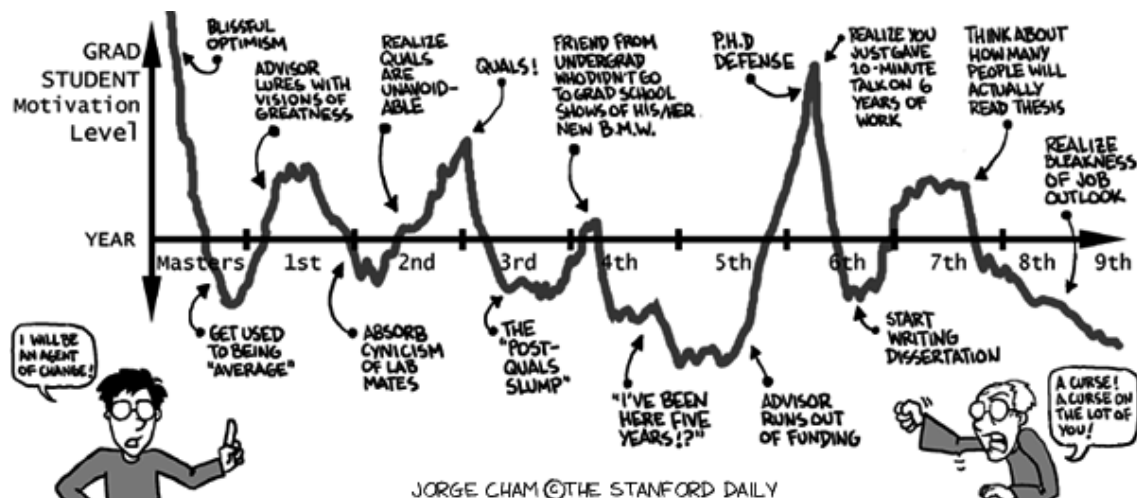
- **J. Agustin**, C. Gil, M. Lopez-Vallejo and P. Ituero, "*Design and Characterization of a Built-In CMOS TID Smart Sensor*," in IEEE Transactions on Nuclear Science, vol. 62, no. 2, pp. 443-450, April 2015. doi: 10.1109/TNS.2015.2404532
- **J. Agustin** and M. Lopez-Vallejo, "*An In-Depth Analysis of Ring Oscillators: Exploiting Their Configurable Duty-Cycle*," in IEEE Transactions on Circuits and Systems I: Regular Papers, vol. 62, no. 10, pp. 2485-2494, Oct. 2015.  
doi: 10.1109/TCSI.2015.2476300
- **J. Agustin**, M. L. Lopez-Vallejo, C. G. Soriano, P. Cholbi, L. W. Massengill and Y. P. Chen, "*Efficient Mitigation of SET Induced Harmonic Errors in Ring Oscillators*," in IEEE Transactions on Nuclear Science, vol. 62, no. 6, pp. 3049-3056, Dec. 2015.  
doi: 10.1109/TNS.2015.2496169

### International Conference Proceedings

- **J. Agustin**, C. G. Soriano, M. L. Vallejo and P. Ituero, "*A built-in CMOS Total Ionization Dose smart sensor*," IEEE SENSORS 2014 Proceedings, Valencia, 2014, pp. 70-73. doi: 10.1109/ICSENS.2014.6984935
- **J. Agustin**, M. L. Lopez-Vallejo, C. G. Soriano, P. Cholbi, L. W. Massengill and Y. P. Chen, "*Efficient Mitigation of SET Induced Harmonic Errors in Ring Oscillators*," in NSREC 2015, Boston, Jul. 2015.
- **J. Agustin** and M. L. Lopez-Vallejo, "*A temperature-independent PUF with a configurable duty cycle of CMOS ring oscillators*," 2016 IEEE International Symposium on Circuits and Systems (ISCAS), Montreal, QC, 2016, pp. 2471-2474. doi: 10.1109/ISCAS.2016.7539093

# Chapter 2

## Foundations



# Chapter 2

---

# Foundations

## 2.1 Ring Oscillators

### 2.1.1 Theory of oscillators

Oscillators are the key block of many electronic systems. They are used to perform countless different operations such as clock for digital circuits, synchronization of communication systems or radio frequency carrier generators. In general, an oscillator can be defined as an autonomous circuit that converts DC power into a periodic waveform. There are many types of oscillators, and many different circuit configurations that produce a variety of periodic waveforms. However, the most commonly used oscillations are reduced only to two different types: the sinusoidal signal and the pulsed signal. Usually, sinusoidal oscillations are used in analog designs while pulse oscillators are the basis of any digital system clock.

Despite the different fundamental mechanisms underneath each electronic oscillatory behavior, the study of every oscillator is based on finding the startup conditions along with the oscillation frequency as accurately as possible. Once these main characteristics have been analyzed and validated, other figures of merit characterize the oscillators to allow their comparison and classification. These features can be referred to physical characteristics —resources, integrability, bias conditions— or to frequency performance —phase noise, jitter or quality factor ( $Q$ )— depending on the requirements of the target application.

In order to analytically define the frequency of an oscillator, three different approaches can be taken from the designer's perspective [Rhe10]. The linear analysis is usually the first step for oscillator design. While this type of analysis does not predict all oscillatory characteristics, it establishes initial starting conditions and forms the foundation of the design. The nonlinear analysis can predict the oscillator fundamental output level, the harmonic content of the output spectrum or internal voltage and current waveform because these issues are consequence of the nonlinearities of the used electronic components. Both types of analysis characterize the oscillators at steady-state while transient techniques consider the time-domain waveform of the oscillation specially at the beginning of the oscillation. As for many applications the linear analysis is enough, this introduction is focused on it, leaving the special considerations of each particular design to the advanced analysis of nonlinear and transient techniques.

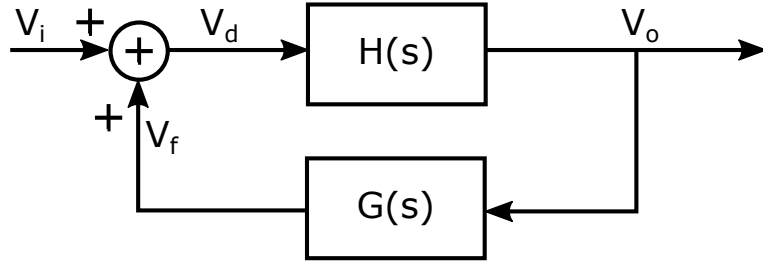


**Figure 2.1:** Feedback model of oscillators using linear analysis.

Linear analysis models an oscillator as a feedback system. The scheme of the basic feedback oscillator is shown in Figure 2.1. According to this model, the system consists of an amplifier, defined by its transfer functions  $H(s)$ , and a feedback network, defined by its transfer functions  $G(s)$ . Qualitatively, the amplifier limits the amplitude of the output signal and the feedback network determines the frequency of oscillation. In this particular case, the system has a positive feedback as the feedback signal is added to the input signal. The signals presented in the Figure 2.1 are: the input signal,  $v_i$ , the output signal,  $v_o$ , the feedback signal,  $v_f$  and the addition of input and feedback signals,  $v_d$ .  $H(s)$  is also called the open-loop gain since it is the gain between  $v_o$  and  $v_i$  when  $v_f = 0$  (feedback network is disconnected).

From Figure 2.1, the next relations can be inferred:

$$V_o = H(s)V_d \quad (2.1)$$

$$V_f = G(s)V_o \quad (2.2)$$

and

$$V_d = V_i + V_f \quad (2.3)$$

Thus, from Equations (2.1) to (2.3), the closed-loop transfer function  $F(s)$  is given by:

$$F(s) = \frac{V_o}{V_i} = \frac{H(s)}{1 - G(s)H(s)} \quad (2.4)$$

replacing  $s = j\omega$

$$F(s)|_{s=j\omega} = \frac{H(j\omega)}{1 - G(j\omega)H(j\omega)} \quad (2.5)$$

To begin an oscillation, the condition is that without any input an output must exist ( $V_i = 0$  and  $V_o \neq 0$ ). In Equation (2.5) this is only achievable at frequencies  $\omega_0$  that makes the denominator equal to zero. That is, when

$$1 - G(j\omega_0)H(j\omega_0) = 0 \quad (2.6)$$

or

$$G(j\omega_0)H(j\omega_0) = 1 \quad (2.7)$$

This equation is known as the Barkhausen criterion and it establishes the initial conditions of any oscillator. It is more often expressed in polar form as:

$$|G(j\omega_0)H(j\omega_0)| = 1 \quad (2.8)$$

$$\angle(G(j\omega_0)H(j\omega_0)) = \pm n360^\circ \quad \text{where } n = 0, 1, 2, \dots \quad (2.9)$$

Equation (2.8) summarizes the fact that for oscillations to occur the loop gain must be unity. And Equation (2.9) shows the need of the feedback signal,  $v_f$  to be in phase with the input signal,  $v_i$ . If the model supposes a negative feedback network instead of the positive one used in Figure 2.1, then this second condition is replaced by:

$$\angle(G(j\omega_0)H(j\omega_0)) = \pm n360^\circ + 180^\circ \quad (2.10)$$

Previous equations analytically express how the oscillation begins without any input excitation. The stability of the system is altered by the amplification of an electronic noise. This noise, presented in every electronic circuit, is a white noise with a constant Power Spectral Density (PSD). The feedback network filters the noise at the output. This filtering makes that only the component  $w_0$  of the noise is added and amplified in the loop what will generate the periodic output at the circuit fundamental frequency.

### 2.1.2 Types of oscillators

Oscillators can be classified depending on different features. We will divide them into two groups according to the type of feedback network: resonant or non resonant oscillators.

Resonant oscillators use some kind of resonator to select or generate the oscillation frequency. The resonator is a system that presents a peak in a parameter such as impedance or vibration, at a fixed frequency which can be used to amplify this frequency component and attenuate the rest. The most used resonant oscillators are:

- LC oscillators. In this type of oscillators, the feedback network is based on the use of inductors and capacitors to form a *tank* circuit able to select a resonant frequency. At this frequency, the equivalent impedance of the network is infinite. The oscillation behavior comes from the conversion of electrostatic energy stored in

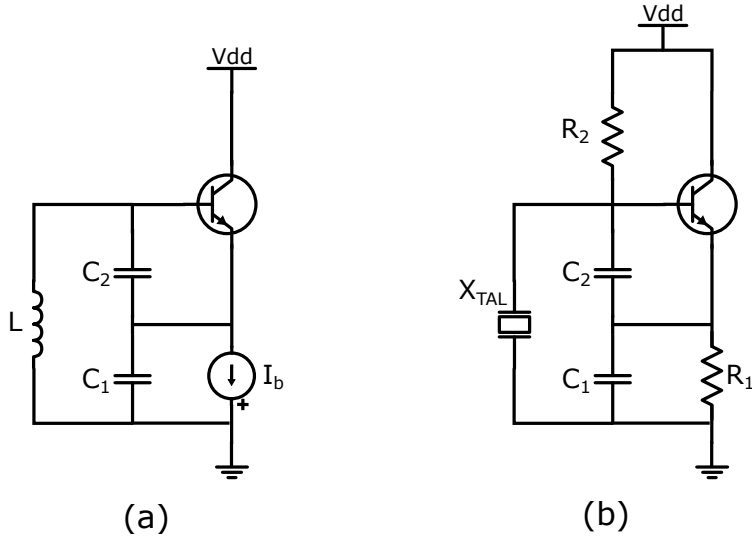


**Figure 2.2:** Schematic of LC-based (*tank*) Colpitts oscillator (a) and its equivalent Colpitts oscillator using a crystal.

capacitors into magnetic energy stored in inductors. One example is the well-known Colpitts oscillator of Figure 2.2(a). These oscillators offer a very good Q (higher Q indicates a lower rate of energy loss relative to the stored energy of the resonator), and their frequencies are suitable for their use at radio frequency applications.

- Crystal oscillators. These oscillators use the piezoelectric properties of certain crystal materials to generate the swinging output. They are very similar to LC oscillator but replacing the *tank* circuit by a piezoelectric crystal as shown in the Colpitts implementation of Figure 2.2(b). Indeed, piezoelectric crystals have an equivalent electric circuit made of impedances, capacitances and resistors. The piezoelectric phenomenon is based on the feature of certain material to be deformed by the presence of an electric field. This property is reversible so, the deformation of the material also generates an electric field. Crystal oscillators give a much better frequency stability than other topologies. Quartz oscillator are the most used in electronic systems. They are able to produce frequencies up to 30 MHz. Usually they stabilize the frequency of oscillators with higher frequencies by using systems such as PLLs.

Non-resonant oscillators have poor Q and relatively poor stability and phase-noise performance. They are used at lower frequencies where inductors are large and expensive. Oscillators without resonators are also used in IC design since high-Q inductors are difficult to realize on chip. They include R-C structures, ring oscillators, and delay line oscillators.

- RC oscillators. In this type of oscillators the feedback network forms a filter using

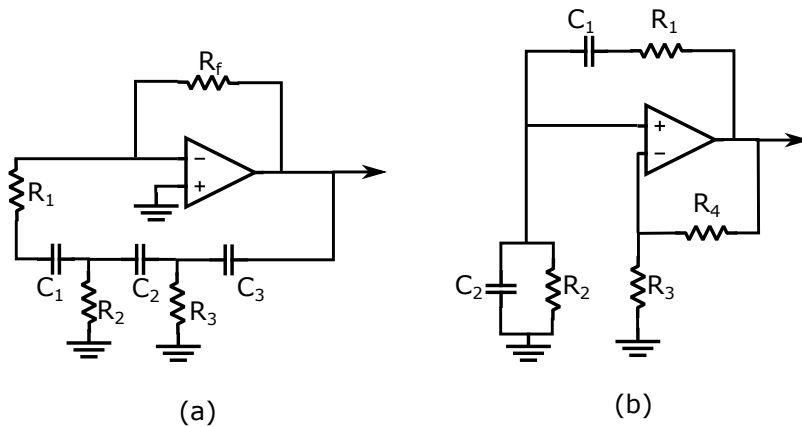


**Figure 2.3:** Schematic of a phase-shift RC oscillator (a) and a Wien oscillator (b).

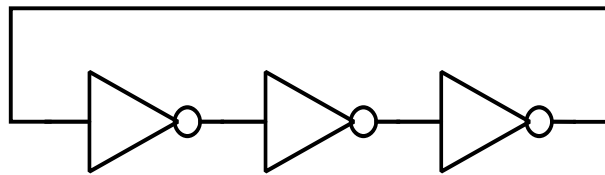


**Figure 2.4:** 3-stage ring oscillator with inverter gates.

capacitors and resistors. They are used to generate lower frequencies. The most common circuits are the phase shift and the Wien bridge oscillator. Their schematics are shown in Figure 2.3.

- Ring oscillators and delay line oscillators. They are based on a closed loop of identical elements. Each element delays the input signal and it also inverts it. The output frequency depends on the number of stages and the delay of each one. They are commonly used in IC circuits.

This thesis is focused on CMOS ring oscillators and their applications, with special emphasis on radiation applications. Therefore, from this point we will only consider ring oscillators for their study.

### 2.1.3 Ring Oscillators

A ring oscillator is a circuit made of a cascade of individual inverter stages in a feedback configuration where the output signal oscillates with a period defined by the addition of all stage delays. Usually, all the stages are identical, therefore the frequency is only dependent on the stage delay and the number of stages. The simplest implementation is the ring oscillator of Figure 2.4 which is made of three stages using inverter gates.

Abidi declares in [A<sup>+</sup>06] that the ring oscillator is one of the most widely manufactured integrated circuits of all. Foundries use ring oscillators on almost every semiconductor wafer to monitor the gate delay and speed-power product of fabricated MOS inverters. Automated measurements of oscillation frequency determine which wafers are acceptable, and which fall outside an acceptable performance and must be discarded. Ring oscillators have occupied this role since the earliest days of MOS IC technology because they are easy to build, always oscillate, and are readily measured.

One of the reasons of the utilization of ring oscillators is their lack of capacitors, inductors and resistors. The feasibility of these elements with practical values and quality required the use of great area in modern integrated circuits against the high density achievable with only transistors [Raz96]. Then designs with the absence of passive elements are suitable for very compact oscillators.

### 2.1.4 Frequency of ring oscillators

As any oscillator, the main feature of a ring oscillator is its output frequency. Several studies have tried to improve the accuracy of the ring oscillator model to calculate the oscillation frequency. All of them have followed different approaches but starting from the simplest equation for a ring oscillator with  $N$  stages:

$$f_0 = \frac{1}{2Nt_d} \quad (2.11)$$

The understanding of this expression is straightforward. If a ring oscillator is made of  $N$  equally designed stages and each stage has a time delay of  $t_d$ , then the total delay of a period  $T$  is equal to twice the value of the propagation along the whole chain. The accuracy of this expression is given by the precision of the calculation of  $t_d$ , the delay of each gate. Therefore, many studies [DS03, SY08, MS10] have focused on finding the most accurate value of this time through the analysis of every possible parameter that affects it. These parameters depend on the type of the implemented stage: CMOS, BJT, differential, etc. For example, Figure 2.5 shows the implementation of a ring oscillator with static CMOS inverters where some of the most relevant parameters that define the frequency are represented:  $W$  and  $L$  are the width and length of transistor channel,  $C$  is the capacitance of a node and  $V_{dd}$  is the bias voltage.

Other studies [JSS10, RBH14] consider that Equation (2.11) is not accurate enough and they propose to use linear analysis to determine the oscillation frequency. That way, the oscillation frequency of a free running ring oscillator can be calculated by the application of the linear analysis explained in Section 2.1.1. The first step is to define each of the components of the linear model: the amplifier and the feedback network.

To define the amplifier we will consider the example of the CMOS ring oscillator and the characteristic of a CMOS inverter [RCN02]. The static CMOS normalized transfer

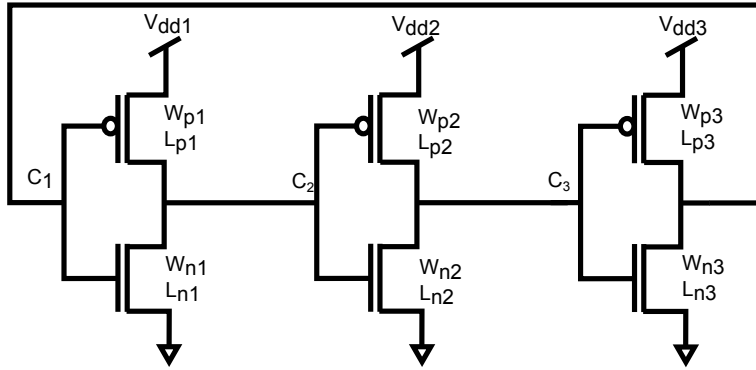


**Figure 2.5:** 3-stage ring oscillator with CMOS inverter gates.

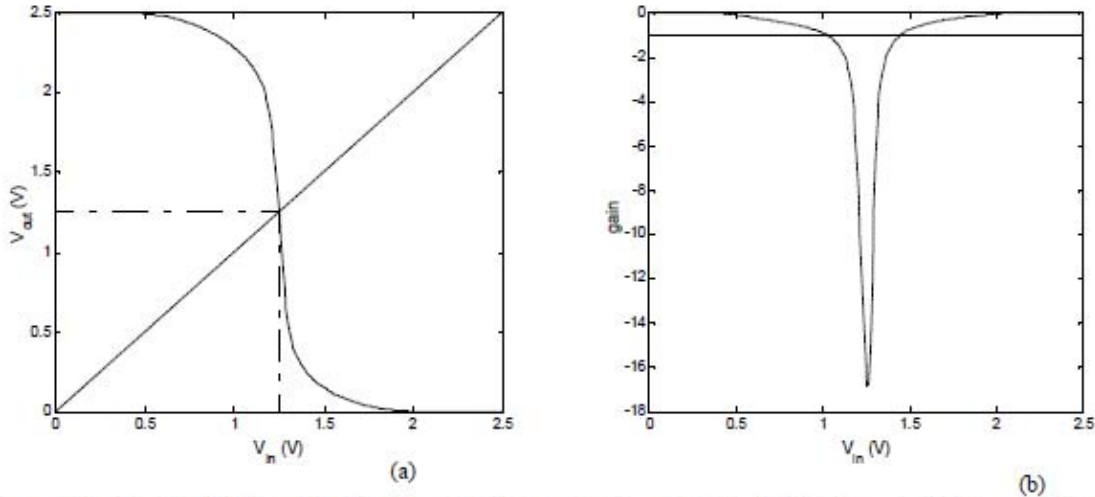


**Figure 2.6:** Simulated Voltage Transfer Characteristic (a) and voltage gain (b) of CMOS inverter [RCN02].

characteristic is plotted in the Figure 2.6 (a). This circuit is usually viewed from the point of view of digital designers considering the operation of the device only in the region of extreme nonlinearity where at the input logic '0' the inverter output is a logic '1' and inversely with an input equal to '1' the output is '0'. However, if the voltage gain of this inverter (Figure 2.6 (b)) is also considered, there is a linear region where the static CMOS inverter acts as an analog amplifier. This region is quite narrow and its characteristics are not the best for an amplifier but they are enough to explain the start of the oscillation fulfilling the Barkhausen criterion. In this case, the feedback network is modeled as a system with a transfer function  $G(s) = 1$ .

Replacing the CMOS inverter by an equivalent amplifier with voltage gain  $A(s)$ , the linear analysis in the s-domain with the closed loop configuration is:

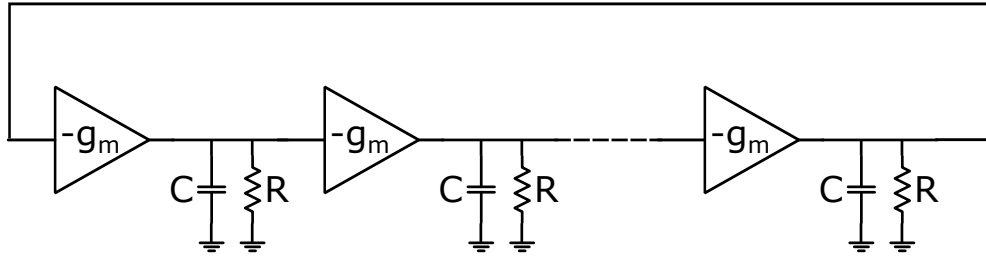


**Figure 2.7:** Model of ring oscillators for Linear Analysis.

$$H(s) = (A(s))^N \quad (2.12)$$

and consequently with the Barhausen criterion:

$$\angle(A(j\omega_0)) = \theta = \pm \frac{n360^\circ}{N} \quad \text{and} \quad |(A(j\omega_0)|^N = 1 \quad (2.13)$$

where  $\theta$  represents the phase shift of each stage.

The linear model also considers the interconnection between the stages to calculate the value of the gain. The interconnection can be modeled by RC elements as shown in Figure 2.7, where  $g_m$  is the transconductance of the inverter. Using this model, the value of  $A(j\omega)$  is:

$$A(j\omega) = \frac{-g_m R}{1 + j\omega R C} \quad (2.14)$$

And putting together Equations (2.13) and (2.14) the start conditions for the ring oscillators are:

$$\omega_0 = \frac{\tan\theta}{RC} \quad \text{and} \quad g_m R \geq \frac{1}{\cos\theta} \quad (2.15)$$

Particularizing for a 3-stage ring oscillator:

$$\omega_0 = \frac{\sqrt{3}}{RC} \quad \text{and} \quad g_m R \geq 2 \quad \text{for } N = 3 \quad (2.16)$$

The oscillation frequency can be calculated from the above equations but this frequency is actually the start frequency of oscillation. However, the characteristics of the CMOS inverter of Figure 2.6 evidence the nonlinearity behavior of these devices. Moreover, some authors [ES08, CLC09, GAS10] argue that linear analysis is not sufficient and fails to detect many behaviors. These models are based on using a nonlinear model of the digital inverter similar to the model of Figure 2.8(b) used in [ES08]. With this model, the nonlinearity is introduced by the transfer function of the inverter:

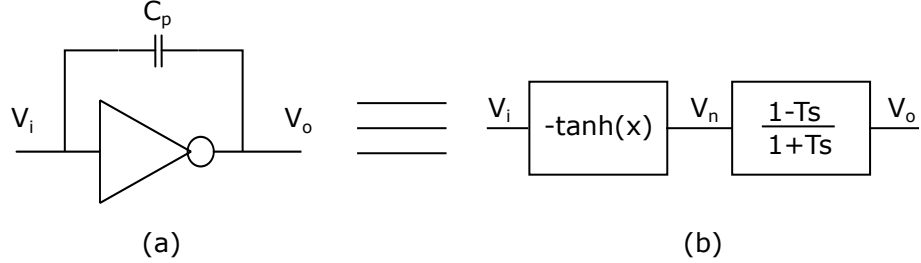


**Figure 2.8:** (a) Digital inverter symbol with parasitic capacitor  $C_p$  and (b) proposed nonlinear model [ES08].

$$V_n = -V_{sat}\tanh(V_i/V_s); \quad (2.17)$$

where  $V_{sat}$  is the saturation voltage of the inverter and  $V_s$  adjusts the slope of the linear region. The interconnection and parasitics are modeled by an all-pass filter with a transfer function:

$$T(s) = \frac{1 - Ts}{1 + Ts} \quad (2.18)$$

where  $T = C_P r_{out}$  is the filter time constant and  $r_{out}$  is the output resistance of the inverter. The following differential equation models the complete behavior of the inverter:

$$V_o + T\dot{V}_o = -V_{sat}\tanh(V_i/V_s) + T\frac{V_{sat}}{V_s}[1 - \tanh^2(V_i/V_s)]\dot{V}_i \quad (2.19)$$

Defining  $x = V_i/V_{ref}$ ,  $y = V_o/V_{ref}$ ,  $\alpha = V_{ref}/V_s$  and  $\beta = V_{sat}/V_{ref}$  that equation transforms into:

$$y + \dot{y} = -\beta\tanh(\alpha x) + \alpha \cdot \beta[1 - \tanh^2(\alpha x)]\dot{x} \quad (2.20)$$

where time is normalized with respect to  $T$  and  $V_{ref}$  is an arbitrary reference voltage. And  $\alpha \cdot \beta$  defines the internal gain  $A$  of the inverting amplifier. Applying this model to a 3-stage ring oscillator, the equations that define the behavior of each node ( $x, y, z$ ) are:

$$\begin{aligned} \dot{x} &= -x - \beta\tanh(\alpha z) + \alpha\beta\dot{z}[1 - \tanh^2(\alpha z)] \\ \dot{y} &= -y - \beta\tanh(\alpha x) + \alpha\beta\dot{x}[1 - \tanh^2(\alpha x)] \\ \dot{z} &= -z - \beta\tanh(\alpha y) + \alpha\beta\dot{y}[1 - \tanh^2(\alpha y)] \end{aligned} \quad (2.21)$$

The solution to these equation makes  $w_0 = T/\sqrt{3}$  and  $> 1$ . Then while the oscillation frequency can be equal in both models, the condition of the inverter gain is less restrictive with the nonlinear analysis than with the linear model. Thus, the application of each model depends on the accuracy and characteristics required in each application.

All of these examples show how the efforts of previous studies have focused on determining, with high accuracy, the frequency of a ring oscillator due to being it considered its most important feature. However, as we will see in this thesis: First, the simplest approach using Equation 2.11 is enough for designing an application of ring oscillator as a Total Ionization Dose Monitor. And second, previous studies have forgotten to explore other features of ring oscillator such as the duty cycle. We will use the same Equation 2.11 to derive a model of duty cycle in ring oscillators. And we will use that model to implement improved ring oscillator based applications.

## 2.2 Radiation Effects in Electronics

The Introduction of this thesis has summarized the most important facts and research topics of radiation effects in electronics along the last decades. Those topics and the relevant concepts needed to understand this thesis are introduced in this section. First, the typical units used to refer the physical magnitudes of radiation effects are outlined. Then, the different environments able to produce radiation effects in electronic systems are characterized. Those radiation effects are classified and briefly described together with some of the mitigation techniques used to overcome their impact. Finally, the potential hazards of ring oscillators working within radiation environments are explained.

### 2.2.1 Radiation Units

The next definitions and units characterize the physical interactions of materials with radiation particles.

#### Rad and Gy

The rad and gray (*Gy*) are the units of absorbed radiation dose. Even though the gray is the International System (SI) unit, the rad is used for most published works by academia and industry community in radiation effects. The absorbed dose is defined as the amount of energy deposited in a material, so one rad corresponds to 100 ergs of energy deposited in one gram of material. As absorption depends on the target material, the radiation dose is indicated with the target material, for example, 100 rad(*SiO<sub>2</sub>*). One *Gy* corresponds to a deposition of 1 joule per kg of target material. Then, one rad corresponds to  $10^{-2}$  *Gy* (1 rad = 1 c*Gy*).

#### Linear Energy Transfer

The interaction of a particle passing through matter results in the transfer of its energy to the material. This interaction is measured by the linear rate of energy loss and it is called

Linear Energy Transfer (LET). Therefore, LET is dependent on the target material and on its density. Usually, the LET use values normalized to a unit density for each material. The result is an energy loss per unit length,  $dE/dx$  ( $MeV/cm$ ), divided by the material density,  $\rho$  ( $mg/cm^3$ )

$$LET = \frac{1}{\rho} \cdot \frac{dE}{dx} \quad (MeV \cdot cm^2/mg) \quad (2.22)$$

## Cross Section

The cross section,  $\sigma$ , is defined by the ratio of the number of single events observed on the device by the particle fluency (particles per  $cm^2$ ) received by the component. Therefore,  $\sigma$  is a measure of the sensitivity of a device. The cross section can also be interpreted as the probability that a particle impact provokes a single event in the hit node. The equation used to calculate the cross section is:

$$\sigma = \frac{\# \text{ of observed events}}{\text{fluency}} \quad (2.23)$$

### 2.2.2 Environments

The design of electronic circuits for radiation applications is highly dependent on the environment they will be exposed. In order to have reliable, cost-effective designs and implement new devices, the nature of the environment must be understood. Underestimating the radiation levels leads to excessive risk and can result in degraded system performance. Overestimating the radiation levels can lead to excessive shielding, reduced payloads, over-design and increased cost [XOO12]. We divide the environments into two different categories: space, which has been extensively characterized in terms of radiation since the first explorations, and terrestrial, where radiation has become a problem in the last years due to the shrinking of the technology.

#### Space Environment

Before the space era the only manifestations of the presence of radiations in space were the deformation of the ionized tail of comets caused by the solar wind, the aurora borealis whose origin was not well understood and the ionization of air produced by cosmic radiation [BX08]. Since the first space missions, it was evident that the space environment is a highly disruptive medium for electronic devices. Beyond the natural protection provided by a planet's atmosphere, various types of radiation can be encountered. Figure 2.9 shows an interpretation of the different environments found in space due to the interaction of particles generated at the Sun and the planets' magnetosphere. These particles are generally

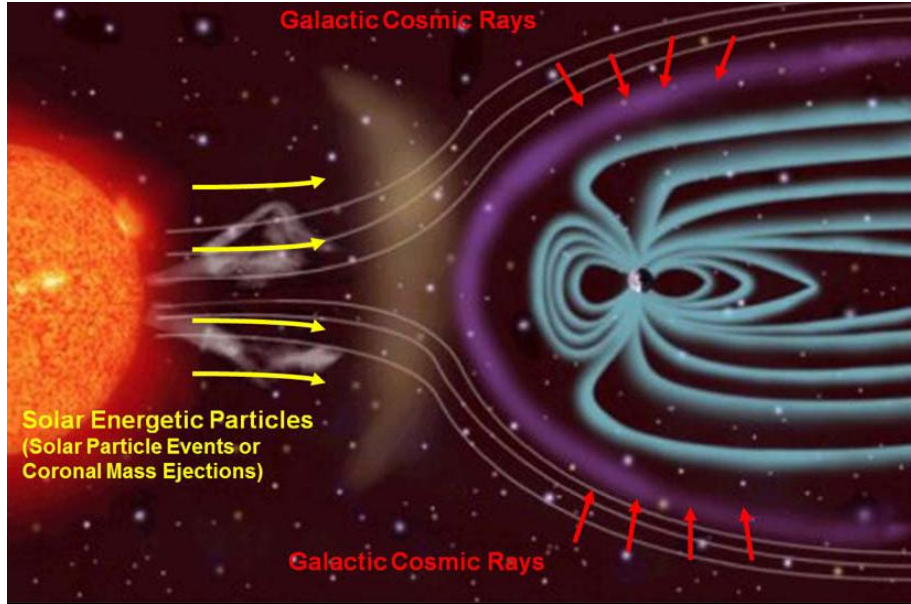


**Figure 2.9:** Radiation space environment and sources (source JPL nasa.gov).

classified into three different groups:

- Galactic Cosmic Rays (GCRs) originated outside our solar system.
- Particles that are emitted from the Sun during solar particle events.
- Particles trapped by planetary magnetic fields.

#### *Galactic cosmic rays*

GCRs consist of stellar energetic particles with frozen-in coronal composition, first injected at MeV energies by stellar activity and then later accelerated to GeV and TeV energies by passing supernova remnant shock waves [MDE97]. They include all the naturally formed elements and they are the most energetic particles of all in space environment. The energies of these particles peak around 1 GeV/am and can be higher than  $10^{10}$  GeV in total kinetic energy. The GCR composition and intensity is highly dependent on the solar cycles that last for 11 and 22 years [WL88]. The important radiation effect from GCRs is SEEs. The electronic components susceptible to SEEs are typically protected by aluminum. Several GCR models have been developed to describe the GCRs and to be able to design the electronic systems according to the radiation risks they will suffer during their lifetime. The models are based on fitting the dataset collected by many space missions that have characterized the types and fluxes of particles. The most important

models are the Badhwar-O’Neill Model [GOS15], the Buchvarova-Velinov Model [BD13], the CHIME Model [CCC<sup>+</sup>94] and the Nymmik Model [Nym06]. All these models were evaluated against an extensive database of published measurements of elemental differential energy spectra spanning the time period from 1954 to the present. The most recent version of Nymmik Model was selected as the international standard model (ISO 15390:2004).

### *Particles generated during solar particle events*

The Sun generates a huge amount of particles through many kinds of eruptions. Among them, the most important and relevant for the study of their impact in electronics are the solar flares and the Coronal Mass Ejections (CME). They are deeply described in [MSHL01, ADK99]. Both involve gigantic explosions of energy, but are essentially quite different. They may occur at the same time — the strongest flares are almost always correlated with coronal mass ejections — but they generate different emissions, they look and travel differently, and they have different effects.

Solar flares result when the localized energy storage in the coronal magnetic field becomes too large and causes a burst of energy to be released. Flares can last minutes to hours. Traveling at the speed of light, it takes eight minutes for the light from a solar flare to reach Earth. Some of the energy released in the flare also accelerates very high energy particles that can reach Earth in tens of minutes. They tend to be electron rich, and have high  ${}^3\text{He}$  content relative to  ${}^4\text{He}$ .

A CME, on the other hand, is a large eruption that hurls solar matter into space (a gas of free ions and electrons) that drives a shock wave outward and accelerates particles. Traveling over a million miles per hour, the plasma takes up to three days to reach Earth. CMEs are proton rich and have small  ${}^3\text{He}$  content relative to  ${}^4\text{He}$ .

It is critical to define the content and energy distribution of solar particle events for bounding the performance of advanced electronics within radiation environments, however it is a really difficult task. To overcome this challenge, several solar particle event models have been created [FSWG93, XBS<sup>+</sup>99, XSB<sup>+</sup>00, ADK99].

### *Particles trapped inside Earth’s magnetosphere*

The magnetosphere is formed by the interaction of the solar wind with Earth’s magnetic field. This dipole field traps protons and electrons within two magnetic field lines called the Van Allen Belts. Since its discovery in 1959 [VAF59a, VAF59b], these radiation belts have been the topic of many studies and an important problem for electronic devices passing through these areas. Trapped protons have energies up to hundreds of MeV with fluxes up to  $105 \text{ cm}^{-2}\cdot\text{s}^{-1}$  for energies  $>10 \text{ MeV}$ .

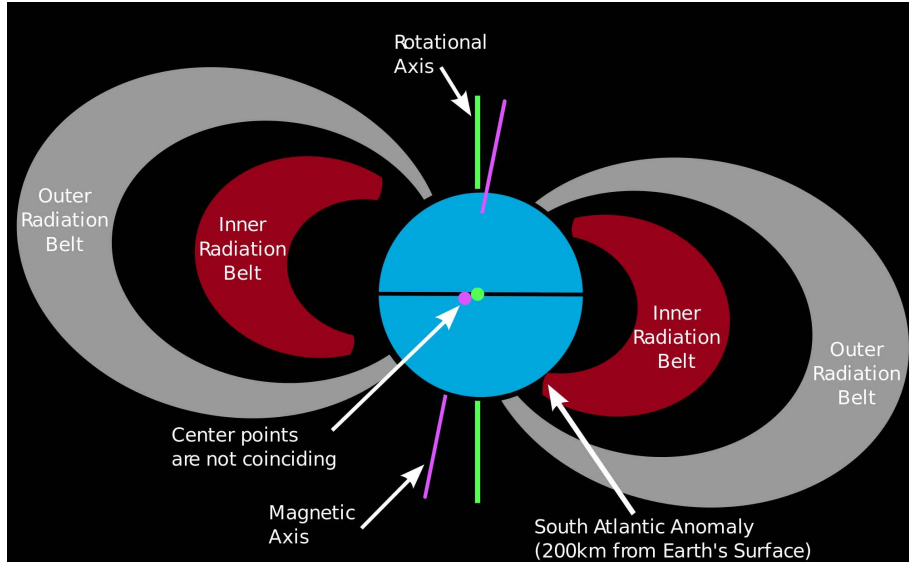


**Figure 2.10:** Sketch of the Van Allen belts as a result of solar particles interaction with Earth's magnetosphere (source JPL nasa.gov).

It is specially important the fact that the rotational and magnetic axes are misaligned by approximately  $11^\circ$  what creates a particular zone called South Atlantic Anomaly (SAA). Because of that tilt and their center displacement, part of the inner edge of the trapped proton belts is at a much lower altitude off the southeast coast of Brazil. The SAA and the Van Allen belts are shown graphically in Figure 2.10.

The composition and dynamics of particles within radiation belts continue being a hot topic nowadays and recently, a pair of probes [SRB<sup>+13</sup>] were sent to explore the characteristics of the radiation belt on Earth's magnetosphere. There are also various Earth-based trapped proton models available, including AP-9, CRRESPRO or AE9 whose data have been reviewed in [JOH<sup>+15</sup>].

The cosmic particles are not only trapped in Earth, it is a phenomenon typical of every magnetized planet. The five strongly magnetized planets in the solar system, Earth, Jupiter, Saturn, Uranus, and Neptune have their own magnetosphere with many similarities and specificities. They have robust electron radiation belts [MF10].

## Terrestrial Environment

At terrestrial level there are mainly two types of particles that contribute to the generation of a radiation environment able to interact with the structure of semiconductor electronic devices. They are the neutrons, generated by cosmic interaction with atmosphere, and the alpha particles, resulted from the natural decay of radioactive materials [RG05].

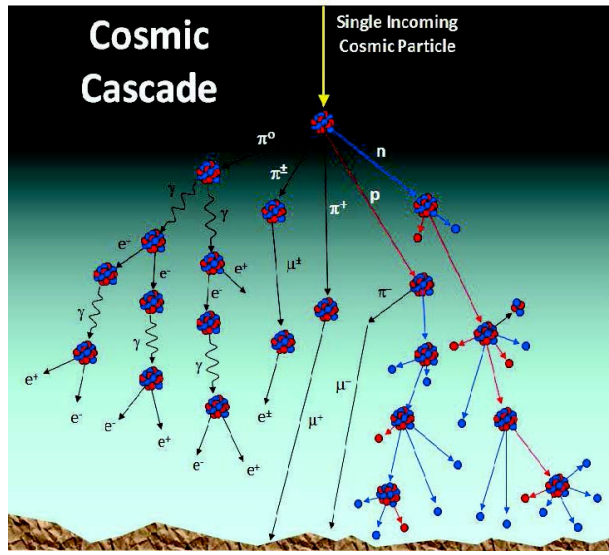


**Figure 2.11:** Cascade interactions of cosmic particles with the atoms of the atmosphere.

### High-Energy Neutrons

As cosmic ray and solar particles enter the top of the Earth's atmosphere, they are attenuated by interaction with the nitrogen and oxygen atoms that conforms the majority of atoms of the atmosphere. The result is a production of complex cascades of secondary particles through nuclear reactions with the nitrogen and oxygen nuclei. These secondary particles continue interacting with the atoms of the atmosphere creating tertiary particle cascades and so on (as shown in Figure 2.11). At terrestrial altitudes, less than 1% of the primary flux reaches sea-level where the particle flux is composed predominantly of electrons, muons, neutrons, and a smaller fraction of protons. Due to the relatively high LET of the resulting secondary particles from neutron reactions and their abundance as compared with most of the other particle types, neutrons are considered the dominant source in terms of radiation effect in electronics [HS00]. Nevertheless the extremely shrinking of technology allows the appearance of single effects as a result of interaction with other particles such as muons [SRM<sup>+11</sup>].

There are three primary factors that modify the neutron flux at a particular terrestrial location and time. The dominant factor is altitude, the neutron flux varies about twenty times from sea-level to high altitudes (around 3000 m). The second factor that modulates the neutron flux is the latitude, at sea level, the neutron flux is twice at equatorial latitude than at polar latitudes. The solar activity cycle also defines the neutron flux of terrestrial environment. This cycle lasts about eleven years and its effects can modify the neutron flux from the minimum to the peak in three times, although solar flares and CMEs activity could also generate sudden and intense changes in the neutron flux [KPnS15].

### *Alpha Particles*

The alpha particles are emitted from the disintegration of unstable isotopes. They are composed of helium atoms with two protons. This process is a natural behavior of this kind of isotopes and it does not need any external interaction or energy. When an alpha particle travels through a material, it loses its kinetic energy predominantly through interactions with the bound electrons of that material and thus leaves a trail of ionization in its wake. The higher the energy of the alpha particle, the farther it travels before being absorbed by the material. The importance of alpha particles is because the ceramic packages used in the fabrication processes of electronic devices are able to emit this kind of particles [SMT94]. Alpha particles are easily stopped by device packaging materials as their range is of few tenths of microns. Thus, alpha emission outside of the device does not need to be considered. Only alpha emission internal to the device can interact with circuits and cause a soft error event.

The impact of alpha particles radiation in electronic devices plays an important role especially for accelerated radiation test. As will be explained in Chapter 4, this kind of radiation is very common for testing circuits reliability against SEEs.

### **2.2.3 Radiation Effects**

The interaction of the energetic particles introduced in the previous section with the materials used for the fabrication of electronic devices causes different types of radiation effects. These effects have been deeply studied for almost every material, fabrication process and technology node developed for semiconductor electronics. As a summary of those studies, the effects are the consequence of the energy deposition as a result of the interactions with the energetic particles. The energy is deposited by the passage of those particles through materials, either through direct or indirect processes. In semiconductor materials, that energy is converted into electron-hole pairs and atomic dislocations. They are usually divided into two different categories: cumulative effects or SEEs.

#### **Cumulative Effects**

Cumulative effects refer to the effects that are the result of long term exposition to radiation environments. Depending on the characteristics of the exposed particles, the cumulative effects can vary just the charge distribution within the device structure what is called TID or they can physically affect the atomic structure of the material what is referred as Displacement Damage Effect (DDE).

#### *Total Ionization Dose*

TID has been the most studied phenomenon of radiation effects in electronic devices. This is because the degradation could be evaluated at the end of the application lifetime without the need of continuously monitoring the system expecting for an error.

The electron-hole pairs generated by the interaction of ionized particles with semiconductor materials leads to a progressive degradation of devices. For example, in MOS transistors, the new generated carriers produce a redistribution of charges in the structure as a consequence of the trapping of the carriers in the interfaces and gate oxides provoking the alteration of threshold voltages. The effect of TID is accumulative but, at the same time, it is generally reversible through the application of annealing techniques what allows the partial recovering of the degradation by thermal processes.

### *Displacement Damage Effects*

DDE refers to the dislodging of atoms from their normal lattice sites in a target material by impinging energetic radiation. The resulting damage causes degradation of the electronic and optical properties of materials and devices. That degradation is generally due to the introduction of new energy levels in the semiconductor bandgap, which changes properties such as recombination lifetime [SP13]. Displacement damage produces permanent changes in material and device properties, although thermal and injection annealing can alter the observed effects.

In general, minority-carrier devices are relatively sensitive and majority-carrier devices are relatively insensitive. For example, MOS devices generally are radiation-tolerant in terms of displacement damage effects. Although at sufficiently high particle fluences, all devices will eventually degrade due to displacement damage effects [SMM03].

### **Single Event Effects**

Opposite to the long term effects that cause the progressive degradation of the electronic devices, the SEEs denote all of the phenomena created by the impact of an individual energetic particle through the semiconductor or insulator materials used in the fabrications of integrated circuits [Nar08]. There are several mechanisms encompassed within the SEE term. The following is a brief list and description of each type:

- Single Event Transient (SET). A SET induces a pulse generated at the hit node and that propagates along the circuit. The pulse dynamics are determined by both process and circuit parameters. Whenever the charged particle passes through a depletion region a transient is created. Whether or not this transient results in an error depends on a number of factors, including the final pulse width, pulse amplitude and circuit dynamics [BEM<sup>+</sup>06]. SETs are a major concern for combinational circuits.

- Single Event Upset (SEU). A SEU is a soft error produced by the modification of a storage element as a consequence of the impact of a radiation particle. This effect can be motivated by two different phenomena. First, if the impact occurs in a sensitive node of the storage element, then the collection of charge can be enough to alter the value of the stored bit. The other mechanism that produces a SEU is the storage of a propagated SET. If a SET occurs in a combinational path ending in a register and the clock edge arrives synchronized with that SET, then the induced pulse is stored and converted into a soft error. These two options make the SEU rate dependent on the technology, the topology of the circuit, the design of storage elements and the frequency of the system. As this effect affects mostly memory elements, the focus on studies of SEUs is on SRAMs and Flip Flops mainly [YSX<sup>+</sup>15].
- Multiple Bit Upset (MBU). MBUs correspond to the generation of multiple and parallel SEUs in some adjacent sensitive nodes. In this case, only the production of soft errors by the collection of charge in the storage element is taken into account. Therefore, this effect requires an interaction that involves more energy than SEUs to flip more than one node. The shrinking of the technology is enhancing the MBU to similar rates than SEUs [TPR<sup>+</sup>06].
- Single Event Functional Interrupt (SEFI). Any SEE that pushes the system to a general malfunction is called a SEFI. SEFIs might be temporal and they usually are solved by resetting [KPCC97]. SEFI can be considered as a second order effect as it is generated by the consequence in the system function of other SEE, generally, as a consequence of a latent SEU in a very sensitive memory.
- Single Event Latchup (SEL). A SEL is the result of the triggering of a parasitic bipolar circuit that provides a positive feedback loop in silicon structures [ARH<sup>+</sup>15]. It can be destructive unless the design limits the current of the circuit.
- Single Event Burnout (SEB) and Single Event Gate Rupture (SEGR). These effects are destructive and they occur mainly in power MOSFETs due to the high voltage level they manage [Tit13]. SEB is caused by the increasing of the drain-source voltage above the second breakdown voltage of power MOSFETs. On the other hand, SEGR usually results in a resistive short between the drain and gate through the gate dielectric.

### 2.2.4 Mitigation Techniques

All the radiation effects previously presented have been studied and characterized in several works. They have not only been studied but many different solutions have also been

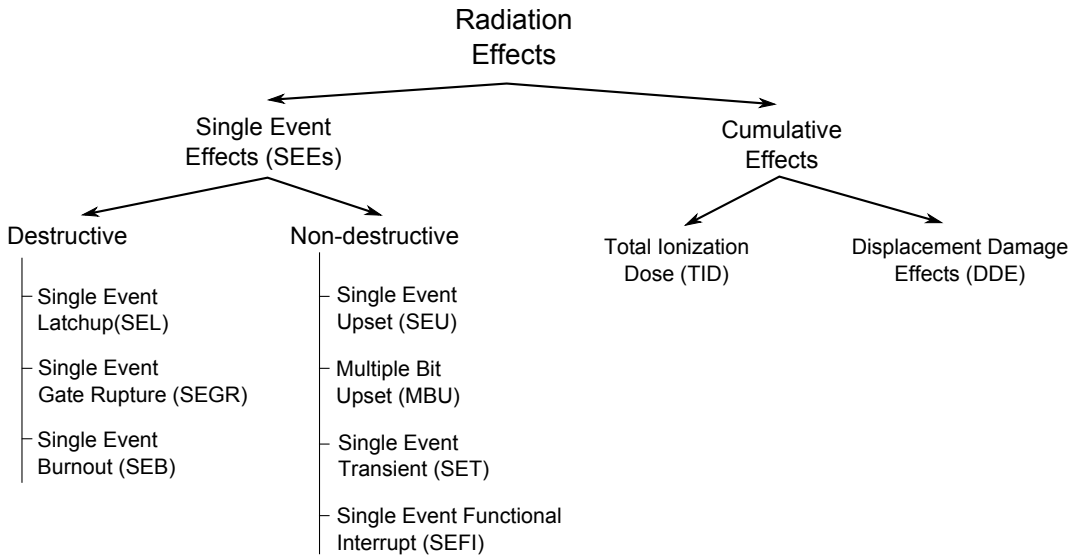


**Figure 2.12:** Classification of Radiation Effects in Electronics.

proposed to remove or mitigate the negative effects they produce in electronic system performance. The mitigation techniques proposed are very diverse and they use different approaches to solve the problems. The selection of a particular methodology depends on the particular constraints of each application such as: environment, resources, cost, etc. In this section the most relevant methods to overcome the radiation effects are summarized and categorized.

## Shielding

The first approach to mitigate the effects of radiation is the use of shielding. This method tries to reduce the flux of particles that reach the electronic circuits by using dummy materials to trap the environment particles. These materials are specially selected for their absorption of radiation particles due to their atomic structure together with other requirements of the particular application such as thermal resistances, lightweight or mechanical features.

In some cases the shielding is intrinsically implemented by the structure of the space-craft in space applications. In other cases, the location of circuits inside the system package must be taken into account to minimize the radiation particles in sensitive circuits. Shielding is predominately used to mitigate TID [ZMG12] but it is also used to protect against single events even though it is not as effective [PXS<sup>+</sup>10].

## Radiation Hardened By Process

Radiation Hardening By Process (RHBP) is a term that describes a method to harden a device to radiation effects using the fabrication process. Opposite to the shielding where the design or the fabrication process of electronic components are unaltered, the RHBP is based on carefully selecting the bulk material or by modifying the process and the design of device layers used to create a semiconductor device.

One of the most extended technology used for RHBP is the Silicon on Insulator (SOI) [RZB<sup>+</sup>12, PAH14]. SOI technologies are designed to be relatively immune to TID and they have also shown some immunity to SEEs [dSFdSR<sup>+</sup>13]. SOI MOSFETs are more tolerant to single event, thanks to the buried oxide layer, that isolates the active silicon region from the substrate, in comparison to transistors implemented with CMOS conventional bulk technology [GRP<sup>+</sup>13, RAGM]. Some of the III-V materials such as Gallium Arsenide (GaAs) [NZS<sup>+</sup>15] and Silicon Germanium (SiGe) [Cre13] have shown resistance to radiation effects. Modern technologies such as FinFETs have also proved being a good alternative to bulk technologies for radiation sensitive applications [HAR15].

The benefit of the RHBP technique is the enhanced hardness without changing any design. While the main drawback of the RHBP technique is the additional process steps required during fabrication or the use of a niche technology. Both approaches increase the cost of fabrication exponentially.

## Radiation Hardened By Design

Another approach to mitigate the radiation effects in electronic systems relies on standard commercial technologies to achieve the hardening by design techniques. This method is called Radiation Hardening By Design (RHBD). As the design of a system is divided into different levels of abstraction, the application of RHBD strategies is also implemented at each different level, from the basic structure level to the system level. These types of techniques have been the goal of most of the studies due to the drastic reduction of costs compared to the use of special RHBP technologies [GMW08, CLS15]. However, in many applications it is not possible to fulfill the requirements by using only RHBD techniques and they are used together with RHBP technologies or shielding designs. Next, we outline some of the most used RHBD methodologies divided according to the three different design levels of abstraction: layout, circuit and system.

### *Layout*

The design modifications that are implemented in the layout level are mainly focused on two aspects, transistor sizing and charge-collection avoidance. At this level TID and SEEs mitigation techniques are feasible in contrast to the circuit and system perspective.

Increasing the overall transistor size improves the transistor performance against radiation effects [ZM04, ZM06]. Instead of just increasing the transistor size, other approaches have also proposed the use of different transistor structures [SGA02, XIS14]. It is important not only the size of the transistor but its location with respect to other sensitive nodes as is shown in [BSA<sup>+</sup>05]. However, the system tends to operate slower due to the increased capacitance of larger devices. While RHBD increases the transistor size, it maintains adherence to the process design rules. This allows RHBD to be implemented on any process without requiring waivers or process modifications. Implementing RHBD is just a matter of creating a new library and then synthesizing the design using that library.

Apart from using different transistor layouts, the rest of layout mitigation techniques tries to avoid the charge collection of radiation induced carriers. This goal is achieved by using special structures such as guard rings or dummy contacts to favor the path of those charges through these structures instead of through device interfaces [BSA<sup>+</sup>05].

### *Circuit*

As mentioned above, working at circuit level is suitable for solving SEEs while cumulative effects are out of the scope from this level of abstraction. Circuit techniques are based on redesigning the most basic gates or devices to tolerate the induced effects of a single event. At this level, flip flops have occupied most efforts to design radiation tolerant circuits. This is a direct consequence of the vulnerability of these devices to SEUs together with their relevancy in every sequential design. To assure the hardening of circuits, every method at circuit level is based on redundancy. Redundancy can be used to mitigate SEE as is shown in the three next implementations of radiation hardened flip flops [LCS<sup>+</sup>16].

- Triple Modular Redundancy

Triple Modular Redundancy (TMR) is a very used structure to mitigate the effect of SEUs or SETs [PK15, CBDN14, MKY<sup>+</sup>13]. Figure 2.13 shows the basic TMR scheme. Using three identical flip flops with a single input, the three outputs are voted on by a majority voter circuit. The voter drives the output with the signal identical at least in two of its inputs. TMR is used because it is very unlikely that more than one circuit would be affected by an upset or transient at a given time. To avoid that special case, the three modules are usually physically separated using layout mitigation techniques so that in new technologies there is not a multiple-node hit creating two simultaneous upsets. In this type of circuits, the voter is the most sensitive part, so it requires special treatment [DGA14].

- Temporal Latch

The TMR flip flop is hardened to SETs if the particle hits only the input of one the replicated flip flops. However, if the particle impacts in the common input, it could

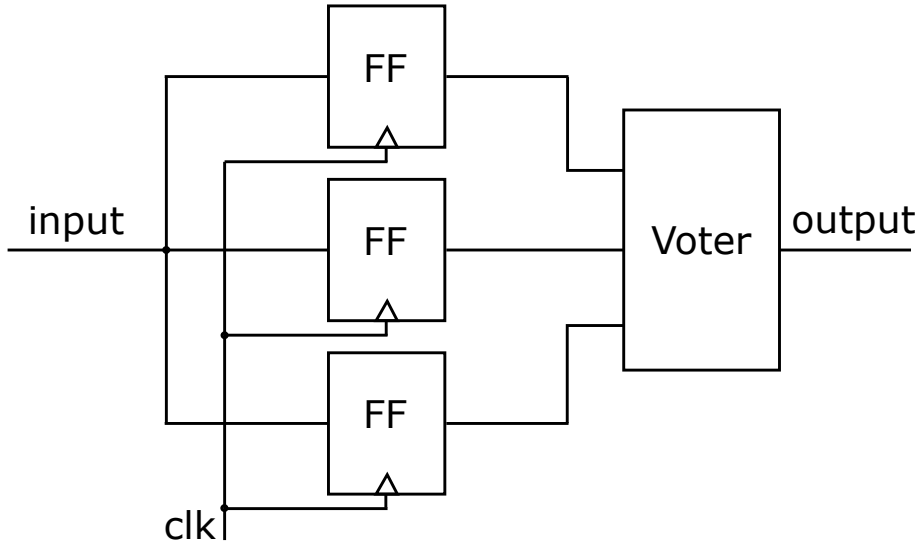


**Figure 2.13:** Triple Modular Redundancy scheme used for SEE tolerant Flip-Flops.

be translated into a failure at the output. This situation is avoided using a temporal latch [MMCK10, SCM<sup>+</sup>11]. The temporal latch is similar to the TMR one but in this design the three inputs to the voter are delayed by a specified time ( $\Delta t$ ). The hardening is based on causing a delay on at least two of the inputs to the majority voter in case a transient occurs on the input with enough energy to change the state of the general input. These delays will provide the majority of the signals, at least two out of three, to be correct.

- Dual Interlocked Cell

The disadvantage of both flip flops designs is the use of resources is tripled with respect to the unhardened design. Instead of replicating the flip flops, the other solution that was proposed and that has been used as a standard to compare the performance of flip flops in radiation environments is the Dual Interlocked Cell (DICE) [CNV96]. This cell replicates the internal storage node of each latch so that a strike on any single node will not create an upset. Using this technique requires careful layout of the physical cell so that two sensitive nodes are not in close proximity.

### System

The system approach is the highest level of abstraction of RHBD techniques. It treats the whole system or part of it as a black box whose outputs are susceptible to be wrong because of radiation effects but they can be corrected. As it is not possible to monitor internal nodes, the system proposal tries to solve the persistent problems such as SEUs or

MBUs and their potential consequences such as SEFIs without dealing with internal SETs. Three of the most used techniques are:

- TMR and Time-Triple Modular Redundancy

TMR is also applicable at system level as it is at circuit level. The general scheme is the same for all types of TMR, three items followed by a voter. In this case it is done at the component level. For example, the component can be a processor [GOB13] or an FPGA [HALV11] or a simple circuit that performs a particular task [SCEGV15]. Then, the TMR would be done using three processor chips or three FPGAs or three identical implementations of the circuit and a voter. Given the complexities of a bigger system, the voter would need to be nearly as complex. Hence, the application of TMR at this level includes complexity in communication and synchronization.

Time-Triple Modular Redundancy (TTMR) is used in a processor application and involves the use of hardware and software to combat errors [CM03]. TTMR combines time and spatial redundancy within a Very Long Instruction Word microprocessor or DSP to achieve its unique SEU mitigation capabilities.

- Scrubbing

Scrubbing is quite frequently performed on memories and SRAM based FPGAs [WH16, HALV13]. SEUs and MBUs in the configuration memory of SRAM based FPGAs can be mitigated by writing a known and correct bitstream to the corruptible device. This technique is often referred to as scrubbing and several types of implementations can be found [SVIE15]: blind/readback, device/frame-oriented, periodic/on-demand or external/internal. The differences between the different implementations are how and when the configuration memory of this devices is read. The two critical points of scrubbing are that the correct bitstream called “golden” needs to be a fully reliable memory and the availability of the system during writing stage depends on the critically of the system.

- Error Detection And Correction

Error Detection And Correction (EDAC) is used to detect errors and allow them to be corrected [CCTM16]. There are many types of EDAC from simple single parity bit schemes to multiple bit coding schemes. Depending on the type of EDAC used, it can detect and correct single or multiple bit errors. EDAC schemes use extra bits to store information necessary to recreate the correct bit.

Figure 2.14 classifies the different strategies presented to design reliable applications within radiation environments. As every design requires different radiation tolerance, the

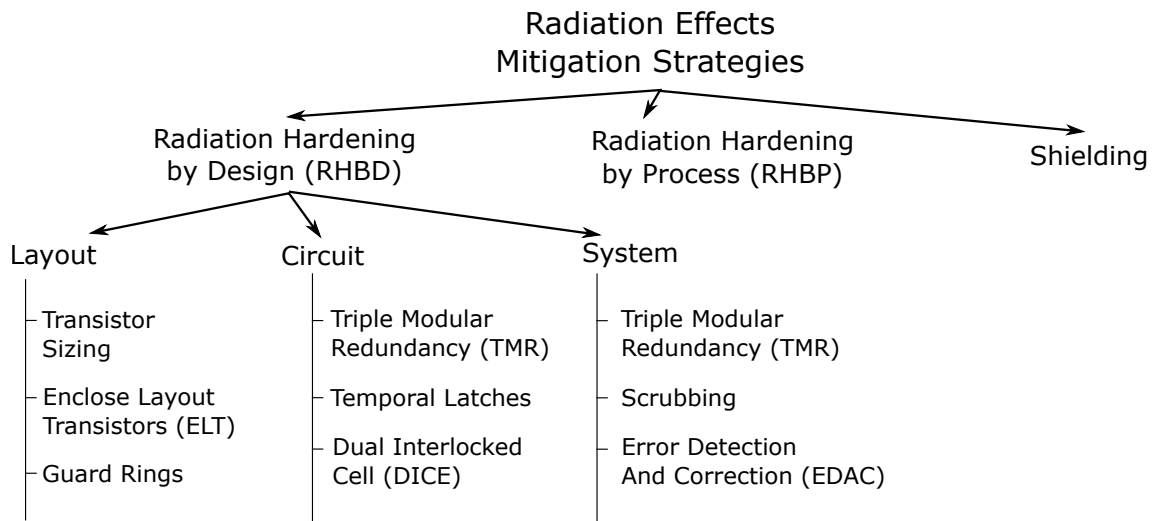


**Figure 2.14:** Classification of Radiation Effects mitigation strategies.

type of mitigation technique to be implemented will hardly depend on each particular application.

Attending to the mentioned mitigation techniques, the industry of semiconductors for radiation environments has utilized mainly three different types of technology to implement systems suitable for operating in those especially hostile conditions. The first approach is the use of technologies that are inherently hardened against radiation effects. They implement some RHBP techniques that assure a high tolerance. The second approach uses RHBD techniques in commercial technologies to generate a system that is tolerant to radiation effects. And the third methodology is based on using Commercial Off-The-Self (COTS) components. COTS term refers to any electronic device that does not have guaranteed radiation tolerance or hardened performance. Therefore, the last option relies on unhardened components to implement systems for radiation environments but taking a high risk of malfunctions. Table 2.1 summarizes the main advantages and disadvantages of each technology approach.

In terms of radiation hardness, the RHBP technologies outperform both RHBD designs and COTS based systems. As the technology is inherently hardened, the level of tolerance is defined by the fabrication process, what assures the robustness against radiation effects. At the same time, these technologies are much more expensive as a consequence of their special processes. The small number of applications that require these particular technologies makes them very expensive because of the non-recurrent costs, low yield and small number of fabricated batches.

On the other hand, the tolerant systems that implement RHBD designs in commercial technologies increase the fabrication cost with respect to unhardened systems just because they usually spend more resources but they do not need a special fabrication process.

**Table 2.1:** Comparison of the different technologies implemented for radiation systems.

	<b>Hardness</b>	<b>Cost</b>	<b>Design</b>	<b>Test</b>	<b>Performance</b>
<b>RHBP Technologies</b>	↑↑↑↑	↑↑↑↑	↓	↓	↓
<b>RHBD Designs</b>	↑↑	↑	↑↑	↑	↓
<b>COTS</b>	↓	↓	↓	↑↑	↑↑

However, the RHBD approach requires more design time than the other approaches. As was presented, the implementation of radiation tolerant systems with RHBD techniques is mainly based on redundancy at different levels of abstraction. Therefore, the design effort is higher than the implementation of designs with tolerant technologies or COTS.

Another important aspect in radiation hardened design is the cost of radiation tests. Regarding this topic, tolerant technologies are the less restrictive because the foundry has already performed all the tests that characterize and assure the level of hardness. RHBD designs require a more complete test campaign but COTS based systems need a very exhaustive test campaign to limit the risks in real operation.

Finally, in terms of device performance, COTS systems are the best option as they can be implemented with the last technology available in the market while the other two approaches are usually implemented with mature technology nodes that imply worst performance in frequency, power consumption, etc.

Putting all together, radiation hardened systems usually implement hybrid solutions to exploit the benefit of each different approach. In this Thesis, as the goal is the improvement of ring oscillators in radiation environments first and then in traditional applications, we will focus on the implementation of ring oscillators in commercial technologies using RHBD techniques to improve the radiation hardening.

## 2.3 Ring oscillators in radiation environments

As the objective of this thesis is the implementation of ring oscillator based applications for radiation environments, in this section the impact of all previous introduced effects and the proposed applications in previous studies are presented.

### Total Ionization Dose

As mentioned in Section 2.1, ring oscillators are integrated in all fabrication processes to monitor the performance and variations of each batch. The same features that make these devices suitable for this task at ground level are exploited for characterizing the different technologies at different radiation environments. In [OLMY98] the same ring

oscillator test vehicle design is used to compare the hardness of four different fabrication process from three different foundries. And every technology characterization uses ring oscillators [BVA<sup>+</sup>12, LOM<sup>+</sup>98, RZB<sup>+</sup>12, OLMY98].

In [SBW<sup>+</sup>13], for example, the authors concluded that irradiation and testing of a ring oscillator reveal that oscillation frequency changes non-linearly with increasing total dose. Testing and analytical examination of ring oscillator frequency shows that nMOS and pMOS gate oxide degradation along with the activation of a parasitic edge nMOS are responsible for the ring oscillator response. The experimental results are confirmed via radiation-enabled circuit simulation.

### Single Event Transients

The topology of ring oscillators as a chain of inverters has allowed to extent the characterization of technologies from TID to SET as well. In [MT08] and [NBS<sup>+</sup>07], two ring oscillators are used to model and characterize the propagation of SETs in different technologies. In this case, the inverters are used to quantify SET signatures such as pulse propagation, pulse attenuation, and pulse broadening.

Opposite to the utilization of ring oscillators as test vehicles, recent works have published an undesirable effect of SET in ring oscillators. It is called *Harmonic Vulnerability Window* [C<sup>+</sup>14] and basically consists on a shift of the frequency to the fundamental to an odd harmonic as a consequence of the impact of a particle. A solution to this problem is proposed in [KT03] by using a double path ring oscillator. This problem is deeply addressed in Chapter 4 and a more efficient solution is proposed in this thesis to mitigate this effect.

### Single Event Upsets

As a ring oscillator is not a memory element, it seems that SEUs do not affect them. But the feedback loop configuration gives some kind of *storage* to this circuit. If a SET generates a glitch that fulfilled certain conditions of energy and time of impact, then this glitch can be trapped into the loop and it becomes into a perpetual glitch. Although it is not a conventional SEU, it can be treated similarly due to it is a SET that impacts in a precise time to be stored. [WFK<sup>+</sup>13] deals with this problem similarly than [KT03]. Again, this problem is deeply addressed in Chapter 4 and a more efficient solution is proposed.

### Single Event Functional Interrupt

Ring oscillator are used as system clock generators in radiation application prototypes because of their simplicity. Furthermore, they are used as the core of other clock generator structures as PLLs [MM15, YHC<sup>+</sup>14] or VCOs [PKPS13], any induced glitch by a SET

at the output of a ring oscillator could leave the system in an unknown state because the maximum frequency of the system has been violated.

### **Single Event Latchup**

Latchup affects to all CMOS circuits, so implementations of CMOS ring oscillators are not an exception. Some previous works have studied the sensitivity of ring oscillators to SEL and their destructibility such as [RP02]. Other works have used RHBD techniques to harden ring oscillator devices for applications in harsh environments. For example, some of these techniques are increasing the distances between doped regions, implementing guard rings or isolating voltage zones [SFB<sup>+00</sup>].

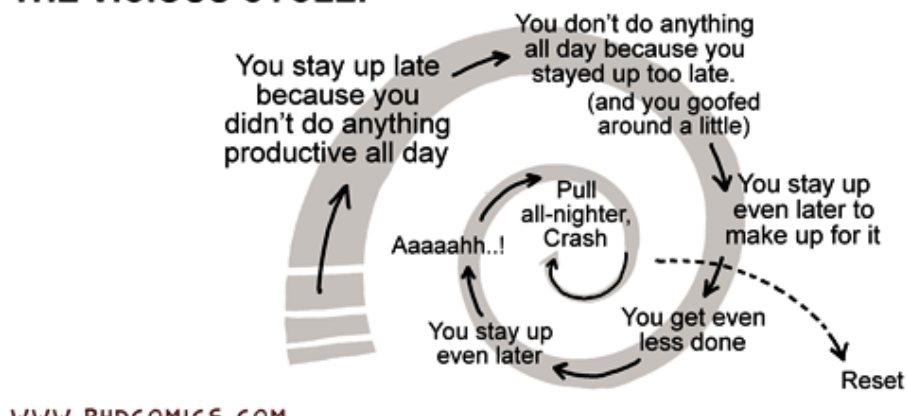
### **Displacement Damage, Single Event Burnout and Single Event Gate Rupture**

These effects are completely dependent on the technology used to fabricate the circuits. As a consequence, they are not mitigated with RHBD methodologies but with RHBP techniques. Therefore, these effects affect the same way ring oscillators than other type of circuits, and this is the reason why we keep them out of the scope of this thesis.

# Chapter 3

## Total Ionization Dose Sensor

### THE VICIOUS CYCLE:



JORGE CHAM © 2008

## Chapter 3

# Total Ionization Dose Sensor

### 3.1 Introduction

Cumulative radiation effects are a main concern in electronic design, especially in hostile environments such as space [Bar06], medical applications [EAP<sup>+</sup>14] or high energy physics (HEP) experiments [BCF<sup>+</sup>11]. Long term ionizing damage may cause devices to suffer from threshold shifts, increased leakage and noise or timing changes [OM03b]. In this scenario, monitoring the degradation suffered by devices becomes a must. Based on reliable measured data, electronic systems can be aware of their health status and, if necessary, take actions. For instance, some techniques take advantage of annealing processes, allowing a partial recovery from the damage caused by ionizing radiation.

There have been developed different methods to measure the dose absorbed by electronic circuits. RADiation-sensing Field-Effect Transistors (RADFETs) [HS74] are the most commonly used dosimeters based on the shift of pMOS threshold-voltage ( $V_t$ ). In [RGM05], forward and reverse biased *p-i-n* silicon diodes are used for radiation dose monitoring in the Large Hadron Collider (LHC) accelerator. Forward-biased diodes use the shift of their I-V characteristic curve. And reverse-biased devices measure the increasing leakage current under exposure to particle radiation. Carbonetto et al. [CLI<sup>+</sup>09] propose the use of ring oscillators as dosimeters exploiting their frequency variation caused by dose accumulation.

RADFETs are used in many applications that require radiation monitoring [MSP<sup>+</sup>13, MDA<sup>+</sup>12, GMP<sup>+</sup>13] but they present some disadvantages. Regarding the production process, a feasible RADFET needs a gate oxide thickness considerably thicker than commercial MOSFETs [HSRG07]. Since RADFETs are discrete components, their measurement is in fact the exposed radiation instead of the dose absorbed by functional devices. Additionally, single RADFETs are not useful for measuring low radiation doses. To meet this goal Goldsten et al. [SBPS04] stack more than one transistor to increase the sensitivity. Finally, its analog character implies a digitization step at the readout system requiring an Analog-to-Digital Converter (ADC) which must be radiation-hardened.

To overcome these drawbacks, in this chapter we propose a TID sensor based on measuring variations in a gated ring oscillator. Our system is fully digital and can be implemented

in many forms, from a built-in sensor in a standard cell Application-Specific Integrated Circuit (ASIC), to configurable structures within programmable devices such as FPGAs. Its small size and its lack of analog parts makes it attractive for systems that require TID monitoring during their lifetime.

Additionally, it is possible to embed the sensor into complex systems taking locally accurate measurements at each area of the design instead of the global radiation sensing that RADFETs provide. Furthermore this sensor has a simple time to digital interface able to be integrated in a multi-purpose on-chip monitoring network such as [ILVMO12].

There are two main phenomena that can alter the sensor accuracy in radiation monitoring: First, the annealing or charge redistribution [KLA96] which is dependent on time and temperature. Second, the device and environmental temperature [GKT<sup>+</sup>14]. Due to MOS transistor characteristic variations caused by these magnitudes, it is necessary a temperature correction for the radiation measurements. Therefore, the calibration process must take into account both magnitudes—radiation and temperature—to adjust the measurements to real values.

The rest of this chapter is organized as follows. First, in Section 3.2 the physics of the Total Ionization Dose is presented. In Section 3.3 we present the basics of the sensor. In Section 3.4 we describe the manufactured prototype, we outline the radiation tests carried out and we analyze the results of the test campaign. In Section 3.5 we study the temperature influence on our sensor performance. We mix both effects in Section 3.6 to calibrate the sensor. Section 3.7 describes the hardware implementation of the readout system. Putting it all together, we propose a self-recovery system for radiation environments in Section 3.8. And finally, we conclude in Section 3.9 summarizing our main contributions.

## 3.2 Total Ionization Dose

The main consequence of the exposition of MOS transistors to high-energy ionizing irradiation, is the creation of electron-hole pairs throughout the oxide. This physical process is the cause of all total dose effects in electronics. The generated carriers induce secondary processes that lead to device degradation. Figure 3.1 [Win89] is a plot of a MOS band diagram for a p-substrate capacitor with a positive applied gate bias. This diagram explains the main mechanisms of the electronic device degradation. The processes occur as follows. First the radiation induced electron-hole pairs are created. After their creation, a small part of the new mobility carriers recombine and the rest of the electrons drift toward the gate and holes drift toward the Si/SiO<sub>2</sub> interface. The ratio of electron-hole pairs that escape recombination is called the electron-hole yield. As the holes approach the interface, some holes are trapped, forming a positive oxide-trap charge. Then, two different

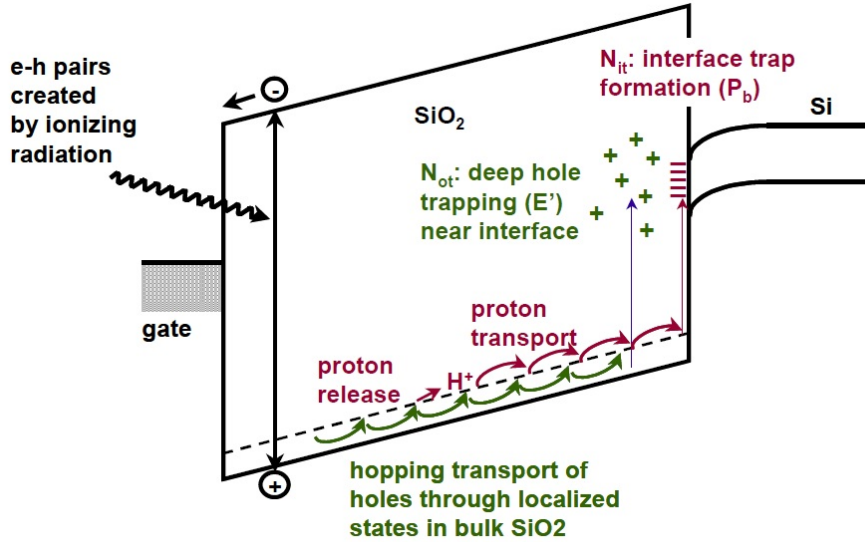


**Figure 3.1:** Band diagram of a MOS capacitor with a positive gate bias [Win89].

mechanisms affect the gate oxide: oxide-traps and interface-traps. In addition to oxide-trapped charge and interface-trap charge in gate oxides, other oxides including field oxides or silicon-on-insulator (SOI) buried oxides are also affected by the same phenomena. As mentioned before, the diagram of Figure 3.1 corresponds to a biased capacitor. However, if the capacitor is not biased, the generation of electron-hole pair occur but they are all recombine without collected the charge in any part of the structure.

The band diagram of the MOS capacitor can be extrapolated to a MOS transistor to understand the effects of TID in such devices. Figure 3.2 [OM03a] illustrates the radiation-induced charge buildup in the gate oxide of an n-channel MOS transistor. As depicted in Figure 3.2, positive charge trapping in the gate oxide can invert the channel interface causing leakage current to flow in the OFF state condition. This will result in an increase of the static power supply current in an IC. Large concentrations of interface-trap charge can decrease the mobility of carriers and increase the threshold voltage of nMOS transistors [SSF<sup>+</sup>08]. These effects will tend to decrease the drive of transistors, degrading timing parameters of an IC. Following the same conclusion than for the MOS capacitor, when the MOS transistors are not biased, their parameters stay stable [WBB<sup>+</sup>15, IA15, CCS<sup>+</sup>14].

Once the charges have been trapped in the interface or the oxide, they are not maintained there indefinitely but they immediately begin to be neutralized. This process is called annealing and it is accelerated with higher temperatures [GMG<sup>+</sup>15, HKM16].

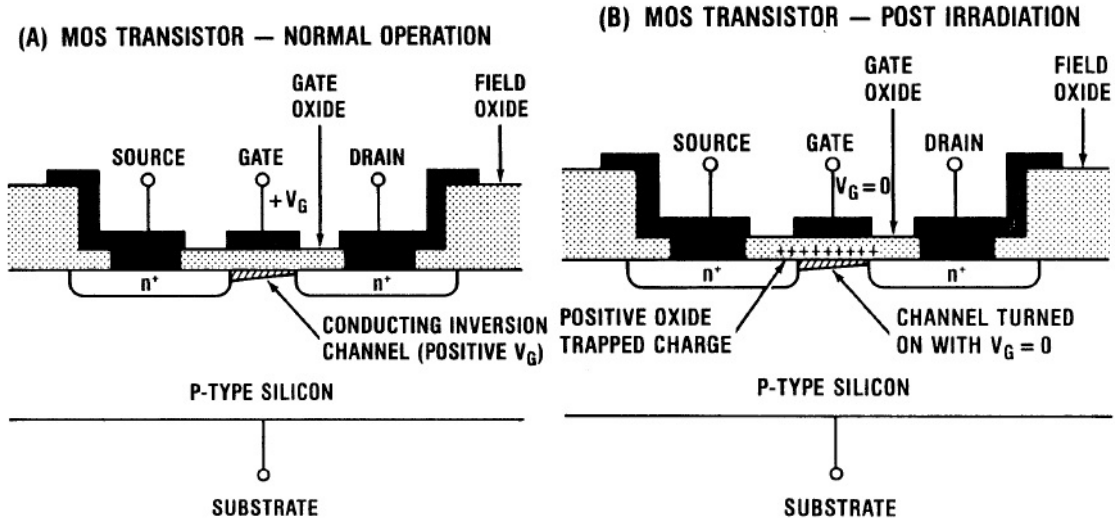


**Figure 3.2:** Schematic of n-channel MOSFET illustrating radiation-induced charging of the gate oxide: (a) normal operation and (b) post-irradiation [OM03a].

### 3.2.1 Effect of TID on MOS Performance

After the understanding of the mechanisms that affects the MOS transistors in long term radiation exposures, the next step is to model those effects. The charge buildup in the oxide structures is finally translated into a threshold-voltage shift. Hence, the total threshold-voltage shift ( $\Delta V_t$ ) for a transistor is the sum of the threshold-voltage shifts due to oxide-trap ( $V_{ot}$ ) and interface-trap charge ( $V_{it}$ ):

$$\Delta V_t = \Delta V_{ot} + \Delta V_{it} \quad (3.1)$$

where each of the contributions (oxide-traps and interface-traps) are calculated in [Dre89]. The threshold voltage is determined by integrating the weighted additional charge density ( $\rho(x)$ ) over the oxide thickness ( $t_{ox}$ ):

$$\Delta V_{ot,it} = \frac{-1}{C_{ox} t_{ox}} \int_0^{t_{ox}} x \rho(x) dx \quad (3.2)$$

The radiation-induced trapped-hole charge is always positive making  $\Delta V_{ot}$  negative for nMOS and pMOS transistors. However, for nMOS transistors, interface-state charge is negative, while for pMOS transistors, it is positive. As a consequence, the addition of both effects can be seen in Figure 3.3. The total effect is different in pMOS, where both effects shifts the threshold voltage in the same direction, than in nMOS, where oxide-trap and interface-trap induce opposite effects. In addition, the trapped-hole spatial charge distribution depends on many factors, including the polarity and magnitude of the applied

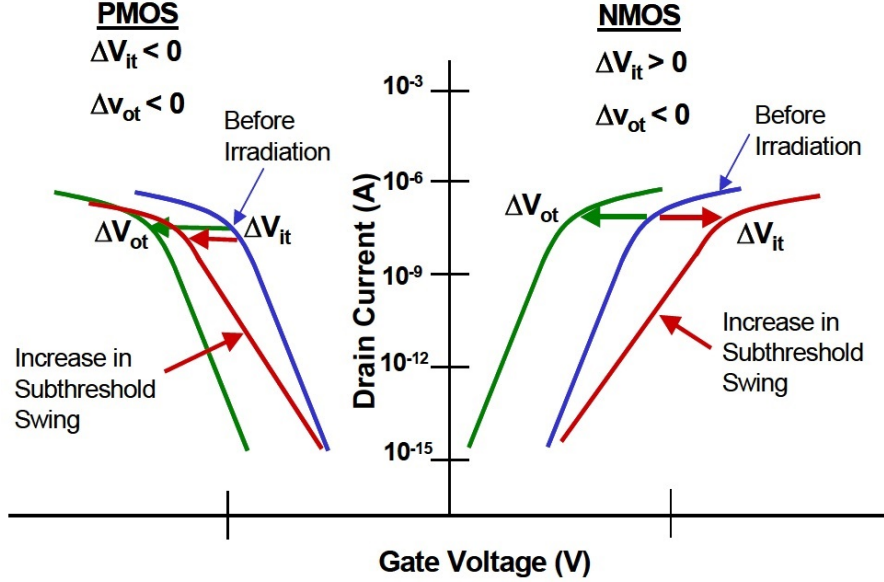


**Figure 3.3:** Threshold voltage shifts and subthreshold swing changes for nMOS and pMOS transistors are shown relative to the preirradiation curves [Lac08].

gate voltage, the gate-oxide processing technology, and the amount of hole neutralization that has occurred [Lac08].

A remarkable conclusion of the quantitative study of the effects of TID in MOS structures summarized in the Equation 3.2 is the dependency of the shift voltage with the evolution of the technology. According to Equation 3.2:

$$\Delta V_{ot,it} \propto \frac{\Delta Q_t}{C_{ox}} \propto t_{ox}^2 \quad (3.3)$$

Then, the thinner the transistor gate oxide the better the performance stands. This conclusion agrees with all practical studies of characterization of new technologies which have gate oxides of a few nanometers [MBH<sup>+</sup>07]. Therefore, in most modern technologies the damage to the thick Silicon Trench Isolation (STI) oxide inducing a parasitic leakage path along the edge of the transistor is the dominant effect of TID.

The quantification of annealing process has also been an important topic of study together with the degradation induced by TID. Some investigations [WKH83, McL88] based on empirically characterizing the response of transistors have conclude that the long-term annealing at room temperature can be expressed by using the next equation:

$$-\Delta V_t(t) = \frac{-A \ln\left(\frac{t}{t_0}\right) + C}{\gamma_0} \quad (3.4)$$

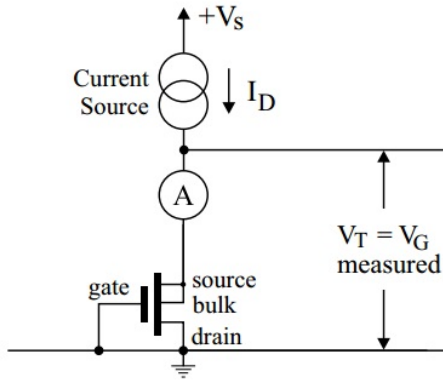


**Figure 3.4:** RADFETs used in [HSGMP14] as discrete components.

where  $A$ ,  $C$  and  $\gamma_0$  depend on the technology and the total dose absorbed at time  $t_0$ . The neutralization of absorbed charges is fundamental on two different physical processes: the tunneling of electrons from the silicon into oxide traps and the thermal emission of electrons from the oxide valence band into oxide traps. These basic processes explain the temperature dependency of annealing with temperature.

The two effects presented in this section (electron-hole generation and annealing) have to be taken into account to design our TID monitor, and they suppose the physical foundations of the prototype presented in the next Sections.

### 3.2.2 RADFETs

So far, the most common dosimeters are RADFETs. They were postulated in 1974 by Andrew Holmes-Siedle [HS74]. RADFETs are based on measuring the shift of threshold voltage in a MOS transistor and converting the voltage shift into absorbed dose following equation 3.1. Then, the typical readout system it requires, consists on a simple current source as shown in Figure 3.4.

According to the definition given by its inventor: "The RADiation-sensing Field-Effect Transistor is a microminiature type of integrating radiation dosimeter. The sensor has a microscopically small sensor volume, which offers opportunities for radical new designs of miniature radiation sensing system. The sensing principle is long-term charge storage. The pMOS responds to the field produced when space-charge is trapped in the oxide region. An electrical measurement then gives a relative value of dose in rad or Gy(Si). Compared to other detector systems, the RADFET system is compact and easily coupled with computer power." The typical characteristics of commercial RADFETs are:

- Chip size: less than 1x1 mm

- Gate Oxide thickness: 0.1 to 1.25 micrometres.
- Typical radiation responses: 0.5 mV/cGy

These characteristics made them suitable for many applications that require monitoring TID, but they also involve some disadvantages to act as dose monitors.

- The minimum chip size and the gate oxide make RADFETs small but not fully integrable with modern nanometer technologies. Then, they monitor the environment exposed radiation instead a more accurate value of the absorbed dose.
- The readout system implies the measurement of an analog magnitude. Hence, their integration with digital technologies requires the use of analog to digital converters.
- Their sensitivity at low radiation doses is quite low and special design is needed to overcome this disadvantage [SBPS04].

Therefore, an alternative monitor to overcome the drawbacks of RADFETs should ideally be fully integrable with modern technologies, present a digital interface and improve the low sensitivity.

### 3.3 Sensor Design

#### 3.3.1 Foundations

Same as RADFETs, our sensor foundation is the transistor  $V_t$  shift caused by dose accumulation in radiation environments [Bar06]. According to the short-channel CMOS transistor model and taking into account the parameters empirically determined from a curve fit of I-V characteristic ( $\alpha$  and  $P_v$ ) [WH11], the time delay ( $t_d$ ) of an inverter is ruled by:

$$t_d(V_t) \approx \frac{(L/W)C_L}{\mu C_{OX} V_{DSAT}} = \frac{(L/W)C_L}{\mu C_{OX} P_v (V_{DD} - V_t)^{\alpha/2}} \quad (3.5)$$

where  $L$  is the channel length,  $W$  the channel width,  $C_L$  the load capacitance,  $\mu$  the carrier mobility,  $C_{OX}$  the gate oxide capacitance and  $V_{DD}$  the bias voltage.

In Equation 3.5 the  $t_d$  shift depends on  $V_t$  variation that in turn is translated into the radiation accumulated dose. There are many studies about how radiation affects  $V_t$  for different commercial technologies. In Section 3.2.1 the analytical expression of the dose absorbed has been presented. However, the dependency on the technology needs to be characterized through empirical experiments. Hence, in our sensor modeling we used  $V_t$  shift values of a technology from the same 0.35  $\mu\text{m}$  node [LOM<sup>+</sup>01] in which we

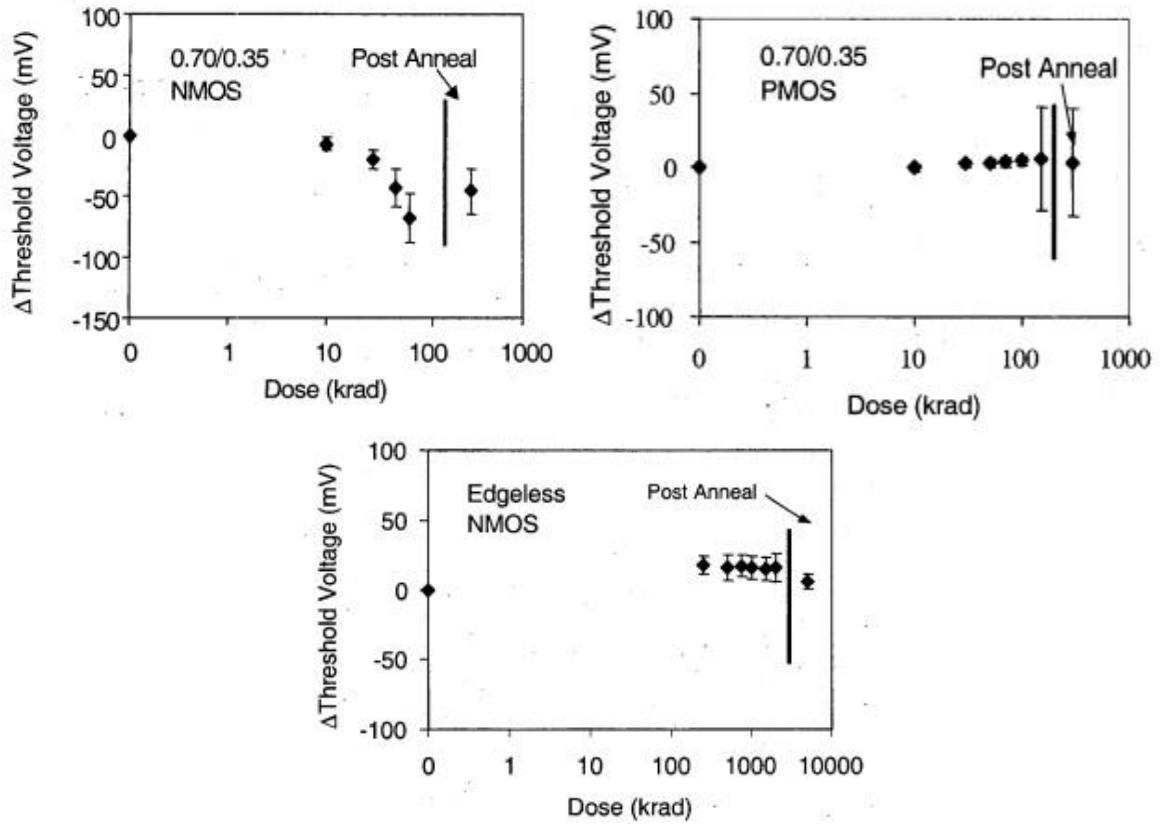


**Figure 3.5:** Radiation results in [LOM<sup>+</sup>01] for 0.35  $\mu\text{m}$  TSMC CMOS technology.

manufactured our sensor. This study characterizes minimum size transistor without any RHBD nor RHPB techniques together with Edgless NMOS transistors (a RHBD layout level technique). Figure 3.5 reproduces the important data acquired in that work used for our modeling.

From Figure 3.5 we can conclude:

- nMOS transistors are the most affected by long term radiation effects and pMOS are almost unaltered by doses up to hundreds of krad.
- Edgeless nMOS transistors have proved being more resistant to TID and suitable for radiation hardened parts in our sensor.
- The study of the annealing process is important because transistors recover partially from the induced degradation.

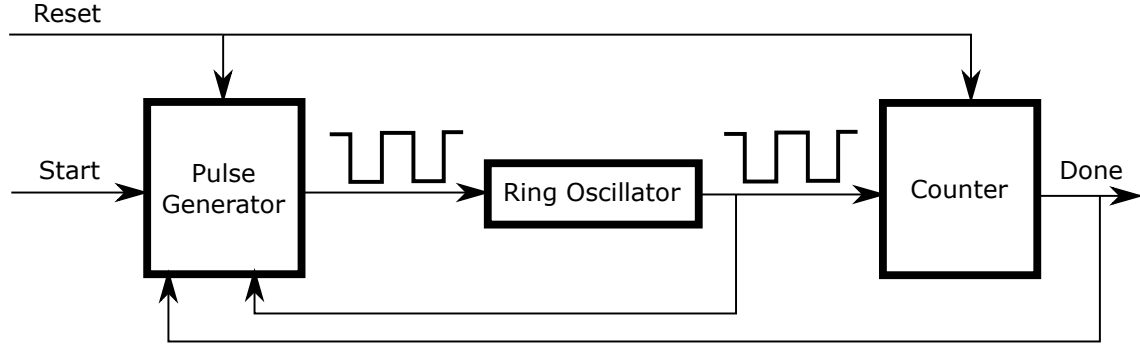


**Figure 3.6:** Self-timed sensor scheme with its three main blocks.

### 3.3.2 Architecture

Using the dependency of Equation 3.5, our sensor is based on measuring the value of  $t_d$  and therefore the shift as a consequence of TID absorbed. A possibility to measure this value is to characterize an individual inverter. This sensor would be fully integrable but the other two conditions (digital interface and low sensitivity) would not be accomplished. Therefore our proposal is based on measuring the average value of  $t_d$  of N equal inverters forming a ring oscillator. Therefore, putting together Equations 2.11 and 3.5, the dependency of a ring oscillator frequency with respect to the threshold voltage ( $V_t$ ) can be expressed:

$$f_o(V_t) = \frac{1}{2Nt_d} \approx \frac{\mu C_{OX} P_v (V_{DD} - V_t)^{\alpha/2}}{2N(L/W)C_L} \quad (3.6)$$

Then, measuring the frequency of a ring oscillator, the shift of this magnitude compared to the nominal value can be translated into dose absorbed according to Equations 3.1 and 3.2:

$$TID \rightarrow \Delta V_{ot} + \Delta V_{it} = \Delta V_t \rightarrow \Delta f_o \quad (3.7)$$

The proposed TID sensor architecture is based on the multi-purpose design published in [OILV13]. That sensor was implemented in an FPGA for temperature and process variation monitoring. We have modified it to sense the total ionization dose following a full-custom design methodology.

Essentially, the sensor is a gated ring oscillator with a parameterizable number of cycles. In a more detailed view, the sensor is composed of three different blocks whose basic scheme is shown in Figure 3.6. First, the pulse generator is a simple combinational logic block that enables the ring oscillator as it includes a NAND gate to enable the beginning of oscillation. Second, a ring oscillator acting as the sensing part and, therefore, its design is adaptable for measuring different magnitudes. It defines the purpose of the sensor and its accuracy. The total delay of the ring oscillator will fix the period of the clock as shows

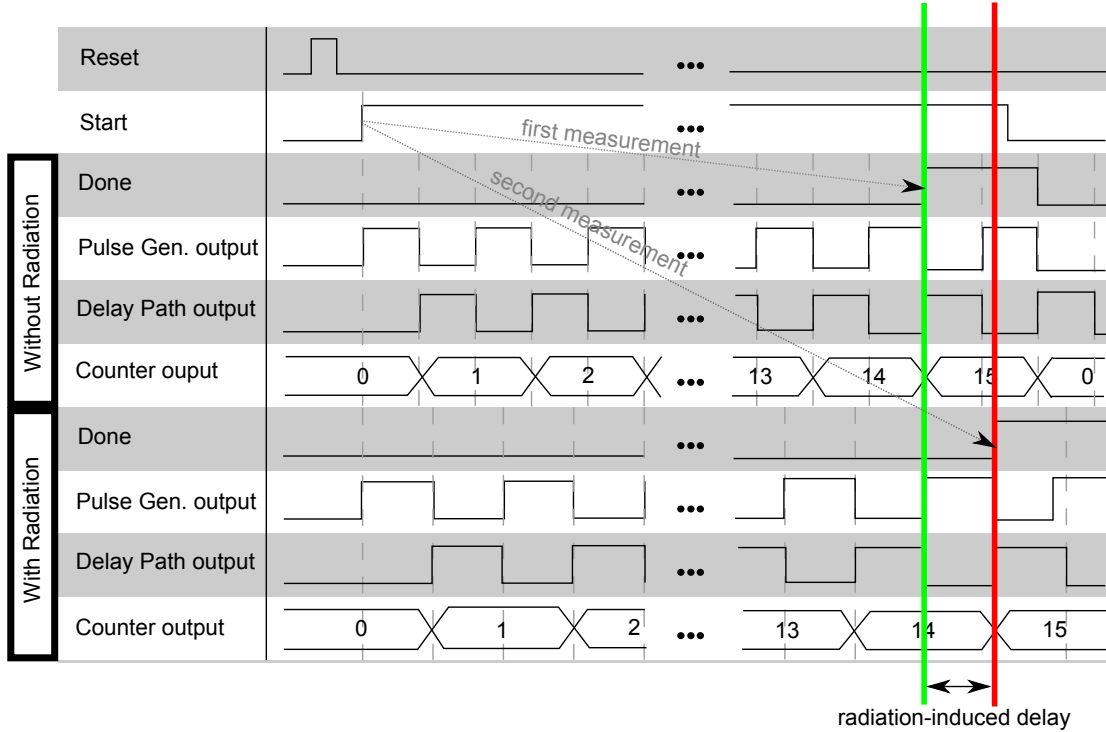


**Figure 3.7:** Timing diagram of the sensor signals and their predicted behavior.

Equation 3.6. And the third block is the counter which confers the sensor the ability to have a configurable sensitivity by changing the number of periods of the ring oscillator counted. In our implementation, the  $V_t$  shift caused by radiation slows down the ring oscillator. This variation modifies the period of the signal that excites the counter input. Our goal is to design a delay path sensitive to ionizing radiation making the rest of the blocks radiation-tolerant.

The fact that the proposed sensor does not need a system clock avoids some disadvantages. For example, the clock tree is very sensitive to radiation environments because a particle impact on it can trigger SEEs on clock buffers or associated sequential elements and may even result on the need of power cycling in case of inducing permanent functional errors. Hence, this sensor does not extend the clock tree and then it maintains the sensitivity area invariable. Another drawback of enlarging the clock tree is that routing this net is usually one of the hardest part of layout designs in big and complex systems.

The sensor has an interface formed by two inputs —*Start* and *Reset*— and an output —*Done*—. It works as follows: the external control system first resets the sensor registers —pulse generator and counter—, then it excites the *Start* signal when it wants to monitor the TID level and it waits until the *Done* output is triggered. This occurs when the counter reaches a predefined value. Since the period of the self-generated clock that excites the

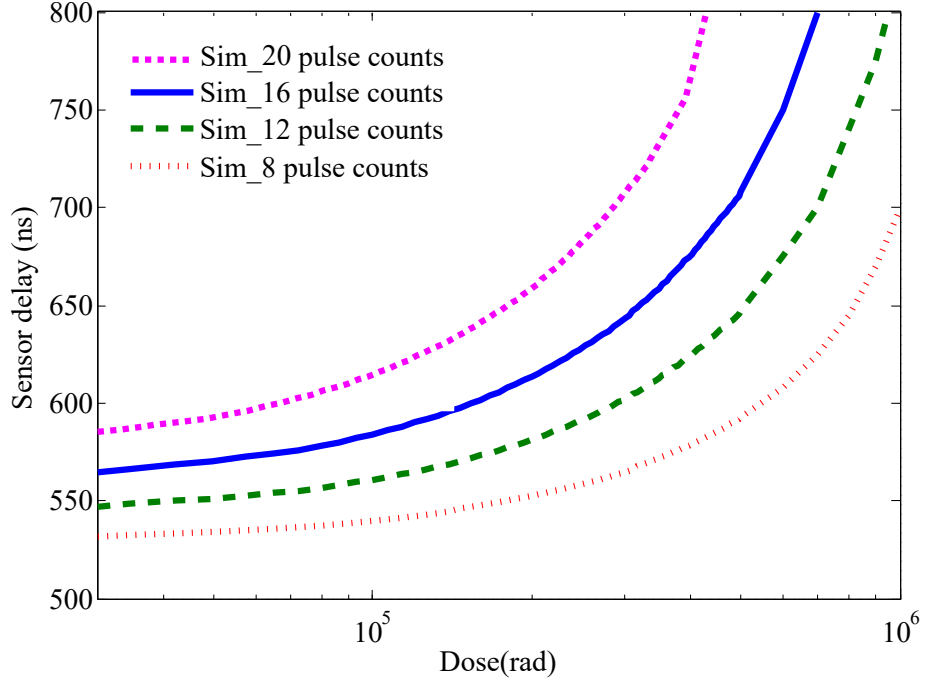


**Figure 3.8:** Radiation Sensor simulations for different values of sensitivity.

counter is directly dependent on the delay path, the *Done* trigger time is dependent on it too. These operations are summarized in Figure 3.7. The measured magnitude is determined by the elapsed time between *Start* and *Done*. So a time-to-digital converter (TDC), for example the one described in [DSH00], is necessary to digitize the sensed value to be used in other blocks. As mentioned, the counter allows to have configurable sensitivity as it determine the number of periods needed to define the TID. If  $t_{Start-Done}$  is the time between *Start* and *Done*,  $T$  is the period of the ring oscillator and  $m$  the value of the counter, then:

$$t_{Start-Done} = mT = m2Nt_d \quad (3.8)$$

The use of a TDC as interface is one of the advantages of using our design. It allows to centralize the conversion stage in just one TDC for the whole sensor network even if this network is formed by multi-purpose sensors. Besides, the TDC requires much less resources than the ADC used in RADFETs sensors.

To predict our sensor behavior we have varied the threshold voltage of transistors in the sensor design netlist according to [LOM<sup>+</sup>01]. And we simulated the time delay with Cadence® Spectre® Software for various sensor sensitivities. Figure 3.8 summarizes the simulation curves of the sensor. The simulation lines represent three different configurations of the sensor sensitivity. The sensitivity is fixed by the value of the maximum counter output. In this figure, the dotted line simulates a count of eight pulses, the slashed line

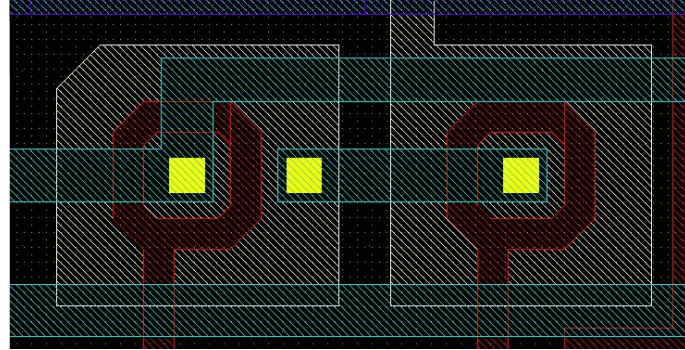


**Figure 3.9:** Layout of ELT used for TID hardening.

12, the solid line 16 and the squared line 20. As can be seen, the sensitivity increases with the number of counted periods.

### 3.3.3 Implementation

We divided the design and implementation into two different parts. On the one hand, the delay chain utilizes common inverters of minimum channel length. Thereby the complete sensor area is minimized improving the integration of a maximum number of delay elements within the delay path.

And on the other hand, with regard to the counter and pulse generator logic, we have followed RHBD techniques to allow the integration in commercial technologies. These RHBD rules assure performance against radiation effects. The addition of all these three techniques provides our sensor with the radiation characteristics we were looking for: a radiation-sensitive delay path and radiation-tolerant logic blocks.

#### Enclosed Layout Transistors

First, we have used broken square Enclosed Layout Transistors (ELTs) [GPM00] such as the one in Figure 3.9. This type of geometry has evidenced better radiation performance for technologies bigger than hundreds of nanometers as shown in [LOM<sup>+</sup>01]. The ELT hardening is achieved by removing the interfaces where charges are trapped thanks to their annular layout. The implementation of this type of transistors requires the use of a new simulation model because this topology involves different electronic mechanisms than normal finger transistor. For this purpose, in [GPM00] the equivalent model follows this equation:

$$\left(\frac{W}{L}\right)_{eff} = 4 \cdot 2 \left( \frac{\alpha}{\ln(\frac{d}{d-2\alpha L})} + \frac{1}{\Delta(\alpha)} \frac{(1-\alpha)}{-\ln(\alpha)} + \frac{1}{2} \frac{w}{L\sqrt{2}} \right) \quad (3.9)$$

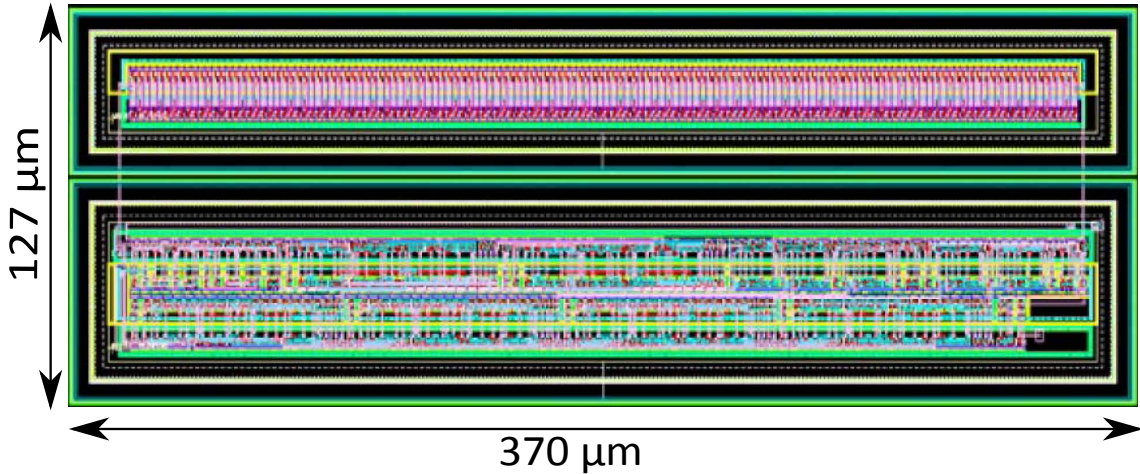


**Figure 3.10:** Layout of the TID proposed sensor. It is physically divided into two different parts, the unhardened and sensitive area (top) and the radiation hardened control (bottom).

where  $\alpha$ , L and d are only dependent on the geometry. (For a more in depth explanation of the model, refer to [GPM00].)

### Guard Rings

Second nMOS transistors are electrically isolated from pMOS transistors by a guard ring [KC06]. The guard ring catches close charges avoiding easy paths for ions through semiconductor interfaces where TID effects are more noticeable. The ring performs an important dual function [NBTA04]. As a channel stop, the ring prevents the inversion of the field oxide at that location by adjusting the local threshold voltage to a very high value. It also maintains the well or substrate bias, depending on the process, through the low resistance guard ring which can mitigate single-event latchup.

### Electrical Isolation

Finally, the sensing part is also physically isolated from the pulse generator and the counter using independent areas provided by this particular commercial technology.

## 3.4 Radiation Test

### 3.4.1 Prototype description

The sensor under test has been manufactured in a  $0.35 \mu m$  commercial technology. Figure 3.10 displays the layout designed taking into account all characteristics presented in

**Table 3.1:** Total Ionization Dose Sensor features.

	<b>Area</b>	<b>Percentage</b>	<b>Energy per conversion</b>
<b>Sensing</b>	$10400\mu m^2$	22% of sensor	300pJ
<b>Logic</b>	$18910\mu m^2$	40% of sensor	163pJ
<b>Physical Isolation</b>	$17680\mu m^2$	38% of sensor	
<b>Total Sensor</b>	$46990\mu m^2$	1.2% of ASIC	463pJ
<b>Total ASIC</b>	$4mm^2$	100%	

the previous section. In this layout, two main parts can be seen. On top the delay path formed by a 256-inverter chain and at the bottom the pulse generator and the counter. As shown, the radiation sensitive and insensitive parts are physically isolated. We fixed the value of the counter constant to the maximum 4-bit pulse-count (16 pulses).

Table 3.1 summarizes the features of the manufactured prototype. In a small chip of  $4 mm^2$ , the sensor only requires 1% of the total area. Within the resources used for each sensor, just the 22% is actually the sensitive part while the rest of the area is employed to control and isolation. The overhead for radiation due to the RHBD techniques implemented represent a high cost close to the 40% of the total area. Another remarkable figure is the low energy per conversion required where the 66% corresponds to the sensitive area as the control logic is idle when a conversion is not requested.

Seven Device Under Tests (DUTs) were fabricated and six of them were inserted in a home-made breadboard and irradiated. The other DUT —DUT7— was treated as a golden copy to compare the radiation effects with the normal configuration. Out of the six irradiated chips, half of them were biased —DUT2, DUT3 and DUT6— and the other half were unbiased —DUT1, DUT4 and DUT5— to test that unbiased chips were less degraded by radiation effects [SSDF08]. The DUTs were biased at 3.3 V with a current limit of 150 mA, by an Ethernet cable though an RJ45 interface. Figure 3.11 (b) shows the board setup for the irradiation test, and Figure 3.11 (c) provides a closer look at the DUTs disposition.

### 3.4.2 Test procedure

The test method to evaluate circuits in terms of total dose irradiation has been homogenized and it is documented in the standard ESA-ESCC-22900. This standard is followed by most of the players in the radiation tolerant electronic industry. We have also followed those recommendations to measure our TID monitor.

Radiation tests were carried out at the NAYADE facility of CIEMAT in Madrid. This

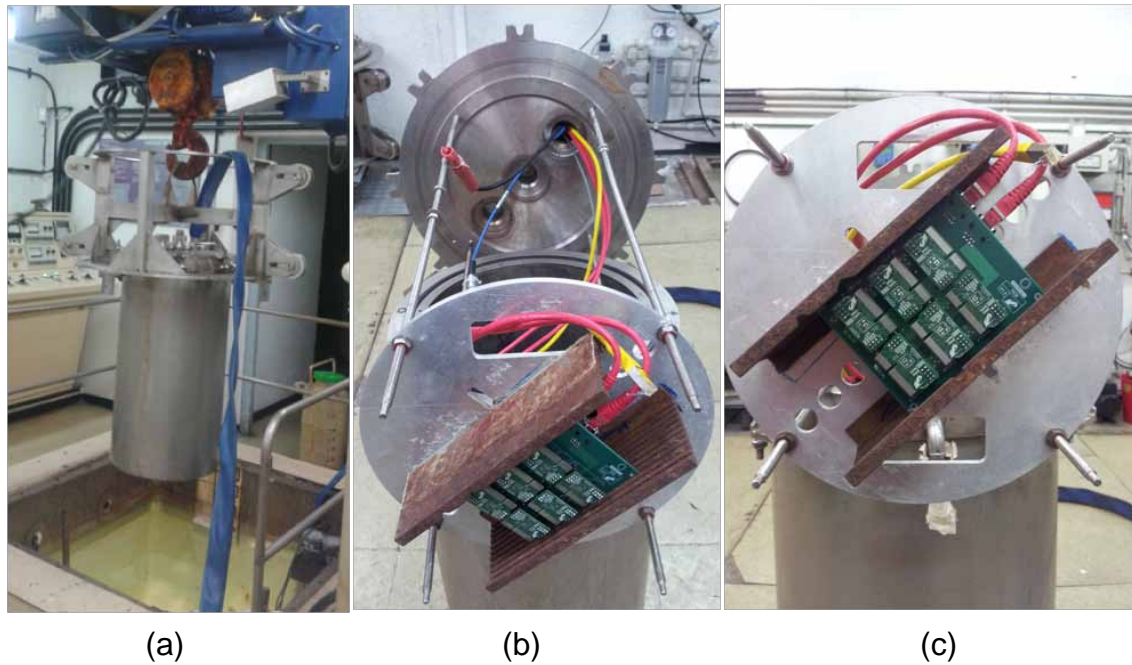


**Figure 3.11:** Test set up for  $^{60}\text{Co}$  radiation test at CIEMAT.

facility fulfills all the requirements of the ESA-ESCC-22900. The pool of the facility appears in Figure 3.11 (a). The  $^{60}\text{Co}$  source is placed at the pool bottom. The main characteristics of this facility are:

- Type of source.  $^{60}\text{Co}$  cylindrical sources (15 mm diam. x 135 mm long) 12 sources are distributed in a circular way providing an inner cylindrical irradiation volume. Two distributions are available.
- High flux.  $\leq 8.3 \text{ 103Gy/h}$  within a 60mm diameter x 100 mm long volume.
- Low flux.  $\leq 1.2 \times 10^2 \text{ Gy/h}$  within a 200 mm diameter x 100 mm long volume.
- Irradiations at controlled temperatures and atmospheres, together with in-situ testing of electrical properties available.
- In this device the irradiations can be carried out at controlled temperature up to 300°C. A gas flow (as dry air or nitrogen) can be introduced during the irradiations to prevent possible effect of humidity. The uncertainty dose rate is better than 20% in a volume about 283 cm<sup>3</sup>.
- Dosimetry system. The routine gamma dosimetry is performed using the commercially available Red Perspex<sup>TM</sup> 4034 Harwell dosimeters. These dosimeters have shown to be valid in the range of 5 to 50 kGy and their accuracy is better than 10%.

**Table 3.2:** Radiation test plan.

Time (min)	Dose (krad)	DUTs						
		1	2	3	4	5	6	7
0	0	X	X	X	X	X	X	X
113	50	X	X	X	X	X	X	
169	75	X	X	X	X	X	X	
225	100	X	X	X	X	X	X	
261	125	X	X	X	X	X	X	
317	150	X	X	X	X	X	X	
+960	575		X			X		

The test plan, summarized in Table 3.2, consisted of six different steps with a dose rate of 26.51 krad/h. The first step was at minute 113 from the beginning. We took 50 krad as the first point of interest because negligible effects would have been observed with lower dose. Next four steps were separated 56 minutes —25 krad— and the final step lasted 16 hours —575 krad. For the long final step all DUTs were removed from the Bread Board except DUT2 and DUT5 —biased and unbiased respectively. We also monitored the DUTs for the next 80 hours of radiation tests to see annealing effects. All chips were working after the whole radiation test, so no hard error took place during tests. All experiments were carried out at constant temperature (24°C in the pool and 28°C at room).

The measurement is accomplished following the diagram of Figure 3.12. Each DUT is measured independently using a Xilinx FPGA board (Virtex5 ML505), an Agilent MSO9051 oscilloscope, a developed test board and a PC. The FPGA board acts as the external control that excites the inputs of the sensor, the oscilloscope captures the input *Start* and the output *Done* and measures their delay, the test board routes all signals to the DUT and produces the oscilloscope inputs and the computer is used for device configuration and data acquisition. All this process is completely automated and the DUTs stayed out of the pool close to 35 minutes for each measurement process (5 minutes per DUT approximately).

### 3.4.3 Radiation Test Results

Figure 3.13 summarizes the whole set of tests we carried out, it depicts the oscilloscope captures acquired during the radiation tests. In this figure the dashed lines represent the sensor *Start* signal, and the rest of the lines are the *Done* signal at the different steps of the radiation test. The main conclusion at first sight is that DUTs 1, 4 and 5 have been almost unaffected by radiation because they stayed unbiased along the test. DUT2 is clearly the most affected DUT because it is the only biased one that remained in the  $^{60}\text{Co}$

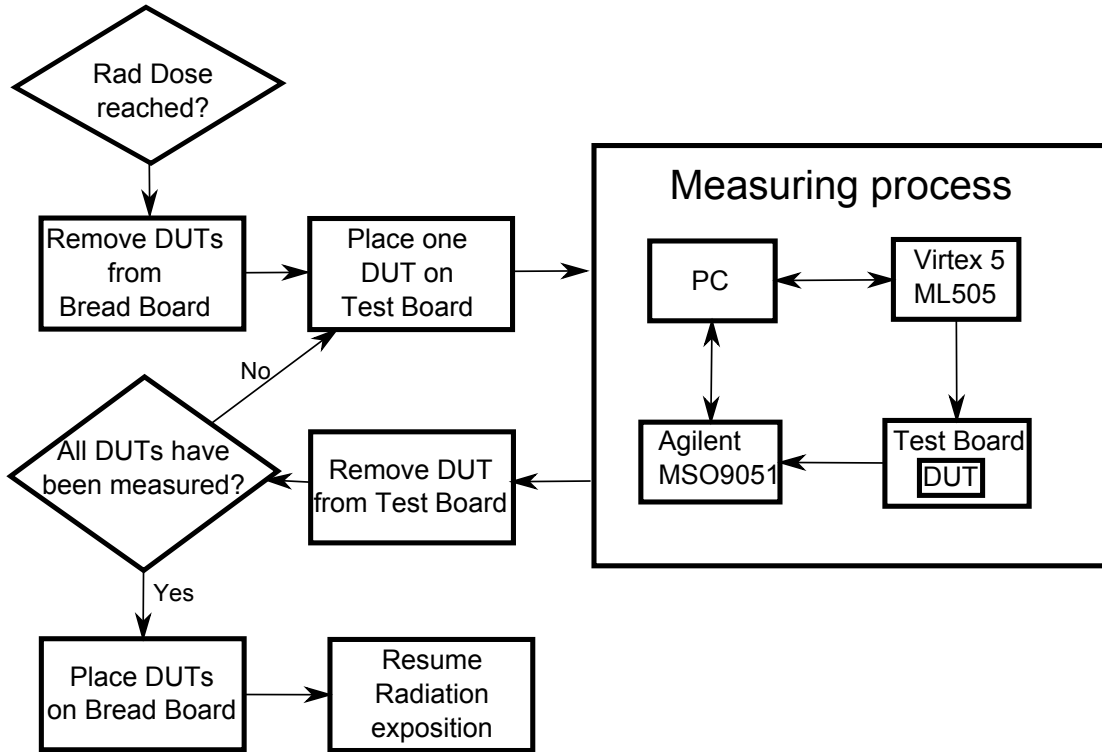


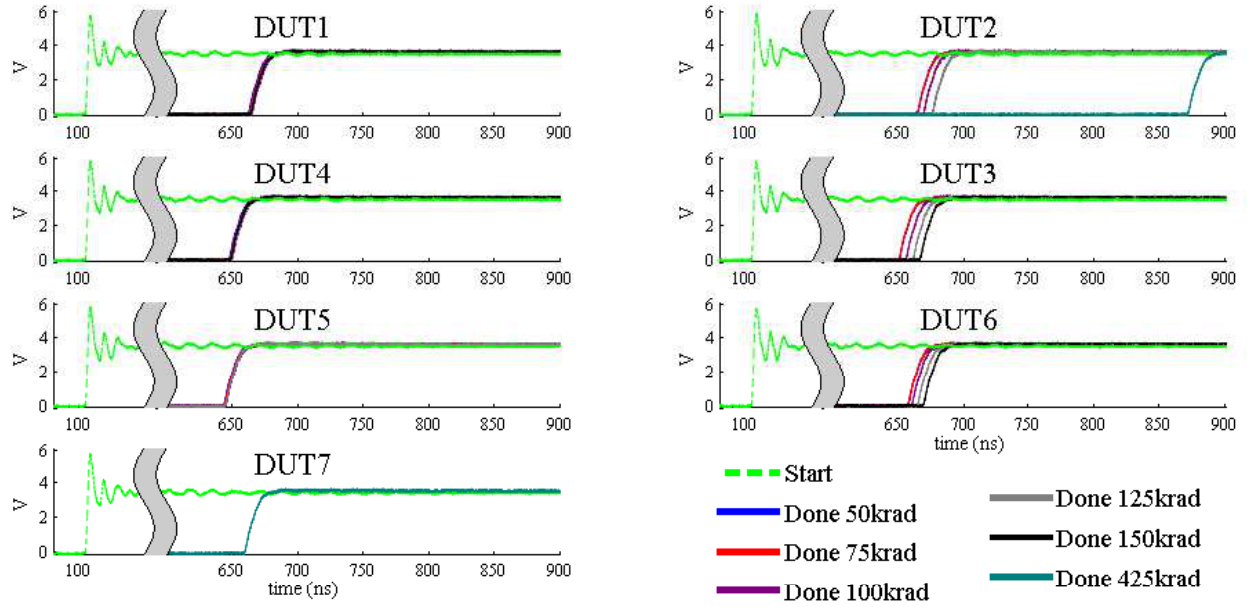
**Figure 3.12:** Diagram of measurement process.

chamber during the last step.

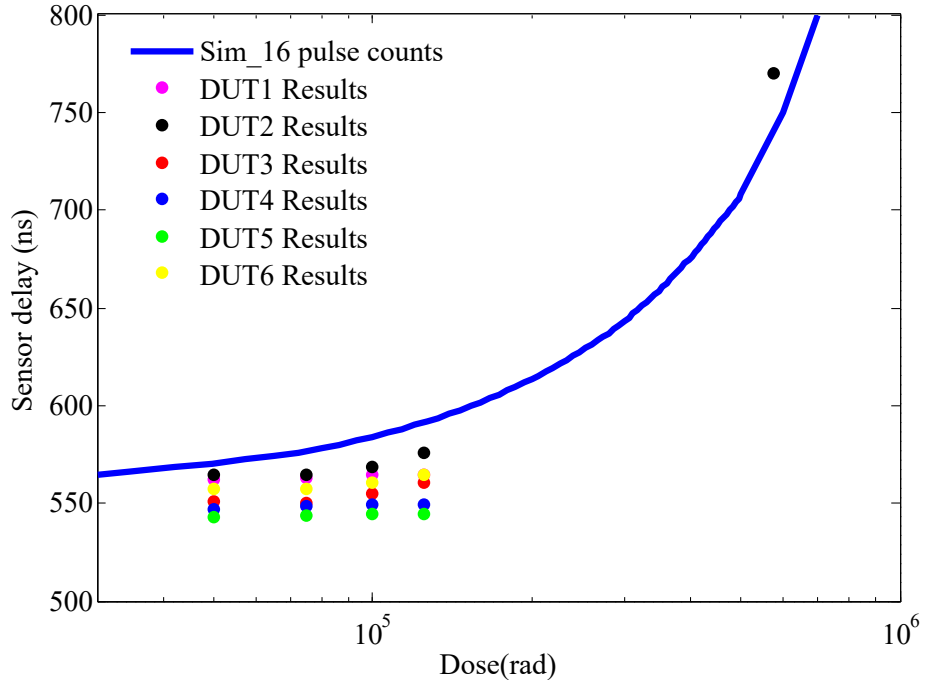
Differences in delay between the first measurements of each chip are due to process variations. All DUTs were manufactured within the same wafer, hence the process variations that took place here were inter-die variations.

Figure 3.14 compares the simulation curve of the sensor with the results achieved through the radiation test. Our sensor has been designed with a 4-bit counter and it counts up to its maximum value —16 pulses. The simulation line reproduces the general behavior of the sensor, but a more accurate estimation would require the use of our commercial technology radiation data instead of the similar TSMC technology of [LOM<sup>+</sup>01].

Figure 3.15 is the result of the periodic measurements of the delay of DUT2 once the radiation test is over. As can be seen, the delay measurement decreases after ceasing irradiation because of annealing taking place. The exponential curve is a good approximation on how this effect behaves in our sensor as is proven by the residuals presented in the bottom figure. The coefficient of determination is greater than 99% and the maximum relative error of the fitting is less than 0.7%. This annealing process study proves that the chip devices recover from radiation performance degradation. And, for example, a forced annealing process could be used to restore devices performance through power and



**Figure 3.13:** Radiation results for every DUT at different doses.



**Figure 3.14:** Radiation Sensor Sensitive comparison between simulation (line) and measurements (dots).

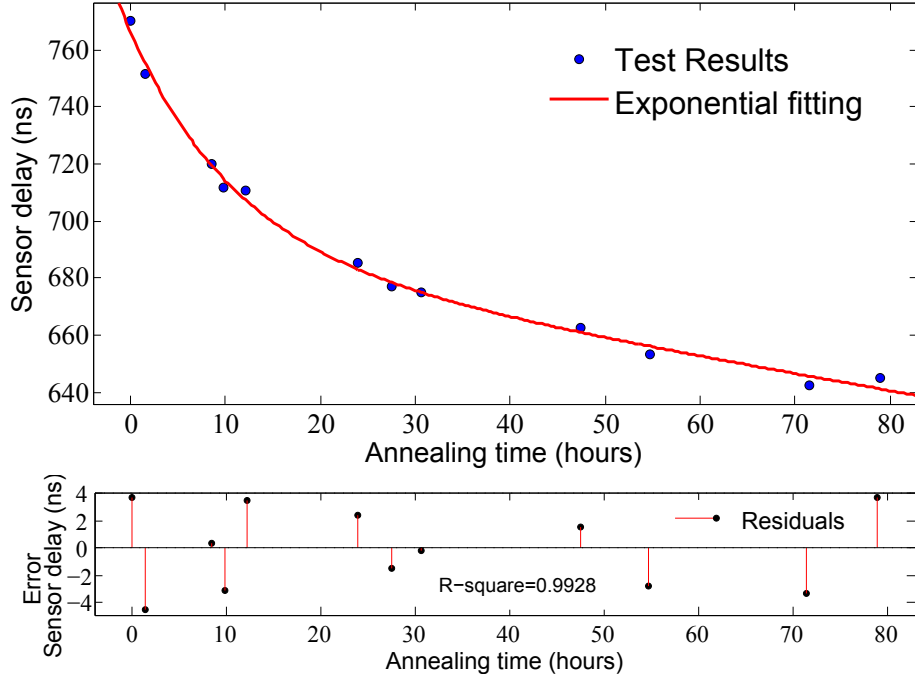


**Figure 3.15:** Delay time vs annealing time in DUT2. Test results, fitting curve and the fitting errors.

**Table 3.3:** Board Power Consumption.

	Dose accumulated (krad)						
	0	50	75	100	125	150	575
Current (mA)	10	10	20	30	50	60	90

temperature control as we will discuss in Section 3.8.

Additionally, we monitored the power consumption of the whole board during all radiation steps, reported in Table 3.3. The power consumption increases along the radiation tests because of the increase in leakage current. The value of this power consumption is the addition of the different test vehicles included in the chip design, not only our sensor.

## 3.5 Temperature Test

### 3.5.1 Setup

Our sensor is based on a ring oscillator manufactured in a commercial technology, hence it is expected that it is also sensitive to temperature. From [OILV13] the expression that rules the delay  $t_d$  can be approximately:

$$t_d \approx k_1 CT \quad (3.10)$$

were C is the number of delay elements, T the temperature and  $k_1$  is a process-dependent parameter.

Once the radiation test and the annealing study are finished, we made a complete temperature analysis to calibrate the readout of our radiation sensor. The tests were carried out with a Votsch VCL 4010 [Ind] temperature chamber able to control the environment temperature with an accuracy of 0.1 °C. The DUT package temperature is monitored by a thermocouple to remove possible inaccuracies caused by self-heating while devices are working. The hardware used for data acquisition is the same that was used for the radiation test measuring process.

The temperature test consisted on the measurement of two different DUTs. The golden DUT (DUT7) which was not exposed to radiation and DUT2, the most exposed. The temperature was varied from 0 °C to 50 °C with 5 °C steps. Moreover, between 20 °C and 30 °C the steps were 2.5 °C for DUT2 and DUT7 because this range is the typical working temperature where we want more accurate results. The temperature range was chosen attending to the constraints of the commercial hardware used for data acquisition.

DUT7 was only measured with increasing temperature, starting at 0 °C and finishing at 50 °C. But DUT2 was measured with increasing and decreasing temperature, forcing an annealing stage between them during 6 hours at 50 °C. At 50 °C automatic measurements were carried out every 10 minutes. These measurements consisted on taking 100 samples in order to achieve a statistically correct result. The test plan is summarized in Table 3.4.

**Table 3.4:** Temperature test plan.

Temperature (Start - Finish)	Step	DUT2	DUT7
0 °C - 20 °C	5 °C	X	X
20 °C - 30 °C	2.5 °C	X	X
30 °C - 50 °C	5 °C	X	X
6 hours at 50 °C	10 min	X	
50 °C - 30 °C	5 °C	X	
30 °C - 20 °C	2.5 °C	X	
20 °C - 0 °C	5 °C	X	

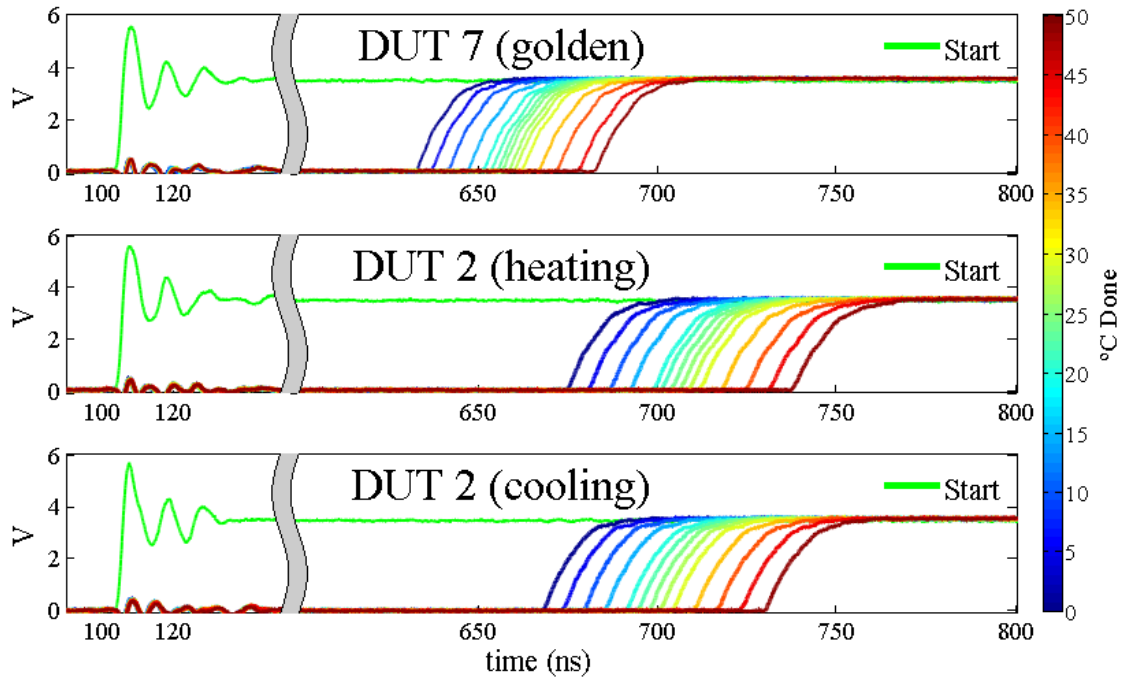


**Figure 3.16:** Oscilloscope measurements of the temperature tests.

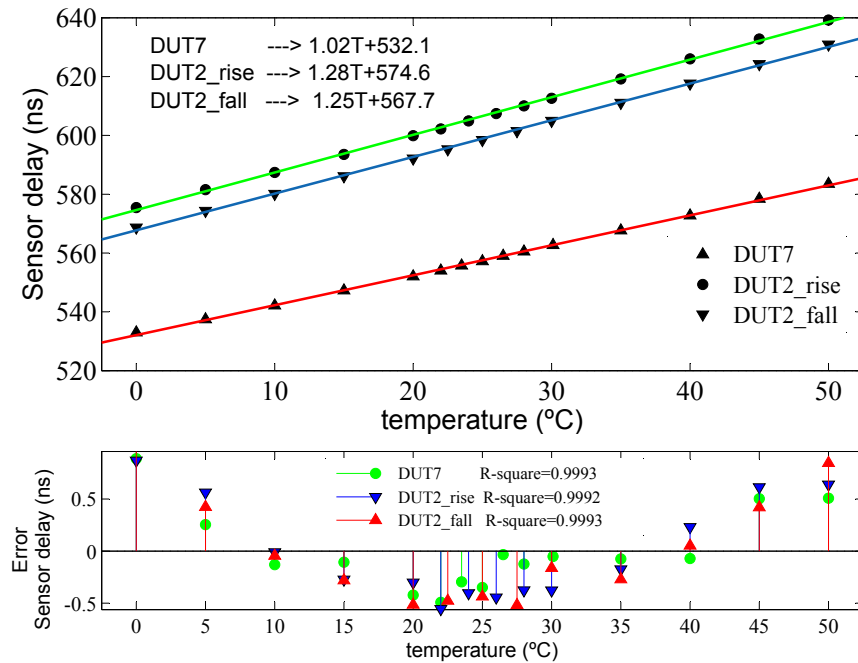


**Figure 3.17:** Temperature transfer function for our sensor design and its associated errors.

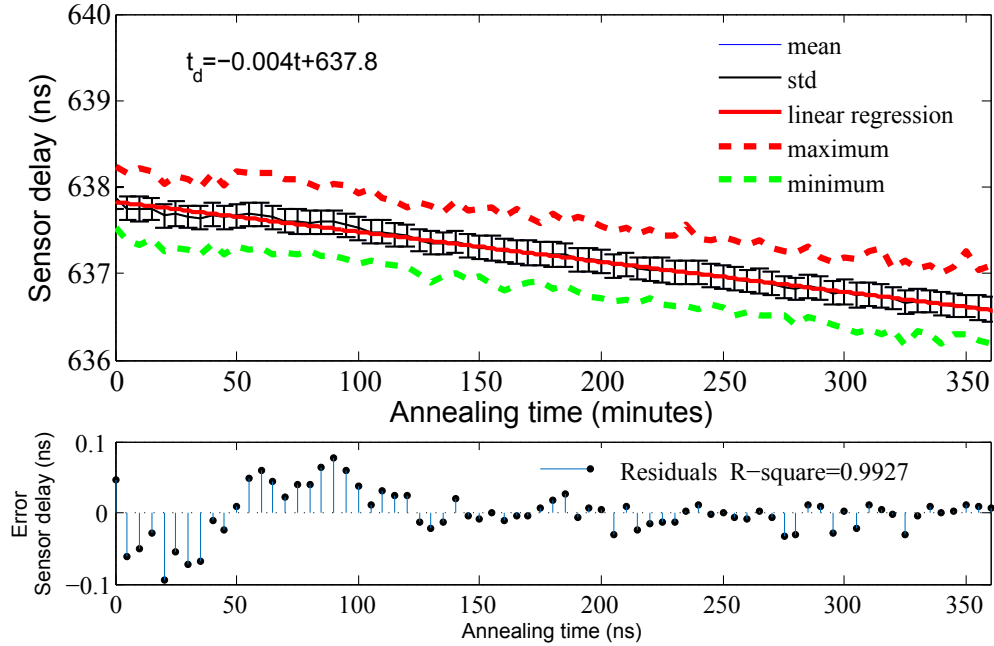


**Figure 3.18:** Sensor response variation and its errors due to accelerated annealing at 50 °C.

### 3.5.2 Temperature Test Results

Figure 3.16 collects the oscilloscope captures of the temperature measurements. As was expected, the delay increases with temperature for both, the golden and the irradiated DUTs. The difference between DUT7 and DUT2 is due to the dose absorbed by radiation exposure. And the difference between DUT2 heating and cooling is due to the annealing process accelerated by the temperature stage at 50°C. Another way of plotting the temperature test results is shown in Figure 3.17. Here a linear regression and its error are calculated.

The sensor has a temperature sensitivity of around 1 ns/°C previous to radiation exposure. After the dose accumulation, the sensitivity increases 20% and the offset 8%. The accelerated annealing step recovers the slope by 2% and decreases the offset by 1%. These results indicate that TID effects can be reversible [KLA96] and high temperatures accelerate the recovering of radiation-induced degradation in electronic systems [GMG<sup>+</sup>15, HKM16]. Of course, high temperatures potentially damage electronic circuits so the temperature range is limited by devices constraints.

The acceleration of the annealing process at 50 °C in DUT2 is shown in Figure 3.18 where upper and lower lines represent the maximum and minimum value of the 100 samples. Curve fitting approximation corresponds to a linear regression because this measurement was made after annealing monitoring for 80 hours, corresponding to the end of the exponential fitting of Figure 3.15.

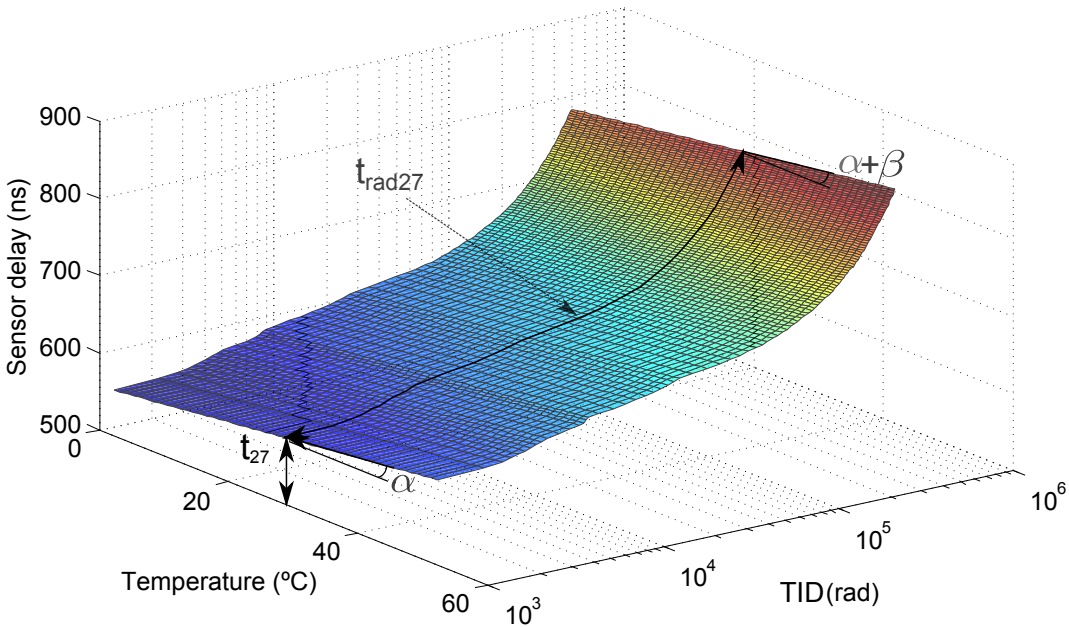


**Figure 3.19:** Representation of Equation 3.11 for DUT2 with measured data.

## 3.6 Calibration

Based on our experimental analysis, we propose the following model for the sensor delay:

$$t_d = t_{27} + \alpha * (T - 27) + t_{rad27}(TID) + \beta(TID) * (T - 27) \quad (3.11)$$

where  $t_{27}$  is the fresh delay at room temperature,  $\alpha$  is the fresh delay slope caused by temperature,  $T$  is the temperature,  $t_{rad27}(TID)$  is the delay caused by the TID at room temperature, and  $\beta$  is the change in the delay slope caused by the TID. Figure 3.19 shows the data measured for our DUT2 sensor, and represents graphically each of the previous parameters.

If we want to extract TID from this equation, first we need to know the value of the current temperature, which can be provided by a different temperature sensor. And second, due to process variations and the uncertainties of the irradiation absorption,  $\alpha$ ,  $t_{27}$ ,  $t_{rad27}(TID)$  and  $\beta(TID)$  are unknown and must be obtained by means of a calibration process.

Concerning  $\alpha$  and  $t_{27}$ , they can be extracted through a two-point calibration process on the fresh circuit, one at room temperature to extract  $t_{27}$ , and another at a different temperature to obtain  $\alpha$ .

As far as  $t_{rad27}(TID)$  and  $\beta(TID)$  are concerned, these complex functions actually need irradiating the circuit with a well calibrated source to be obtained. As this is a destructive process, since the sensor only recovers partially from the degradation induced by

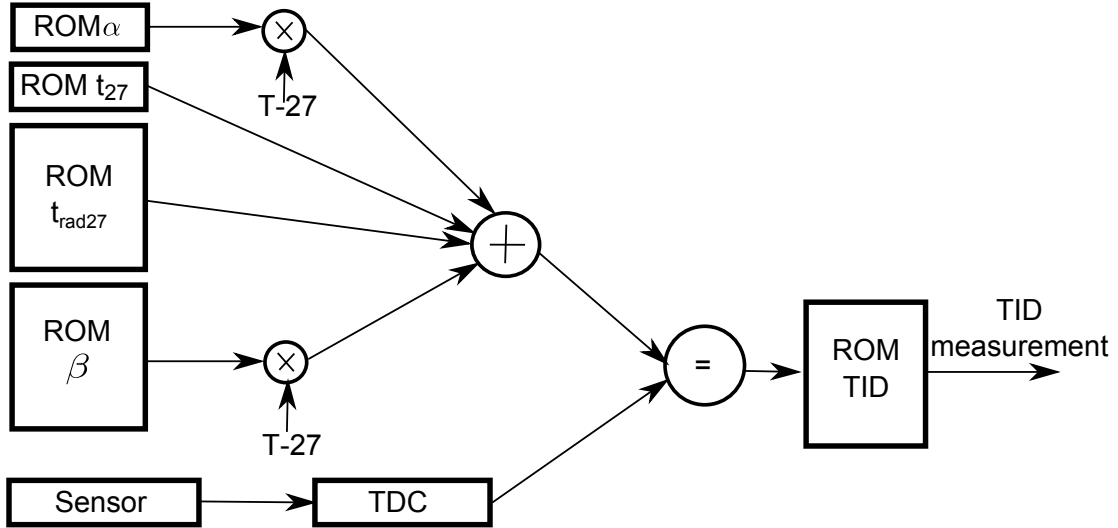


**Figure 3.20:** Conversion process from delay to TID value.

the irradiation, instead of the calibration of each design, we propose a statistical calibration of the technology. The idea consists on running irradiation tests at room temperature on a set of identical sensors in order to obtain  $t_{rad27}(TID)$  and take measurements at different temperatures for each TID step to obtain  $\beta(TID)$ .

The current TID can be extracted for a given  $t_d$  measurement. The process is depicted in Figure 3.20. Our sensor produces a pulse whose width is converted into a digital word by a TDC. The circuit comprises three ROMs, two of them store  $t_{rad27}$  and  $\beta$  —each word of the memories corresponding to a specific TID value—, the other one stores the correspondence between address of the former memories and the TID value. Besides, the circuit has two ROM registers that store  $\alpha$  and  $t_{27}$ . We must find a TID value that fulfills Equation 3.11, to accomplish this task, we propose an iterative search on the ROM memories until the correct value of the TID is found. Putting together the measurement process and the calibration stage, the accuracy of the measurement is fixed by the depth of the  $t_{rad27}$  and  $\beta$  ROMs.

## 3.7 Discussion

Taking into account the results from the radiation and temperature tests of our sensor, we propose the implementation of a similar dynamic self-recovery system for radiation environments. Reconfigurable designs have already been studied for space applications [JCG<sup>+</sup>12, GSC11] that allows to change the purpose of circuits, but they do not contemplate the possibility of adapting the system following the dose absorbed. Other works [GMG<sup>+</sup>15, SH13], have presented methods of increasing the operating life of a semiconductor device

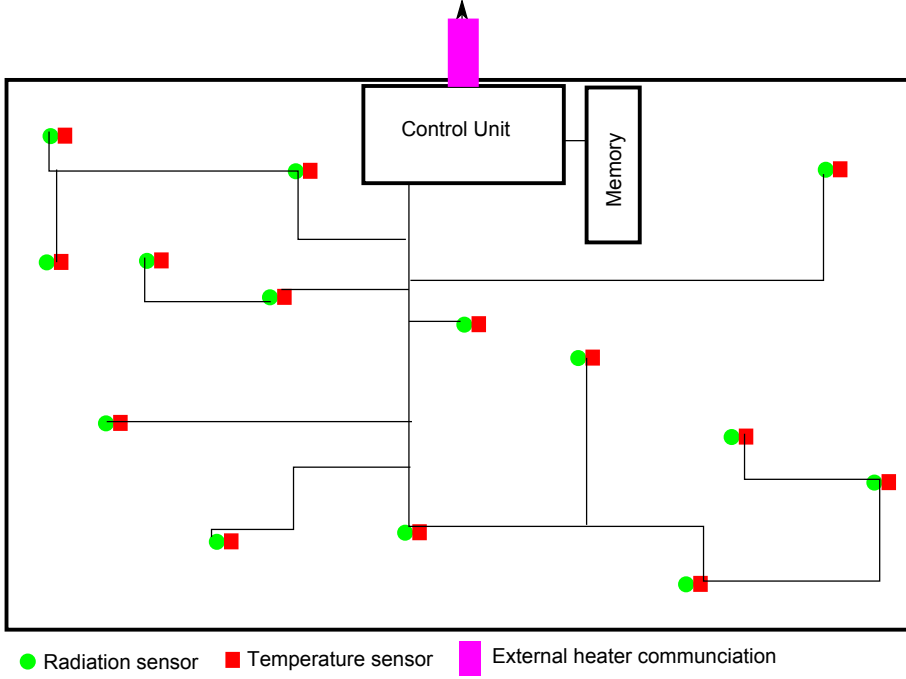


**Figure 3.21:** Scheme of the proposed radiation self-recovery system.

used in a harsh ionizing radiation environment. Our proposal tries to take advantage of the annealing recovery and temperature acceleration processes studied in our sensor response. The objective is to implement a dynamic self-recovery system that can be fit in most of electronic devices, from reconfigurable systems such as FPGAs, to ASICs.

In Figure 3.21 the proposal of the TID monitoring scheme for a self-recovery system is presented. The main characteristics of this design are:

- Radiation sensors configure a network to monitor the most critical pieces of the die design in order to keep them into the security margins.
- Temperature sensors of minimum size [IALV08] designed with RHBD techniques can be used to compensate the radiation measurement for temperature variations. They share the same interface [ILVMO12] as the proposed TID sensor.
- External heating devices could be used to accelerate annealing in order to recover the transistor nominal  $V_t$ .
- A radiation hardened Control Unit is used to control the process of measurement, evaluation and decision, where the unit can choose between powering off the parts with too much dose, forcing annealing process by temperature control or staying idle.

- Rad-hard memories perform the conversion of radiation and temperature measurements according to the proposed calibration methodology.
- An interesting point is that calibration might be unnecessary if the sensor network goal is monitoring the degradation of electronics in different parts of the circuit. In this case, controlling the delay shift is enough, thus TID conversion can be skipped.

Using this scheme, an example of its operation would be: the control unit sweep periodically the measurement of each radiation sensor to monitor the absorbed dose of each part of the circuit. Each measurement needs to monitor the adjacent temperature sensor that compensates the variation of the radiation sensor due to temperature. If the dose absorbed is above the limit of secure operation, then the control unit is able to apply different policies to recover the system. These policies could be: stop the system, stop just a part close to the affected area, heating the system to accelerate the annealing or use micro-heaters to recover just the most radiated zone.

In the implementation of this type of systems, the overhead of designing an additional sensor network is desirable to be as small as possible and the power consumption should have a very small impact in the consumption of the whole design. Hence, both characteristics are perfectly fulfill by our TID built-in smart sensor.

## 3.8 Conclusions

In this chapter, a TID sensor has been designed, manufactured, radiated and characterized. It is a digital CMOS sensor based on the relationship between the accumulated radiation and the performance degradation of the frequency in ring oscillators. The bigger the dose absorbed, the slower the ring oscillator frequency. The main advantages of this sensor compared to RADFET, the reference sensor used by nearly all applications, is that our design actually measures the dose absorbed by an electronic circuit instead of the amount of radiation it has been exposed to.

The design of the sensor has been divided into two different areas, the sensitive part and the control logic. As the control logic needs to be robust against radiation, RHBD mitigation techniques have been used to harden this block.

Extensive experimental tests have been carried out to fully characterize the proposed sensor. In the radiation tests biased DUTs have shown a response that matches their expected behavior under radiation while unbiased sensors were almost immune to TID effects. Charge redistribution has been also observed after the radiation test what supports the possibility of implementing dynamic recovery systems.

Additionally to the radiation characterization, we have characterized the sensor in terms of temperature sensitivity to be able to compensate the deviation produced by temperature

variation. The sensor proved to be almost linearly dependent on this magnitude, hence easy to compensate by a previous calibration. A calibration system has also been proposed. It is based on the use of memories, adders and multipliers that remove the radiation measurement deviation.

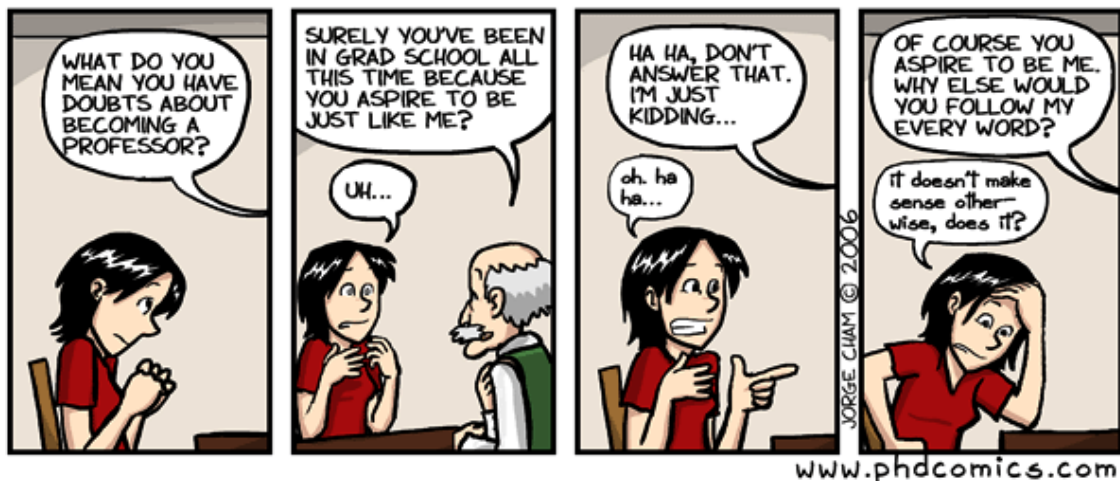
The main features of our prototype are: small size, low power consumption, fully integrable, digital interface and configurable sensitivity. All of them make our proposal suitable for its implementation in every circuit that needs to monitor the dose absorbed in order to maintain the devices in safe operation conditions. The versatility of the design makes it possible to use in all kind of electronic systems. Moreover, the control of actual absorbed dose can be used to implement a self-recovery system using heaters to force annealing in the affected areas.

### 3.9 Related Publications

- **J. Agustin**, C. G. Soriano, M. L. Vallejo and P. Ituero, "*A built-in CMOS Total Ionization Dose smart sensor*," IEEE SENSORS 2014 Proceedings, Valencia, 2014, pp. 70-73. doi: 10.1109/ICSENS.2014.6984935
- **J. Agustin**, C. Gil, M. Lopez-Vallejo and P. Ituero, "*Design and Characterization of a Built-In CMOS TID Smart Sensor*," in IEEE Transactions on Nuclear Science, vol. 62, no. 2, pp. 443-450, April 2015. doi: 10.1109/TNS.2015.2404532

# Chapter 4

## Efficient Mitigation of SET Induced Harmonic Error



## Chapter 4

# Efficient Mitigation of SET Induced Harmonic Error

### 4.1 Introduction

Soft errors are an important source of fault injection that reduces the reliability of modern nanometer technologies [SYW13]. Since the detection of first radiation induced soft errors, SEUs were the principal contribution to the system errors. Therefore, many different applications and solutions have been investigated and proposed for the hardening of this kind of effects. On the other hand, SETs were not considered so important because they were mostly masked without altering any output of the systems. However, technology scaling has enhanced the severity and relevance of SET effects. The occurrence and propagation of SETs increases as geometric dimension and capacitance scale down, while the probability of SET capture grows with higher operational frequencies [FCMG13]. Therefore, for the last decade, SETs have emerged as the main contribution to soft error rate in electronics [HA13]. Consequently, SET research has became an important topic in radiation effects field. Nowadays, many efforts are focused on studying of the phenomenon through experimental observation, modeling and simulation at different levels of abstraction.

The study of SETs has been closely linked to the impact of this transitory effect into a chain of inverters [FCPM<sup>+</sup>07, GAN<sup>+</sup>10] because they are a simple enough structure that allows to easily understand the basic mechanisms of the generation and propagation of SETs. Recent works have observed that SETs can cause the shift of the output oscillation from the fundamental frequency to an odd harmonic in ring oscillators [CBN<sup>+</sup>09]. And it has been also reported an analytical harmonic window model [C<sup>+</sup>14] that characterizes those harmonic induced errors and sets the conditions that ring oscillators and SETs must fulfill together in order to be affected by this phenomenon. Since the frequency shift produced by the odd harmonic appearance may result in system errors, synchronization problems or SEFIs, it is necessary to harden the design of ring oscillators for radiation applications.

This chapter is focused on completely removing the harmonic induced errors in ring oscillators by an effective design with negligible area overhead. To accomplish this task, we propose a new design of ring oscillators that makes use of asymmetric stages in order

to force the electrical masking of the SET pulse induction. The asymmetric design confers the ability of configuring the duty cycle on the ring oscillator outputs. The hypothesis of harmonic removal using this new approach has been validated by two different methods: Firstly by the simulation of SET injection with a 40 nm commercial technology. Secondly by the measurement of SET emulation into two different manufactured test circuits. These designs are implemented with a  $0.35\text{ }\mu\text{m}$  commercial technology. To guarantee a SET occurrence in the ring oscillator test circuits, instead of taking a very expensive radiation test campaign, we have designed a SET emulation injection based on forcing a third harmonic oscillation by introducing three different enabled nodes instead of just one. The emulated SET satisfies all the conditions [C<sup>+14</sup>] required to provoke a third harmonic shift, but as was expected, our design fully masks them all. Therefore, the model has been validated with two different technologies and topologies.

The rest of the chapter is organized as follows: First in Section 4.2, the SET effects are explained from the physical basics to the testing methods. Section 4.3 summarizes the analytical model of Chen et al. [C<sup>+14</sup>] for the induction of harmonic errors in ring oscillators. After that, the SET-removal proposal is presented and characterized in Section 4.4. Then the model and the proposed SET mitigation strategy is simulated in Section 4.5. The manufactured prototype and the designed SET emulation system are described in Section 4.6. Section 4.7 deals with the validation of the model through electrical measurements. And finally Section 4.8 concludes with the main contributions of this chapter.

## 4.2 Single Event Transients in Electronics

### 4.2.1 Introduction

When an energetic nuclear particle hits a semiconductor structure, it loses energy through the interaction with the material lattice structure. Unlike TID which causes the permanent degradation of device parameters, a single event is an instantaneous effect. As the charged particles pass through the material, the ions generate electron-hole pairs through their path. Those free electrons and holes liberation creates an unexpected electric current in the semiconductor device. That induced electric current is the foundation of all SEEs. Attending to the effect produced by that transient current, SEEs are classified according to the list presented in Chapter 2 (SEU, SET, SEFI, etc.). Among all of these effects, this chapter is focused on solving a SET effect in ring oscillators, which can be considered the source of all other effects.

There are three stages involved in the formation of SETs: charge generation, charge collection and circuit response. The charge generation is defined as the amount of electron-hole pairs generated by the particle hit and it depends on the LET of the incident ion. The charge collection includes the process of charge redistribution and diffusion. It depends on

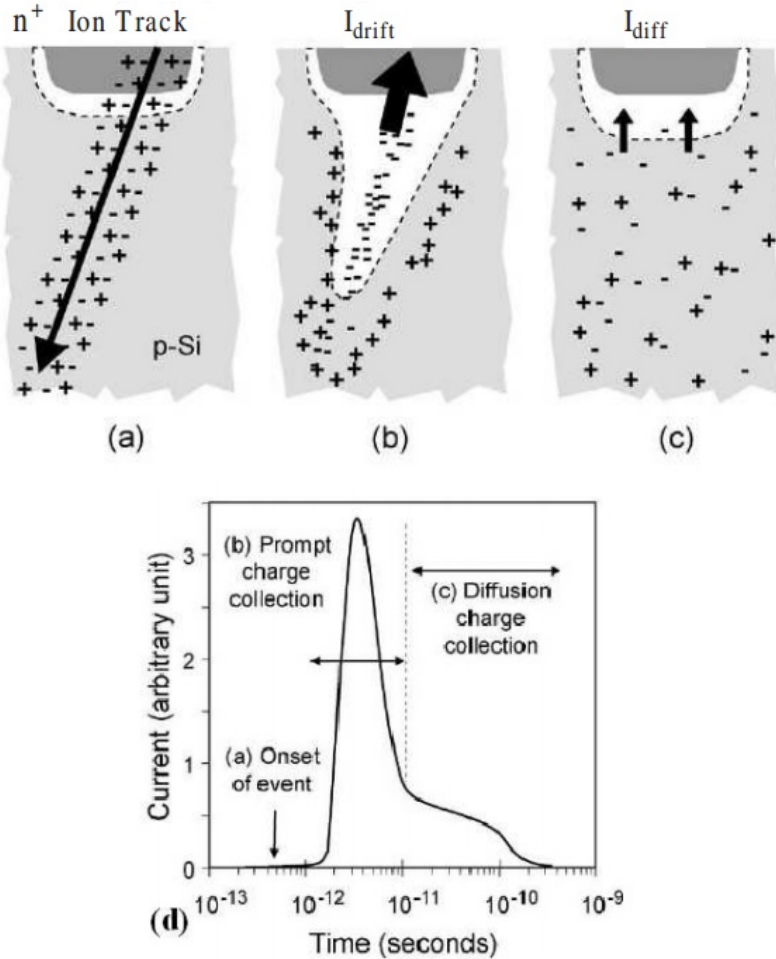


**Figure 4.1:** Charge generation and collection phases in a reverse-biased junction and the resultant current pulse caused by the passage of a high-energy ion [Bau05a].

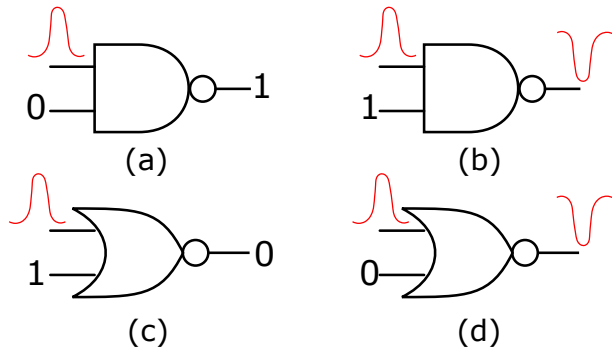
electrical parameters such as the applied bias and technology doping levels. The charge collection varies widely from one circuit to another and from one transistor to another in the same circuit. The third stage, the circuit response, depends on the topology of the circuit, and it is the characteristic that differentiates SETs from SEUs. If the ion strike flips a storage element, it is a SEU. Otherwise, if the ion impact is into combinational logic, the result is a SET whose amplitude and duration depend on several factors as ion LET, region sensitivity or on the layout of the circuit. Thus, from the circuit designer perspective, the mitigation techniques for SET effects are focused on optimizing the factors that affect the circuit response while the improvement of charge generation and collection in semiconductors corresponds to RHBP techniques.

Figure 4.1 depicts the first two processes—charge generation and collection—to produce a SET. First, the ion strike is produced close to a sensitive device node. Then,

the particle generates radial distribution of electron-hole pairs such as in Figure 4.1 (a). The charge distribution induces a temporary funneling effect where some charges are recombined but most of them are redistributed (Figure 4.1 (b)). The funneling effect lasts around tens of picoseconds, after what, the diffusion dominates the redistribution of charges in Figure 4.1 (c). Diffusion could last about nanoseconds. The combination of all these processes results in a current pulse at the junction as illustrated in Figure 4.1 (d). The current transient typically lasts hundreds of picoseconds.

Regarding the circuit response, not all generated SETs in a circuit are visible at the outputs. Even an ion with enough energy and striking into a very sensitive area inducing a high current can be mitigated. When this occurs, the SET is masked. There are three factors that determine whether an SET will propagate and result in an error:

- Logical masking. A SET is masked due to the value of the other inputs. For example, in Figure 4.2 (a,c), the outputs are not switched while the same hit node with different inputs in Figure 4.2 (b,d) swing.



**Figure 4.2:** Logical Masking (a and c) and propagation (b and d) of SET by NAND and NOR gates.

- Electrical masking. It refers to the process whereby the induced current propagates through a combinational path. The spontaneous glitch is able to propagate just through a finite number of stages. The reason is that the slopes of the ion current are greater than the delay of combinational logics and therefore, the gate cannot drive the next node at that speed, degrading the pulse as in Figure 4.3.
- Temporal masking. SETs are only an issue if at the end of the combinational path the glitch is latched into a register. So, there is only a vulnerability window in which the glitch can be converted into a SEU. In Figure 4.3 the two different scenarios are presented (latched and non-latched).

The increasing relevance of SETs with shrinking technology nodes can be explained through the analysis of the dependency of technology into masking effects. First, the

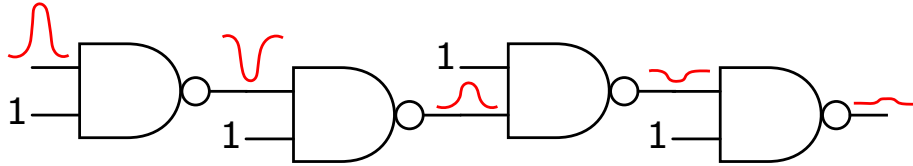


**Figure 4.3:** Electrical masking of SET due to the propagation delay of combinational gates.

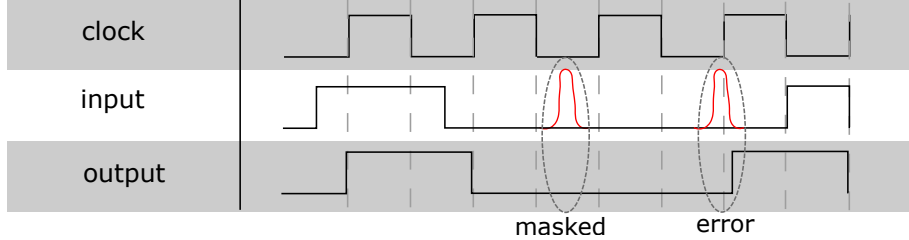


**Figure 4.4:** The temporal masking of SETs depends on the vulnerability window of registers.

implementation of transistors with smaller dimensions increases the density of active zones in system layouts what increases the probability of an ion track to impact in sensitive nodes. Second, the smaller capacitance of nodes facilitates wider induced pulsewidths. Third, the electrical masking decreases with wider pulsewidths and faster gates. Finally, the temporal masking is also reduced because the vulnerability windows increases with higher frequencies. The vulnerability window is defined as the relationship between the part of the clock period where a glitch makes the output swing with the part where it is unaltered. This value is determined by the setup and hold times of registers and the frequency. Set up and hold times decrease with technology but not as much as the operational period. Therefore, the affected ratio increase significantly. The addition of these effects has made SET the major contribution to the Single Event Rate (SER) in modern circuits.

### 4.2.2 Testing

Routine SEE testing in real operation conditions is impractical because of three main reasons:

- The integration of devices into space experiments are extremely expensive and the access is highly limited due to the small amount of missions and the high demand of area in spacecrafts.
- The control of the impact particles to sensitive regions for testing critical points in electronic designs is unfeasible due to the randomness of natural environments.

**Table 4.1:** Guidelines and Standards for SEEs testing.

Test Standard	Description	Source
JESD57	Test Procedures for the Measurement of Single-Event Effects in Semiconductor Devices from Heavy Ion Irradiation	Heavy Ions
JESD89	Test guideline for Alpha and Neutron SEE testing	Alpha and Neutrons
ASTM F-1192	Test guideline for heavy ion testing	Heavy Ions
ESCC 25100 ISSUE 1	SEE testing of integrated circuits and discrete semiconductors devoted to space applications	Protons and Heavy Ions

- The time required to perform an in-depth characterization would take a long time using the fluxes presented in ground or space environments.

Therefore, testing is done using ground facilities. Although every facility offers different kinds of test, all of them obey the guidelines approved by standard organization to homogenize their results. There are different guidelines and standards to test and characterize electronic components and circuits in terms of SEE response. The most important procedures are outlined in Table 4.1. The approved methods to test SEE use accelerators, radioactive sources and pulsed lasers. Each of these techniques has its own strengths and limitations.

## Accelerators

Most SEE testing is done at accelerators with relatively low-energy ions (tens of MeV/amu) because of the much greater cost and more limited accessibility of high-energy ion accelerators [GRD<sup>+</sup>16, CLT<sup>+</sup>14]. Because low-energy ions are unable to pass through thick material, packaged parts must be delidded and placed in a vacuum chamber.

Although accelerators are necessary for SET testing, they do not, in general, provide any spatial or temporal information about the origins of SETs, which restricts their use to qualifying parts rather than obtaining detailed information about the actual mechanisms responsible for SETs [PBS<sup>+</sup>16].

## Radioactive Sources

Radioactive sources ( $\text{Cf}^{252}$  [YYCS14, EHA<sup>+</sup>15] and  $\text{Am}^{241}$  [ZJA<sup>+</sup>16, MGJ<sup>+</sup>13]) may be used for laboratory measurements of SET sensitivity.  $\text{Cf}^{252}$  is more widely used in the space community because the ions emitted from the nucleus have higher LETs than the alpha

particles emitted by Am<sup>241</sup>. Unfortunately, both radioactive sources emit ions with limited range and, in the presence of passivation layers, the ions are not able to reach the sensitive volume in which SETs are generated. In addition, for detailed studies of SET mechanisms, the technique does not provide spatial information, although some temporal information may be obtained from time-of-flight measurements.

### Pulsed Lasers

The pulsed laser has been used successfully to investigate the nature of SETs in both analog and digital integrated circuits [SFW<sup>+</sup>16, AHG<sup>+</sup>13]. A pulsed laser is well suited for studying SETs because the beam of light can be focused to a spot about a micron in diameter and positioned on any desired location in the circuit to inject SEEs. Pulsed laser light produces no radiation damage in the semiconductor. This makes it possible to probe in detail SET-sensitive regions in the circuit for which it is necessary to irradiate for long periods of time. Another feature of pulsed laser testing is that the arrival time of the light pulse can be adjusted relative to the circuit clock [BMPM13], a capability needed for measuring frequency dependent capture probabilities of SETs in latches. Additional useful features are that the technique requires no vacuum and it is convenient because it can be used in both laboratory and fabrication facilities. There are two limitations to this technique. One is that metal layers and multilayer dielectrics interfere with the transmission of the light, further complicating the establishment of a reliable and accurate threshold energy. And the other is that, in very dense circuits with the minimum feature size less than the diameter of the focused light beam, it is unlikely that SET thresholds can be obtained.

#### 4.2.3 SET Modeling

Testing is a mandatory stage to assure the reliability of circuits. However, the cost of test campaigns is so expensive that testing every prototype is not affordable. In order to be able to preview the effects of SETs in circuits, different models have been developed. In general, the role of modeling is to provide designers with a set of tools that they may be used to:

- Better understand the physical mechanisms.
- Analyze and predict the results of testing.
- Develop appropriate hardening strategies.

A commonly used analytical model to simulate the induced transient current waveform is the double-exponential function with a fast rise time and a slower fall time [BRW<sup>+</sup>15].

This model has been validated with many different technologies [WVK07,CRL<sup>+</sup>03,WVNK08] and it is the most used in transistor-level simulations.

$$I(t) = \begin{cases} 0 & t < t_{d1} \\ I_{peak} \left( 1 - e^{\frac{-(t-t_{d1})}{\tau_1}} \right) & t_{d1} < t < t_{d2} \\ I_{peak} \left( e^{\frac{-(t-t_{d2})}{\tau_2}} - e^{\frac{-(t-t_{d1})}{\tau_1}} \right) & t_{d2} < t \end{cases} \quad (4.1)$$

where  $t_{d1}$  is the onset of the rise of the current,  $t_{d2}$  is the onset of the fall of the current,  $I_{peak}$  is the maximum current to be approached,  $\tau_1$  is the rise time constant, and  $\tau_2$  is the fall time constant

Recent studies have improved the model for nanometer technologies. In technologies under hundreds of nm, a new effect has appeared in the charge collection process when a transistor is embedded into a combinational path. Instead of a double exponential, in the middle of the falling step, it exists an interval where the induced current remains almost constant as can be seen in Figure 4.5. This phenomenon named “plateau” has been attributed to the collapse of potential at the struck junction and a subsequent balance of charge collection current and resupply current from the restoring device [DWB<sup>07</sup>]. This effect has been shown to be critically important to the SET pulsewidths under for technologies 100-nm.

To translate this behavior into a circuit discrete component to be integrated in a transistor-level model, in [BRW<sup>15</sup>] a dual double exponential current source is proposed. The “plateau” phenomenon can be modeled by two components: a long double-exponential current source equal to the shelf current and a short double-exponential current source to add the extra current for the short peak. [BRW<sup>15</sup>] validates this double source model against an IBM 90 nm technology and more recently, [QXW<sup>16</sup>] has also applied this model to a 65 nm commercial technology.

## 4.3 SET Induced Harmonic Errors in Ring Oscillators

Once the SET effect has been introduced, this Section analyzes the problem that this kind of radiation effects produces in ring oscillators. Ring oscillators are formed by a chain of inverter gates connected in a loop configuration. Since they are made of combinational logic, they are not affected by SEUs. But, at the same time, the loop configuration enables the lock of a SET in the circuit and, consequently, a persistent error instead of a transient glitch.

If a SET induced current is produced in a node of a ring oscillator, then its output can change its properties. Casey et al. [CBN<sup>09</sup>] outlined the potential consequences of a SET impact in a ring oscillator. They used laser strikes at different energies to induce SETs

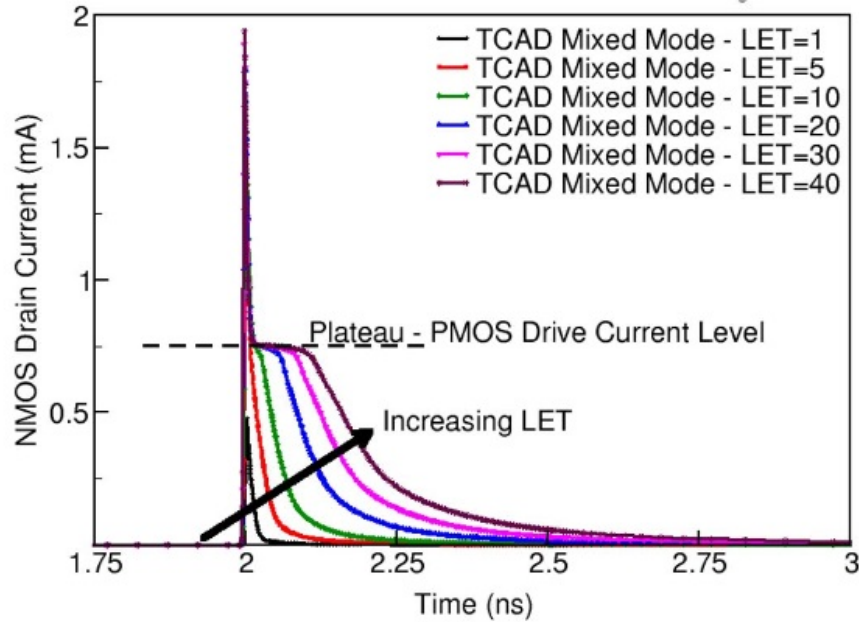


**Figure 4.5:** Plateau effect presented in [DWB<sup>+</sup>07] as a consequence of SETs in technologies under 100 nm.

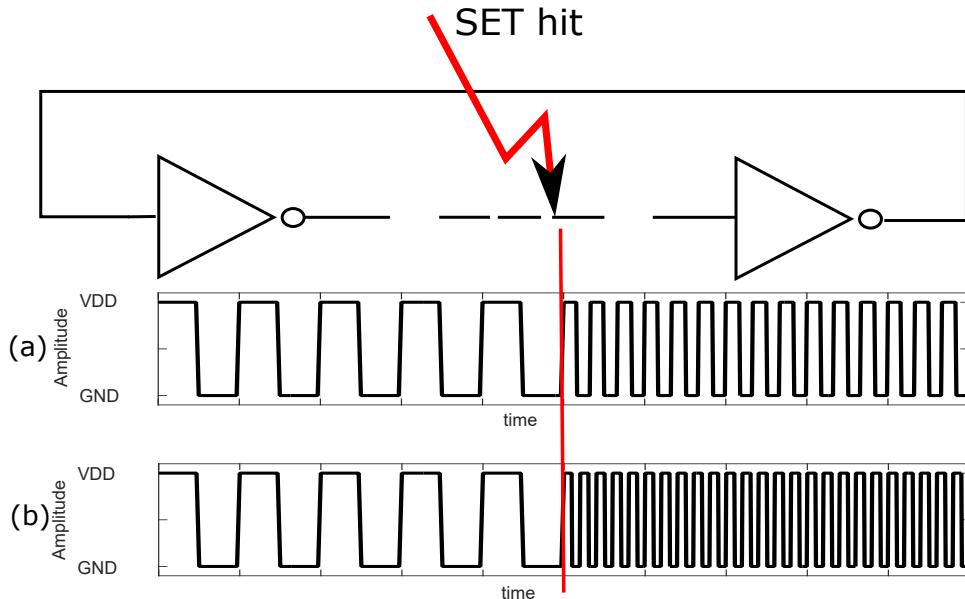


**Figure 4.6:** SET impact in a ring oscillator and the potential 3rd (a) and 5th (b) induced harmonic oscillations.

and they conclude that a SET in a ring oscillator can shift the output frequency to an odd harmonic of the fundamental oscillation as can be seen in Figure 4.6.

In addition, Chen et al. [C<sup>+</sup>14] observed that the harmonic induced oscillation can be transitory or it can be permanently changed. To define those possibilities they developed an analytical model called “Harmonic Vulnerability Window” model. That model sets the requirements that a SET must fulfill to produce and sustain the third harmonic induced error in a Digitally Controlled Ring Oscillator. In that work, the next assumptions and notations are made:

- A ring oscillator consists of N inverter gates with propagation delays  $(t_{d0}, \dots, t_{di}, \dots, t_{d(N-1)})$ .
- The period of the output clock signal is:

$$T/2 = t_{d0} + \dots + t_{di} + \dots + t_{d(N-1)} \quad (4.2)$$

- The maximum propagation delay ( $t_{dmax}$ ) is defined by:

$$t_{dmax} = \max\{t_{d0}, \dots, t_{di}, \dots, t_{d(N-1)}\} \quad (4.3)$$

Using these assumptions, the three requirements for maintaining the third harmonic oscillation in a steady state are:

1) *The SET must introduce one rising edge and one falling edge transition within half the oscillation period.*

This condition defines a maximum limit for a SET induced pulselength ( $t_{SET}$ ). If it is greater than this limit, the impact at the output is an increased instant skew.

2)  *$t_{SET}$  should be greater than the largest gate propagation delay in the ring oscillator.*

$$t_{SET} > t_{dmax} = t_{SET(min)} \quad (4.4)$$

Otherwise the SET would be electrically masked by the slowest gate. This condition defines a minimum limit.

3)  *$t_{SET}$  should be smaller than the total loop delay ( $L$ ) minus two times  $t_{dmax}$ .*

Furthermore, if  $t_a$  and  $t_b$  are defined at the hit node as the time between one clock edge and the start of SET and between the end of the SET and the other clock edge according to Figure 4.7, then the upper limit is adjusted by:

$$t_a > t_{dmax} \quad \text{and} \quad t_b > t_{dmax} \quad (4.5)$$

$$t_{SET(max)} = L - t_a - t_b < L - 2t_{SET(min)} < L - 2t_{dmax} \quad (4.6)$$

If any of all of these times is violated, then the SET is electrically masked in a few clock cycles.

The three initial assumptions include the case of different  $t_{di}$  but they suppose a ring oscillator formed by balanced gates in which the fall delay time ( $t_{dfall}$ ) and rise delay time ( $t_{drise}$ ) are equal. The solution proposed in this thesis does not meet this assumption, so the “Harmonic Vulnerability Window” model will be reformulated in an unbalanced ring oscillator.

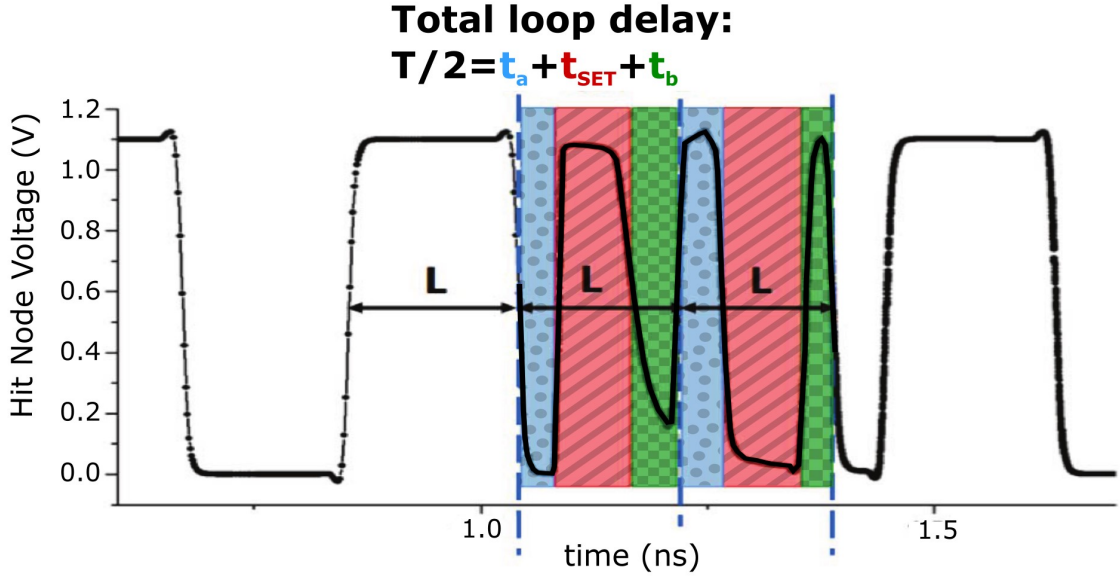


**Figure 4.7:** SET pulse parameters defined in [C<sup>+</sup>14] for Induced Harmonic Errors characterization.

## 4.4 Proposed Solution

Considering the three requirements of SET harmonics introduced in [C<sup>+</sup>14], our goal is designing a ring oscillator whose output lacks of the vulnerability window of Figure 4.7. To accomplish this task, this thesis devises a procedure that generates an output with a duty cycle that is not 50% and it is big enough to overlap  $t_a$  and  $t_b$ . Then the SET would be electrically masked as the three requirements previously assumed are not fulfilled. This design also avoids the induction of higher harmonics [Cas10] but from now on, the chapter will be focused on the third harmonic to validate the concept. In this Section the schematic of the proposal and its mathematical analysis is introduced to understand the behavior. The explanation of the SET mitigation process is described in the next Section.

The proposed solution is based on the ring oscillator schematic of Figure 4.8. This ring oscillator is made of an odd number,  $N$ , of gate inverters. All transistor gate lengths ( $L$ ) are the minimum allowed by the technology. The difference with conventional ring oscillators is the introduction of asymmetry in the design of transistor aspect ratios which results in unbalanced ring stages ( $t_{dfall} \neq t_{drise}$ ). The  $N$  nodes are divided into odd and even nodes. At odd nodes, the pMOS devices are larger than the nMOS devices and therefore can sink more current than the nMOS devices. As a result, the pull-up path ( $t_{drise}$ ) is faster than the pull-down path ( $t_{dfall}$ ) ( $t_{dfall} > t_{drise}$ ). Even nodes are designed upside down with a smaller pMOS ( $W_{pe}$ ) and a larger nMOS ( $W_{ne}$ ). Then, at even nodes, the pull-up path ( $t_{derise}$ ) is slower than the pull-down path ( $t_{defall}$ ) ( $t_{defall} < t_{derise}$ ).

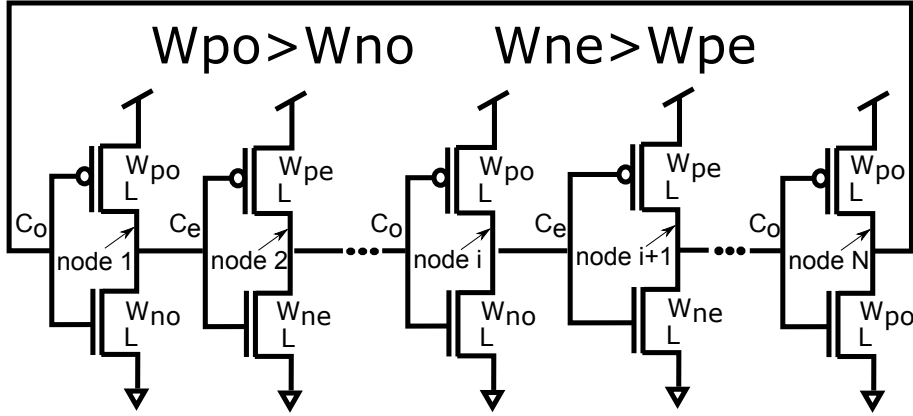


**Figure 4.8:** Proposed asymmetric solution for Harmonic Error Mitigation in ring oscillators.

Taking into account the previous parameters and constraints, we define some relationships between them to reduce the degrees of freedom and simplify the model:

- $W_{pe} = \beta * W_{no}$  where  $\beta$  is equal to the ratio between hole and electron mobility  $\mu_n / \mu_p$  to match  $t_{dofall}$  with  $t_{derise}$ ,  $t_{dofall} = t_{derise}$
- $W_{ne} = \beta * W_{po}$  to match  $t_{defall}$  with  $t_{dorise}$ ,  $t_{defall} = t_{dorise}$
- $W_{ne} = \gamma * W_{no}$  where  $\gamma$  introduces the asymmetry that breaks the assumption of the model in [C<sup>+</sup>14] for  $\gamma \neq 1$  resulting in  $t_{dorise} \neq t_{derise}$ .
- $C_o \approx C_e$  thanks to the previous relationships.

With all these definitions, the expression of the period ( $T$ ) of a ring oscillator depending on the new delay parameters is ruled by:

$$\begin{aligned} T &= t_{d1fall} + t_{d1rise} + \dots + t_{dNfall} + t_{dNrise} = \\ &= N * (t_{dorise} + t_{derise}) \end{aligned} \tag{4.7}$$

As a consequence of the implementation of a ring oscillator using unbalanced inverters, the duty cycle of the signals at each node are different. The duty cycle ( $d$ ) is defined as the ratio between the time a periodic square-signal is high ( $t_{high}$ ) and  $T$ . For odd nodes,  $t_{high}$  is the time the signal is at high level, and for even nodes,  $t_{high}$  is calculated for the inverted signal in order to keep a continuous model. For instance, in a simple 5-stage ring oscillator, the duty cycle distribution along the ring oscillator is calculated in Table 4.2. The notation of even nodes is  $\bar{X}$  to make clear that the duty cycle is calculated for the inverted signal.

**Table 4.2:** 5-Stage ring oscillator duty-cycle distribution.

node	$t_{high}$	$t_{low}$	$T$	$d$
1	$4t_{dorise} + t_{derise}$	$4t_{derise} + t_{dorise}$	$5t_{derise} + 5t_{dorise}$	$\frac{4t_{dorise} + t_{derise}}{5(t_{derise} + t_{dorise})}$
$\bar{2}$	$3t_{dorise} + 2t_{derise}$	$3t_{derise} + 2t_{dorise}$	$5t_{derise} + 5t_{dorise}$	$\frac{3t_{dorise} + 2t_{derise}}{5(t_{derise} + t_{dorise})}$
3	$2t_{dorise} + 3t_{derise}$	$2t_{derise} + 3t_{dorise}$	$5t_{derise} + 5t_{dorise}$	$\frac{2t_{dorise} + 3t_{derise}}{5(t_{derise} + t_{dorise})}$
$\bar{4}$	$t_{dorise} + 4t_{derise}$	$t_{derise} + 4t_{dorise}$	$5t_{derise} + 5t_{dorise}$	$\frac{t_{dorise} + 4t_{derise}}{5(t_{derise} + t_{dorise})}$
5	$5t_{derise}$	$5t_{dorise}$	$5t_{derise} + 5t_{dorise}$	$\frac{5t_{derise}}{5(t_{derise} + t_{dorise})}$

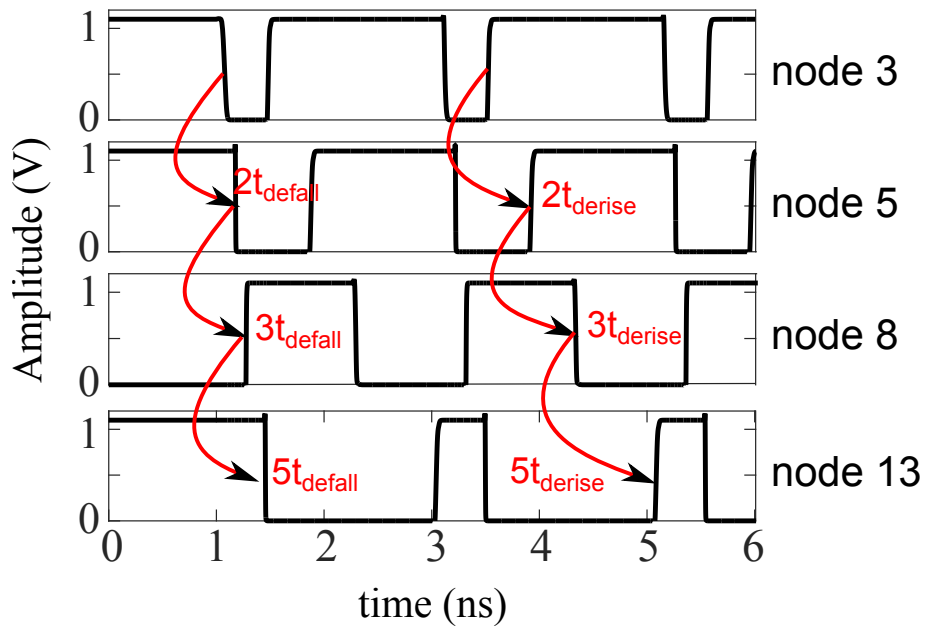
If we generalize the expression of the duty cycle (column  $d$ ) to a ring oscillator of  $N$  stages, the equation that rules the duty cycle is:

$$d_i = \frac{(N - i)(t_{dorise}) + i(t_{derise})}{N(t_{dorise} + t_{derise})} \quad (4.8)$$

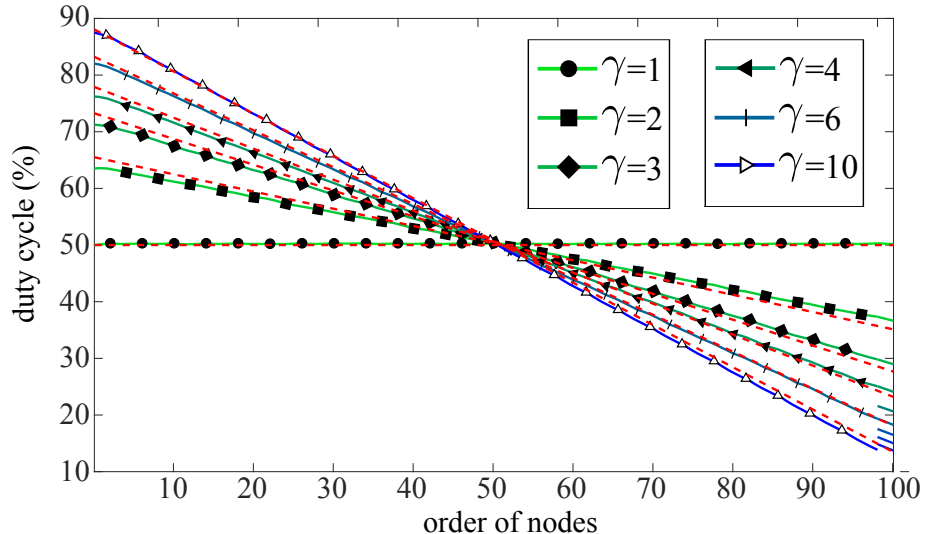
This equation is based on the assumption that different duty cycles in a ring oscillator is correct. It also matches to the conventional ring oscillators based on balanced gates ( $t_{dofall} = t_{derise} = t_{defall} = t_{dorise}$ ) and an output duty cycle of 50%.

Figure 4.9 plots the simulated signal of four internal nodes of a 15-stage ring oscillator with  $\gamma = 4$ . As can be seen, the values of the duty cycles are approximately 80%, 65%, 50%, and 20% as calculated from Equation 4.8. We simulated a bigger ring oscillator of 99-stage using commercial 40 nm technology models to get more accurate results. Figure 4.10 compares the results of the theoretical and simulated duty cycle distributions of that ring oscillator with different  $\gamma$  values. An important characteristic shown by both, the theoretical study and the simulations, is that there is always a node with a 50% duty cycle which can be used as a clock signal or as the conventional output ring oscillators usually provide. The analytical model is a simple model that only considers the transistor gate capacitances. Although it is a very simple model, the maximum absolute error is less than 2%, proving the fundamental behavior of the design.

The main drawback of this proposal is the maximum achievable frequency of the ring oscillator. Since the implemented transistors are asymmetric and different from the fastest design, the maximum frequency is indirectly proportional with respect to  $\gamma$ . Concerning



**Figure 4.9:** Internal nodes (3, 5, 8, 13) of a 15-stage ring oscillator where different duty cycles are observed.



**Figure 4.10:** 99-stage ring oscillator duty cycle distribution for different  $\gamma$  ratios. Dotted lines are theoretical results and solid lines are simulation results.

to the phase noise and jitter measurements, our simulations show the same behavior as conventional ring oscillator with a difference of less than 1%.

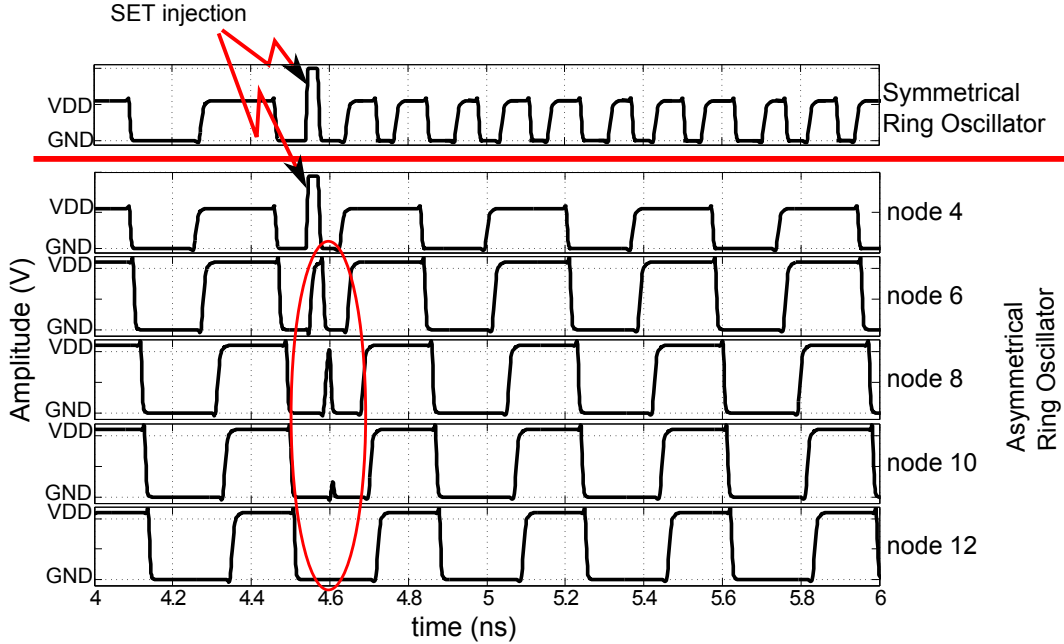


**Figure 4.11:** 15-stage RO internal nodes (4, 6, 8, 10 and 12) with an injected SET at node 4 and its mitigation thanks to the proposed asymmetry.

## 4.5 SET Induced Harmonic Error Mitigation

To validate the hypothesis of using an asymmetric ring oscillator for the SET mitigation, this Section shows the simulation of the design using the models of a commercial 40 nm technology and injecting the SETs by means of double exponential current sources with a “plateau” phase as has been introduced in Section 4.2.3.

Simulations have been carried out for a 15-stage ring oscillator because it is complex enough to verify the SET harmonic induced mitigation without requiring large CPU loads for simulation. The SET injection is configured with the parameters of a current source which controls the injected node ( $\text{node } i$ ), the pulselength of the SET ( $\text{SET}_{pw}$ ) and the time of the impact ( $t_{impact}$ ). We tested SET injections with the characteristics proposed in Chen’s model [C<sup>+</sup>14], hence all simulations met the three criteria summarized in Section 4.3 and they should cause a shift to the third harmonic oscillation.

Figure 4.11 depicts the simulation results for symmetrical and asymmetrical ring oscillators. The conventional symmetrical one is represented by the output of one node. The asymmetrical one uses the signals at the injected even node and at the four next even nodes ( $\gamma = 2$ ). This simulation corroborates the assumption of using asymmetric ring oscillators for harmonic mitigation is correct. As can be seen, every stage attenuates the initial  $\text{SET}_{pw}$ . According to Chen model, if the SET meets the three criteria the ring oscillator should be affected by a harmonic error as the symmetrical ring oscillator output

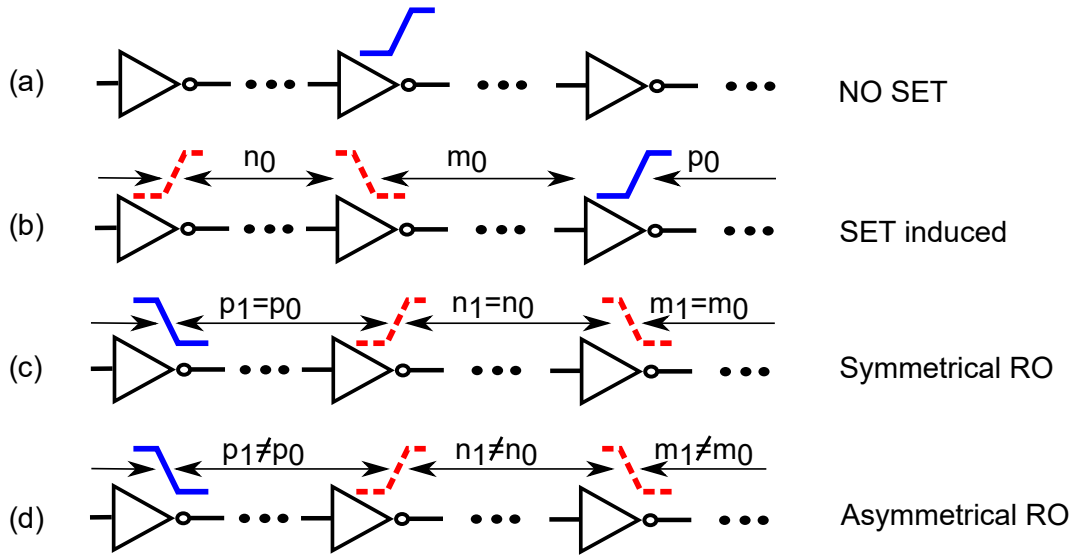


**Figure 4.12:** SET propagation within the ring oscillator nodes. Dashed-lines are the edges induced by a SET.

shown on the top of Figure 4.11. In Figure 4.11 the node 12 is not altered by the injection at node 4, therefore the output node N is also unaffected.

It may seem that the attenuation is because  $t_{dmax}$  is longer in our proposal than in conventional ring oscillators but this is not the real reason, which is depicted in Figure 4.12. When this circuit is working at its fundamental frequency, there is only one node switching at a time as in Figure 4.12(a). We divided its operation into two modes: first, the rising edge propagation while node N is low; second, the falling edge while it is high. If the SET third harmonic appears as described in [C<sup>+</sup>14], then there are three nodes switching simultaneously instead of just one according to Figure 4.12(b).  $n_0$  is the number of nodes between the two edges excited by the SET impact,  $m_0$  is the number of nodes between the first node induced by the SET and the edge of the normal behavior and  $p_0$  is the number of nodes between the edge of the normal behavior and the second node induced by the SET. The three values are defined just at the moment when the particle hits. In ring oscillators composed by balanced gates, the time of falling and rising edges propagation is the same, so the edges keep their distance constant a long time as in Fig 4.12(c).  $n_1$ ,  $m_1$  and  $p_1$  are the same parameters but a certain time after the ion impact. On the other hand, our asymmetric design establishes different paths for rising and falling edges with different time delays ( $N * t_{dorise}$  and  $N * t_{derise}$ ). This difference is shown in Fig 4.12(d), it lets the fast edges “catch” the slow ones neutralizing the third harmonic excitation.

The proposed ring oscillator has shown the total mitigation of harmonic induced errors, but there is still a chance of the SET to appear at the ring oscillator output. From Figure 4.11 we conclude that a SET with a pulselength  $SET_{pw}$  propagates through a number of

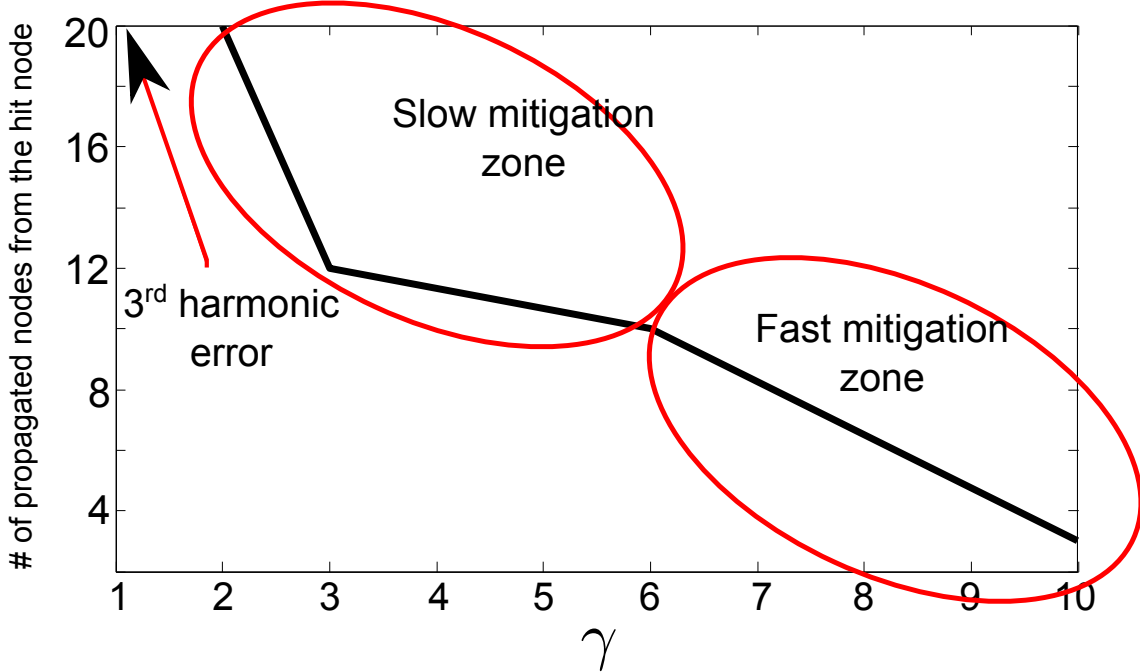


**Figure 4.13:** Nodes propagated of a  $SET_{pwmax}$  with respect to  $\gamma$  ratio in a 99-stage RO.

nodes before its removal. If there is not a significant number of stages between the particle strike and the output node, that impact would result in a transient glitch. Figure 4.13 represents the number of nodes that a SET of maximum pulselwidth is able to be propagated. Therefore, the bigger  $\gamma$  ( $\gamma = W_{ne}/W_{no}$  ratio of asymmetry), the sooner the faster edge “catches” the slower one. According to Figure 4.13, with  $\gamma = 1$  a SET propagates through a infinite number of nodes, that means that the third harmonic is induced; with  $\gamma \neq 1$  the third harmonic is removed, for example with  $\gamma = 2$  the induced pulse can modify 20 different nodes and wit  $\gamma = 10$  the glitch just alters 2 nodes. As the ratio between big and small transistor increases, the drive strength of big transistor charge faster the next node capacitance while the small transistors need to charge a greater node capacitance. Both effects together facilitate the quicker remove of the SET.

## 4.6 Implemented Test Circuits

The validation of the hypothesis of SET mitigation by the asymmetric ring oscillator design has been also carried out through the implementation and manufacturing of two different test circuits. The first design is based on *layout* design and the second one is a *voltage-controlled* ring oscillator. Both are 255-stage ring oscillators. The designs have been manufactured with a  $0.35\text{ }\mu\text{m}$  technology.

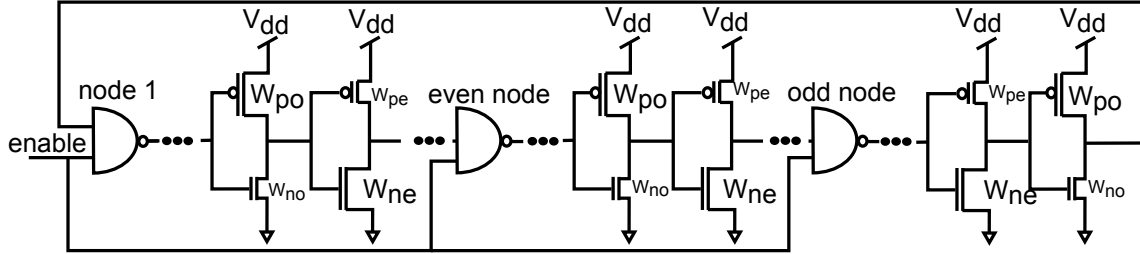


**Figure 4.14:** Schematic of the ring oscillator used for SET emulation in electrical validation.

The injection of controlled SETs in manufactured test circuits is not a simple task as it is at simulation where a current source with a function defined by the expected type of SET is defined. In Section 4.2.2, the standard test for SEE has been introduced. However, all of those test methods require special equipment and are expensive ranging from \$1000 per day, to \$1000 per hour. To avoid those costs, some previous works have developed an emulation system such as fault emulation systems with additional boards [EGVFC<sup>+</sup>12] or built-in self-test design [LKJ<sup>+</sup>12]. The first one presents advantages for configurable platforms like FPGA systems, while the last procedure seems the most suitable for the case of study of this thesis.

Then for emulating a SET into the manufactured chip we want to force the ring oscillator to oscillate at its third harmonic frequency instead of its fundamental. The ring oscillator loop configuration gives the opportunity of exciting the third harmonic oscillation just when the enable is triggered following the schematic of Figure 4.14. Additionally, forcing the third harmonic during steady oscillation requires a perfect synchronization to excite an additional pulse that fulfills the SET harmonic error criteria. This synchronization was achieved with an auxiliary circuit.

The schematic of Figure 4.14 differs from the other ring oscillators in the number of enable inputs in the design. Conventional ring oscillators just use one NAND gate to enable the oscillation. But we use three different NAND gates to start the ring oscillator. This emulation technique removes the randomness of ion strikes but it deals with the worst case of third harmonic error induction. The relative positions between them define the characteristic of the emulated SET:

- The distance between two consecutive NAND gates must be an odd number of ring oscillator stages. For example, if we consider the first NAND at node 1, then the second one has to be at an even node, and the third one at an odd node.
- The distance between two consecutive NAND gates must be configured to generate a SET pulselength ( $t_{SET}$ ) that fulfills the criteria of Harmonic Vulnerability Window.

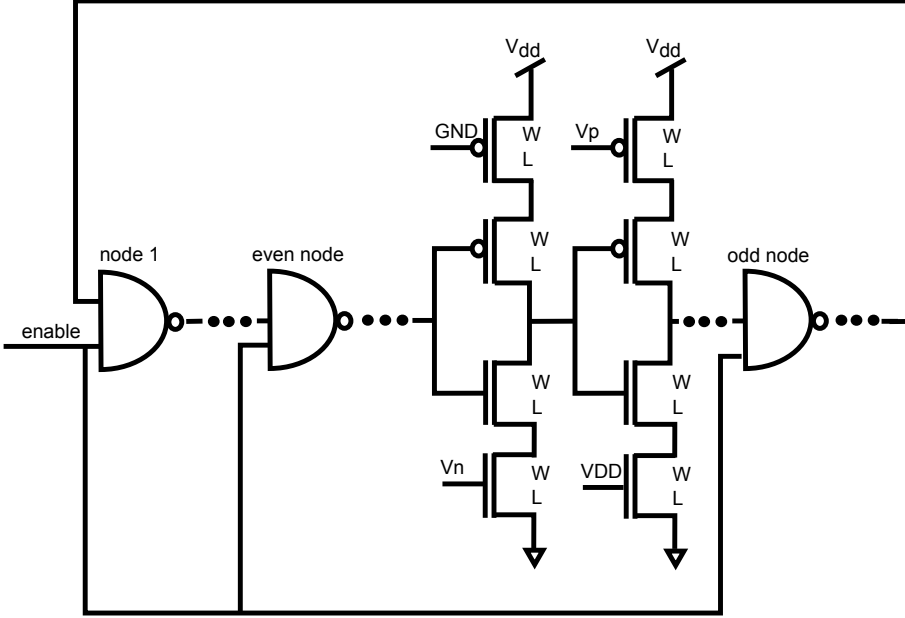


**Figure 4.15:** Schematic of the ring oscillator used for SET emulation in electrical validation based on voltage controlled asymmetry.

- Including additional pairs of NAND gates can emulate the oscillation of greater odd harmonics (5th,7th,...).

If the theoretical analysis and simulation results are correct, the output of the manufactured circuit following this new schematic should not change and the output frequency has to be the fundamental one. Hence to observe the mitigation of the induced SET we have to be able to measure every node simultaneously. This measurement is not feasible for a medium size ring oscillator and limited measurement equipment. We solved this problem designing a new and equivalent configurable asymmetric ring oscillator.

This new design is based on the schematic of Figure 4.15. The foundations of this design to achieve the SET harmonic removal is exactly the same. It is based on implementing asymmetric stages in ring oscillators. In this case, the asymmetry is set with current-starved transistors connected to bias rails. Hence the faster and slower pull-ups and pull-downs depend on the input voltages because the saturation current ( $I_{DSAT}$ ) of a CMOS transistor decreases if  $|V_{GS}|$  is reduced. At odd nodes, the pull-up path can be starved by  $V_p$  and the pull-down control gate is fixed to  $V_{DD}$ . The even nodes are inversely designed with the pull-up current fixed and the pull-down controlled by  $V_n$ . When  $V_n = V_{DD}$  and  $V_p = V_{GND}$  the stages are balanced and the third harmonic at the output will be observable. On the other hand, when those voltages move away from those values, the third harmonic will be mitigated and the output will oscillate at the fundamental frequency. The simulation of this new design with the commercial 40 nm technology is depicted in Figure 4.16. The

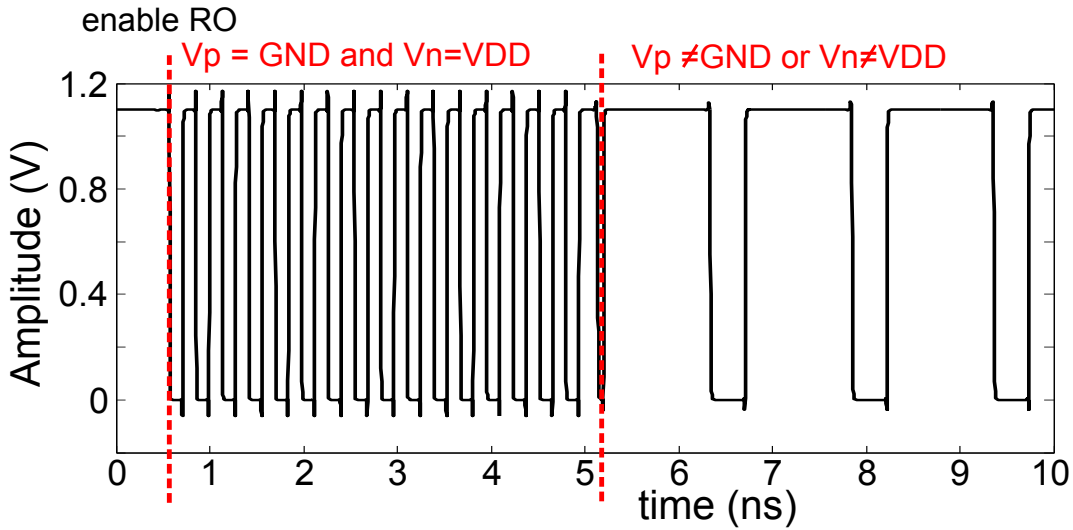


**Figure 4.16:** Output waveform of the third harmonic removal in the simulation of the *voltage-controlled* test circuit validation.

third harmonic disappearance is clearly observable when the voltages are changed.

Finally the device under test (DUT) has two analog inputs ( $V_n$  and  $V_p$ ), one digital input (*enable*) and three digital outputs (*ROLayout*, *ROVC1* and *ROVC2*). *ROLayout* is the output of the *layout* solution, *ROVC1* is the output of the final node of the *voltage-controlled* test circuit and *ROVC2* is an intermediate node (node 126). The manufactured layout is shown in Figure 4.17. The three outputs are different to the NAND gate outputs because from Figure 4.13 these nodes will always experience a glitch.

The Layout-based design was implemented with  $\gamma = 2$ . The technology design rules constrain the minimum area of the ring oscillator design. With this value of  $\gamma$  the area is the same as the minimum area ( $\gamma = 1$  and minimum transistors) ring oscillator therefore there is no area overhead. For larger values of  $\gamma$  the area overhead increases, for instance with  $\gamma = 8$  the area is twice.

## 4.7 Electrical Validation

The electrical validation of the manufactured designs consists in emulating the SET injections and analyzing the observable signals at the outputs of the two different test circuits. The *layout* implementation has been designed to mitigate SETs in any scenario. The *voltage-controlled* solution allows to configure the asymmetry of the design in order to define the degree of the needed asymmetry to remove the third harmonic induced error.

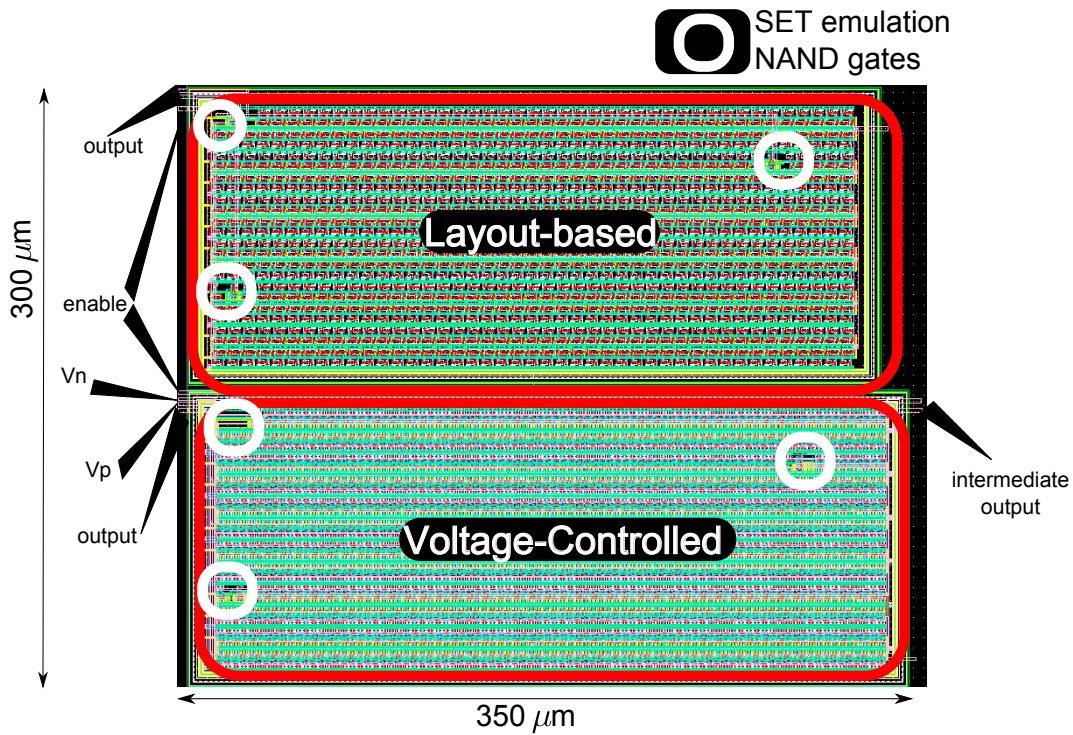


**Figure 4.17:** Layout of the two different manufactured test circuits with their inputs and outputs. (top) layout-based. (bottom) voltage-controlled.

#### 4.7.1 Test Set Up

Figure 4.18 illustrates the workbench used for the electrical test. The measurements were carried out with this equipment:

- A custom test-board to allocate the DUT. It was designed to be versatile for different types of tests.
- A custom bread-board to route the I/O signals of the DUT with relays and adaptive stages.
- A Virtex5 ML505 Xilinx FPGA development board to generate the input signals of the DUT and to perform the configuration of the bread-board.
- An Agilent MSO9051 oscilloscope to capture the output signals of the DUT.
- A PC to control the test through the communication interfaces: Ethernet and USB.
- An Ethernet switch that connects the equipment.

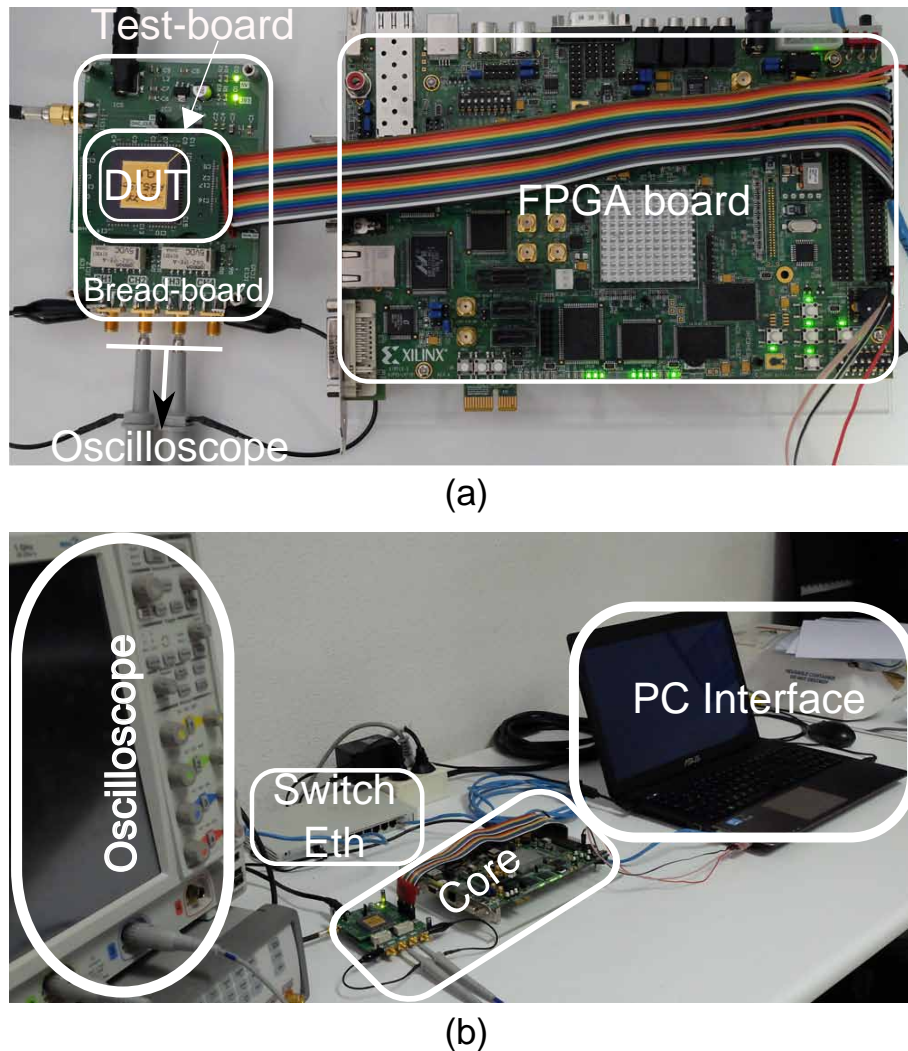


**Figure 4.18:** Set Up used for the validation tests of our new ring oscillator design.

### 4.7.2 Experimental Results

The test plan we carried out considered different scenarios. All the measurements were made at two different stages: first, at the oscillation start; and, second, at a steady oscillation 500 ms after the enable activation. In addition each measurement was repeated 20 times to remove any spurious situation or anomalous signal. Then we measured the two different block outputs. The *layout-based* ring oscillator was made following the explained procedure. The *voltage-controlled* ring oscillator required a previous plan of the input voltages. We measured 121 different inputs. We divided this voltage into 11 intervals and we tested all combinations for  $V_p$  and  $V_n$ .

The main situations that took place during all the tests are collected in Figure 4.19. Figure 4.19 (a) is the result of the *layout-based* ring oscillator. As was expected, the result

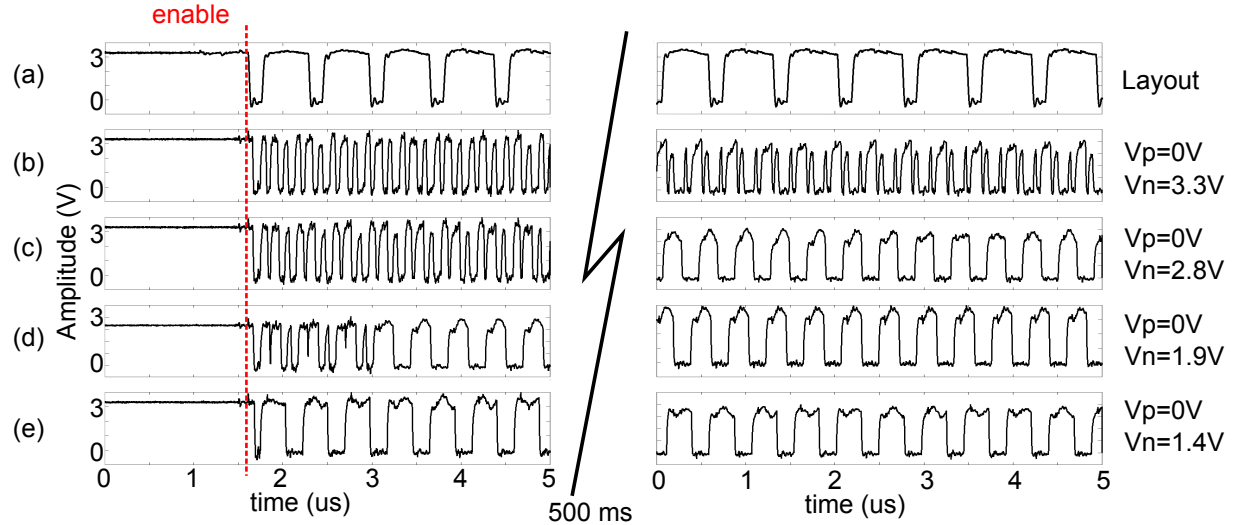


**Figure 4.19:** Waveform captures of the different scenarios occurred during emulated SET injection in electrical validation depending on the test circuit and its configuration. Start of oscillation (left). Steady oscillation (right).

is the same for the initial and the steady measurements. The frequency oscillation is the fundamental frequency of the ring oscillator design and the SET emulation is mitigated. This test confirms that the proposed solution, the asymmetric ring oscillator, is a SET-free design without area overhead.

Figure 4.19 (b), (c), (d) and (e) plot different tests of the *voltage-controlled* circuit. In Figure 4.19 (b) the gate voltages are  $V_p=GND=0$  V and  $V_n=V_{DD}=3.3$  V. This configuration makes the ring oscillator symmetric and consequently the SET emulation is visible in the start and steady stages because the emulated SET fulfills the criteria of Chen's [C<sup>+</sup>14] model. In Figure 4.19 (c)  $V_p=GND=0$  V and  $V_n=2.8$  V. A small asymmetry is introduced. As a result, the emulated SET appears at the beginning of the oscillation but it does not appear at steady measurement. The asymmetric ring oscillator is able to mitigate the third harmonic induced error even with a small asymmetry between odd and even stages. In Figure 4.19 (d) the asymmetry is increased and  $V_p=GND=0$  V and  $V_n=1.9$  V. Similarly to the previous case, the emulated SET tries to force the third harmonic oscillation, but in this case, it is mitigated in just a few clock cycles. Finally, in Figure 4.19 (e)  $V_p=GND=0$  V and  $V_n=1.4$  V. This configuration is enough to make invisible the emulated SET at the output of the ring oscillator. The conclusion of the tests of the two different ring oscillators is that the introduced asymmetry in the ring oscillator design has been validated as a RHBD technique and the SET emulation system in ring oscillators is also useful to test this type of circuits.

All of the performed tests of the *voltage-controlled* ring oscillator are plotted together in Figure 4.20. Figure 4.20 (a) shows the oscillation frequency with respect to the inputs

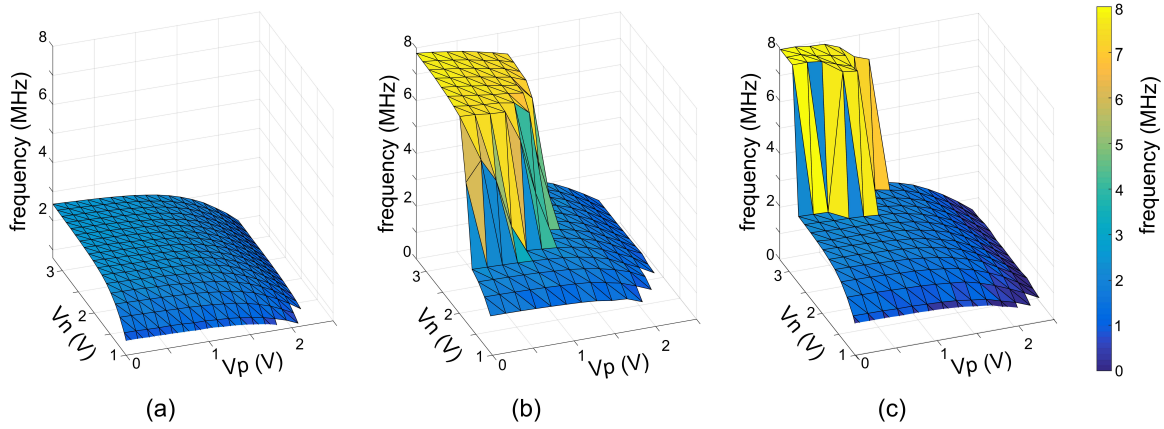


**Figure 4.20:** Representation of the measured frequencies of the *voltage-controlled* design with respect to the input voltages. (a) behavior without SET emulation. (b) frequency at the start of the oscillation. (c) frequency at steady oscillation.

$V_p$  and  $V_n$  without SET injection. The maximum frequency achievable at  $V_p=GND$  and  $V_n=V_{DD}$  is 2.5 MHz. The operational region is limited by the transistor threshold voltage ( $V_t$ ) therefore  $V_n > V_t$  and  $V_p < V_{DD} - V_t$ . Figure 4.20 (b) collects the data at the start stage. As can be seen, some input voltages shift the oscillation to 7.5 MHz. This frequency is exactly the third harmonic of the (a) configuration. The points of this figure with the same value as Figure 4.20 (a) correspond to similar cases to Figure 4.19 (e) and the different points include the rest of the situations. Figure 4.20 (c) plots the data at steady oscillation. The differences between Figure 4.20 (b) and Figure 4.20 (c) are the scenarios like Figure 4.19 (c) and (d) where the initial induced harmonic disappears at steady measurement.

As a consequence, two types of approaches can be implemented. On the one hand, a *layout* ring oscillator works as a conventional ring oscillator but hardened against SET disturbances. On the other hand, a self-recovery VCO based on the *voltage-controlled* ring oscillator controls the output frequency and simultaneously the input voltages determine its degree of SET tolerance. In the last choice, the further  $V_p$  and  $V_n$  are from bias voltages, the faster the SET is removed but the lower the frequency is. If the minimum frequency of a system is in the unhardened combination of  $V_p$  and  $V_n$ , then a SET monitor could be used to lower the frequency in case a SET locks into the loop and recover the original frequency once the SET has disappeared.

### 4.7.3 Comments on the third harmonic oscillation

Although this work and previous works call the effect of SET in a ring oscillator a third harmonic error, this claim is not completely accurate. A Fourier analysis of the implicated

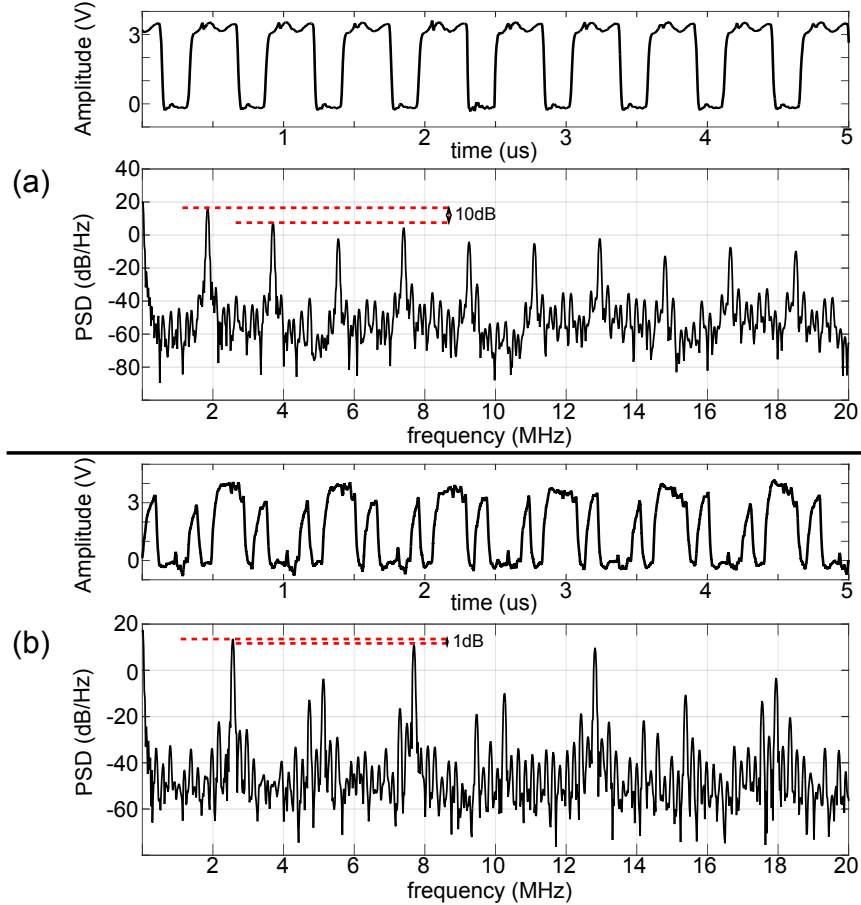


**Figure 4.21:** Output measurements and their FFTs for a SET-free output (a) and an induced third harmonic error ring oscillator (b).

signals reveals the real frequency shifts of SET injections. The Fast Fourier Transform (FFT) converts time to frequency and it allows to decompose a signal into the frequencies that make it up. Figure 4.21 depicts two different plots of the ring oscillator output and their Power Spectral Density (PSD). Figure 4.21 (a) represents the measured output of a non induced SET example. Its FFT maximum peak is at the fundamental frequency, 2 MHz, the rest of the lower peaks are placed at the harmonic frequencies but more than 5 dB lower. This PSD function is typical of periodic square signals and the duty cycle parameter determines the relevance of each harmonic component.

Figure 4.21 (b) illustrates one of the measurements of an induced SET harmonic effect. The fundamental frequency is 2.5 MHz and it is still the highest peak. Meanwhile the third harmonic has became much more relevant and its level is similar to but still lower than the fundamental one but it is not the highest although the error has been induced. Just in the case of the SET hit is completely centered in the original oscillation signal, the shift of the frequency is a real third harmonic shift.

## 4.8 Conclusions

This chapter has addressed the harmonic induced error, presented in [C<sup>+</sup>14], caused by SETs in ring oscillators. We have proposed a new ring oscillator design that fully tolerates this error. Our solution supposes a negligible area overhead compared to the common ring oscillator implementation. This new design differs from conventional ring oscillators in the utilization of non-equal and unbalanced inverters for their stages. Moreover, odd and even nodes are designed asymmetrically. It means that odd nodes use faster pull up networks while even nodes use faster pull downs. This modification provides the ability of designing a configurable duty cycle output depending on the implemented degree of asymmetry with negligible area overhead.

We have introduced the approach by theoretical analysis, we have validated it with simulations and we have manufactured two approaches based on the same foundations to perform an electrical characterization. The first approach fixes the asymmetry of the ring oscillator with the size of transistors. The second design uses two different input voltages to dynamically control the unbalanced stages. We have also designed a methodology for the emulation of SET injection in ring oscillators to avoid the high costs of a SET radiation campaign. Both approaches have contributed to the validation of the hypothesis.

Our solution contributes to improve the tolerance of ring oscillator based applications to radiation effects and as a consequence to increase the reliability of circuits that use them. For example, ring oscillators are used as simple clock generators for many test circuits in radiation characterizations, therefore a harmonic error produced by an induced transient will mislead about the real characteristics of the tested circuits.

At the same time, the work presented in this chapter has generated a new design of ring oscillators, it also opens a new perspective into ring oscillator utilization. So far, ring oscillators have been used to generate clock signals with 50% duty cycle. But, as the next chapter will explain, the use of duty cycle can open the door to new unexplored possibilities of these circuits.

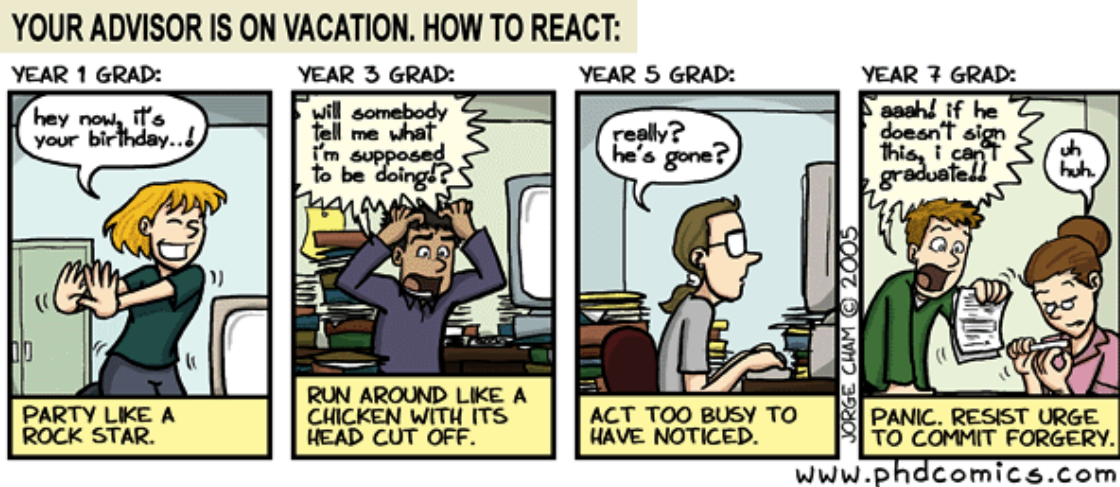
## 4.9 Related Publications

- **J. Agustin**, M. L. Lopez-Vallejo, C. G. Soriano, P. Cholbi, L. W. Massengill and Y. P. Chen, "*Efficient Mitigation of SET Induced Harmonic Errors in Ring Oscillators*," in NSREC 2015, Boston, Jul. 2015.
- **J. Agustin**, M. L. Lopez-Vallejo, C. G. Soriano, P. Cholbi, L. W. Massengill and Y. P. Chen, "*Efficient Mitigation of SET Induced Harmonic Errors in Ring Oscillators*," in IEEE Transactions on Nuclear Science, vol. 62, no. 6, pp. 3049-3056, Dec. 2015.  
doi: 10.1109/TNS.2015.2496169



# Chapter 5

## Analytical Model of the Duty Cycle in Ring Oscillators



## Chapter 5

---

# Analytical Model of the Duty Cycle in Ring Oscillators

## 5.1 Introduction

In Chapter 4 we have introduced a solution to mitigate SETs that implies a new approach to the design of ring oscillators. This approach is based on implementing a ring oscillator with unbalanced gates. As has been validated in the previous chapter, using this technique allows to fully configure the duty cycle of ring oscillators.

Previously, in Chapter 2, the relevancy of ring oscillators in electronics has been shown. Some applications are listed in that chapter (DLLs, PLLs, PVT sensors, TDCs, etc.), but all of those applications take advantage of the ring oscillator output frequency and its shift for different stimulus variations. Moreover, systems that require clock signals with configurable duty cycles or different from 50% leave this task to complementary blocks such as in [AG11, KHZS07, VGB07, AHM03]. Then, the implementation of a ring oscillator design with parameterizable duty cycle saves resources and, at the same time, supposes a step further in the utilization of ring oscillator features. In [VAFK14] a similar approach to this problem is presented, but it is just a simple implementation using just one node of ring oscillators while we present in this chapter a fully analytical model for the configuration of duty cycle in every node of ring oscillators. Our model is derived from the generalization of the implemented ring oscillator for SET mitigation.

The development of this task has to begin with the analytical study of the parameters that define the output duty cycle. This analysis leads to two different parameters, the aspect ratio of transistors and the bias voltage. Therefore, this chapter develops two different techniques with negligible or low area overhead to achieve the variation of the output duty cycle. On the one hand, a *hard* implementation that uses an individual transistor sizing methodology. This first strategy is defined at the layout level making each implementation unique and invariable after its fabrication. On the other hand, the *soft* approach uses different bias voltages for each ring oscillator stage. This strategy allows a dynamic configuration of the output duty cycles during its operation time. Both models confirm analytically the circuits used in Chapter 4 —*layout* and *voltage-controlled*. We use different terms to refer the generalized models *hard* and *soft* from the particular

implementations *layout* and *voltage-controlled*.

Our proposal is modeled, characterized and validated in this chapter considering different configurations, process variations and phase noise. The results of this study set this new design approach as a potential block for many different electronic systems to improve their actual performance. For instance, in the next chapter will take advantage of this formulation to build a particular application, a PUF, that uses the output duty cycle of ring oscillators to improve the robustness of conventional ring oscillator based PUFs.

This chapter is organized as follows: First in Section 5.2 an analysis of CMOS ring oscillators is presented, which seeks to establish the analytical basis in order to understand this electronic circuit and the potential of its duty cycle variation. Using the conclusions of this analysis, in Section 5.3 the two models of duty cycle variation —hard and soft— are developed. These models are validated and characterized through simulation with a 40 nm commercial technology in Section 5.4. In Section 5.5 we study the jitter and phase noise of the ring oscillator depending on the duty cycle configuration. Finally the conclusions of the main contributions of this chapter are drawn in Section 5.7.

## 5.2 Model Analysis

The final goal of this analysis is to implement a ring oscillator that provides outputs with configurable duty cycles. Achieving this target makes necessary firstly to understand how a ring oscillator works and how it oscillates. Therefore we explain the foundations of this circuit in this Section 5.2. After that description, design variables that affect the ring oscillator output properties will be analyzed to support which parameters are suitable to control the oscillation duty cycle.

We only take into consideration single-ended CMOS ring oscillators whose delay elements are made of simple inverter gates. In spite of this limitation, the conclusions can be directly extrapolated to the rest of ring oscillator topologies.

Single-ended ring oscillators are composed of an odd chain inverter stages whose last output is fed back to its first input gate. The basis of the oscillation is the instability of nodes thanks to the odd number of delay stages. This property makes nodes fluctuate with a period proportional to the addition of the propagation delay of each individual inverter. Therefore, the first step to understand the behavior of the complete ring oscillator is exploring how the design of the simplest component —individual CMOS inverter gates in this case— impacts on the output frequency and duty cycle.

### 5.2.1 CMOS Inverter

We follow the long-channel model of MOS transistors [WH11] to analyze the CMOS inverter delay. According to this model, the source-drain current of an individual transistor is ruled

by the equation:

$$I_{ds} = \frac{Q_{ch}}{L/v} = \mu C_{ox} \frac{W}{L} (V_{gs} - V_t - V_{ds}/2) V_{ds} \quad (5.1)$$

where  $Q_{ch}$  is the charge inside the channel,  $L$  is the channel length,  $v$  is the average velocity of carriers,  $\mu$  is the electron/hole mobility constant,  $C_{ox}$  is the capacitance per unit area of gate oxide,  $W$  is the channel width,  $V_t$  is the transistor threshold voltage,  $V_{gs}$  is the gate-source voltage and  $V_{ds}$  is the drain-source voltage.

(5.1) is traditionally divided into three<sup>1</sup> different regions depending on the input voltages:

$$I_{ds} = \begin{cases} 0 & V_{gs} < V_t \quad \text{Off} \\ \beta(V_{gs} - V_t - \frac{V_{ds}}{2})V_{ds} & V_{ds} < V_{DSAT} \quad \text{Linear} \\ \frac{\beta}{2}(V_{gs} - V_t)^2 & V_{ds} > V_{DSAT} \quad \text{Saturation} \end{cases} \quad (5.2)$$

where  $V_{DSAT}$  splits ohmic mode from saturation mode and  $\beta$  is defined by  $\beta = \mu C_{ox} W / L$ .

To set the propagation delay of an inverter the load capacitance must be known. Since the inverters of a ring oscillator are disposed in a loop configuration, the load capacitance of each inverter is highly influenced by the gate capacitance of the next inverter. Thus another important parameter to determine the propagation delay of CMOS inverters within ring oscillators is their gate capacitance which is defined as:

$$C_g = C_{ox}(W_n + W_p)L \quad (5.3)$$

It is not our aim to develop the most accurate model of ring oscillators but modeling its behavior as easy as possible to outline the designing factors that affect its performance and a way to vary it. Therefore to simplify the chain of inverters we make these assumptions: First, each transistor is replaced by an equivalent current source characterized by its source-drain current; Second, the load capacitance of a node is equal to the gate capacitance of the next stage —we consider negligible for this first approximation the rest of node capacitances. Hence if pMOS transistors charge a  $C_l$  and nMOS transistors discharge it, then the expression that rules the discharge of a node by an nMOS transistor can be defined as:

$$C_l \frac{dV_{ds}}{dt} = -I_{dsn} \quad (5.4)$$

Taking into account the different operational modes in (5.2) in which transistors are not cutoff and using  $V_{DD}$  instead of  $V_{gs}$ , (5.4) can be split into these two zones:

---

<sup>1</sup>Velocity saturation and other secondary effects are not considered in this model, but their consideration does not affect the conclusion of our model, as will be shown by the experiments we have carried out.

$$\frac{dV_{ds}}{dt} = \frac{-\beta_n}{C_l} \begin{cases} \frac{(V_{DD} - V_t)^2}{2} & V_{ds} > V_{DD} - V_t \\ (V_{DD} - V_t - \frac{V_{ds}}{2})V_{ds} & V_{ds} < V_{DD} - V_t \end{cases} \quad (5.5)$$

where  $\beta_n$  is the result of replacing  $\mu$  by electron mobility  $\mu_n$ .

Although the transistor first operates in linear mode and later in saturation mode, we only use the saturation operational region for current source replacement. (5.5) is reduced to just one expression:

$$\frac{dV_{ds}}{dt} = -\frac{\beta}{C_l} \frac{(V_{DD} - V_t)^2}{2} \quad (5.6)$$

and solving (5.6):

$$V_{ds} = -\frac{\beta}{C_l} \frac{(V_{DD} - V_t)^2}{2} t + V_{DD} \quad (5.7)$$

We define the propagation delay fall time  $t_{pdf}$  as the time lapsed to change a node voltage from  $V_{DD}$  to  $V_{DD}/2$ . Thus  $t_{pdf}$  is calculated from (5.6) as:

$$t_{pdf} = \frac{V_{DD}C_l}{\beta_n(V_{DD} - V_t)^2} \quad (5.8)$$

We also define the propagation delay rise time  $t_{pdr}$  as the time lapsed to change a node voltage from 0 to  $V_{DD}/2$ . The difference is that a pMOS transistor charges the node instead of an nMOS. Consequently  $t_{pdr}$  is:

$$t_{pdr} = \frac{V_{DD}C_l}{\beta_p(V_{DD} - V_t)^2} \quad (5.9)$$

where  $\beta_p$  is the result of replacing  $\mu$  by electron mobility  $\mu_p$ .

From (5.8) and (5.9) we can conclude that the propagation delay —fall and rise— of an inverter depends on the bias voltage, the load capacitance and the transistor size ratio:

$$tpd(V_{DD}, C_l, \frac{W}{L}) \quad (5.10)$$

Finally, the design parameters that we identify as best candidates to change ring oscillator performance are: bias voltage and transistor size ratio (the previous simplification and (5.3) have settled the  $C_l$  dependency on the inverter transistor ratio of the next ring oscillator stage).

### 5.2.2 Ring Oscillator

The next step is to study the ring oscillator as the chain of various CMOS inverters using the developed equations in the previous subsection. The first and the most used property

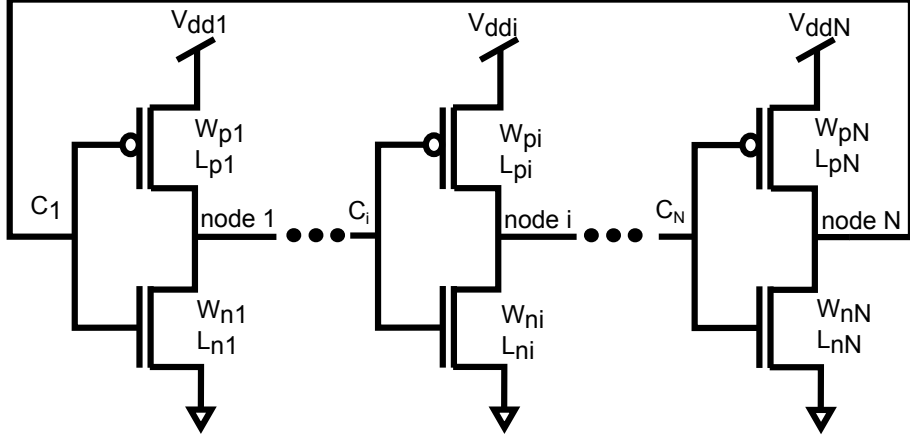


**Figure 5.1:** Ring Oscillator notation.  $W$  (transistor width),  $L$  (transistor channel length),  $C_i$  (node  $i$  capacitance), and  $V_{ddi}$  (bias voltage of inverter  $i$ ).

of a ring oscillator is the output frequency. The ring oscillator period  $T$  can be estimated as the addition of all inverter propagation delays:

$$T = 2 * \sum tpd_i \quad (5.11)$$

But this work is mainly focused on controlling the duty cycle of every stage output instead of the output frequency. Thus, the period can be divided into  $t_{high}$  —the output is higher than  $V_{DD}/2$ — and  $t_{low}$  —the output is lower than  $V_{DD}/2$ . Therefore (5.11) is redefined as:

$$T = t_{low} + t_{high} \quad (5.12)$$

A more specific analysis of the terms of this partitioning requires a new division for each individual node. Figure 5.1 sets the notation we follow to differentiate nodes within a ring oscillator. The output of a ring oscillator is usually just one node and its frequency is a general feature because all internal nodes oscillate with the same period. But our study assumes  $N$  potential outputs—one per node—that are dependent but different. So if  $T$  refers to the period of node  $N$ , then  $t_{low}$  and  $t_{high}$  in (5.12) can be defined, generalizing the 5-stage ring oscillator internal nodes of Figure 5.2, by:

$$t_{low_N} = tpdr_N + \sum_1^{\frac{N-1}{2}} (tpdf_{2i} + tpdr_{2i-1}) \quad (5.13)$$

$$t_{high_N} = tpdf_N + \sum_1^{\frac{N-1}{2}} (tpdf_{2i-1} + tpdr_{2i}) \quad (5.14)$$

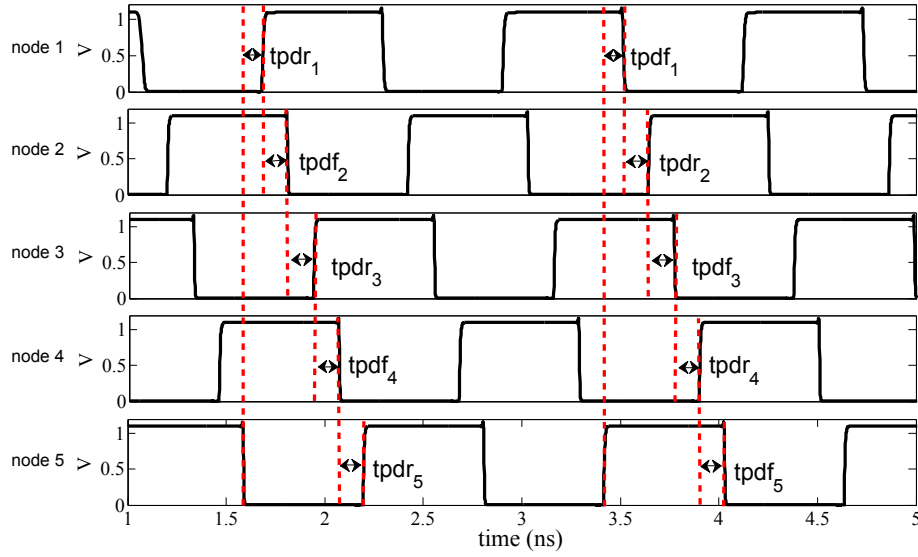


**Figure 5.2:** Internal nodes of a balanced 5-stage ring oscillator and the times in which the period,  $T$  is divided.

The particularization of the dependency in (5.10) for the ring oscillator nodes results in:

$$\begin{aligned} tpdf_i(V_{DD_{i+1}}, C_{l_{(i+1)}}, (\frac{W_{ni}}{L_{ni}})) &= \\ = tpdf_i(V_{DD_{i+1}}, (\frac{W_{n(i+1)}}{L_{n(i+1)}}), (\frac{W_{p(i+1)}}{L_{p(i+1)}}), (\frac{W_{ni}}{L_{ni}})) \end{aligned} \quad (5.15)$$

$$\begin{aligned} tpdr_i(V_{DD_i}, C_{l_{(i+1)}}, (\frac{W_{pi}}{L_{pi}})) &= \\ = tpdr_i(V_{DD_i}, (\frac{W_{n(i+1)}}{L_{n(i+1)}}), (\frac{W_{p(i+1)}}{L_{p(i+1)}}), (\frac{W_{pi}}{L_{pi}})) \end{aligned} \quad (5.16)$$

Putting all together, the variables that can modify the characteristics of the output signal and make each node signal different from the others are the aspect ratio design of every single MOS transistor and the bias voltage of inverters.

The duty cycle of a digital signal is defined as the ratio between  $t_{high}$  and its period  $T$ . Traditional ring oscillators do not consider this parameter because it is supposed to be 50%. However we can infer from (5.12)-(5.16) that this assumption can be modified. Generally, the duty cycle of the signal at node  $i$  in a ring oscillator is defined as:

$$d_i = \frac{t_{high_i}}{T} \quad (5.17)$$

All ring oscillator designs make use of inverters that are exactly the same, then all  $tpdr_i$  and  $tpdf_i$  are equal and the duty cycle referred to node N is determined from

(5.13), (5.14) and (5.17) by:

$$d_N = \frac{\frac{N+1}{2}t_{pdr} + \frac{N-1}{2}t_{pdf}}{N(t_{pdr} + t_{pdf})} = \frac{1}{2} + \frac{t_{pdr} - t_{pdf}}{2(t_{pdr} + t_{pdf})} \quad (5.18)$$

In (5.18) the duty cycle of the ring oscillator output is 50% when the inverters are balanced ( $t_{pdr} = t_{pdf}$ ), otherwise the duty cycle slightly varies from this value.

## 5.3 Duty Cycle Configuration Models

The conclusion of Section 5.2 is that the duty cycle of the ring oscillator nodes can be modified by controlling  $V_{DD}$  and the transistor aspect ratios. For this reason we have developed two different methods to vary the duty cycle of each node: a *hard* method based on layout design, and a *soft* one founded on bias voltage variation. In our models we define the duty cycle of odd nodes as the ratio  $t_{high}/T$  and the duty cycle of even nodes as the ratio  $t_{low}/T$  to re-invert the signal and *normalize* its value.

### 5.3.1 Hard duty cycle configuration

Our first proposal is based on studying the duty cycle at every node for general  $W_i/L_i$  implementations. For all transistors  $L_i$  is equal to the minimum gate length  $L$  imposed by the technology rules. All inverter stages are also biased at the same voltage  $V_{DD}$ . (5.13) and (5.14) are referred to the last node  $N$ , but those equations can be redefined for a general node  $i$ . To shorten the notation, we declare the function  $\Gamma_N(x) = [mod(x-1, N)+1]$  where  $mod(x, N)$  is the remainder of the division  $x/N$ . Thus  $t_{high}$  and  $t_{low}$  referred to node  $i$  are:

$$t_{high_i} = tpdf_i + \sum_{j=i}^{j=i+\frac{N-3}{2}} (tpdf_{\Gamma_N(2j+1)} + tpdr_{\Gamma_N(2j)}) \quad (5.19)$$

$$t_{low_i} = tpdr_i + \sum_{j=i}^{j=i+\frac{N-3}{2}} (tpdr_{\Gamma_N(2j+1)} + tpdf_{\Gamma_N(2j)}) \quad (5.20)$$

If we bring the definition of  $\beta$ , (5.3) and (5.8) together, then we can define  $t_{pdf_i}$  for each inverter with respect to the transistor widths  $W_i$ . This definition remains as:

$$\begin{aligned}
t_{pdf_i} &= \frac{V_{DD}C_{ox}(W_{n_{i+1}} + W_{p_{i+1}})L_{n_{i+1}}}{\mu_n C_{ox} \frac{W_{p_i}}{L_{p_i}}(V_{DD} - V_t)^2} = \\
&= \frac{V_{DD}L^2}{\mu_n(V_{DD} - V_t)^2} \frac{W_{n_{i+1}} + W_{p_{i+1}}}{W_{p_i}} = \\
&= \alpha_n \frac{W_{n_{i+1}} + W_{p_{i+1}}}{W_{p_i}}
\end{aligned} \tag{5.21}$$

where  $V_t$  ( $V_t = V_{tn} = -V_{tp}$ ) is supposed the same for every transistor and  $\alpha_n$ :

$$\alpha_n = \frac{V_{DD}L^2}{\mu_n(V_{DD} - V_t)^2} \tag{5.22}$$

The same way,  $tpdr_i$  is the result of the aggregation of the definition of  $\beta$ , (5.3) and (5.9) and consequently its dependency with respect to  $W_i$  is:

$$t_{pdr_i} = \alpha_p \frac{W_{n_{i+1}} + W_{p_{i+1}}}{W_{n_i}} \tag{5.23}$$

with  $\alpha_p$ :

$$\alpha_p = \frac{V_{DD}L^2}{\mu_p(V_{DD} - V_t)^2} \tag{5.24}$$

We define the new parameter  $\lambda = \alpha_p/\alpha_n = \mu_n/\mu_p$  which depends on the technology and whose value is close to two ( $\lambda \approx 2$ ).

Replacing (5.21) and (5.23) in (5.19) and (5.20),  $t_{high}$  and  $t_{low}$  at each node are more exhaustively specified by:

$$\begin{aligned}
t_{high_i} &= \alpha_n \left( \sum_{j=i}^{i+\frac{N-1}{2}} \frac{W_{n_{\Gamma_N(2j)}} + W_{p_{\Gamma_N(2j)}}}{W_{p_{\Gamma_N(2j-1)}}} + \right. \\
&\quad \left. + \sum_{j=i}^{i+\frac{N-3}{2}} \frac{W_{n_{\Gamma_N(2j+1)}} + W_{p_{\Gamma_N(2j+1)}}}{\lambda W_{n_{\Gamma_N(2j)}}} \right)
\end{aligned} \tag{5.25}$$

$$\begin{aligned}
t_{low_i} &= \alpha_n \left( \sum_{j=i}^{i+\frac{N-1}{2}} \frac{W_{n_{\Gamma_N(2j)}} + W_{p_{\Gamma_N(2j)}}}{\lambda W_{n_{\Gamma_N(2j-1)}}} + \right. \\
&\quad \left. + \sum_{j=i}^{i+\frac{N-3}{2}} \frac{W_{n_{\Gamma_N(2j+1)}} + W_{p_{\Gamma_N(2j+1)}}}{W_{p_{\Gamma_N(2j)}}} \right)
\end{aligned} \tag{5.26}$$

Finally, the generalization of (5.17) that rules the duty cycle of each node  $i$  depending exclusively on every transistor width for this *hard* configuration proposal is:

$$\begin{aligned}
d_i = & \frac{\sum_{j=i}^{i+\frac{N-1}{2}} \frac{W_{n_{\Gamma_N}(2j)} + W_{p_{\Gamma_N}(2j)}}{W_{p_{\Gamma_N}(2j-1)}} + }{\sum_{j=1}^N \left( \frac{W_{n_{\Gamma_N}(j+1)} + W_{p_{\Gamma_N}(j+1)}}{W_{p_{\Gamma_N}(j)}} + \frac{W_{n_{\Gamma_N}(j+1)} + W_{p_{\Gamma_N}(j+1)}}{\lambda W_{n_{\Gamma_N}(j)}} \right)} + \\
& + \frac{\sum_{j=i}^{i+\frac{N-3}{2}} \frac{W_{n_{\Gamma_N}(2j+1)} + W_{p_{\Gamma_N}(2j+1)}}{\lambda W_{n_{\Gamma_N}(2j)}}}{\sum_{j=1}^N \left( \frac{W_{n_{\Gamma_N}(j+1)} + W_{p_{\Gamma_N}(j+1)}}{W_{p_{\Gamma_N}(j)}} + \frac{W_{n_{\Gamma_N}(j+1)} + W_{p_{\Gamma_N}(j+1)}}{\lambda W_{n_{\Gamma_N}(j)}} \right)}
\end{aligned} \tag{5.27}$$

(5.27) explains any case for different  $W_i$  distributions in ring oscillators. But to understand how it works and what is the behavior of internal nodes under this expression we present some particular  $W_i$  patterns. The first example represents the traditional implementation of a ring oscillator, the ratio between pMOS and nMOS transistors is fixed ( $\gamma = W_p/W_n$ ) then the duty cycle expression is:

$$\begin{aligned}
d_i = & \frac{\left(\frac{N+1}{2}\right)\left(\frac{\gamma+1}{\gamma}\right) + \left(\frac{N-1}{2}\right)\left(\frac{\gamma+1}{\lambda}\right)}{N\left(\frac{\gamma+1}{\gamma} + \frac{\gamma+1}{\lambda}\right)} = \\
& = \frac{1}{2} + \frac{\lambda + (\lambda - 1)\gamma - \gamma^2}{2N(\lambda + (\lambda + 1)\gamma + \gamma^2)}
\end{aligned} \tag{5.28}$$

At first sight, the duty cycle does not depend on  $i$  so it is the same for every node within the ring oscillator. (5.28) should agree with the common assumption that the duty cycle of a ring oscillator is 50%. This hypothesis is fulfilled in two different cases. First, if  $\gamma = \lambda$  what solves the second degree equation  $(\lambda + (\lambda - 1)\gamma - \gamma^2)$ , then the inverters are balanced ( $t_{pdr} = t_{pdf}$ ) and (5.18) and (5.28) match the solution. Second, if  $N$  tends to infinity.  $\lambda$  is fixed by the technology and  $\gamma$  is fixed by the design then:

$$\lim_{N \rightarrow \infty} d_i = \frac{1}{2} + \frac{\kappa}{2N} = \frac{1}{2} \tag{5.29}$$

where  $\kappa$  is a constant equal to:

$$\kappa = \frac{\lambda + (\lambda - 1)\gamma - \gamma^2}{\lambda + (\lambda + 1)\gamma + \gamma^2} \tag{5.30}$$

So if  $N$  tends to infinity, then the duty cycle of every node tends to 50%.

The second example that helps to understand how the duty cycle can be modified according to (5.27) follows the schematic depicted in Figure 5.3. In this case the inverters are divided into odd and even gates. Odd gates have a strong pMOS transistor and a weak nMOS transistor. And even nodes follow the opposite distribution —strong nMOS and weak pMOS. If the relationships set between the different transistor widths are  $W_{po} = W_{ne} = \varphi W_{pe} = \varphi W_{no}$  to remove some degrees of freedom, the duty cycle of each node with these assumptions is approximately:

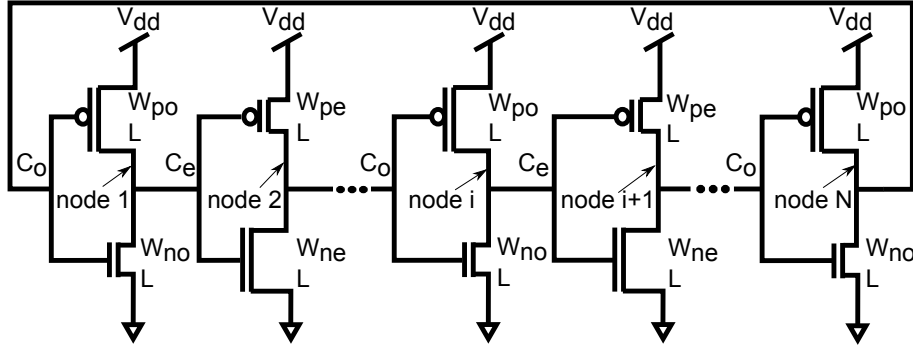


**Figure 5.3:** Ring Oscillator with asymmetric odd and even nodes (smaller transistors means narrower channel).

$$\begin{aligned}
 d_i &= \frac{\left(\frac{N-i}{2}\right)[\left(\varphi + 1\right) + \left(\frac{\varphi+1}{\lambda}\right)] + \left(\frac{i}{2}\right)[\left(\frac{\varphi+1}{\varphi}\right) + \left(\frac{\varphi+1}{\lambda\varphi}\right)]}{\left(\frac{N+1}{2}\right)[\left(\frac{\varphi+1}{\varphi}\right) + (\varphi + 1) + \left(\frac{\varphi+1}{\lambda\varphi}\right) + \left(\frac{\varphi+1}{\lambda}\right)]} = \\
 &= \frac{\varphi N + i(1 - \varphi)}{(N + 1)(\varphi + 1)}
 \end{aligned} \tag{5.31}$$

In this case, (5.31) shows a dependency on  $i$ , therefore the duty cycle is different at different nodes. Besides the duty cycle variation, the schematic of Figure 5.3 produces a linear duty cycle distribution along the ring oscillator and the slope of this distribution depends on the  $\varphi$  ratio. If  $\varphi = 1$  —all transistor widths are the same—, (5.31) gives a constant duty cycle for all nodes with a value that tends to 50% as expected from the previous example ( $\varphi = 1 \Rightarrow [W_{po} = W_{ne} = W_{pe} = W_{no}]$  and  $\gamma = 1 \Rightarrow [W_p = W_n]$ ). Moreover, at the central node the duty cycle always tends to 50% independently of the rest of parameters defined in this example.

The two previous particularizations of the *hard* model allow a direct simplification of (5.27), but next examples are plotted directly replacing transistor widths in (5.27). Figure 5.4 represents four width distributions for four different theoretical examples. These examples have been calculated for a 51-stage ring oscillator. The **K-ratio** distribution follows the schematic of Figure 5.3 with  $\varphi = 3$ . The **Linear** distribution is similar to the **K-ratio** but  $\varphi$  value is not constant, it follows a linear function with  $\varphi(1) = \varphi_0 = 10$  and  $\varphi(N) = \varphi(51) = 1/\varphi_0 = 1/10$ , and the minimum width is not constant neither with a linear function with  $W_{po}(1) = W_0$  and  $W_{po}(N) = W_{po}(51) = \varphi_0 W_0$ . The **Increasing** distribution sets the relationships  $W_{po} = W_{no} = \varphi W_{pe} = \varphi W_{ne}$  with  $\varphi$  and  $W_{po}$  changing as in **Linear** distribution. The **Triangle** distribution is the result of concatenating two linear distributions, the first increasing and the second one decreasing with  $\varphi(1) = \varphi_0 = 5$ ,  $\varphi((N + 1)/2) = \varphi(26) = 1/\varphi_0 = 1/5$ ,  $\varphi(N) = \varphi(51) = \varphi_0 = 5$  and  $W_{po}(1) = W_0$ ,  $W_{po}((N + 1)/2) = W_{po}(26) = \varphi_0 W_0$ ,  $W_{po}(N) = W_{po}(51) = W_0$ . Figure 5.5 depicts the resulting duty cycle when applying these distributions to (5.27). **K-ratio** distribution

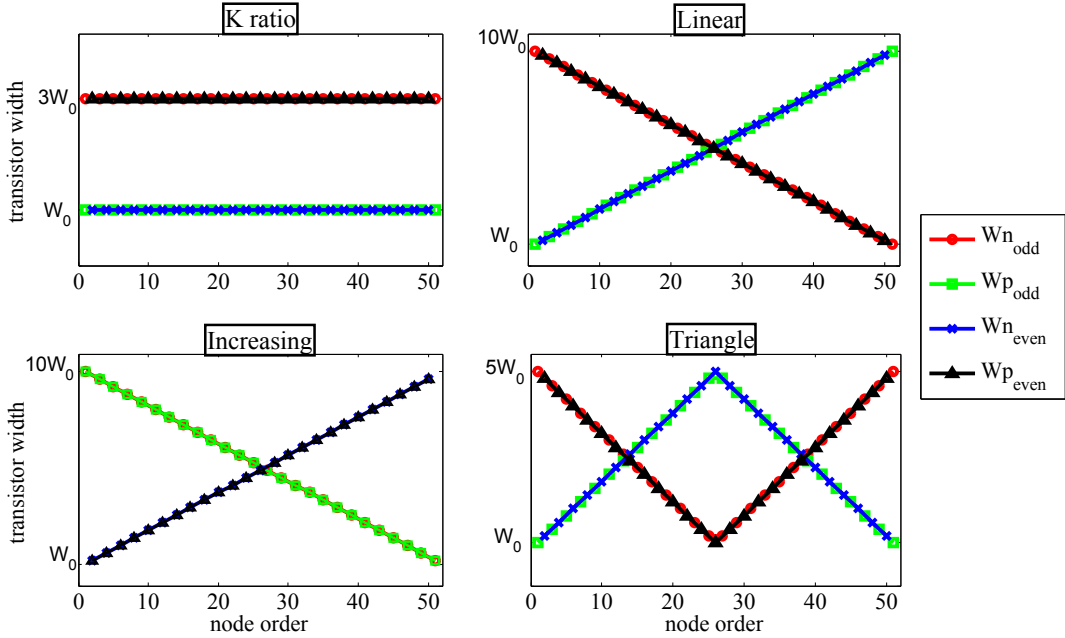


**Figure 5.4:** Transistor size distribution in four different examples of *hard* duty cycle configuration.

produces a linear distribution of the duty cycle. Replacing  $\varphi = 3$  in (5.31) the maximum value of the duty cycle is 75% and the minimum 25% what matches the calculated function. The results of **Linear** and **Increasing** distributions are parabolic-shapes, the first concave and the second convex. And the **Triangle** distribution causes a concave duty cycle in the first half of the ring oscillator and a convex one in the second half.

These examples make clearer the expression of (5.27) and they show the possibility of generating ad-hoc duty cycle distributions just with a careful design of the ring oscillator transistor sizes.

### 5.3.2 Soft duty cycle configuration

The second proposal to vary the duty cycle of ring oscillator nodes is based on individually controlling the bias voltage  $V_{DDi}$  of each inverter gate as the schematic of Figure 5.6. This model assumes that all transistors are equal with a fixed size of  $W$  and  $L$ .

Using this model, (5.7) is different for pMOS and nMOS transistors. For pMOS the new equation is:

$$V_{ds,pMOSi} = -\frac{\beta_p}{C_l} \frac{(V_{DDi} - V_t)^2}{2} t + V_{DDi} \quad (5.32)$$

and for nMOS:

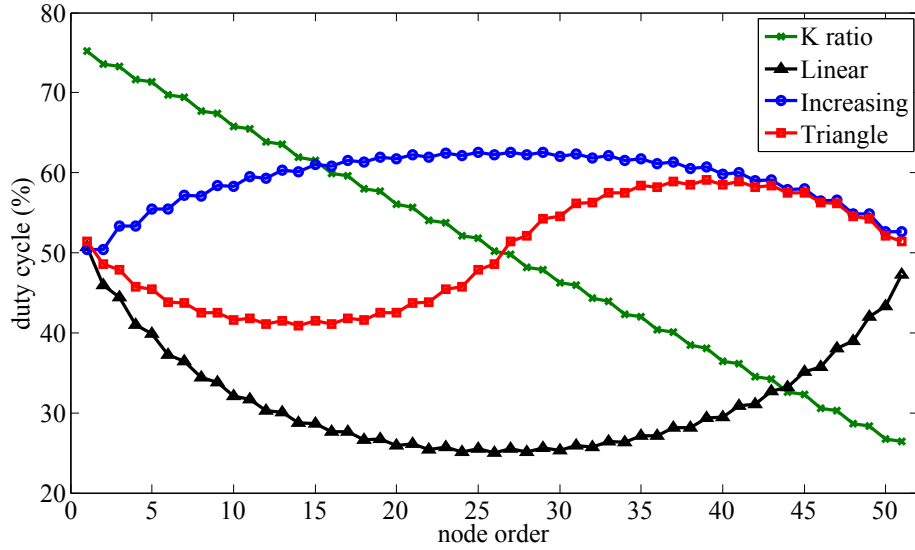


**Figure 5.5:** Theoretical duty cycle distribution for the four different cases of study at every internal node of a 51-stage ring oscillator.

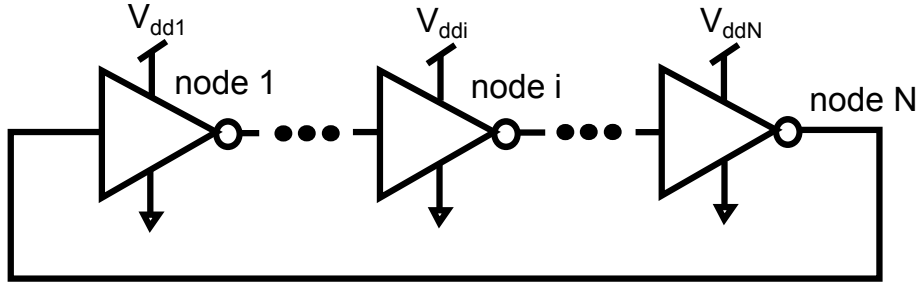


**Figure 5.6:** Schematic of a ring oscillator to independently control each inverter gate bias voltage.

$$V_{ds_{nMOSi}} = -\frac{\beta_n}{C_l} \frac{(V_{DDi-1} - V_t)^2}{2} t + V_{DDi} \quad (5.33)$$

Thus the propagation delay is defined as the time lapsed to change  $V_{ds}$  from  $V_{DDi}$  to  $V_{DDi+1}/2$ . The solutions of (5.32) and (5.33) result in the rise and fall propagation times which can be expressed by:

$$t_{pdr_i} = \frac{(2V_{DDi} - V_{DDi+1})C_l}{\beta_p(V_{DDi} - V_t)^2} = \xi_p \frac{(2V_{DDi} - V_{DDi+1})}{(V_{DDi} - V_t)^2} \quad (5.34)$$

$$t_{pdf_i} = \frac{(2V_{DDi} - V_{DDi+1})C_l}{\beta_n(V_{DDi-1} - V_t)^2} = \xi_n \frac{(2V_{DDi} - V_{DDi+1})}{(V_{DDi-1} - V_t)^2} \quad (5.35)$$

with  $\xi_p$  and  $\xi_n$ :

$$\xi_p = \frac{C_l}{\beta_p} \quad \text{and} \quad \xi_n = \frac{C_l}{\beta_n} \quad (5.36)$$

We also define the same parameter  $\lambda = \xi_p/\xi_n = \alpha_p/\alpha_n = \mu_n/\mu_p$  for this model. Replacing (5.34) and (5.35) in (5.19) and (5.20),  $t_{high}$  and  $t_{low}$  at each node with individually controlled bias voltages are:

$$\begin{aligned} t_{high_i} = & \alpha_p \left( \sum_{j=i}^{i+\frac{N-1}{2}} \frac{(2V_{DD_{\Gamma_N(2j-1)}} - V_{DD_{\Gamma_N(2j)}})}{(V_{DD_{\Gamma_N(2j-2)}} - V_t)^2} + \right. \\ & \left. + \sum_{j=i}^{i+\frac{N-3}{2}} \frac{(2V_{DD_{\Gamma_N(2j)}} - V_{DD_{\Gamma_N(2j+1)}})}{\lambda(V_{DD_{\Gamma_N(2j)}} - V_t)^2} \right) \end{aligned} \quad (5.37)$$

$$\begin{aligned} t_{low_i} = & \alpha_p \left( \sum_{j=i}^{i+\frac{N-1}{2}} \frac{(2V_{DD_{\Gamma_N(2j-1)}} - V_{DD_{\Gamma_N(2j)}})}{\lambda(V_{DD_{\Gamma_N(2j-1)}} - V_t)^2} + \right. \\ & \left. + \sum_{j=i}^{i+\frac{N-3}{2}} \frac{(2V_{DD_{\Gamma_N(2j)}} - V_{DD_{\Gamma_N(2j+1)}})}{(V_{DD_{\Gamma_N(2j-1)}} - V_t)^2} \right) \end{aligned} \quad (5.38)$$

In this case the generalization of the duty cycle of (5.17) results in the expression:

$$\begin{aligned} d_i = & \frac{\sum_{j=i}^{i+\frac{N-1}{2}} \frac{(2V_{DD_{\Gamma_N(2j-1)}} - V_{DD_{\Gamma_N(2j)}})}{(V_{DD_{\Gamma_N(2j-2)}} - V_t)^2}}{\sum_{j=1}^N \left( \frac{(2V_{DD_j} - V_{DD_{j+1}})}{(V_{DD_{j-1}} - V_t)^2} + \frac{(2V_{DD_j} - V_{DD_{j+1}})}{\lambda(V_{DD_j} - V_t)^2} \right)} + \\ & + \frac{\sum_{j=i}^{i+\frac{N-3}{2}} \frac{(2V_{DD_{\Gamma_N(2j)}} - V_{DD_{\Gamma_N(2j+1)}})}{\lambda(V_{DD_{\Gamma_N(2j)}} - V_t)^2}}{\sum_{j=1}^N \left( \frac{(2V_{DD_j} - V_{DD_{j+1}})}{(V_{DD_{j-1}} - V_t)^2} + \frac{(2V_{DD_j} - V_{DD_{j+1}})}{\lambda(V_{DD_j} - V_t)^2} \right)} \end{aligned} \quad (5.39)$$

To validate this expression we evaluate the case of the same  $V_{DD_i}$  at each node, the duty cycle is:

$$d_i = \frac{1}{2} + \frac{(\lambda - 1)}{2N(\lambda + 1)} \quad (5.40)$$

what agrees with the previous proposal cases for  $\gamma = 1$  or  $\varphi = 1$ . This case also tends to a fixed duty cycle of 50% in every node of the ring oscillator.

The following examples of the soft duty cycle configuration are direct applications of different bias voltage distributions to (5.39) for a 51-stage ring oscillator. Figure 5.7 represents the six different model cases theoretically calculated. For these applications,

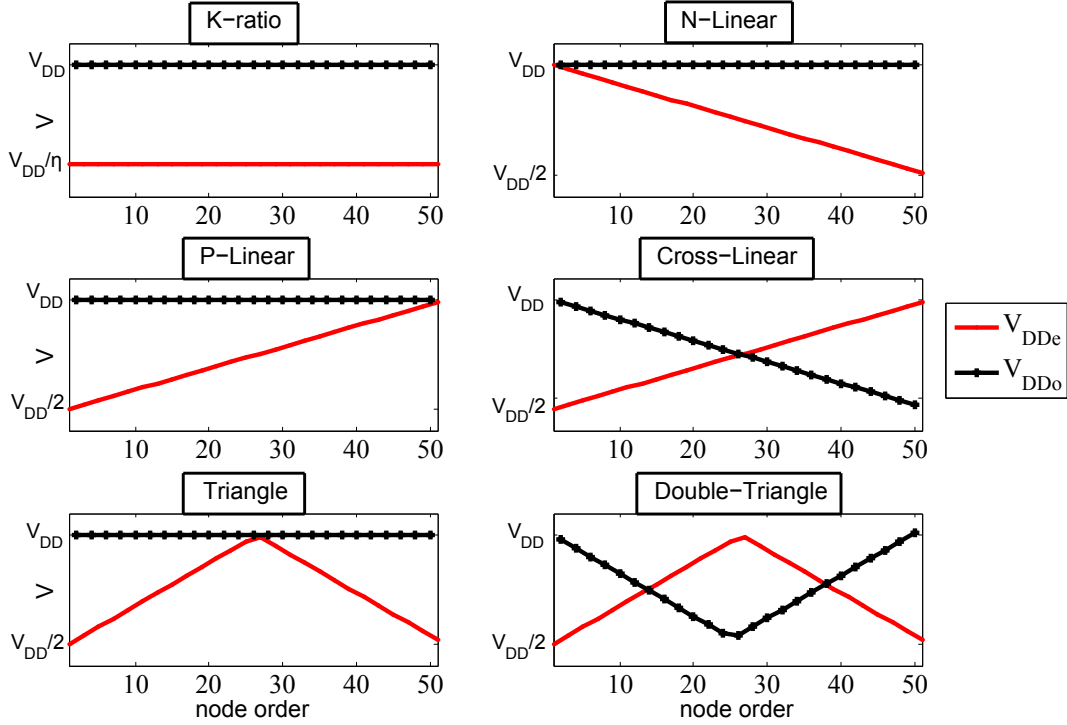


**Figure 5.7:** Examples of  $V_{DDi}$  distributions of the *soft* duty cycle configuration.

bias voltages have been divided into odd —black lines— and even nodes —red lines— ( $V_{DDo}$  and  $V_{DDe}$ ). In the first example, **K-ratio**, the ratio between  $V_{DDo}$  and  $V_{DDe}$  is fixed  $V_{DD} = V_{DDe} = \eta V_{DDo}$ . In the he **N-Linear** case  $V_{DD} = V_{DDe}$  and  $V_{DDe}$  linearly decreases from the first node to the last ( $V_{DDo}(1) = V_{DD}$  and  $V_{DDo}(N) = V_{DD}/2$ ). The **P-Linear** instance is the opposite of the last **N-Linear** example ( $V_{DD} = V_{DDe}$ ,  $V_{DDo}(1) = V_{DD}/2$  and  $V_{DDo}(N) = V_{DD}$ ). The **Cross-Linear** varies both voltages — $V_{DDo}$  and  $V_{DDe}$ — linearly, one decreases and the other increases. The **Triangle** example makes  $V_{DD} = V_{DDe}$  and  $V_{DDo}$  firstly linearly increases up to the central node ( $V_{DDo}(1) = V_{DD}/2$  and  $V_{DDo}(\frac{N-1}{2}) = V_{DD}$ ) and then it linearly decreases  $V_{DDo}(N) = V_{DD}/2$ . Finally, in the **Double-Triangle** one voltage follows the distribution of the **Triangle** example and the other voltage follows just the opposite.

The results of applying those voltage distributions in (5.39) are plotted in Figure 5.8. Each different example produces different duty cycle distributions along the ring oscillator nodes (linear, parabolic-shaped, sinusoidal-shaped). Therefore, it seems feasible to design ad-hoc duty cycle distributions for the *soft* configuration model.

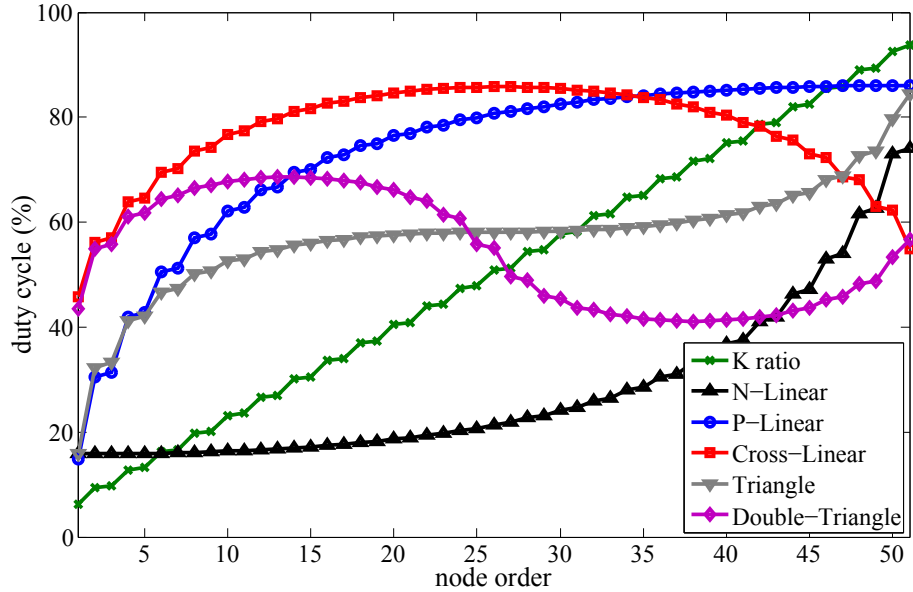


**Figure 5.8:** Theoretical duty cycle distribution in the 6 different cases of soft configuration study.

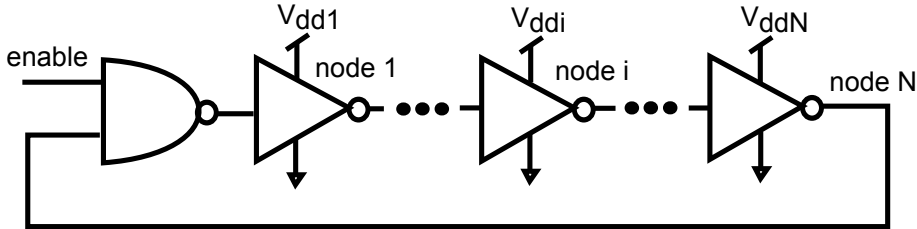


**Figure 5.9:** Ring Oscillator with NAND gate to enable the oscillation.

## 5.4 Models Validation

The validation of the duty cycle configuration models introduced in Section 5.3 has been carried out with Spectre simulation of a 40 nm commercial technology. Different schematics have been tested in order to validate both approaches, *hard* and *soft* configurations. The generic circuit whose parameters have been modified is depicted in Figure 5.9. The main difference between this schematic and the one analyzed in Section 5.3 is the use of a NAND gate that enables and disables the oscillation. The NAND transistors are implemented with the minimum size fixed by the technology and they are not changed for all tests carried out.

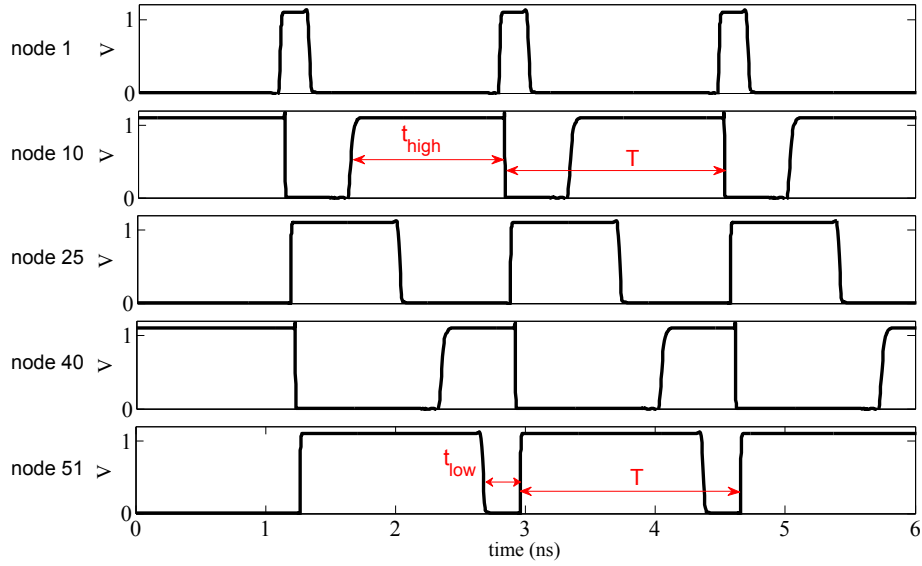


**Figure 5.10:** Internal nodes of a 51-stage ring oscillator where different duty cycle are observed.

### 5.4.1 Hard Configuration Validation

To validate the model based on the layout design the simulations are focused on three of the four different examples presented in Section 5.3.1—**K-ratio**, **Linear** and **Triangle**. In Figure 5.10 some nodes are plotted to show the distribution of duty cycles in different nodes within the chain of inverter gates. This specific case corresponds a **K-ratio** simulation of a 51-stage ring oscillator with  $\varphi = 10$ . In the calculation of duty cycle the inverter and non-inverter nodes are normalized according to the different definition of the duty cycle for odd and even nodes made in Section 5.3. This means, for example in Figure 5.10, node 10 has a duty cycle close to 70% and for the node 51 the duty cycle is 85%, but for our representations we consider node 10 as 70% and node 51 as 15%.

**K-ratio** simulations are divided into two different studies collected in Figures 5.11 and 5.12. In Figure 5.11 theoretical —dashed lines— and simulated —solid lines— results of the **K-ratio** configuration model for different values of  $\varphi = 1, 2, \dots, 10$  are compared. The simulations validate the linear duty cycle distribution previously predicted and they show the variation of the slope distribution with respect to  $\varphi$ . Figure 5.12 plots the duty cycle distributions for ring oscillators with different  $N$  and a fixed  $\varphi = 10$ . For small  $N$  the impact of the NAND design is not negligible and a small alteration is observed. But for  $N$  bigger than 20 stages the maximum and the minimum of the duty cycle distribution changes less than 2% what concludes that the value of  $\varphi$  fixes the maximum and minimum of duty cycle in the **K-ratio** model independently of the number of stages of the ring oscillator, and the central node is always a clock signal with a 50% duty cycle.

The **Linear** configuration simulations correspond to the plot theoretically presented

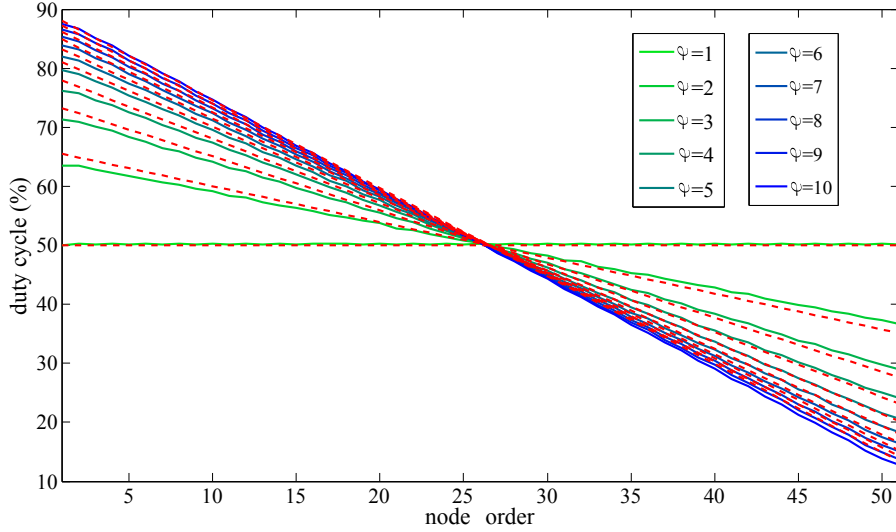


**Figure 5.11:** 51-stage ring oscillator duty cycle distribution for different  $\varphi$  values. Solid lines are simulation results and dashed lines are theoretical values.

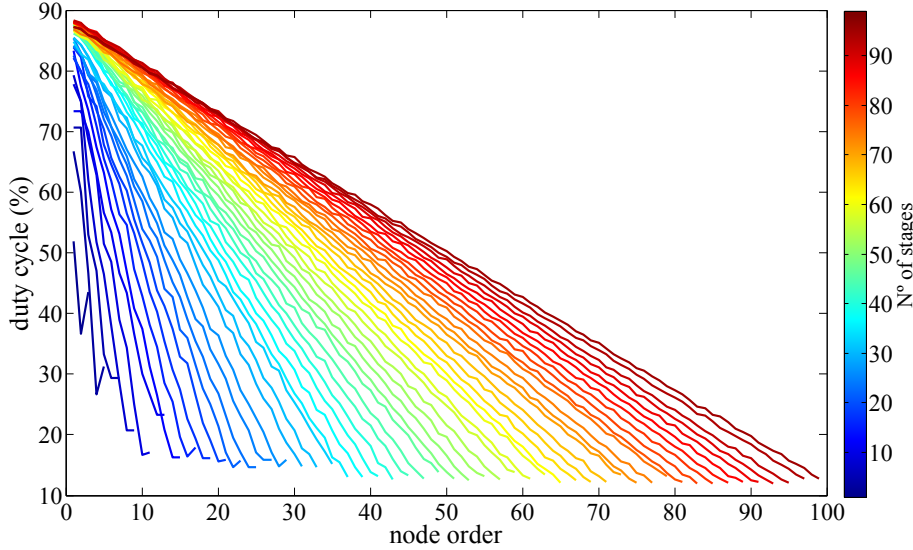


**Figure 5.12:** Duty cycle of a K-ratio distribution for ring oscillators with different number of stages.

in Section 5.3.1 with  $\varphi(1) = \varphi_0 = 10$ ,  $\varphi(N) = 1/\varphi_0 = 1/10$ ,  $W_{po}(1) = W_0 = 120\text{ nm}$  and  $W_{po}(N) = \varphi_0 W_0 = 1200\text{ nm}$  for different odd  $N$  stages from 3 to 99. The results of these simulations are represented in Figure 5.13 compared to the calculated solutions from (5.27). In this figure the x-axis represents the nodes normalized to easily compare the distributions with different number of nodes. The normalization is defined by  $i/N$  in percentage. As the previous figure, the impact of the minimum size NAND gate used for the simulation has a visible impact for the accuracy of the model in small ring oscillator,

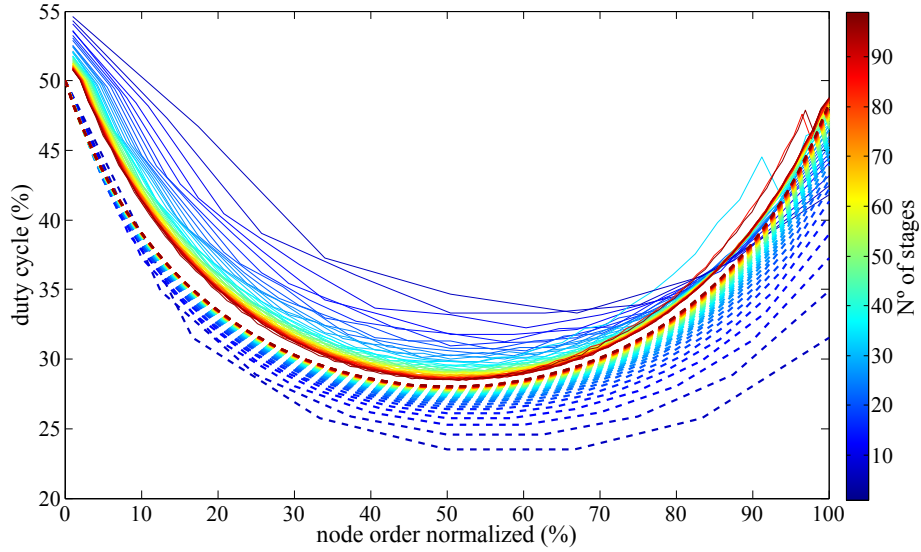


**Figure 5.13:** Duty cycle for the linear distribution example. Solid lines are simulation results and dashed lines are theoretical values.

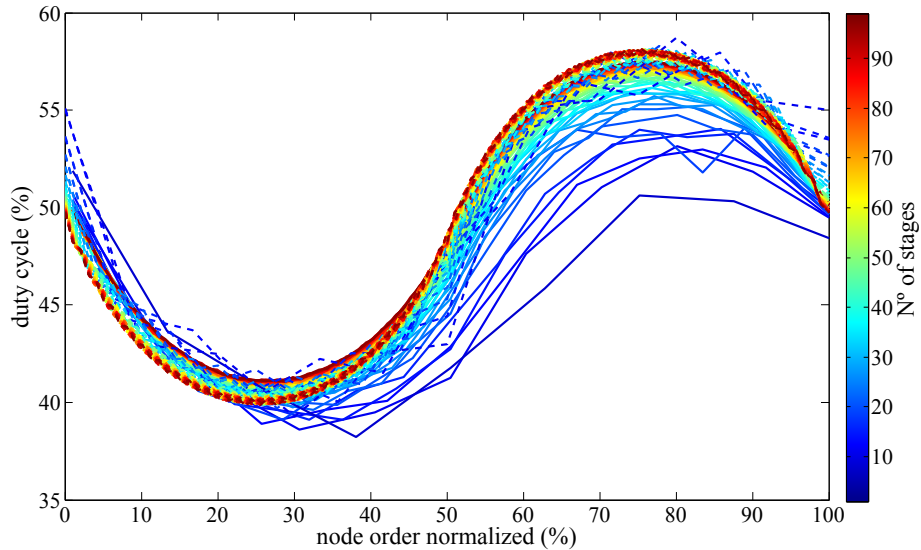


**Figure 5.14:** Duty cycle for the triangular distribution case. Solid lines are simulation results and dashed lines are theoretical values.

but for a big enough number of stages,  $N$ , the model and the simulations tend to the same distribution with absolute error less than 2%.

The last simulations that validate our *hard* duty cycle configuration test the **Triangle** design case. Figure 5.14 plots the result of this example validation. In this case the absolute error of (5.27) is also less than 2% at every node of the ring oscillator for increasing  $N$  stages.

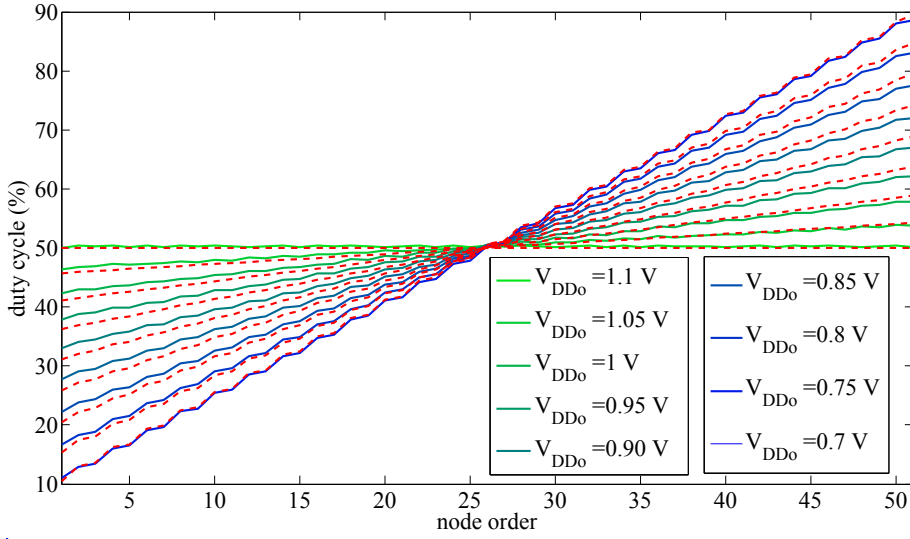


**Figure 5.15:** 51-stage ring oscillator duty cycle distribution for different  $\eta$  values. Solid lines are simulation results and dashed lines are theoretical values.

### 5.4.2 Soft Configuration Validation

The validation of the *soft* configuration follows the same steps that the *hard* one. In this case, the simulations carried out concerned the examples of **K-ratio** and **Double-Triangle**.

**K-ratio** simulations are plotted in Figure 5.15. As was expected from Figure 5.8, the duty cycle distribution along the ring oscillator is linear. The value of  $V_{DD0}$  behaves likewise the value of  $\varphi$  in the *hard* configuration fixing the maximum and the minimum of the duty cycle distribution or changing its slope.

Finally, in Figure 5.16 the **Double-Triangle** simulated results are depicted. The sinusoidal-shaped distribution previously anticipated is confirmed by the simulations. As in previous examples, the model improves its accuracy with increasing number of stages,  $N$ , and from 30 stages, the error of the model is close to 3%.

Both models have been simulated and validated and the hypothesis of designing a ring oscillator with internal duty cycles signals different from 50% have been confirmed. The simulations and equations prove also that fully-configurable duty cycle distributions can be implemented with our proposed models.

### 5.4.3 Transistor Mismatch

Since our proposal relies on varying the duty cycle of ring oscillator nodes, the validation of the models must include a study of fabrication mismatch impact. The fabrication of integrated circuits is not a perfect process and the stochastic nature of the physical processes implies that identical designs have random differences in their performance. Device

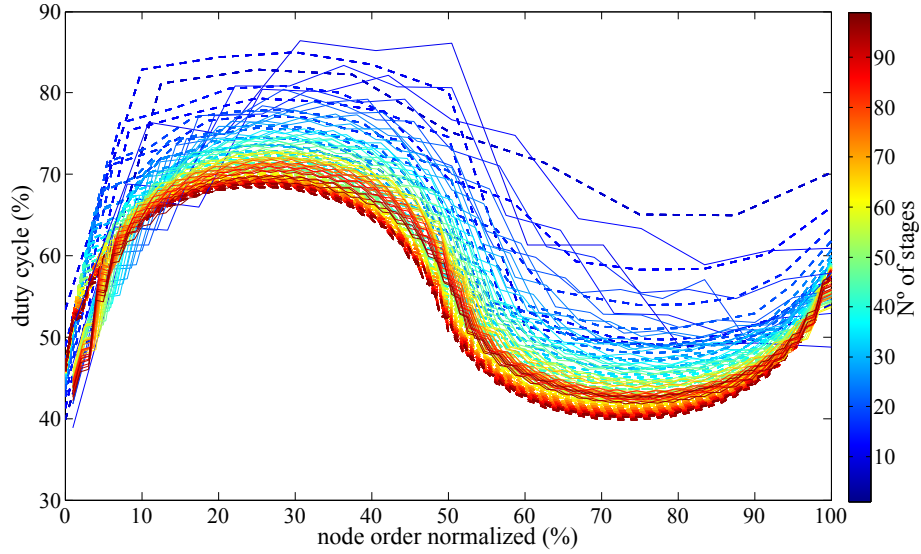


**Figure 5.16:** Duty cycle for the double-triangular distribution case. Solid lines are simulation results and dashed lines are theoretical values.

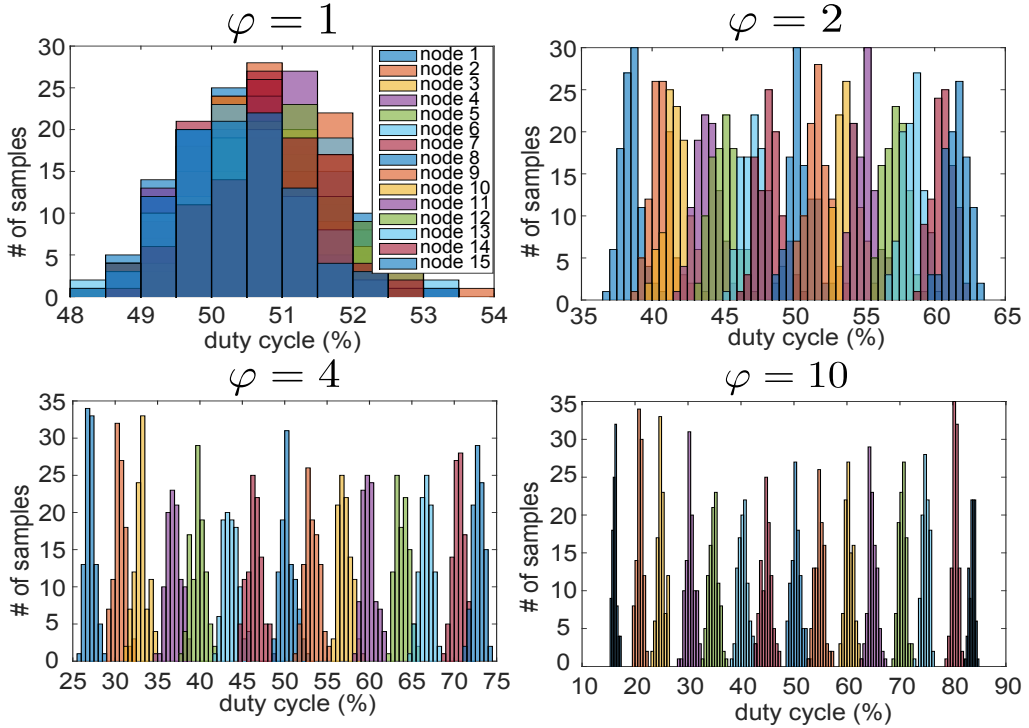


**Figure 5.17:** Mismatch variability of a 15-stage ring oscillator with  $\varphi = 1$  (top left), 2 (top right), 4 (bottom left) and 10 (bottom right).

mismatch limits the accuracy of models, so its study is mandatory for achieving affordable yields in electronic system designs. In our case, the mismatch analysis is based on

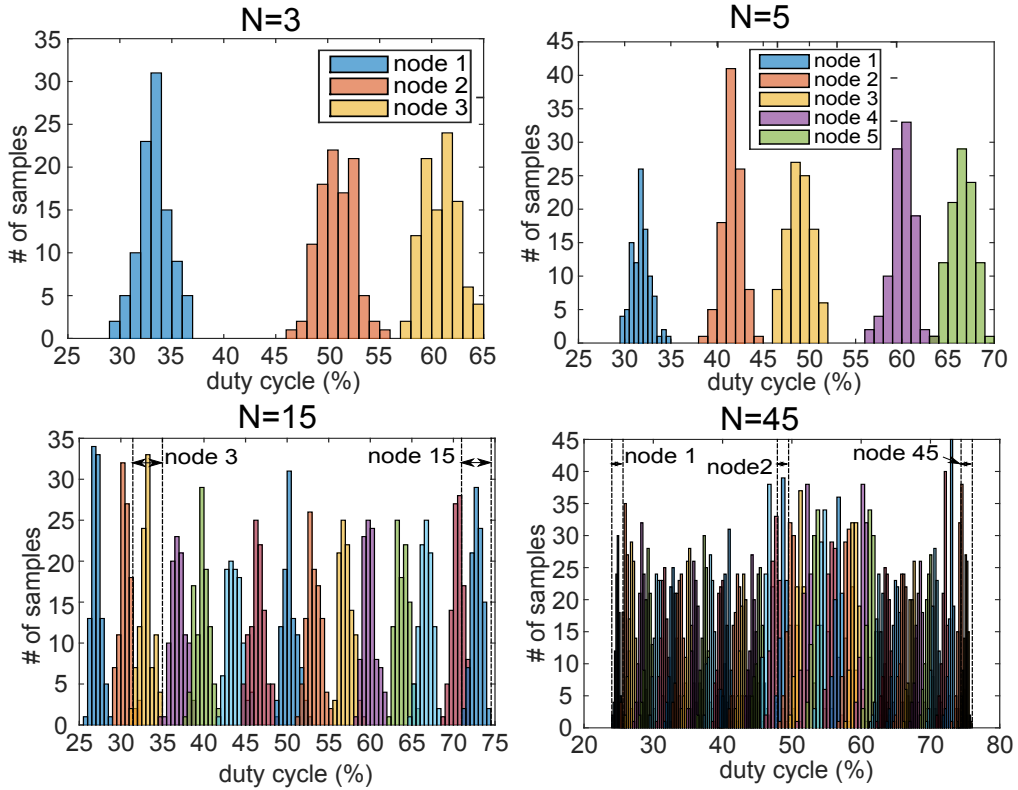


**Figure 5.18:** Mismatch variability of an  $N$ -stage ring oscillator with  $\varphi = 4$  and  $N=3$ (top left), 5 (top right), 15 (bottom left) and 45 (bottom right).

MonteCarlo simulations of 100 different samples according to the manufacturer variability models.

The presented analysis of mismatch is carried out for the *hard* configuration model and the **K-ratio** structure. The results are extrapolated to the rest of potential configurations.

On the one hand, we explore the impact of  $\varphi$  ( $W_{po} = W_{ne} = \varphi W_{pe} = \varphi W_{no}$ ) on the duty cycles at each node. Hence, we fixed the value of  $N$  to 15 stages and we changed  $\varphi$ . The results of these simulations are depicted in Figure 5.17. For this specific design, mismatch can alter the mean value of the duty cycle by  $\pm 1\%$  using the minimum transistor and it negligibly decreases for bigger gate widths. With the correct configuration values the design works properly for node identification reading its duty cycle.

On the other hand, we analyze the duty cycle variability caused by mismatch in increasing ring oscillators. Figure 5.18 is the result of fixing  $\varphi = 4$  and changing  $N$ . In this case, the variability of the duty cycle is inversely proportional to the number of ring oscillator stages. With a minimum 3-stage ring oscillator, the transistor mismatch implies a variability of  $\pm 2.5\%$  from its nominal value, and with a bigger ring oscillator, 45-stages, it is reduced to  $\pm 0.5\%$ .

In conclusion, process variability may affect the accuracy of the ring oscillator duty cycle, but the design parameters,  $\varphi$  and  $N$ , can be used to limit the variation of the output. A required maximum deviation can be achieved by designing bigger,  $N$ , ring oscillators using the level of asymmetry,  $\varphi$ , to adjust the mean of the duty cycle at each stage in Figures 5.17 and 5.18.

## 5.5 Jitter and Phase Noise

In this section, the jitter and phase noise of the proposed asymmetrical ring oscillator is analyzed. Both magnitudes characterize the random deviation of the oscillation frequency and they are the most used quality factors for evaluating and comparing different oscillator performances. The methodology presented in this section is based on the analysis made in [A<sup>+</sup>06]. Abidi makes in [A<sup>+</sup>06] an exhaustive study of phase noise and jitter in CMOS ring oscillators.

First of all, he establishes the relation between jitter and phase noise. Phase noise is a continuous stochastic process indicating random accelerations and decelerations in phase ( $\phi$ ) as an oscillator orbits at a nominally constant frequency ( $f_0$ ) in steady-state. Jitter arises from sampling the orbit at certain points. Usually, baseband communication systems specify clock purity in terms of jitter while oscillators are specified by phase noise. This qualitative relation is mathematically expressed as:

$$\sigma_\tau^2 = \int_0^\infty S_\phi(f) \frac{\sin^2(\pi f/f_0)}{(\pi f_0)^2} df \quad (5.41)$$

where  $\sigma_\tau$  is period jitter and  $S_\phi$  is the double sideband PSD of phase noise. If all phase noise arises from white noise sources, then that equation is simplified to:

$$L(f) = \sigma_\tau^2 \frac{f_0^3}{f^2} \quad (5.42)$$

where  $L(f)$  is the definition of phase noise which is defined as one-half of the double sideband PSD.

Once the previous definitions have been introduced, the next analytical expressions suppose the application of the discussion in [A<sup>+</sup>06] to the ring oscillator with individually design transistors. The main sources to the phase noise in ring oscillators are the white noise generated at each transistor as a consequence of the charge or discharge of node capacitances. The total jitter caused by one of the stage charging node is:

$$\sigma_{t_{pdr}P}^2 = \frac{4kT\gamma_P t_{pdr}}{I_P(V_{DD} - V_t)} + \frac{kTC}{I_P^2} \quad (5.43)$$

where  $k$  is the Boltzmann's constant,  $T$  is the temperature,  $\gamma$  is a technology factor with a value between 0.6 and 0.9 and  $I_P$  is the pMOS source-drain current. (5.43) has two different terms, the first one is the noise generated by the integration of the noise arises from the pMOS transistor in the charging capacitance. And the second term comes from the initial noise deposited by the pull-down nMOS transistor. Respectively, the jitter of the discharge of a node capacitance is:

$$\sigma_{t_{pdf}N}^2 = \frac{4kT\gamma_N t_{pdf}}{I_N(V_{DD} - V_t)} + \frac{kTC}{I_N^2} \quad (5.44)$$

All of these sources are independent and uncorrelated, therefore the total variance of the period jitter is:

$$\sigma_\tau^2 = \sum_{i=1}^N (\sigma_{t_{di}N}^2 + \sigma_{t_{di}P}^2) \quad (5.45)$$

From (5.43) and (5.44):

$$\sigma_\tau^2 = \sum_{i=1}^N \left( \frac{4kT\gamma_N t_{pdf_i}}{I_{Ni}(V_{DD} - V_t)} + \frac{kTC}{I_{Ni}^2} + \frac{4kT\gamma_P t_{pdr_i}}{I_{Pi}(V_{DD} - V_t)} + \frac{kTC}{I_{Pi}^2} \right) \quad (5.46)$$

Using (5.9):

$$\sigma_\tau^2 = \sum_{i=1}^N \left( \frac{4kT\gamma_N t_{pdf_i}}{I_{Ni}(V_{DD} - V_t)} + \frac{2kTt_{pdf_i}}{I_{Ni}V_{DD}} + \frac{4kT\gamma_P t_{pdr_i}}{I_{Pi}(V_{DD} - V_t)} + \frac{2kTt_{pdr_i}}{I_{Pi}V_{DD}} \right) \quad (5.47)$$

and making  $\gamma_N = \gamma_P$  to simplify:

$$\sigma_\tau^2 = \kappa \sum_{i=1}^N \left( \frac{t_{pdf_i}}{I_{Ni}} + \frac{t_{pdr_i}}{I_{Pi}} \right) \quad (5.48)$$

where  $\kappa$  is only dependent on the technology and defined as:

$$\kappa = 2kT \left( \frac{(2\gamma + 1)V_{DD} - V_t}{V_{DD}(V_{DD} - V_t)} \right) \quad (5.49)$$

Thus, the phase noise according to (5.42):

$$L(f) = \kappa \left( \frac{f_0^3}{f^2} \right) \sum_{i=1}^N \left( \frac{t_{pdf_i}}{I_{Ni}} + \frac{t_{pdr_i}}{I_{Pi}} \right) \quad (5.50)$$

In [A<sup>+</sup>06] the phase of a CMOS ring oscillator with equal delay stages is defined as:

$$L(f) = \frac{2kT}{I_{DSAT}} \left( \frac{1}{V_{DD} - V_t} (\gamma_N + \gamma_P) + \frac{1}{V_{DD}} \right) \left( \frac{f_o}{f} \right)^2 \quad (5.51)$$

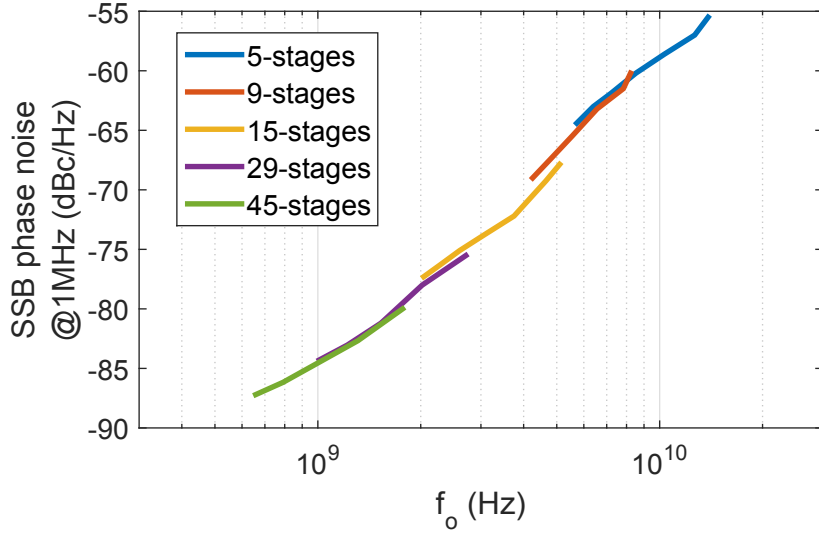


**Figure 5.19:** Phase noise of a **k-Ratio** CMOS ring oscillator measured at 1MHz for different  $\varphi$  (greater  $\varphi$  produces lower  $f_o$ ) and N.

From (5.51) we conclude that the phase noise is independent of the number of delay stages in a ring oscillator and it only depends on the frequency of oscillation and the technology-dependent parameters  $V_t$  and  $\gamma$ .

To compare (5.50) with (5.51), the particularization of Equation (5.50), when all inverters in the ring oscillator are the same and they are balanced, makes the phase noise:

$$L(f) = \kappa \left( \frac{f_0^3}{f^2} \right) \sum_{i=1}^N \left( \frac{t_{pdf}}{I} + \frac{t_{pdr}}{I} \right) = \frac{\kappa}{I} \left( \frac{f_0}{f} \right)^2 \quad (5.52)$$

Then, the expressions are equivalent and therefore the conclusions are valid as well. Instead of applying the equation to a symmetrical ring oscillator, we validate the theoretical phase noise of the **K-ratio** design with simulations. With the **K-ratio** model, there are four different times ( $t_{pdf_o}, t_{pdr_o}, t_{pdf_e}, t_{pdr_e}$ ), and two different currents ( $I_o, I_e$ ), but according to the definition of the relationship of the design parameters, ( $t_{pdf_o} = t_{pdr_e}$ ,  $t_{pdr_o} = t_{pdf_e}$  and  $I_o = \lambda I_e$ ). With these assumptions, the phase noise of this case is defined by:

$$\begin{aligned} L(f) &= \kappa \left( \frac{f_0^3}{f^2} \right) \sum_{i=1}^{\frac{N+1}{2}} \left( \frac{t_{pdf_o} + t_{pdr_e}}{I_o} + \frac{t_{pdf_e} + t_{pdr_o}}{I_e} \right) = \\ &= \kappa \left( \frac{f_0^3}{f^2} \right) \left( \frac{1}{2f_0 I} + \frac{1}{2f_0 \lambda I} \right) = \frac{\kappa}{2I} \left( \frac{\varphi + 1}{\varphi} \right) \left( \frac{f_0}{f} \right)^2 \end{aligned} \quad (5.53)$$

Figure 5.19 shows the phase noise simulation for different asymmetrical ring oscillators with a **K-ratio** and *hard* configuration. All the plotted measurements are taken at 1MHz

from the oscillator frequency. In the figure, five different frequency overlapped ring oscillators are presented, with 5, 9, 15, 29 and 45 stages. With a fixed number of stages, the frequency is controlled by  $\varphi$ . Each colored line represents the frequency for  $\varphi$  from 1 to 10. Lower values of  $\varphi$  produce higher oscillation frequencies. The aggregated phase noise function forms a continuous line that validates (5.51). The phase noise of the ring oscillator is independent of the number of stages but it depends on the oscillation frequency. The tradeoff between a faster oscillator and a good performance in terms of phase noise is maintained in the proposed ring oscillator.

## 5.6 Discussion

The model of the duty cycle of ring oscillators presented in this chapter has followed a simple approach to ease the understanding of the foundations of the configurable duty cycle feature. Despite the explained simplifications, the validation of the model, with a 40 nm commercial technology, has evidenced that the accuracy of the model is very good with an absolute error of 3% in a medium size ring oscillators.

However, the accuracy can be improved avoiding some of the assumed limitations. In the development of our model we have made three main simplifications. First, we have used the long-channel model of MOS transistors. Second, we have only used the saturation region of that model to define the propagation time delay. And third, we have modeled the capacitance at each node of a ring oscillator only as the gate capacitance of the next stage.

To overcome these three simplifications and to improve the accuracy of the model, the next steps would be:

- Taking into account the non-ideal effects of MOS transistors current model: mobility degradation, velocity saturation or channel length modulation.
- Modeling the node capacitance by a more complex model which includes the input-output coupling capacitance, the capacitance dependence on the layout or a more complex model of gate capacitance [XDH<sup>+</sup>03].
- Including a more accurate definition of the charging and discharging of nodes according to each region of the current model.

The evolution of our model would be parallel to the improvement process followed by the studies that have defined the propagation delay of CMOS inverters which are summarized in the work of Roselló and Segura [RS04]. In that work, the authors reviewed the different techniques proposed to accurately define the propagation delay of a CMOS inverter [HOT98, BNK98, KAKAK03], and they proposed a new model to go a step further.

## 5.7 Conclusions

This chapter is an in-depth study of the well-known electronic system ring oscillator. To the best of our knowledge, so far ring oscillators have been used for several applications but for all of them the system output is a clock signal with 50% duty cycle. Our work sets the analytical basis for understanding and designing a ring oscillator whose outputs are clock signals with a duty cycle different from 50% and fully-configurable.

To vary the output duty cycle, we have begun analyzing the possible design parameter that affect the duty cycle. This analysis have revealed two different values, the size of transistors and the bias voltage. According to those two possibilities, we have presented two models in order to vary the output duty cycle, a first model, *hard*, is based on layout design, focusing on transistor sizing along the chain of inverter gates, and the second model, *soft* establishes a relation between duty cycle and different bias voltage schemes with no area overhead.

Additionally, these models are validated by simulation analysis using a commercial 40 nm technology and they are also characterized in terms of mismatch variability and phase noise performance. The variability has shown a dependency with the number of stages of the ring oscillator which can reduce it from 2.5% with minimum size to less than 0.5% in a 45-stage ring oscillator. Regarding the phase noise, our model fits with previous ring oscillator works which concluded that the phase noise is independent on the stages of a ring oscillator but dependent on its frequency.

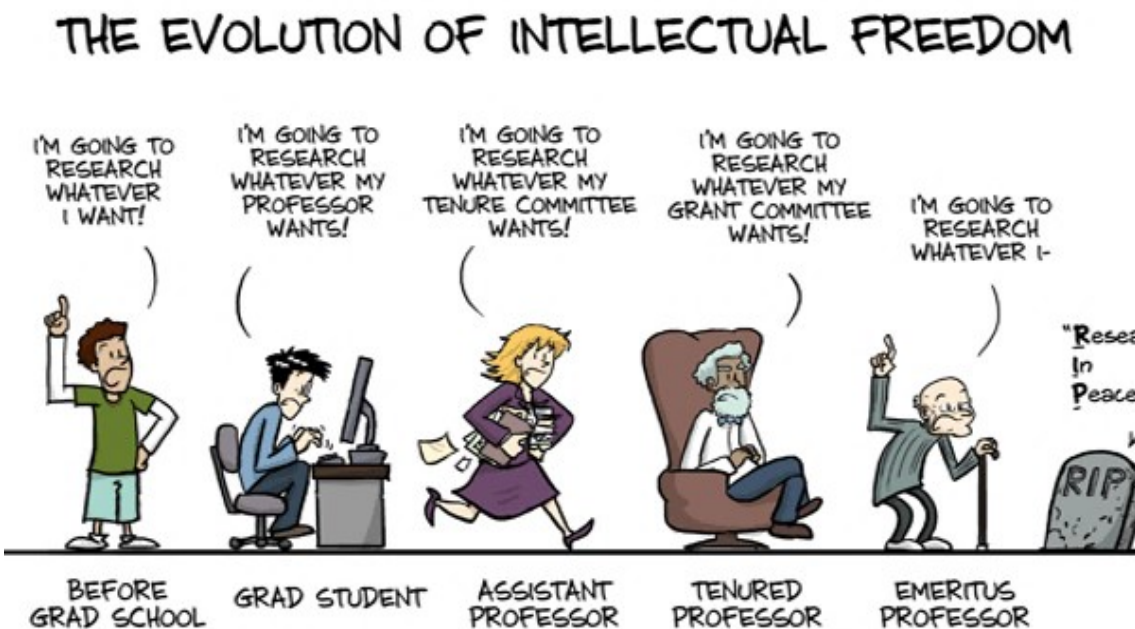
## 5.8 Related Publications

- **J. Agustin** and M. Lopez-Vallejo, "*An In-Depth Analysis of Ring Oscillators: Exploiting Their Configurable Duty-Cycle*," in IEEE Transactions on Circuits and Systems I: Regular Papers, vol. 62, no. 10, pp. 2485-2494, Oct. 2015.  
doi: 10.1109/TCSI.2015.2476300



# Chapter 6

## Application of the Duty Cycle Ring Oscillator Model to Improve PUF Reliability



## Chapter 6

---

# Application of the Duty Cycle Ring Oscillator Model to Improve PUF Reliability

## 6.1 Introduction

The advance of electronic industry has enhanced the ubiquity of electronic systems. Furthermore, the IoT era tends to connect as many electronic systems as possible. Following this trend, as the number of networked smart objects, programs, and data is constantly increasing, there is an equally growing demand to ensure the security and reliability of these units [RDK12]. Therefore, the security hardware has become a hot topic for researchers during the last decade. Three main applications are referred when this term is applied to electronic systems: identification, authentication and key generation. In identification a known ID is uniquely assigned to an unknown entity. Authentication is the procedure to verify a claimed ID of an entity. And key generation is a fundamental block of modern cryptographic systems to secure communication protocols.

For many years, security hardware applications trusted on Non-Volatile Memories (NVMs) [STP08] to store the secure keys without requiring constant power. However, several works have proved the vulnerability of digital keys in NVMs to invasive physical attacks [BS97, Sko05]. Dealing with this vulnerability entails the implementation of complex additional circuits that result in area and power overhead. In this context, Physically Unclonable Functions (PUFs) were postulated 15 years ago and they have emerged as very promising primitives for security hardware since then.

To solve the drawbacks of NVM based security applications, PUFs exploit the ability of hardware devices to store or generate a unique, secure and unpredictable key in order to avoid hacker attacks or unlicensed use of hardware designs. Even though all chips are manufactured in huge quantities, every chip is unique because of the intrinsic variability of fabrication processes. Indeed, as the technology keeps scaling down, such differences become more and more significant, affecting not only the chip performance, but circuit functionality too. Therefore, in the past couple of decades, there have been many efforts to reduce or control manufacturing variability. Simultaneously, researchers have discovered

methods to put such variation for good uses in security applications [ZQLZ14]. Compared to the NVM approach [HYKD14] PUF hardware is simpler and requires less power consumption; since the chip must be powered on to operate and PUFs usually work for a short period of time, any physical attack is harder; invasive attacks modify the physical characteristics, so their use would modify the PUF outputs; and memory based systems are more expensive to fabricate.

Different definitions have been proposed for PUFs, and recently, in [PM15], Plaga and Merli have unified previous works to define a PUF as a physical information-storage system that is protected by a security mechanism which: 1) has the security objective to render it more difficult to duplicate a precisely described storage functionality of the system in another, separate system. 2) is meant to remain effective against an active attacker with temporary physical access to the whole system in its original form. Many hardware systems have been presented that fit into this definition. Among all of them, one of the most common and mature designs uses ring oscillators as the basic structure. Hence, ring oscillators are playing a fundamental role in the development of PUFs.

Unfortunately, as in any other design, the performance of the electronic circuits used in PUFs are intrinsically dependent on external variables. Among all of them, the most relevant ones are temperature, bias voltage and aging. The effects of all of these variables in the performance of ring oscillators have been extensively studied, specially how they affect their output frequencies. In the particular application of PUFs, the reliability of the system is highly compromised by the variation of circuit outputs.

As has been shown in this Thesis, the radiation is also an important source of unreliability. It has also been mentioned how the shrinking technology is enhancing the occurrence of radiation effects in environments where they were negligible. Since PUFs are very critical blocks whose failure would affect the integrity of the whole system, we introduce the study of radiation impact in the study of PUF reliability.

In this chapter we propose an improvement on ring oscillator based PUFs. Conventional RO PUFs measure the output frequency of several identical ring oscillators and they generate an output depending on their relationships. Instead of using this approach, we design a PUF based on measuring differences in the duty cycle of different signals. Chapter 5 has already introduced the methodologies to fully configure the duty cycle of ring oscillators. Our PUF topology allows to increase the potential relationships between different ring oscillator outputs and it also improves their robustness by using the duty cycle instead of the frequency magnitude. Furthermore, we have proven that the implementation of a configurable duty cycle ring oscillator makes them fully tolerant to SETs in Chapter 4.

The rest of the chapter is organized as follows. First, in Section 6.2 the foundations of PUF and related work is presented. The RO PUF and its variants and advances are summarized in Section 6.3. Sections 6.4 and 6.5 describe our PUF proposal by exploring the potential of the duty cycle as output parameter for PUFs, explaining the proposed ar-

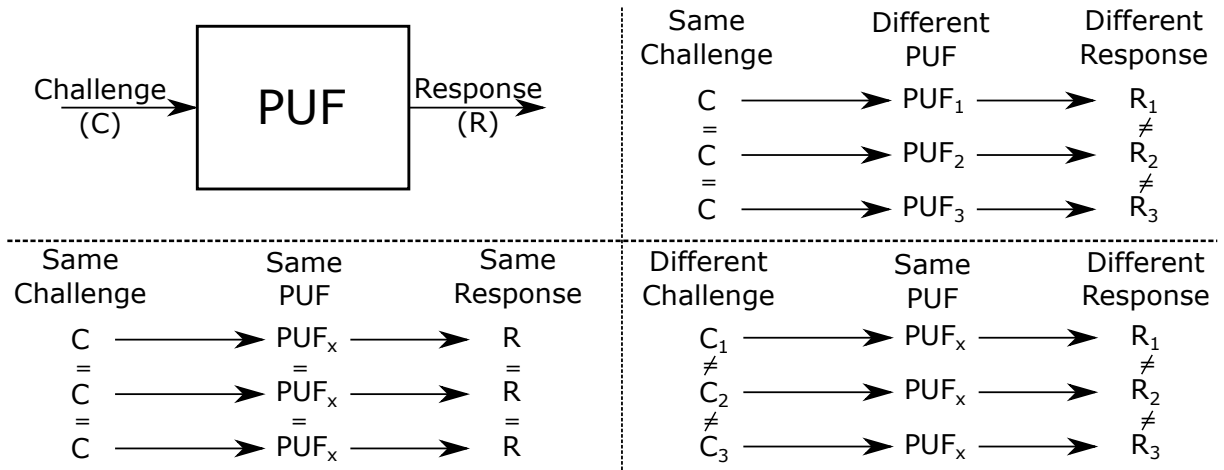


**Figure 6.1:** PUF basic operation as a CRP pair system and its ideal operation.

chitecture and presenting the simulation results for nominal conditions and environmental variations. In Section 6.6 we explain the fabricated circuit to validate the PUF proposal and the test plan for the future test campaign. Finally, in Section 6.7 the main conclusions of this chapter are drawn.

## 6.2 Related Work

### 6.2.1 PUF Foundations

PUFs are Challenge Response Pair (CRP) architectures [TŠ07]. These systems are characterized for generating a response when a specific challenge drives their input. PUF responses are completely unique for every chip thanks to the uncontrollable manufacturing process variations. Figure 6.1 explains the fundamental operation of a CRP architecture. The first condition of these systems is that for the same challenge and the same PUF, the response must be consistently the same. Any other result would be an error. Other characteristic is that given a challenge, the response for the application of that challenge to different PUFs must be different. And finally, the use of the same challenge to excite different PUFs will also generate different responses. Moreover, all the CRPs have to be completely unforeseeable.

To compare different types and designs of PUFs, it is necessary to define a set of parameters that quantify their features. To this purpose, in [MGS13], Maiti presents the most important quality factors of PUFs that we summarize in this section: randomness, reliability and robustness.

## Randomness

The randomness of a PUF is measured by statistically analyzing the CRPs for a set of challenges in different instances of the same PUF implementation. The randomness is analyzed by calculating three parameters:

- Uniqueness. The uniqueness is a measurement of how unique are the responses generated from different chips. It is estimated by the average value of the inter-die Hamming Distance (HD) of responses. Where the HD is a parameter of information theory defined as the number of different bits of two words of the same bitwidth. For  $k$  different PUF chips with responses  $R$  of  $n$  bits, the expression that defines the uniqueness is:

$$\text{Uniqueness} = \frac{2}{k(k-1)} \sum_{i=1}^{k-1} \sum_{j=i+1}^k \frac{\text{HD}(R_i, R_j)}{n} \quad (6.1)$$

- Uniformity. It is a random variable that measures the distribution of '0's and '1's in the response of a particular PUF. As the response of PUF must be completely random, the number of '0's and '1' should be ideally the same. It can be calculated by the mean of the Hamming Weights of a set of responses:

$$\text{Uniformity} = \frac{1}{n} \sum_{l=1}^n r_l \quad (6.2)$$

where  $r_l$  is the  $l$ -th bit of the response.

- Bit aliasing. The aliasing refers to the generation of similar responses for different PUFs that can derive in authentication errors. It is estimated by the average number of '0's and '1's of the  $l$ -th bit of the  $n$  bit responses among  $k$  different chips.

$$(\text{BitAliasing})_l = \frac{1}{k} \sum_{i=1}^k r_{i,l} \quad (6.3)$$

where  $r_{i,l}$  is the  $l$ -th bit of a response of PUF <sub>$i$</sub> .

Attending to the three definitions, the ideal value for all of the parameters is 50 %. It means that the probability of every response bit to be '0' or '1' is the same and independent on the PUF device, bit position or the rest of bits within the same response.

## Reliability

The randomness is able to measure the characteristics of PUF responses. These characteristics are expected to be static, but they can actually vary as a consequence of external factors. So far, the factors that have been taken into account by most of the studies are temperature variation [MRV<sup>+</sup>12a,Che15] and stability of bias voltage [MRV<sup>+</sup>12b,ZFC<sup>+</sup>14]. Moreover, aging has also been included in some recent analysis [MS14,GN14]. Aging effects produce temporal degradation of chips that can provoke irreversible changes destroying the device functionality.

The reliability of PUFs measures their dependency with respect to those factors. It can be measured by the intra-chip Hamming Distance. If a PUF  $i$  generates a  $n$ -bit response,  $R_i$ , at nominal conditions, it should generate the same response  $R'_i$  at different conditions and time  $t$ . With this notation, given  $m$  measurements of the response of a specific PUF for the same challenge, the reliability of that PUF can be calculated as:

$$\text{Reliability} = 1 - \frac{1}{m} \sum_{t=1}^m \frac{HD(R_i, R'_{i,t})}{n} \quad (6.4)$$

As mentioned in the introduction of this chapter, radiation has become an important source of unreliability. While it has remained out of the scope of previous PUF works, its increasing relevancy, even at ground level, makes it an important factor to consider. In this thesis, both of the categories of radiation effects, cumulative and SEE have been analyzed. Their interaction with electronic circuits has revealed some of the possible effects, such as the variation of oscillation frequency by TID, that clearly affect the PUF performance. To the best of our knowledge, it is the first time that a PUF is characterized in terms of radiation effects.

## Robustness

The robustness refers to the characteristic of PUFs to keep their secret from malicious attacks. There is no qualitative variable to measure the robustness because there are only two possibilities, it can be “hacked” or it cannot. Instead of a parameter, PUFs can be robust against certain types of attacks. At the same time, the attack suitable to force a PUF is highly dependent on its implementation. Many different attacks have been developed to show the weakness of almost every proposal. Although they are specific for each particular PUF, the types of attacks are usually divided into four different categories:

- Active attack. Active attacks are based on altering the normal operation of the system in order to deduce the CRPs [BM09]. By manipulating the system or its environment, the response is modified and monitored. A relationship can be established between the variation of responses and the inner mechanism of the PUF. This type

of attacks can be invasive or non-invasive depending on the possibility of destruction of the device during the attack [NSHB13].

- Passive attack. Passive attacks observe and collect information of the working PUF instead of trying to change it [BK<sup>+</sup>14]. A PUF may be attacked by using side-channel attack information such as power consumption or electromagnetic radiation while it is in operation.
- Replay attack. This attack replaces a CRP, copied during the phase of authentication, to use it instead of the original PUF [ZLQ15]. If the security system only uses each CRP once, this attack is useless. However, this condition makes challenging the construction of a PUF with a great number of CRPs.
- Modeling attack. The physical behavior of a PUF can be modeled mathematically [RvD13, MRMK13]. This way, an equivalent circuit to a specific PUF can be designed to replace the genuine device. PUF randomness is highly linked with the difficulty of modeling it as the variations come from physical phenomena.

### 6.2.2 Types of PUF

Once the concept of PUFs and the quality factors that allow to characterize them have been introduced, this section summarizes the types of PUFs that have been proposed in previous works. The amazing popularity of PUFs during the last decade has contributed to the generation of a huge and heterogeneous number of proposals. Together with these proposals, some works have tried to create a taxonomy of the devices resulting in different types of classification:

- Based on the implementation technology: non-silicon versus silicon.
- Based on a more general set of physical properties: nonintrinsic versus intrinsic.
- Based on the properties of their CRP behavior: weak versus strong.

#### Silicon/Non-Silicon

Non silicon PUF refers to the proposals that are implemented with non-electronic technology such as optical [PRTG02] or magnetic [DSR<sup>+</sup>15] PUFs. On the other hand, silicon PUFs use the uncontrollable variations of semiconductor electronic manufacturing processes to generate the unique signature for each IC. According to the different sources of variation, silicon PUFs are also divided into three different categories: analog electronic PUFs, memory-based PUFs [GK14], and delay-based PUFs [MS09]. Since silicon PUFs

**Table 6.1:** Classification of previous works according to different features.

PUF Proposal	Silicon/ Non-Silicon	Intrinsic/ Nonintrinsic	Weak/ Strong
Optical PUF [PRTG02]	Non-Silicon	Nonintrinsic	Strong
Coating PUF [ŠTO05]	Silicon	Nonintrinsic	Strong
SRAM PUF [MTV09]	Silicon	Intrinsic	Weak
Butterfly PUF [KGM <sup>+</sup> 08]	Silicon	Intrinsic	Strong
Ring Oscillator PUF [SD07]	Silicon	Intrinsic	Weak
Arbiter PUF [FSF <sup>+</sup> 11]	Silicon	Intrinsic	Strong
RRAM PUF [MRFA15]	Non-Silicon	Intrinsic	Weak
Nanotube PUF [LLZH16]	Non-Silicon	Nonintrinsic	Strong
Magnetic PUF [DSR <sup>+</sup> 15]	Non-Silicon	Nonintrinsic	Strong

are fully integrable with all electronic circuits, they have been raised as the main type of PUF architectures in research works.

### Intrinsic/Nonintrinsic

A PUF is considered intrinsic if it fulfills both of these conditions: 1) Its evaluations are performed internally by embedded measurement equipment. It means that the response is generated inside the chip and there is no need to make any additional processing outside the chip. 2) Its random device specific features are implicitly introduced during its production process. This condition separates the PUFs that require additional processes to enhance the variability of the conventional fabrication process.

### Weak/Strong

Depending on the number of CRPs that a PUF produces, it can be classified into two general categories: weak and strong. Weak PUFs generate a limited number of CRPs, so they can be fully read out within a very short time. In this type of PUFs, the number of CRPs is linearly or polynomially dependent on the number of challenge bits. Opposite, strong PUFs can be driven by almost an unlimited amount of challenges. A strong PUF needs to prove its security under a strong attack model. Their very large number of CRPs avoid using malicious attacks based on brute force within a realistic time. They are also resilient to modeling attacks making really hard to predict the response of a PUF to a randomly selected challenge.

Table 6.1 outlines and classifies some of the proposals of the literature for PUF implementations according to these three different classifications.

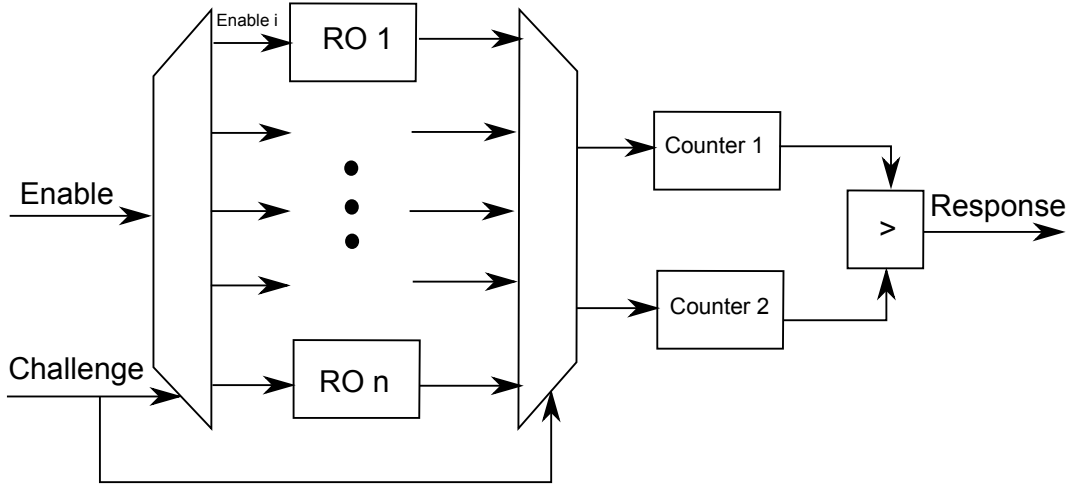


**Figure 6.2:** Conventional RO PUF architecture based on frequency variability [MS09].

### 6.3 Ring Oscillator PUF

A Ring Oscillator PUF (RO-PUF) is a silicon, intrinsic and weak PUF that generates the response using the output frequencies of ring oscillators. It is silicon because it is implemented using on-chip oscillators. It is intrinsic as it is based on measuring process variations on the frequencies and the responses are evaluated within the PUF. And it is weak since it can generate  $\log_2(n!)$  independent responses from a PUF with  $n$  identical ring oscillators.

The first proposal of using a ring oscillator to build a PUF was made by Gassend et al. [GCvDD02]. They proposed to use a single ring oscillator whose output drives a counter that monitors the number of cycles in a fixed time interval. This value is quantized and converted into the response of the PUF. That implementation proved to be valid as the frequency of equal implementations on different chips suffered enough variation to generate unique responses. However, the influence of environmental conditions on the frequency of ring oscillators is well-known and the unreliability of this proposal was immediately pointed out.

Suh and Devadas [SD07] proposed an alternative architecture to the Gassend et al. [GCvDD02] approach. Their proposal uses more than only one ring oscillator and considers the relative frequencies of pairs of oscillators instead of using the absolute value of a single oscillator. It follows the architecture depicted in Fig. 6.2. It is made of  $n$  identical  $N$ -stage ring oscillators. The challenges of this PUF consist in selecting a pair of ring oscillators (a,b) and comparing their output frequencies expecting a deviation due to process variations. Then, if  $f_a$  is greater than  $f_b$  the response is '1', otherwise the output is '0'.

The implementation of Suh and Devadas has become one of the most studied architec-

tures of silicon PUFs and it appears in all comparisons for new PUF approaches. Moreover, it is the base for many proposals that try to solve the problems that this RO-PUF presents.

The first problem is the small number of independent CRPs. If a RO-PUF is made of  $n$  ring oscillators, a total of  $\binom{n}{2} = \frac{n(n-1)}{2}$  are the potential bit responses. However, those evaluations are not completely independent, for instance, if  $f_a$  is greater than  $f_b$  and  $f_b$  is greater than  $f_c$  then  $f_a$  is directly greater than  $f_c$  and the response is not unforeseeable as it is required in PUFs. Therefore, the real number of independent comparison of  $n$  frequencies decreases to  $\log_2(n!)$ . At the same time, this number fixes a maximum theoretical limit which is achieved depending on the specific implementation. Finally, just  $n/2$  response bits are guaranteed to be fully independent. In [SD07] the authors even reduce the number of responses in order to improve the reliability by a technique called *1-out-of-k-masking* where only  $\lfloor \frac{n}{k} \rfloor$  ring oscillators are used.

To solve this problem, but keeping the upper limit, different modifications have been proposed, such as the PUF designed by Maiti et al. [MS09], where the inverters of ring oscillator stages are configurable to increase the intrinsic process variations. Another approach is presented by Maiti et al. [MKS12] where the number of CRPs is increased by using an identity-mapping function that post-processes the output frequencies to increase the entropy.

Another important problem is the reliability of the RO-PUF. Many works have shown very good quality factors of RO-PUF implementations at nominal conditions. However, environmental and aging variations lead the PUF to generate unreliable bits. In [GN14], the effects of aging in RO-PUFs are studied and in [RFFT14] a possible solution to improve its resilience is shown. The solution in [RFFT14] tries to reduce the degradation of ring oscillators by controlling the Negative-Bias Temperature Instability (NBTI) and the Hot Carrier Injection (HCI) phenomena in pMOS and nMOS. Those phenomena are the most relevant agents in the degradation of transistors as a consequence of aging. Vivekraja and Nazhandali [VN09] showed how the bias voltage variation is able to decrease the uniqueness of RO-PUFs from the ideal 50% to almost 25%. The temperature is also a problem to keep the reliability of the RO-PUF close to 100% as it is studied in [YQ09] where a solution is proposed. This solution is based on defining zones of secure operation for each pair of ring oscillators.

Many works are focused on compromising the robustness of new PUF proposals as they are intended to be placed in security systems. The maturity of the RO-PUF has led to the development of several attempts to break its “secret” using the different approaches introduced in the previous section. For example, Ruhrmair et al. [RSS<sup>+</sup>13] showed that modeling attacks using machine learning techniques can foresee RO-PUF responses to a given challenge with prediction rates up to 99%. Merli et al. [MSSS11] pointed out that a side channel attack is possible to RO-PUFs. They analyzed the frequencies of ring oscillators by measuring the electromagnetic radiation together with attacks on the fuzzy

extractor which successfully extracted the cryptographic keys generated by RO-PUFs.

Therefore, there are still some problems to overcome in order to make RO-PUFs reliable enough for high security system.

## 6.4 Duty Cylce PUF Proposal

In order to solve some of the mentioned drawbacks, we propose a new perspective based on ring oscillators. Our PUF proposal will generate the responses by comparing the duty cycle of an array of ring oscillators instead of by comparing the output frequencies. To design this system, we use the duty cycle configuration modeled in Chapter 5. We will only use the *hard* configuration of the asymmetrical implementation of ring oscillators because the *soft* configuration uses as duty cycle control one of the external variables, bias voltage, that directly affects the reliability of the PUFs. Using our new approach, we assume that two main issues are tackled:

- The number of CPRs will increase as the duty cycle at each internal node is different, so more than just one output —frequency— can be exploited.
- The reliability of the RO-PUF will improve as a consequence of measuring a relative magnitude —duty cycle— instead of an absolute one —frequency.

### 6.4.1 Duty Cycle PUF Exploration

First of all, to understand how the frequency of ring oscillators is affected by the variation of each of the main environmental variables, we begin summarizing how they affect the output individually. Bringing back Equations (5.25) and (5.26), the frequency of a ring oscillator can be defined as:

$$f = \frac{1}{\sum_{j=1}^N (t_{high_i} + t_{low_i})} = \frac{1}{\alpha_n \sum_{j=1}^N \left( \frac{W_{n_{\Gamma_N}(j+1)} + W_{p_{\Gamma_N}(j+1)}}{W_{p_{\Gamma_N}(j)}} + \frac{W_{n_{\Gamma_N}(j+1)} + W_{p_{\Gamma_N}(j+1)}}{\lambda W_{n_{\Gamma_N}(j)}} \right)} \quad (6.5)$$

In this equation there are two type of components:  $W_x$  and  $\alpha_n$ . The values of  $W_x$  are fixed at design time and they are independent on any external variation. Indeed, they are the source of the variation of frequency due to process variation and mismatch. Consequently, the source of the modification of frequency with respect to environmental parameters must be produced by the alteration of the value of  $\alpha_n$ . It was defined as:

$$\alpha_n = \frac{V_{DD}L^2}{\mu_n(V_{DD} - V_t)^2} \quad (6.6)$$

How temperature, bias voltage and aging modify the value of each of the parameters implied in the definition of  $\alpha_n$  will explain the impact of these parameters into the ring oscillator frequency and therefore the RO-PUF reliability.

## Temperature

In [SBN05], Socher et al. explain that the drain current temperature dependence of standard CMOS transistors is derived from three main sources: the threshold voltage, the inversion layer charge concentration and the mobility. The threshold voltage dependence upon temperature is obtained from the expression:

$$V_t = \phi_{MS} - \frac{qN_{ss}}{C_{ox}} + 2\phi_F + \sqrt{\frac{4qN_B\epsilon_0\epsilon_S\phi_F}{C_{ox}^2}} \quad (6.7)$$

where  $\phi_{MS}$  is the Fermi potential difference between the gate and bulk materials,  $N_B$  is the substrate doping,  $C_{ox}$  is the gate capacitance,  $q$  is the electron charge,  $\epsilon_0$  is the vacuum permittivity,  $\epsilon_S$  is the relative permittivity of silicon, and  $\phi_F$  is the Fermi potential of the bulk. The temperature dependence is mainly due to the energy gap temperature dependence, causing the threshold voltage to change about a millivolt per degree.

The mobility of carriers is calculated with this expression:

$$\mu(T) = \mu_0 \left( \frac{T_0}{T} \right)^b \quad (6.8)$$

where  $b$  is typically between 1 and 2 around room temperature, causing the mobility to decrease by about half a percent per degree.

The addition of the different temperature effects in the transistor drain current is translated into a decreasing of current in saturation region with increasing temperatures. This change makes slower the delay of each stage and consequently the frequency of a ring oscillator decreases with increasing temperatures.

## Bias Voltage

The variation of  $\alpha_n$  with respect to bias voltage is direct from its definition. Bigger voltages make faster oscillators. In fact, this property has been used to implement ring oscillator based VCOs. Moreover, the expression for the channel mobility can be further complicated by introducing velocity saturation and mobility degradation [VLPB98]. This would mean that the mobility at the reference temperature  $\mu_0 = \mu(T_0)$  depends on the bias voltages and the threshold voltage as well. Both contributions reflect the dependency of frequency output with the bias voltage.

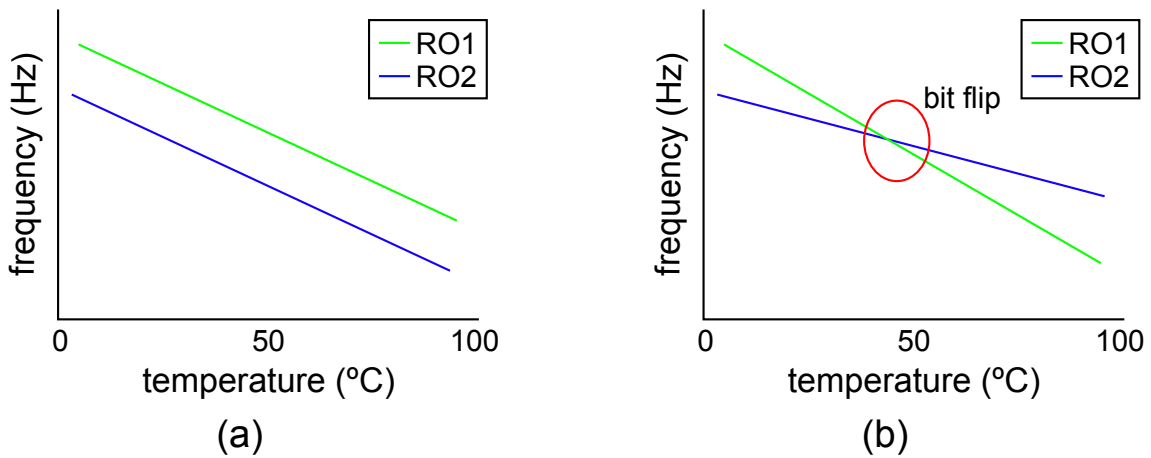


**Figure 6.3:** PUF error source as a consequence of different sensitivities to temperature.

### Aging

The effect of aging in the threshold voltage of CMOS transistors is deeply studied and validated with ring oscillators in [ZVR<sup>+</sup>09]. This study takes into account the effects of NBTI and HCI to define the variation of  $V_t$  as:

$$\Delta V_t \approx \left( \frac{16n^4 K_v^2 \alpha \eta t}{\xi^2 (1 - \alpha)(1 - \eta)} \right)^n \quad (6.9)$$

where  $n$ ,  $K_v$ , and  $\xi$  are dependent on the technology,  $\alpha$  and  $\eta$  refer to the activity factor and the wake/sleep ratio and  $t$  denotes the age of the circuit.

### Radiation

In terms of radiation, the shift of  $V_t$  has already been presented in Section 3.2.1. Actually, this dependency has been exploited to design the TID sensor of Chapter 3.

### Duty Cycle

The variation of the output frequency is not the source of unreliability itself. The real problem is the different sensitivities between the identical implementations of ring oscillators that will be compared. For example, in Figure 6.3 (a), the frequency of two ring oscillators is monitored for a range of temperatures (0°C to 100°C). In this case, the sensitivity is the same for both instances and therefore the relationship between both frequencies is constant. However, in Figure 6.3 (b), the sensitivities are different and at a specific temperature, the relationship flips which is translated into an error in the generation of the response.

To avoid this source of error, we propose to avoid the dependency on external parameters by using the duty cycle of ring oscillator nodes instead of the output frequency. As

was concluded in Equation 5.27, the duty cycle for the internal nodes in a *hard* configuration of ring oscillators is only dependent on the size of the ring oscillator transistors. Therefore, using a relative magnitude, such as the duty cycle, removes the dependency on environmental variables and maintains the variability of process fabrication. For our prototype, we will focus on the **K-ratio** implementation (defined in Section 5.3.1). The duty cycle of that configuration was deduced as:

$$d_i = \frac{\varphi N + i(1 - \varphi)}{(N + 1)(\varphi + 1)} \quad (6.10)$$

where  $\varphi$  was defined as the asymmetry relationship between transistor sizes of pMOS and nMOS transistors in odd and even nodes ( $W_{po} = W_{ne} = \varphi W_{pe} = \varphi W_{no}$ ).

Once the sources of error have been removed, it is time to explore the potential of using the duty cycle measurement for implementing a Duty Cycle PUF (DC-PUF) based on **K-ratio** ring oscillators. The variability of this configuration has already been studied in Section 5.4.3 with the results plotted in Figures 5.17 and 5.18 (reproduced in Figures 6.4 and 6.5). The variability characterization was carried out with a 40 nm commercial technology and Monte Carlo simulations. The simulations consist in 100 different samples which include the particular technology variability models provided by the foundry. A first group of results showed the impact of the  $\varphi$  value in a medium size (15 stages) ring oscillator. The results of these tests are summarized in Figure 6.4 for  $\varphi = 1; 2; 4; 10$ . For  $\varphi = 1$  all transistors are designed with balanced stages as in the conventional ring oscillator and as expected the value of the duty cycle at any node is around 50%. The rest of the simulations showed that increasing  $\varphi$  makes the differences of internal node duty cycles bigger. Then each node can be separated as an individual value with an independent duty cycle measurement multiplying by  $N$ , the number of stages in a ring oscillator, the only one measurement of the frequency output in a traditional ring oscillator. In the 15-stage ring oscillator example, the value  $\varphi = 4$  would be enough for separating each node duty cycle values from the rest of nodes.

The next design parameter we analyzed is the impact of  $N$  in the duty cycle variation. In this case of study, we fixed  $\varphi = 4$  and we implemented different ring oscillators with  $N = 3; 5; 15; 45$ . The results are plotted in Figure 6.5. The variability range decreases if the number of stages increases but the maximum and minimum value of the duty cycle nearly keep constant. Thus, for a given value of  $\varphi$ , the ring oscillator which would be more affected by process variability is the minimum size (3 stages). On the contrary, a bigger ring oscillator gives more potential distributions to be analyzed and included in the CRP generation. Therefore, the DC-PUF is a valid candidate to implement a highly reliable PUF with these characteristics:

- Greater  $\varphi$  makes easier the differentiation of nodes.

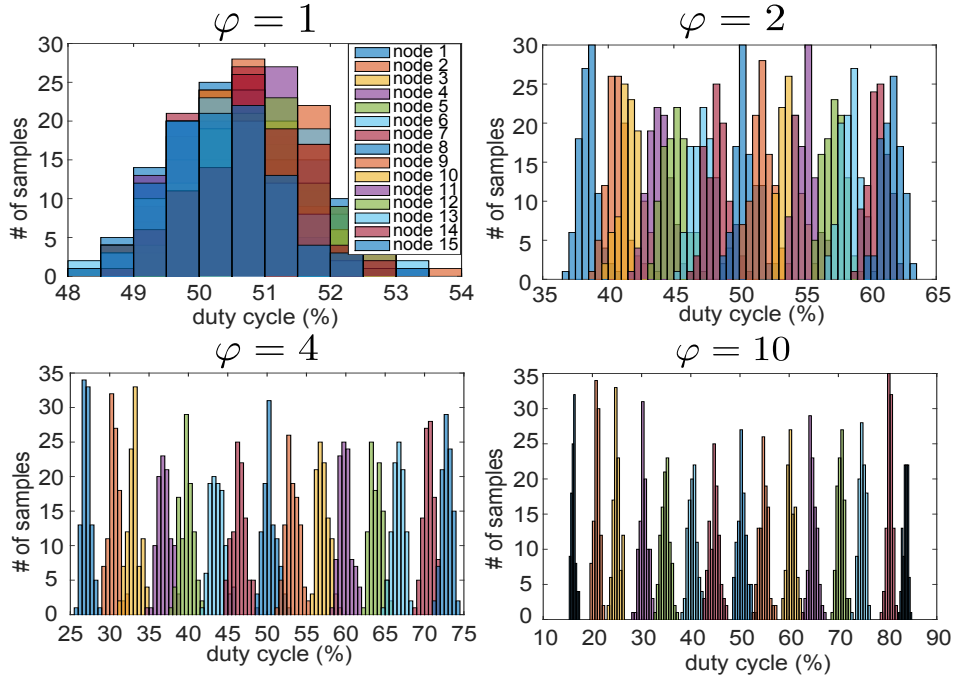


**Figure 6.4:** Mismatch variability of a 15-stage ring oscillator with  $\varphi=1$  (top left), 2 (top right), 4 (bottom left) and 10 (bottom right).

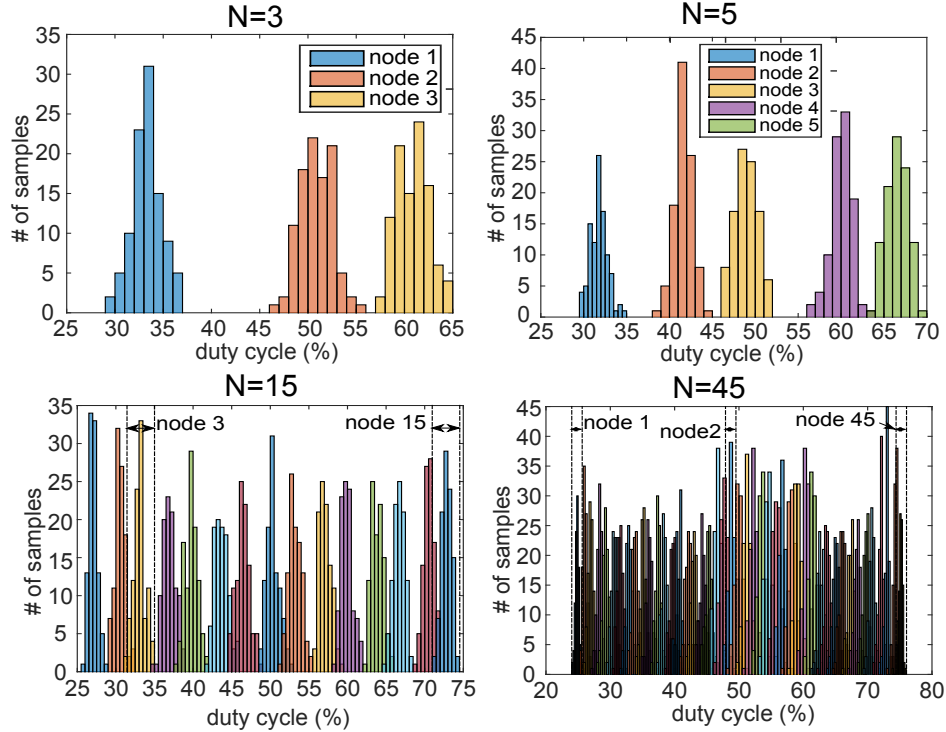


**Figure 6.5:** Mismatch variability of an  $N$ -stage ring oscillator with  $\varphi=4$  and  $N=3$ (top left), 5 (top right), 15 (bottom left) and 45 (bottom right).

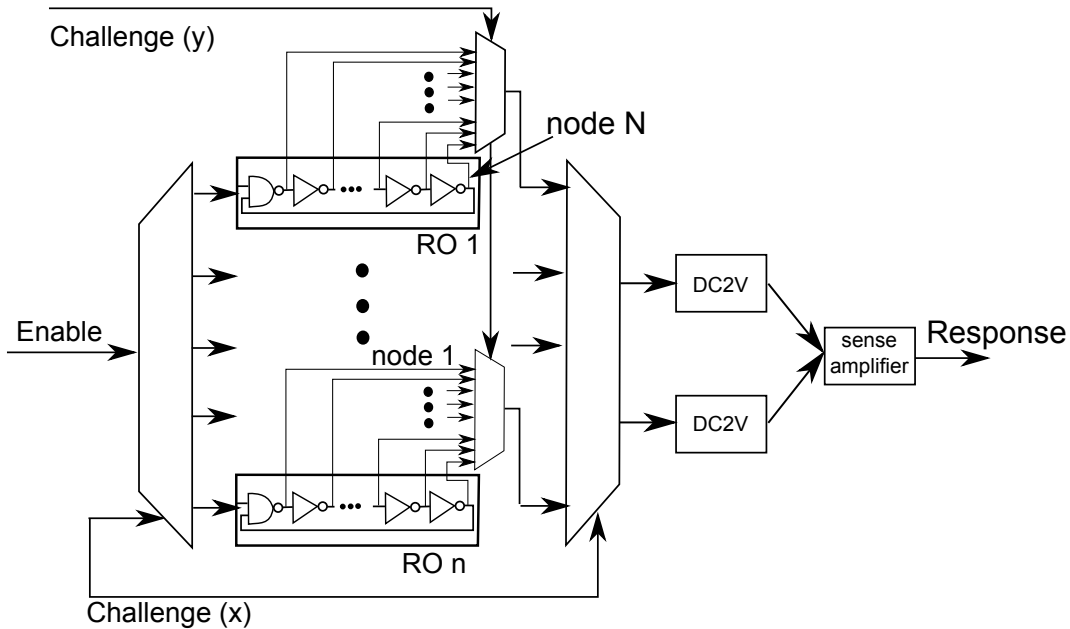


**Figure 6.6:** DC-PUF proposed architecture with  $(N,n)$  CRPs.

- Greater  $\varphi$  implies more area.
- Greater  $N$  decreases the variability of each node.
- Greater  $N$  increases the number of CRPs.

#### 6.4.2 Architecture

The next step to exploit the duty cycle in a DC-PUF is the design of the PUF architecture. We propose a variation of the conventional RO-PUF [SD07] that is depicted in Figure 6.6. The elements that make the complete system are:

- An  $N$  decoder that enables a pair of ring oscillators to generate the response.
- $n$  identical  $N$ -stage K-rate ring oscillators with  $\varphi \neq 1$ .
- $n$   $N$ -input multiplexers to select the internal node of ring oscillators.
- An  $N$ -to-2 demultiplexer to drive the output of ring oscillators to the response generator.
- Two Duty Cycle to Voltage Converters (DC2V) that generate a voltage dependent on the input duty cycle.

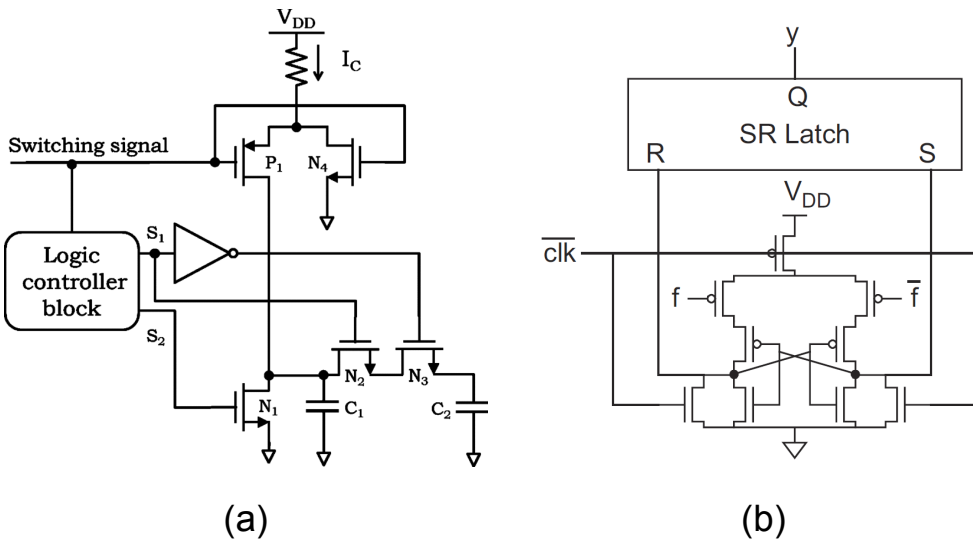


**Figure 6.7:** Response generator blocks: a) DC2V converter [VAFK14], b) Sense amplifier [WH11].

- A sense amplifier that clamps the bit response to one of the bias rails depending on the relationship of the inputs.

The challenge of our PUF architecture is formed by a pair of values  $(x, y)$ .  $x$  selects the node of the ring oscillators that will be evaluated and therefore it is a value between 1 and  $N$ .  $y$  is used to select the pair of ring oscillators whose nodes are selected, so it is a number between 1 and  $n$ . Therefore the challenge consists of a word with a maximum limit of bits of  $\log_2(N) + \log_2(n)$ . The response of this particular implementation is a single bit like the RO-PUF response.

The generation of the response is implemented with two different blocks. The first block is a DC2V converter. This circuit is based on the proposed block in [VAFK14]. The schematic of the circuit is depicted Figure 6.7 (a). This circuit generates an output proportional to the duty cycle of the input by charging and discharging the capacitances  $C_1$  and  $C_2$ . It works at three different stages. The first stage charges the capacitor  $C_1$  while the input signal is high. When it goes low, the charge stored in  $C_1$  is shared between  $C_1$  and  $C_2$ . And just before the next edge of the input  $C_1$  is discharged. After a few cycles, the voltage stored at  $C_2$  stays steady and proportional to the duty cycle.

The last block is a sense amplifier. This block is based on a conventional sense amplifier of Figure 6.7 (b) explained in [WH11]. This circuit drives the output to gnd or VDD depending on which of the inputs is greater. Therefore, a minimum difference between the output of both DC2V converters is amplified to generate the final bit response.

Hence our proposal requires more resources than the traditional RO-PUF but it multiplies the number of CRPs by up to  $N$  for the same number of ring oscillators, or it is able

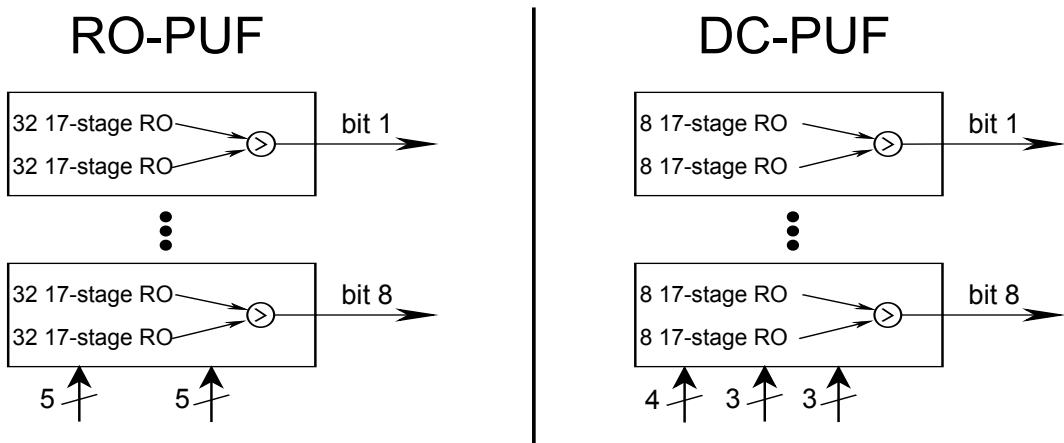


**Figure 6.8:** Simulation Set-Up for the characterization of the RO-PUF and the DC-PUF.

to offer the same number of CRPs with a number of ring oscillator divided by up to  $N$ . Therefore, both goals sought with the use of duty cycle instead of frequency (increasing the CRP and improving the reliability) have proven being theoretically correct.

## 6.5 Simulation Results

The validation of the proposed DC-PUF was carried out with circuit simulations. These simulations were made with the models of 40 nm commercial technology. First of all, we will describe the system we simulated to generate the data set to validate our hypothesis. The diagram of the tested PUFs is depicted in Figure 6.8. Two different PUFs have been implemented in order to be able to compare a conventional RO-PUF to our new approach, the DC-PUF.

Both types of PUF share the CRP morphology, the challenge is a 10 bit word and the response is a 8 bit word. The generation of the responses is made by simulating 8 identical PUF devices in parallel where each instance generates one bit. However the bits of the challenges are used in a different way depending on the type of PUF. In the implemented RO-PUF, the 10 input bits are divided into two different groups. The first 5 bits select the first ring oscillator of a subset formed by half the ring oscillators. And the second group of 5 bits selects the other ring oscillator within the other half of ring oscillators. Therefore each subset of ring oscillators is made of 32 instances and the total PUF is made of 512 ring oscillators. All of them are implemented with a 17-stage ring oscillator.

On the other hand, the generation of the responses in the DC-PUF is slightly different. The first 4 bits are used to select the node of each 17-stage ring oscillator asymmetrically designed with  $\varphi = 4$ , while the other 6 bits work like the bits in the RO-PUF but with subsets made of 8 ring oscillator instances. The result is that for the same number of CRPs,

the number of ring oscillators are  $N$  times less, where  $N$  is the number of bits required to select the internal node. As a consequence, the proposed DC-PUF saves resources while keeping the number of CRPs.

At the same time that the instances are replicated to generate an 8 bit response, the simulations are based on a Monte Carlo analysis that introduces the process and mismatch variations for 100 different implementations of each of the PUFs under test. To summarize, the data set is made of:

- $2^{10}$  different CRPs.
- 100 8-bit RO-PUF.
- 100 8-bit DC-PUF.
- The RO-PUF is made of 512 17-stage ring oscillators.
- The DC-PUF is made of 128 17-stage ring oscillators.

### 6.5.1 Randomness

The desirable feature that a PUF must fulfill is the randomness. As was previously introduced, the randomness of PUFs is measured by the uniqueness, uniformity and bit aliasing of their responses which were defined in Equations (6.1), (6.2) and (6.3). According to those definitions and using the complete data set generated by the simulations of both types of PUF, the results of all of those three parameters are plotted in Figure 6.9.

The histograms represent the number of occurrences among the 1024 CRP calculations that correspond to that value in uniqueness and uniformity parameters and the average value for a specific response for bit aliasing (it is bit by bit defined in Equation 6.3).

In terms of uniqueness and uniformity the comparison is very similar. In both cases, the RO-PUF seems to present a better performance than the DC-PUF because the number of parameter evaluations that are in the interval 49-51% is 7% bigger. However, in terms of Bit Aliasing, the DC-PUF outperforms the RO-PUF. The 90% of Bit Aliasing samples are in the range 49-51%. Even though there are differences between both implementations, the results of both architectures are quite good to implement a robust PUF. So, our proposal of using the duty cycle measurements instead of output frequencies is feasible and comparable in terms of security characterization.

### 6.5.2 Reliability

After the randomness of the DC-PUF has been tested, the next figure of merit to explore our proposal is the reliability. Moreover, the improvement of the reliability is the main

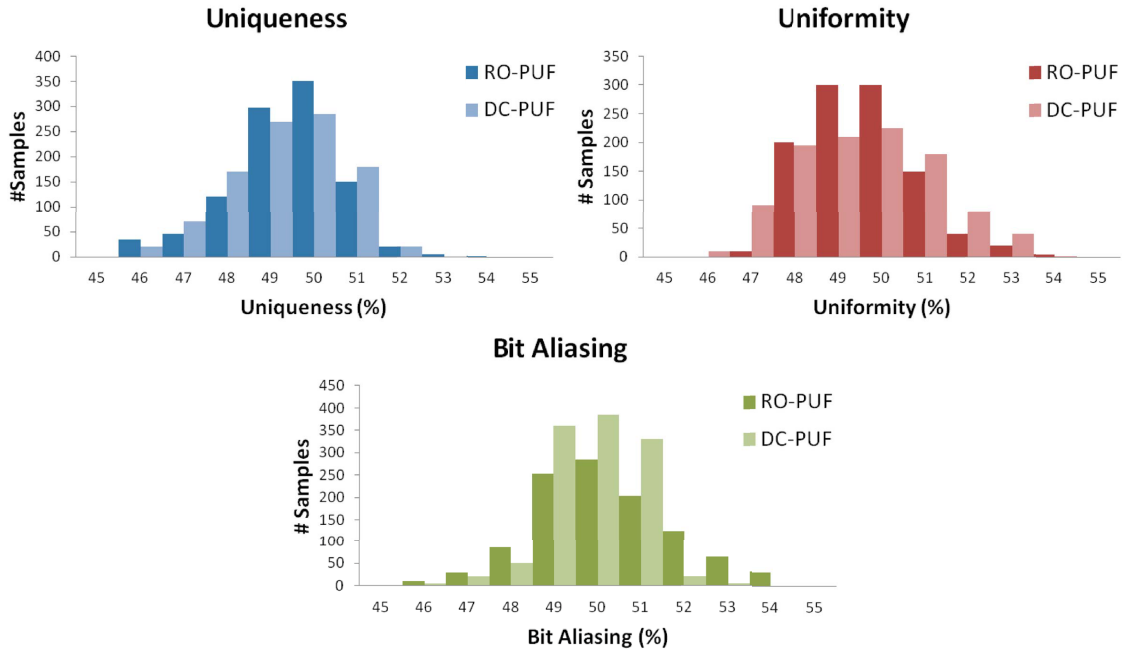


**Figure 6.9:** Randomness of the RO-PUF and the DC-PUF implemented in simulations.

reason why we propose to change the traditional perspective of RO-PUF where the output is based on measuring an absolute magnitude, to the DC-PUF where the response is generated based on the relative magnitude of the duty cycle. As was analytically explained in Section 6.4.1, this point is *a priori* feasible.

The simulations carried out are based on the same devices and architectures of RO-PUF and DC-PUF used in the previous section but modifying the environmental variables of temperature, bias voltage and radiation. These three variables were analyzed independently, only one of them changes at a time while the other two stay at their nominal values. In the case of our technology, the nominal bias voltage is 1.1 V, the nominal temperature is 25 °C and the nominal radiation dose is 0 rad.

In order to clarify how the environmental variables are a source of unreliability for PUFs, we are going to explain how the temperature simulations were made and how the bit flips are produced. The temperature tests are summarized and simplified in Figure 6.10. As was previously introduced, the data set is made of 100 identical instances of 1024 CRPs with 8-bit responses. This amount of data is impossible to be clearly represented in a single figure, hence in Figure 6.10 only 10 ring oscillators are plotted to ease the visibility of the effects.

First, in Figure 6.10 (a) the frequency of the ring oscillators is monitored for a temperature range from -50 °C to 100 °C. In this figure, it is evident how for different implementations, the variability introduced by process is translated into different sensitivities of

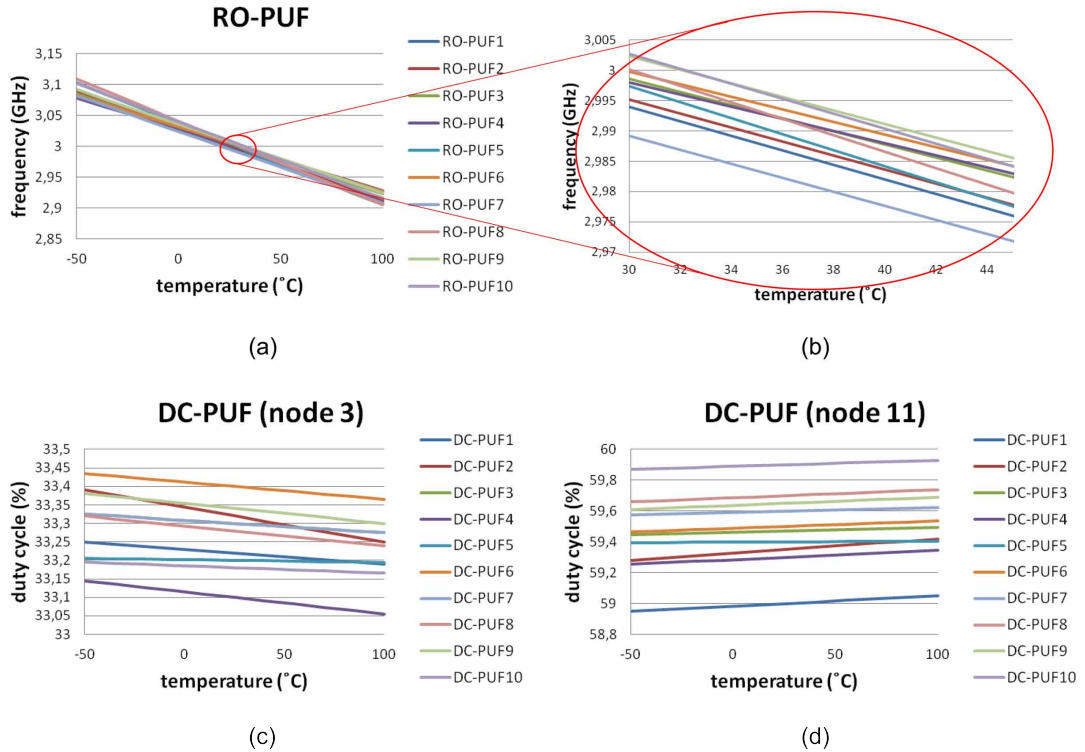


**Figure 6.10:** Temperature results of simulations carried out to characterize the reliability of RO-PUFs and DC-PUFs.

frequency with respect to temperature. Figure 6.10 (b) is a zoom in the region of 30 °C to 45 °C. In this figure, we can see how the instances RO-PUF6 and RO-PUF8 crossed. If two lines are crossed, it means that the response generated with that pair of ring oscillators will flip as was presented in Figure 6.3. Therefore, it will affect the reliability of the PUF.

Figures 6.10 (c) and (d) represent the duty cycle of 10 ring oscillators at nodes 3 and 11 respectively. As can be seen, for the same temperature variation, the variation of the duty cycle is less than  $\pm 0.1\%$  from the nominal value while the frequency varies more than  $\pm 4\%$ . At the same time, the stability of this magnitude makes that there is only one flip of lines among the 10 measurements of ring oscillators while with frequency, there are more. Furthermore, there are no relationship between duty cycles at nodes 3 and 11, therefore the duty cycle at different nodes does not imply any correlation from one node to another, what would become less robust against side channel attacks.

The other two environmental variables are tested in the same way. The bias voltage is simulated for a range of  $\pm 10\%$  of the nominal value (1.1 V). And for the radiation dose, the PUFs are simulated for a dose from 0 to 1 Mrad. The simulation of the radiation dose has been carried out using the same technique that the used for the sensor in Chapter 3. We have used the results of the characterization of a similar technology of 65 nm [BVA<sup>+</sup>12]

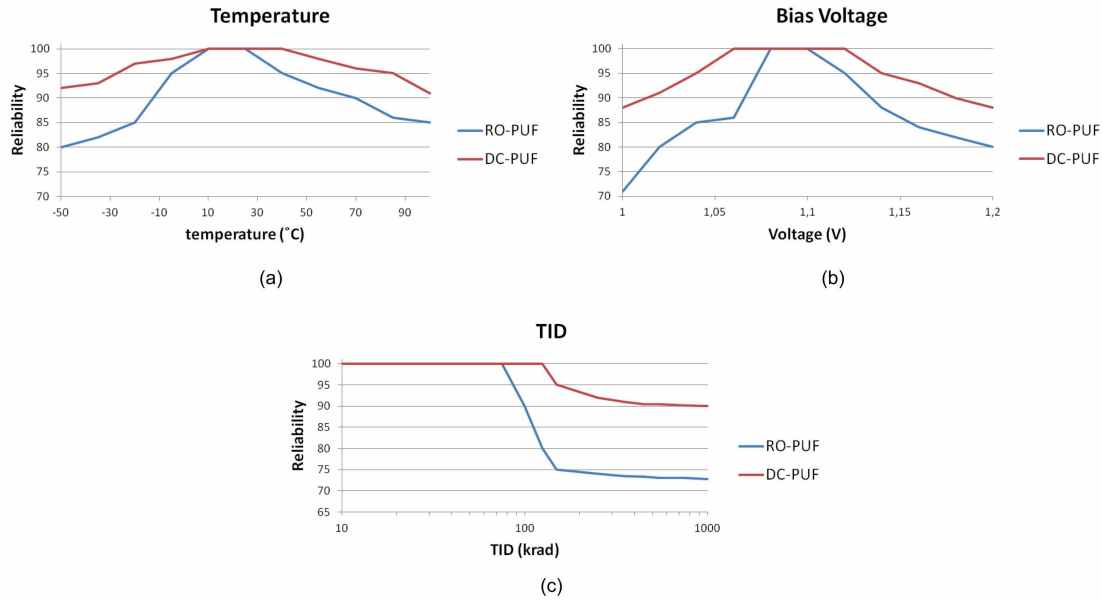


**Figure 6.11:** Reliability of RO-PUF and DC-PUF for temperature, bias voltage and radiation dose variation.

to shift the threshold voltage,  $V_t$ , and the leakage current of CMOS transistors.

The results of the three different types of reliability analysis are presented in Figure 6.11. In these plots, at nominal conditions, the reliability is considered 100% due to the fact that in simulations there is no option to make different measurements of the same conditions with different results. However, in real implementations, this case can be less than 100%. As can be seen, the DC-PUF outperforms the traditional RO-PUF in terms of reliability. In all of the three different scenarios it is more robust against the variation of environmental variables with an improvement of more than 20% at the worst case in radiation dose simulation. According to the simulation results, it is clear that the improvement of using a relative variable instead of an absolute one outperforms the reliability of the system for the variation of environmental parameters.

### 6.5.3 Robustness

In terms of robustness, the DC-PUF proposal is similar to the traditional RO-PUF. As it is a silicon and intrinsic PUF, both are good against passive, active and replace attacks. However, the strong characteristic of the DC-PUF, with a much higher number of CRPs makes that model attacks are much more difficult than the attacks to the RO-PUF. The quantitative study of the robustness of our proposal will be carried out with the manufactured proof of concept explained in the next Section.

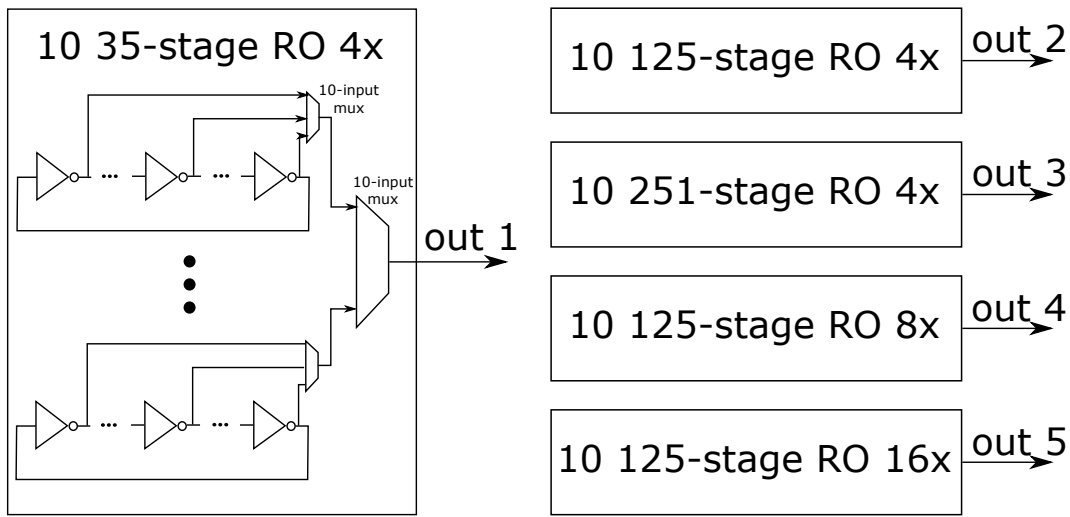


**Figure 6.12:** Diagram of the implemented test architecture for DC-PUF exploration.

## 6.6 Proof of concept

Simulations have supported the use of duty cycle for the DC-PUF. To validate them, we have fabricated a chip with a set of asymmetrical ring oscillators. It is a proof of concept to explore the duty cycle characteristics and reliability in real circuits beyond the possible inaccuracies and simplifications made by simulations. It has been implemented with the same 40 nm technology used for simulations.

Instead of fabricating a complete DC-PUF, we have implemented independent ring oscillators with different configurations to compare their performance and potential to be included in the DC-PUF architecture proposed in Section 6.4.2. The test structure follows the scheme of Figure 6.12. It is made of 50 different ring oscillators divided into 5 groups:

- 10 35-stage ring oscillators with  $\varphi = 4$ .
- 10 125-stage ring oscillators with  $\varphi = 4$ .
- 10 251-stage ring oscillators with  $\varphi = 4$ .
- 10 125-stage ring oscillators with  $\varphi = 8$ .
- 10 125-stage ring oscillators with  $\varphi = 16$ .

Each group of ring oscillators drives only one output. Therefore two stages of multiplexers have been designed. The first stage selects one node out of 10 possibilities and the second stage selects one ring oscillator out of the 10 implemented. Therefore, the amount of duty cycle measurements per chip is 500 (10 nodes x 10 ring oscillators x 5 groups).

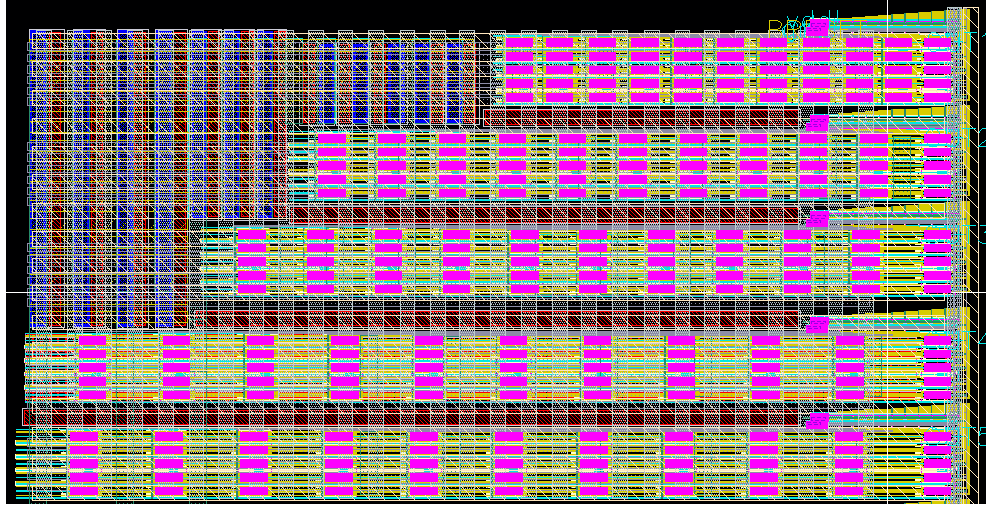


**Figure 6.13:** Layout of the fabricated proof of concept for the duty cycle exploration.

Figure 6.13 is the layout of the implemented test circuit. In this figure we can see the distribution and the resources needed for each group of ring oscillators. With all data, the goal is to analyze the randomness and the reliability of the duty cycle based PUF and to compare these results against simulations.

So far, the implementation of the proof of concept has been fabricated. The next step will be to completely characterize those designs. This process will be implemented following the same scheme used for the characterization of the sensor presented in Section 3.4.3 and the characterization of the SET tolerant ring oscillator in Section 4.7.1. The tests of the DC-PUF will use the same measurement hardware (Xilinx FPGA board Virtex5 ML505, the Agilent MSO9051 oscilloscope and a PC) than the previous tests. The breadboard and test boards are different and adapted to the implemented 40 nm chip.

## 6.7 Conclusions

In this chapter we have presented a novel approach for a ring oscillator based Physically Unclonable Function. First we have summarized the state of the art of these security primitives by outlining the different types of PUFs and their characteristic. And we have also introduced the most extended quality factors used for measuring and comparing different PUF approaches. Then we have focused on RO-PUFs as one of the most mature and developed architectures for implementing this type of systems.

So far, RO-PUFs have been a silicon, intrinsic and weak PUF that generates the response using the output frequencies of ring oscillators. All the implementations are focused on measuring and comparing the frequencies. This approach has shown two main

disadvantages. The first one is the limited number of CRPs they use for generating their "secret". The second disadvantage is their decreasing reliability as a consequence of the great dependency of ring oscillators frequency on the environmental parameters.

With our new design we address both problems. Our approach is based on the fully configurable duty cycle ring oscillator modeled in Chapter 5. Particularly, we use the *hard* configuration which configures the duty cycle of internal nodes by designing the size of oscillator transistors individually. The reason to use the duty cycle instead of the frequency is because it is a relative magnitude and it is intrinsically more robust against environmental variations. Moreover, using the *hard* configuration, the number of possible CRPs is multiplied by the number of stages of the implemented ring oscillators.

We have explored theoretically the characteristics of the duty cycle that makes our proposal more robust against variations. Additionally to the conventional characterization of PUF reliability against temperature, bias voltage and aging, we have proposed the introduction of radiation absorbed dose as a non-negligible source of unreliability as a consequence of the enhancement of radiation effects due to shrinking of the technology.

We have also simulated our proposed architecture with a 40 nm commercial technology. These simulations have shown a good quality as PUFs and a great improvement in RO-PUF reliability up to 20% in the worst case. We have finally fabricated a chip to validate the proof of concept and the test plan is being designed and implementing for a future characterization.

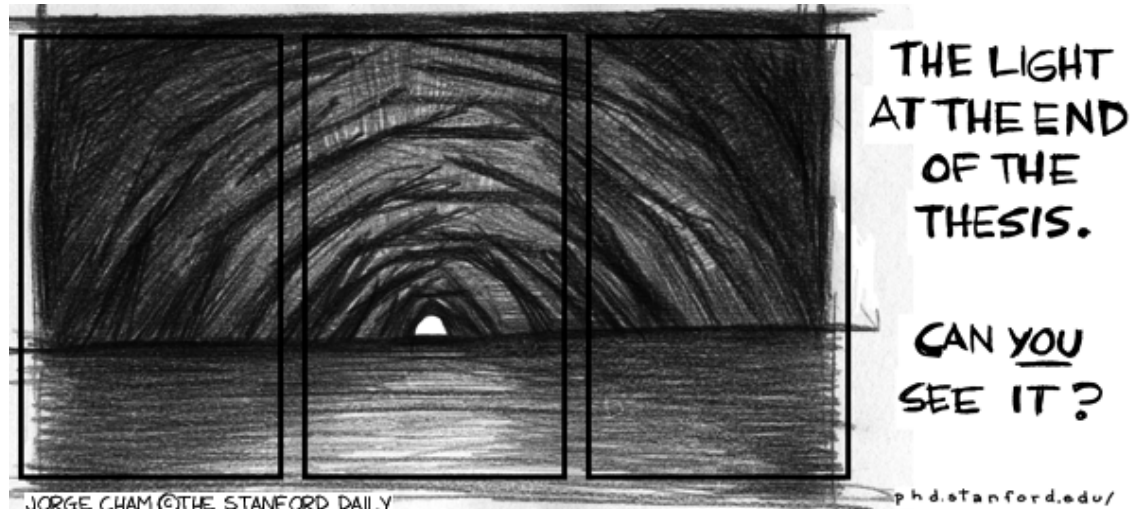
## 6.8 Related Publications

- **J. Agustin** and M. L. Lopez-Vallejo, "*A temperature-independent PUF with a configurable duty cycle of CMOS ring oscillators*," 2016 IEEE International Symposium on Circuits and Systems (ISCAS), Montreal, QC, 2016, pp. 2471-2474. doi: 10.1109/ISCAS.2016.7539093



# Chapter 7

## Conclusions and Future Work



## Chapter 7

# Conclusions and Future Work

*Modeling and Design of Ring Oscillators and their Application in Radiation Environments* is the title of this Thesis and it summarizes the topics addressed in it. As the title says, this work has been focused on the convergence of two complementary subjects: ring oscillators and radiation environments. First, we have generally introduced both themes: the effects of radiation environments in electronics to understand the involved physical interaction, and the structure of ring oscillators to understand their operation. The combination of these two relevant topics has resulted in the original contributions of Chapters 3, 4, 5 and 6.

The first application of ring oscillators within radiation environments we have proposed has dealt with the problem of Total Ionization Dose (TID) in electronic systems. This cumulative effect shifts the nominal performance of electronic devices due to the modification of charge distribution within the structure of semiconductors. Therefore, monitoring the degradation of electronics plays a very important role in radiation applications to ensure the reliability of systems. So far, the most extended devices to perform this task have been the RADFETs. RADFETs have proven to be suitable for many applications but their main drawback is that they only monitor the exposed dose instead of the real absorbed dose. In order to implement a real absorbed dose sensor, we have proposed a new architecture based on ring oscillators. The achievements of this work can be summarized as:

- Modeling and design of a smart sensor. The designed sensor is a self-timed design, fully integrable, digital and with a configurable sensitivity. Its response has been analytically modeled where the absorbed dose has been introduced in the model through experimental results provided by a previous published work.
- Fabrication of the sensor. We have implemented and fabricated the TID sensor with a commercial  $0.35\text{ }\mu\text{m}$  technology. The implementation has divided the area of the sensor into two different parts: the sensitive zone and the control. While the control has used RHBD techniques to minimize the impact of dose in the measurements, the sensitive zone is unhardened in order to maximize the absorption of radiation and increase the sensitivity of the sensor.
- Radiation test and validation. A set of test have also been performed with a  $^{60}\text{Co}$

---

source using the NAYADE facility at CIEMAT. This set of tests swept radiation doses up to 575 krad with a dose rate of 26.51 krad/h. The test has validated the developed model and the hypothesis of using a ring oscillator as the sensitive part of a TID sensor.

- Temperature characterization. The impact of temperature has also been studied due to its influence on our proposal reliability measurements. As a result, we proposed a calibration system and we discussed the utilization of this ring oscillator based sensor in a self-recovery system.

The second design of ring oscillators for radiation applications has addressed the harmonic induced error. This error was introduced and characterized by Chen in [C<sup>+</sup>14]. It is caused by SETs and it is potentially dangerous for every system that uses ring oscillator in radiation environments. It causes a shift in the fundamental frequency of ring oscillator up to higher odd harmonics. This change in operation could be translated into a temporary error or even a SEFI. Our approach to solve these problems breaks with the traditional view of ring oscillators which only considers the output frequency. In order to avoid the harmonic induced error, we designed an asymmetrical ring oscillator whose duty cycle is different from 50% to remove the vulnerability window. Within this topic the main conclusions we draw are:

- We have modeled and designed a SET tolerant ring oscillator. This ring oscillator uses a special design based on asymmetrical configurations of odd pull up and even pull down networks with respect to even pull up and odd pull down. This methodology electrically masks the SET-induced glitches within the ring oscillator loop.
- We have fabricated two types of test vehicle to validate our hypothesis and simulations with a commercial  $0.35\text{ }\mu\text{m}$  technology. Each vehicle is based on modifying the pull up and pull down networks with different techniques. The first one uses the size of transistors to make faster or slower networks while the second approach uses voltage controlled current starved transistors to perform the same task.
- Both implementations have been validated against the Harmonic Induced Error. Instead of validating our proposal with expensive tests using a conventional source of SETs (accelerometers, cyclotrones or pulsed lasers) we have implemented an emulation SET system that infers the third harmonic to the ring oscillator.
- The design we have proposed to solve this particular problem is not only a solution to it but it also opens a new perspective to exploit the duty cycle characteristic of ring oscillators ignored so far.

As an extension of the SET tolerant ring oscillator, we have extensively modeled the duty cycle of ring oscillators. Previous works have been focused only on the frequency of ring oscillators or on the figures of merit of these devices as oscillators (phase noise, jitter, etc.) but none has analyzed their duty cycle. Moreover, systems that require clock signals with configurable duty cycles or different from 50% leave this task to complementary blocks. Opposite to those approaches, our work allows to implement a fully configurable duty cycle ring oscillator without using any additional resource. The conclusions of the developed model can be outlined as:

- We have set the analytical basis for understanding and designing a ring oscillator whose outputs are clock signals with a duty cycle different from 50% and fully-configurable. Our first analysis has revealed the design parameters that can be used to configure the duty cycle.
- According to the revealed parameters, we have developed two different models that agree with the two different implementations of the SET tolerant ring oscillator. One uses different transistor sizes and the other is supported by using different bias voltage schemes.
- The models have been simulated and validated with a commercial 40 nm technology. Many different simulations have been carried out and all of them converge to our model with a maximum deviation of 6% in the worst case and 2% for ring oscillators with high number of stages.
- Additionally to the duty cycle model, we have analyzed two important features: the variation of duty cycle due to PVT variations and the phase noise characteristics of our design. Regarding PVT variations, the duty cycle has shown to be dependent on the size of the ring oscillator and on the asymmetric ratio. The analysis of the phase noise has proven to be consistent with the previous works about this subject applied to the conventional ring oscillators.

Finally we have applied the model of the configurable duty cycle of ring oscillators to a particular application, a Physically Unclonable Function (PUF). This application is not specific of radiation environments, however, as the radiation effects are becoming a concern even at ground level, it is important to consider them for critical applications such as PUFs. As security hardware, the reliability of PUFs cannot be compromised by external factors, but conventional RO-PUFs have not successfully overcome their effects. We have designed and implemented a DC-PUF that outperforms the reliability of RO-PUFs. The achievements we have reached so far with our DC-PUF are:

- We have analyzed the independence of duty cycle against external variations using the developed model based on configuring the duty cycle by individually designing

---

the size of each transistor. This design has shown a high reliability against the worst conditions improving the conventional PUF in more than 20%.

- We have introduced the analysis of radiation dose in the study of PUF reliability, which has not been considered in PUF works so far.
- We have proposed an architecture for the DC-PUF that increments the number of CRPs even for implementations with less resources. Moreover we have fabricated a proof of concept of our proposal in a commercial 40 nm technology to validate our hypothesis of using the duty cycle to improve the reliability of RO-PUFs.

As the main conclusion of this work, we have explored the performance of ring oscillators in radiation environments with the goals of improving their applications and pushing forward their implementations. We have not only accomplished those tasks but we have also developed a new model with the potential to improve the ring oscillator based applications at any circumstance.

Therefore, from the point of view of a circuit designer, we have covered all stages of a design flow, from the modeling to the design, implementation, fabrication, measurement and characterization. And our contributions to the state of the art have been also diverse as the different publications show.

- In the field of modeling, we have proposed an original model of the duty cycle of ring oscillators while the rest of works so far have been focused on the definition of the output frequency. The big contribution of this model is the change of paradigm for the use of ring oscillators. From now, the duty cycle is a new parameter to be exploited in this kind of systems.
- In the field of design, we have made a SEE free ring oscillator design. This design helps to solve a recently presented problem for ring oscillators in radiation environments and it contributes to solve the increasing problem of single event effects in electronics as a consequence of the shrinking technology and increasing operation frequency.
- In terms of implementation, we have improved the implementation of a security hardware system. This contribution is not only restricted to the field of PUFs but it is also applicable to any other implementation of ring oscillators where the reliability against environmental variables is crucial.
- Regarding measurement and characterization, we have created a TID smart sensor that actually measures the absorbed dose of electronics instead of the exposed dose as the rest approaches. These data is important for self-recovery systems in radiation environments as it allow to increase the lifetime of devices and their availability.

## 7.1 Future Work

The work developed in this Thesis is the product of a high effort in research activity whose results have been published in the international conferences and journals pointed out in Section 1.4. We hope that the outputs of our work will inspire other researchers and that our contributions will set the seed of new projects. We would like to put forward some ideas that would continue with our work. We divide these lines depending on the advanced work by this thesis and the estimated time for their development into short-term, medium-term and long-term future works.

### **Short-Term**

In the future short-term work we collect the immediate future work that is a direct extension from this work. Some of these works are:

- Implementation of the TID Smart Sensor in an FPGA device. As mentioned in Chapter 3, the sensor is able to be integrated in all kind of electronic devices. The implementation in an FPGA would generate a valuable information about the effect of radiation in the counter and the pulse generator because in those devices, we will not be able to implement the RHBD techniques we propose in this Thesis.
- Improvement of the ring oscillator duty cycle model. The discussion in Chapter 5 has pointed out how the accuracy of the presented model could be improved by removing some of the simplifications we made to develop the actual model presented in our work.
- We have fabricated a proof of concept of the designed DC-PUF. The future work will be the characterization of the PUF. These tests will be focused on the characterization of the randomness, reliability and robustness. In terms on randomness, we will perform a NIST statistical test suite for randomness [RSN<sup>+</sup>01]. The reliability will take into account the three variables we have simulated in the thesis and we will add the impact of aging in the reliability of PUFs. The aging tests will be performed by an accelerated aging process with temperature and bias voltage stress. Regarding robustness, we will try to foresee the response of PUFs by attacking our fabricated devices with model attacks and power attacks.

### **Medium-Term**

We categorize as medium-term future work those lines that require significant effort to develop them but that they are not enough to generate a new research line.

- Development of an automated tool to analyze the most TID sensitive areas of an electronic chip and to place our integrated TID sensor within a TID monitor network. This topic would be focused on two points. First, it will implement the self-recovery system discussed Section 3.7. Second, the automated tool will be able to integrate the monitor network in any design without adding effort to the design stage and in an optimized topology for each particular implementation.
- Application of the asymmetrical pull down and pull up networks to combinational logic paths to mitigate SETs in RTL designs. SETs are becoming the main concern of radiation effects in modern technologies, therefore new approaches to mitigate them will be necessary for future designs. The same mitigation technique that enhances the removal of a SET in a ring oscillator could be used in a non-feedback combinational path. Some constraints may be taken into account to implement this solution, such as, maximum frequency of the system, critical path, minimum number of gates to apply the measurements, etc.
- The duty cycle model has opened the possibility of changing the paradigm of ring oscillators from frequency sources to duty cycle. This model can be applied to many of the traditional applications based on ring oscillators, for example, True Random Number Generators, Pulse Width Modulators or Time to Digital Converters. The possibility of individually configuring the duty cycle of each node within a ring oscillator change makes possible the generation of new devices such as a Linearization Readout System or a Configured Function Generator.

### Long-Term

We refer as long-term future works those new research lines able to generate new full projects.

- Impact of new technologies in the accuracy of gate delay and duty cycle ring oscillator models. The last fabrication nodes are pushing the silicon based technologies to the limit of physics. During the last decade, many different proposals have been developed to replace the traditional silicon CMOS devices for new materials and structures. For example, the first approach to continue with Moore's law was the use of FinFETs. Among the new alternative technologies would be the carbon nanotubes transistors or different heterojunctions materials such as III-V semiconductors. In these new proposals, the previous models of transistor current differ from actual models, and their accuracy impact on the theoretical gate delay of each technology. This parameter has fixed the maximum frequency of a particular technology since the beginning of semiconductor industry. The accuracy of new technology models

will also impact in the accuracy of our proposed model of ring oscillators and it must be taken into account.

- Standardization of radiation hardening in the definition of standard libraries for commercial technologies. The development of standard cell libraries supposed a huge step in the evolution of semiconductor industry. It allowed the implementation of extremely complex designs in a short time thanks to the automated tools that synthesize, place and route a particular solution. In this context, the open source Liberty library modeling format is the semiconductor industry's most widely supported library standard. In order to introduce the radiation variable in the automated design flow, we propose the introduction of this process in the definition of the Liberty standard. With this approach, it would be possible an automated design process of a design with a configurable radiation hardened level.
- Security hardware attacks inducing radiation effects. In this Thesis we have seen how radiation modifies the reliability of PUFs. This weakness of PUFs can be extrapolated to other security systems and it can also be useful to attack them. In this line, radiation effects could be used to compromise the security of those systems. For example, the TID effects could modify the challenge response pair of a particular system to break the system or to replace an original system by a corrupt one. And SEEs could individually control the value of a particular node if the impact of a particle is completely controlled in time and area.

---

## References

- [A<sup>+</sup>06] Asad Abidi et al. Phase noise and jitter in CMOS ring oscillators. *Solid-State Circuits, IEEE Journal of*, 41(8):1803–1816, 2006.
- [ADK99] S. K. Antiochos, C. R. DeVore, and J. A. Klimchuk. A Model for Solar Coronal Mass Ejections. *The Astrophysical Journal*, 510(1):485, 1999.
- [AG11] Karim Abdelhalim and Roman Genov. Cmos dac-sharing stimulator for neural recording and stimulation arrays. In *IEEE International Symposium on Circuits and Systems (ISCAS), 2011*, pages 1712–1715. IEEE, 2011.
- [AHG<sup>+</sup>13] J. R. Ahlbin, N. C. Hooten, M. J. Gadlage, J. H. Warner, S. P. Buchner, D. McMorrow, and L. W. Massengill. Identification of pulse quenching enhanced layouts with subbandgap laser-induced single-event effects. In *Reliability Physics Symposium (IRPS), 2013 IEEE International*, pages 6C.2.1–6C.2.6, April 2013.
- [AHM03] Clive M Alabaster, Evan J Hughes, and John H Matthew. Medium prf radar prf selection using evolutionary algorithms. 39(3):990–1001, 2003.
- [ARH<sup>+</sup>15] L Artola, NJ-H Roche, G Hubert, A Al Youssef, A Khachatrian, P McMarr, and H Hughes. Analysis of Angular Dependence of Single-Event Latchup Sensitivity for Heavy-Ion Irradiations of CMOS Technology. *IEEE Transactions on Nuclear Science*, 62(6):2539–2546, 2015.
- [Bar06] H.J. Barnaby. Total-Ionizing-Dose Effects in Modern CMOS Technologies. *Nuclear Science, IEEE Transactions on*, 53(6):3103–3121, Dec 2006.
- [Bau05a] R. C. Baumann. Radiation-induced soft errors in advanced semiconductor technologies. *IEEE Transactions on Device and Materials Reliability*, 5(3):305–316, Sept 2005.
- [Bau05b] Robert Baumann. Soft errors in advanced computer systems. *IEEE Design & Test of Computers*, 22(3):258–266, 2005.
- [BCF<sup>+</sup>11] G Bianchi, N Costantino, L Fanucci, J Incandela, G Magazzu, C Tongiani, and S Saponara. Radiation tolerant IP Cores for the control and readout of Front-End electronics in High Energy Physics experiments. In *Nuclear Science Symposium and Medical Imaging Conference (NSS/MIC), 2011 IEEE*, pages 2124–2127. IEEE, 2011.
- [BD13] M Buchvarova and D Draganov. Cosmic-ray spectrum approximation model: experimental results and comparison with other models. *Solar physics*, 284(2):599–614, 2013.
- [BEM<sup>+</sup>06] JM Benedetto, PH Eaton, DG Mavis, M Gadlage, and T Turflinger. Digital single event transient trends with technology node scaling. *IEEE Transactions on Nuclear Science*, 53(6):3462–3465, 2006.

- [BG15] Marta Bagatin and Simone Gerardin. *Ionizing Radiation Effects in Electronics: From Memories to Imagers*, volume 50. CRC Press, 2015.
- [BK<sup>+</sup>14] Georg T Becker, Raghavan Kumar, et al. Active and Passive Side-Channel Attacks on Delay Based PUF Designs. *IACR Cryptology ePrint Archive*, 2014:287, 2014.
- [BM09] Musard Balliu and Isabella Mastroeni. A weakest precondition approach to active attacks analysis. In *Proceedings of the ACM SIGPLAN Fourth Workshop on Programming Languages and Analysis for Security*, pages 59–71. ACM, 2009.
- [BMPM13] S. P. Buchner, F. Miller, V. Pouget, and D. P. McMorrow. Pulsed-laser testing for single-event effects investigations. *IEEE Transactions on Nuclear Science*, 60(3):1852–1875, June 2013.
- [BNK98] L Bisdounis, S Nikolaidis, and O Koufopavlou. Analytical transient response and propagation delay evaluation of the cmos inverter for short-channel devices. *IEEE Journal of Solid-State Circuits*, 33(2):302–306, 1998.
- [BRW<sup>+</sup>15] D. A. Black, W. H. Robinson, I. Z. Wilcox, D. B. Limbrick, and J. D. Black. Modeling of single event transients with dual double-exponential current sources: Implications for logic cell characterization. *IEEE Transactions on Nuclear Science*, 62(4):1540–1549, Aug 2015.
- [BS97] Eli Biham and Adi Shamir. Differential fault analysis of secret key cryptosystems. In *Annual International Cryptology Conference*, pages 513–525. Springer, 1997.
- [BSA<sup>+</sup>05] J. D. Black, A. L. Sternberg, M. L. Alles, A. F. Witulski, B. L. Bhuva, L. W. Massengill, J. M. Benedetto, M. P. Baze, J. L. Wert, and M. G. Hubert. HBD layout isolation techniques for multiple node charge collection mitigation. *IEEE Transactions on Nuclear Science*, 52(6):2536–2541, Dec 2005.
- [BSH75] D Binder, EC Smith, and AB Holman. Satellite anomalies from galactic cosmic rays. *IEEE Transactions on Nuclear Science*, 22(6):2675–2680, 1975.
- [BVA<sup>+</sup>12] S Bonacini, P Valerio, R Avramidou, R Ballabriga, F Faccio, K Kloukinas, and A Marchioro. Characterization of a commercial 65 nm CMOS technology for SLHC applications. *Journal of Instrumentation*, 7(01):P01015, 2012.
- [BX08] Sebastien Bourdarie and Michael A Xapsos. The space radiation environment. 2008.
- [C<sup>+</sup>14] Yongpin P Chen et al. Single-Event Transient Induced Harmonic Errors in Digitally Controlled Ring Oscillators. 61(6):3163–3170, Dec 2014.
- [Cas10] Megan Colleen Casey. *Single-event Effects in Digital CMOS Circuits Operating at Ultra-low Power*. PhD thesis, Vanderbilt University, Nashville, TN, 2010.
- [CBDN14] Luca Cassano, Alberto Bosio, and Giorgio Di Natale. A novel adaptive fault tolerant flip-flop architecture based on TMR. In *2014 19th IEEE European Test Symposium (ETS)*, pages 1–2. IEEE, 2014.
- [CBN<sup>+</sup>09] Megan C Casey, Bharat L Bhuva, Sarah A Nation, Oluwole A Amusan, T Daniel Loveless, Lloyd W Massengill, Dale McMorrow, and Joseph S Melinger. Single-event effects on ultra-low power CMOS circuits. In *IEEE International Reliability Physics Symposium*, pages 194–198, Apr 2009.
- [CCC<sup>+</sup>94] DL Chenette, J Chen, E Clayton, TG Guzik, JP Wefel, M Garcia-Munoz, C Lopate, KR Pyle, KP Ray, EG Mullen, et al. The CRRES/SPACERAD heavy ion model of the environment (CHIME) for cosmic ray and solar particle effects on electronic and biological systems in space. *IEEE Transactions on Nuclear Science (Institute of Electrical and Electronics Engineers);(United States)*, 41(CONF-940726–), 1994.
- [CCS<sup>+</sup>14] J. S. Chang, K. S. Chong, W. Shu, T. Lin, J. Jiang, N. K. Z. Lwin, and Y. Kang. Radiation-hardened library cell template and its total ionizing dose (TID) delay characterization in 65nm CMOS process. In *2014 IEEE 57th International Midwest Symposium on Circuits and Systems (MWSCAS)*, pages 821–824, Aug 2014.
- [CCSP11] Poki Chen, Shou-Chih Chen, You-Sheng Shen, and You-Jyun Peng. All-Digital Time-Domain Smart Temperature Sensor With an Inter-Batch Inaccuracy of After One-Point Calibration. *Circuits and Systems I: Regular Papers, IEEE Transactions on*, 58(5):913–920, 2011.

- [CCTM16] Carlos Colodro-Conde and Rafael Toledo-Moreo. "Improving the Implementation of EDAC Functions in Radiation-Hardened FPGAs", pages 189–200. Springer International Publishing, Cham, 2016.
- [Che15] An Chen. Utilizing the variability of resistive random access memory to implement reconfigurable physical unclonable functions. *IEEE Electron Device Letters*, 36(2):138–140, 2015.
- [CLC09] Steven Chingyei Chung, S Lu, and Shengyong Chen. Nonlinear feedback system for an inverter-based ring oscillator. In *WSEAS International Conference. Proceedings. Mathematics and Computers in Science and Engineering*, number 8. World Scientific and Engineering Academy and Society, 2009.
- [CLI<sup>+</sup>09] S. Carbonetto, J. Lipovetzky, M.G. Inza, E. Redin, and A Faigon. Ring oscillators response to irradiation and application to dosimetry. In *Micro-Nanoelectronics, Technology and Applications, 2009. EAMTA 2009. Argentine School of*, pages 1–4, Oct 2009.
- [CLS15] Ying Cao, Paul Leroux, and Michiel Steyaert. Radiation Hardened by Design. In *Radiation-Tolerant Delta-Sigma Time-to-Digital Converters*, pages 25–38. Springer, 2015.
- [CLT<sup>+</sup>14] D. Cardoza, S. D. LaLumondiere, M. A. Tockstein, D. L. Brewe, N. P. Wells, R. Koga, K. M. Gaab, W. T. Lotshaw, and S. C. Moss. Comparison of single event transients generated by short pulsed x-rays, lasers and heavy ions. *IEEE Transactions on Nuclear Science*, 61(6):3154–3162, Dec 2014.
- [CLZ12] Ralph K Cavin, Paolo Lugli, and Victor V Zhirnov. Science and engineering beyond Moore’s law. *Proceedings of the IEEE*, 100(Special Centennial Issue):1720–1749, 2012.
- [CM03] David Czajkowski and Merrick McCartha. Ultra low-power space computer leveraging embedded SEU mitigation. In *Proc. IEEE Aerospace Conf*, volume 5, pages 2315–2328, 2003.
- [CNV96] T. Calin, M. Nicolaidis, and R. Velazco. Upset hardened memory design for submicron CMOS technology. *IEEE Transactions on Nuclear Science*, 43(6):2874–2878, Dec 1996.
- [Con94] E. E. Conrad. Radiation effects research in the 60’s. *IEEE Transactions on Nuclear Science*, 41(6):2648–2659, Dec 1994.
- [Cre13] J. D. Cressler. Radiation Effects in SiGe Technology. *IEEE Transactions on Nuclear Science*, 60(3):1992–2014, June 2013.
- [CRL<sup>+</sup>03] K. A. Clark, A. A. Ross, H. H. Loomis, T. R. Weatherford, D. J. Fouts, S. P. Buchner, and D. McMorrow. Modeling single-event effects in a complex digital device. *IEEE Transactions on Nuclear Science*, 50(6):2069–2080, Dec 2003.
- [DCHB83] JAMES T Diehl, ROBERT F Cali, NORMAN R Hertzler, and EDWIN G Beven. Complications of abdominal aortic reconstruction. An analysis of perioperative risk factors in 557 patients. *Annals of surgery*, 197(1):49, 1983.
- [DGA14] Igor A Danilov, Maxim S Gorbunov, and Andrey A Antonov. SET tolerance of 65 nm CMOS majority voters: a comparative study. *IEEE Trans Nucl Sci*, 61:1597–1602, 2014.
- [DPMT<sup>+</sup>11] PO Lucas De Peslouan, Cédric Majek, Thierry Taris, Yann Deval, Didier Belot, and Jean-Baptiste Begueret. A new frequency synthesizers stabilization method based on a mixed Phase Locked Loop and Delay Locked Loop architecture. In *Circuits and Systems (ISCAS), 2011 IEEE International Symposium on*, pages 482–485. IEEE, 2011.
- [Dre89] Paul V Dressendorfer. Radiation effects on MOS devices and circuits. *Ionizing Radiation Effects in MOS Devices and Circuits*, edited by TP Ma and Paul V. Dressendorfer, John Wiley & Sons, New York, pages 256–332, 1989.
- [DS03] Stephen Docking and Manoj Sachdev. A method to derive an equation for the oscillation frequency of a ring oscillator. *IEEE Transactions on Circuits and Systems I: Fundamental Theory and Applications*, 50(2):259–264, 2003.

- [dSFdSR<sup>+</sup>13] L. N. de Souza Fino, M. A. Guazzelli da Silveira, C. Renaux, D. Flandre, and S. P. Gimenez. Total ionizing dose effects on the digital performance of irradiated octo and conventional fully depleted soi mosfet. In *Radiation and Its Effects on Components and Systems (RADECS), 2013 14th European Conference on*, pages 1–4, Sept 2013.
- [DSH00] P. Dudek, S. Szczepanski, and J.V. Hatfield. A high-resolution CMOS time-to-digital converter utilizing a Vernier delay line. *Solid-State Circuits, IEEE Journal of*, 35(2):240–247, Feb 2000.
- [DSR<sup>+</sup>15] Jayita Das, Kevin Scott, Srinath Rajaram, Drew Burgett, and Sanjukta Bhanja. MRAM PUF: A novel geometry based magnetic PUF with integrated CMOS. *IEEE Transactions on Nanotechnology*, 14(3):436–443, 2015.
- [DWB<sup>+</sup>07] S DasGupta, AF Witulski, BL Bhuva, ML Alles, RA Reed, OA Amusan, JR Ahlbin, RD Schrimpf, and LW Massengill. Effect of well and substrate potential modulation on single event pulse shape in deep submicron cmos. *IEEE Transactions on Nuclear Science*, 6(54):2407–2412, 2007.
- [EAP<sup>+</sup>14] Michela Esposito, Thalis Anaxagoras, Tony Price, Spyros Manolopoulos, Philip Evans, Kevin Wells, Nigel Allinson, et al. Ionizing and non Ionizing radiation damage in a large area CMOS active pixel sensor for medical applications. *IEEE Transactions on Nuclear Science*, 2014.
- [EGVFC<sup>+</sup>12] Luis Entrena, Mario Garcia-Valderas, Raul Fernandez-Cardenal, Almudena Lindoso, Marta Portela, and Celia Lopez-Ongil. Soft error sensitivity evaluation of microprocessors by multilevel emulation-based fault injection. 61(3):313–322, Mar 2012.
- [EHA<sup>+</sup>15] D. Englisch, M. Horstmann, S. Athanasiou, R. J. E. Jansen, and B. Glass. Measurement of set injected charge from a californium-252 source in 340 nm straight and enclosed layout nmos and pmos transistors. In *2015 15th European Conference on Radiation and Its Effects on Components and Systems (RADECS)*, pages 1–4, Sept 2015.
- [ES08] AS Elwakil and KN Salama. Nonlinear models of some ring oscillators. In *Circuits and Systems and TAISA Conference, 2008. NEWCAS-TAISA 2008. 2008 Joint 6th International IEEE Northeast Workshop on*, pages 217–220. IEEE, 2008.
- [ESK<sup>+</sup>15] O. Elhadidy, S. Shakib, K. Krenek, S. Palermo, and K. Entesari. A Wide-Band Fully-Integrated CMOS Ring-Oscillator PLL-Based Complex Dielectric Spectroscopy System. *Circuits and Systems I: Regular Papers, IEEE Transactions on*, 62(8):1940–1949, Aug 2015.
- [EU04] Yalcin Alper Eken and John P Uyemura. A 5.9-GHz voltage-controlled ring oscillator in 0.18- $\mu\text{m}$  CMOS. *Solid-State Circuits, IEEE Journal of*, 39(1):230–233, 2004.
- [FCMG13] V. Ferlet-Cavrois, L. W. Massengill, and P. Gouker. Single event transients in digital cmos;a review. *IEEE Transactions on Nuclear Science*, 60(3):1767–1790, June 2013.
- [FCPM<sup>+</sup>07] V. Ferlet-Cavrois, P. Paillet, D. McMorrow, N. Fel, J. Baggio, S. Girard, O. Duhamel, J. S. Melinger, M. Gaillardin, J. R. Schwank, P. E. Dodd, M. R. Shaneyfelt, and J. A. Felix. New insights into single event transient propagation in chains of inverters;evidence for propagation-induced pulse broadening. *IEEE Transactions on Nuclear Science*, 54(6):2338–2346, Dec 2007.
- [FSF<sup>+</sup>11] K. Fruhashi, M. Shiozaki, A. Fukushima, T. Murayama, and T. Fujino. The arbiter-PUF with high uniqueness utilizing novel arbiter circuit with Delay-Time Measurement. In *Circuits and Systems (ISCAS), 2011 IEEE International Symposium on*, pages 2325–2328, May 2011.
- [FSWG93] J Feynman, G Spitale, J Wang, and S Gabriel. Interplanetary proton fluence model: JPL 1991. *Journal of Geophysical Research: Space Physics*, 98(A8):13281–13294, 1993.
- [GAN<sup>+</sup>10] M. J. Gadlage, J. R. Ahlbin, B. Narasimham, B. L. Bhuva, L. W. Massengill, R. A. Reed, R. D. Schrimpf, and G. Vizkelethy. Scaling trends in set pulse widths in sub-100 nm bulk cmos processes. *IEEE Transactions on Nuclear Science*, 57(6):3336–3341, Dec 2010.

- [GAS10] Xiaoqing Ge, Murat Arcak, and Khaled N Salama. Nonlinear analysis of ring oscillator and cross-coupled oscillator circuits. *Dynamics of Continuous, Discrete and Impulsive Systems Series B: Applications and Algorithms*, 2010.
- [GCvDD02] Blaise Gassend, Dwaine Clarke, Marten van Dijk, and Srinivas Devadas. Silicon Physical Random Functions. In *Proceedings of the 9th ACM Conference on Computer and Communications Security*, CCS '02, pages 148–160, New York, NY, USA, 2002. ACM.
- [GK14] A. Garg and T.T. Kim. Design of SRAM PUF with improved uniformity and reliability utilizing device aging effect. In *Circuits and Systems (ISCAS), 2014 IEEE International Symposium on*, pages 1941–1944, June 2014.
- [GKT<sup>+</sup>14] P. Goncalves, A Keating, A Trindade, P. Rodrigues, M. Ferreira, P. Assis, M. Muschitiello, B. Nickson, and C. Poivey. Modeling the response of the ESAPMOS4 RADFETs for the ALPHASAT CTTB experiment. *Nuclear Science, IEEE Transactions on*, 61(3):1439–1443, June 2014.
- [GMG<sup>+</sup>15] M. Gaillardin, M. Martinez, S. Girard, V. Goiffon, P. Paillet, J. L. Leray, P. Magnan, Y. Ouerdane, A. Boukenter, C. Marcandella, O. Duhamel, M. Raine, N. Richard, F. Andrieu, S. Barraud, and O. Faynot. High Total Ionizing Dose and Temperature Effects on Micro- and Nano-Electronic Devices. *IEEE Transactions on Nuclear Science*, 62(3):1226–1232, June 2015.
- [GMP<sup>+</sup>13] JO Goldsten, RH Maurer, PN Peplowski, AG Holmes-Siedle, CC Herrmann, and BH Mauk. The engineering radiation monitor for the radiation belt storm probes mission. *Space Science Reviews*, 179(1-4):485–502, 2013.
- [GMW08] Jody W Gambles, GK Maki, and SR Whitaker. Radiation hardening by design. *International Journal of Electronics*, 95(1):11–26, 2008.
- [GN14] Dinesh Ganta and Leyla Nazhandali. Study of IC aging on ring oscillator physical unclonable functions. In *Fifteenth International Symposium on Quality Electronic Design*, pages 461–466. IEEE, 2014.
- [GOB13] Massoud M Ghahroodi, Emre Ozer, and David Bull. SEU and SET-tolerant ARM Cortex-R4 CPU for space and avionics applications. In *Workshop on Manufacturable and Dependable Multicore Architectures at Nanoscale*, 2013.
- [GOS15] S Golge, PM O'Neill, and TC Slaba. NASA Galactic Cosmic Radiation Environment Model: Badhwar-O'Neill (2014). 2015.
- [GPM00] A Giraldo, A Paccagnella, and A Minzoni. Aspect ratio calculation in n-channel MOSFETs with a gate-enclosed layout. *Solid-State Electronics*, 44(6):981–989, 2000.
- [GRD<sup>+</sup>16] M. J. Gadlage, A. H. Roach, A. R. Duncan, M. R. Halstead, M. J. Kay, P. Gadfort, J. R. Alhbin, and S. Stansberry. Alpha-particle and neutron-induced single-event transient measurements in subthreshold circuits. In *2016 IEEE International Reliability Physics Symposium (IRPS)*, pages SE-1–1–SE-1–6, April 2016.
- [GRP<sup>+</sup>13] M. Gaillardin, M. Raine, P. Paillet, M. Martinez, C. Marcandella, S. Girard, O. Duhamel, N. Richard, F. Andrieu, S. Barraud, and O. Faynot. Radiation effects in advanced SOI devices: New insights into Total Ionizing Dose and Single-Event Effects. In *2013 IEEE SOI-3D-Subthreshold Microelectronics Technology Unified Conference (S3S)*, pages 1–2, Oct 2013.
- [GSC11] R. Graczyk, M. Stolarski, and P. Cormery. Exploratory study about the use of new reconfigurable FPGAs in space. In *Adaptive Hardware and Systems (AHS), 2011 NASA/ESA Conference on*, pages 220–226, June 2011.
- [HA13] G. Hubert and L. Artola. Single-event transient modeling in a 65-nm bulk cmos technology based on multi-physical approach and electrical simulations. *IEEE Transactions on Nuclear Science*, 60(6):4421–4429, Dec 2013.
- [HALV11] Ignacio Herrera-Alzu and Marisa López-Vallejo. Self-reference scrubber for TMR systems based on xilinx virtex FPGAs. In *International Workshop on Power and Timing Modeling, Optimization and Simulation*, pages 133–142. Springer, 2011.

- [HALV13] Ignacio Herrera-Alzu and Marisa Lopez-Vallejo. Design techniques for Xilinx Virtex FPGA configuration memory scrubbers. *IEEE Transactions on Nuclear Science*, 60(1):376–385, 2013.
- [HAR15] G Hubert, L Artola, and D Regis. Impact of scaling on the soft error sensitivity of bulk, FDSOI and FinFET technologies due to atmospheric radiation. *Integration, the VLSI journal*, 50:39–47, 2015.
- [HG64] Harold L Hughes and Ronald R Giroux. Space Radiation Affects MOS FET’s. *Electronics (US)*, 37(32), 1964.
- [HKK<sup>+</sup>13] Sewook Hwang, Jabeom Koo, Kisoo Kim, Hokyu Lee, and Chulwoo Kim. A 0.008 500/spl mu/W 469 kS/s Frequency-to-Digital Converter Based CMOS Temperature Sensor With Process Variation Compensation. *Circuits and Systems I: Regular Papers, IEEE Transactions on*, 60(9):2241–2248, 2013.
- [HKM16] J. W. Han, M. Kebaili, and M. Meyyappan. System on microheater for on-chip annealing of defects generated by hot-carrier injection, bias temperature instability, and ionizing radiation. *IEEE Electron Device Letters*, PP(99):1–1, 2016.
- [HOT98] Akio Hirata, Hidetoshi Onodera, and K Tamura. Estimation of propagation delay considering short-circuit current for static cmos gates. *IEEE Transactions on Circuits and Systems I: Fundamental theory and applications*, 45(11):1194–1198, 1998.
- [HS74] Andrew Holmes-Siedle. The space-charge dosimeter: General principles of a new method of radiation detection. *Nuclear Instruments and Methods*, 121(1):169–179, 1974.
- [HS00] P. Hazucha and C. Svensson. Impact of CMOS technology scaling on the atmospheric neutron soft error rate. *IEEE Transactions on Nuclear Science*, 47(6):2586–2594, Dec 2000.
- [HSGMP14] A. G. Holmes-Siedle, J. O. Goldsten, R. H. Maurer, and P. N. Peplowski. RadFET Dosimeters in the Belt: the Van Allen Probes on Day 365. *IEEE Transactions on Nuclear Science*, 61(2):948–954, April 2014.
- [HSRG07] Andrew Holmes-Siedle, Federio Ravotti, and Maurice Glaser. The dosimetric performance of RADFETs in radiation test beams. In *Radiation Effects Data Workshop, 2007 IEEE*, pages 42–57. IEEE, 2007.
- [HTG89] KJ Hass, RK Treece, and AE Giddings. A radiation-hardened 16/32-bit microprocessor. *IEEE Transactions on Nuclear Science*, 36(6):2252–2257, 1989.
- [HYKD14] Charles Herder, Meng-Day Yu, Farinaz Koushanfar, and Srinivas Devadas. Physical unclonable functions and applications: A tutorial. *Proceedings of the IEEE*, 102(8):1126–1141, 2014.
- [IA15] F. Irom and S. G. Agarwal. Compendium of Single-Event Latchup and Total Ionizing Dose Test Results of Commercial Digital to Analog Converters. In *Radiation Effects Data Workshop (REDW), 2015 IEEE*, pages 1–8, July 2015.
- [IALV08] P. Ituero, J.L. Ayala, and M. Lopez-Vallejo. A Nanowatt Smart Temperature Sensor for Dynamic Thermal Management. *Sensors Journal, IEEE*, 8(12):2036–2043, Dec 2008.
- [ILVMO12] Pablo Ituero, Marisa Lopez-Vallejo, MAS Marcos, and Carlos Gómez Osuna. Light-weight on-chip monitoring network for dynamic adaptation and calibration. *Sensors Journal, IEEE*, 12(6):1736–1745, 2012.
- [Ind] Votsch Industrietechnik. VTL and VCL for temperature and climatic tests. [Online]. Available: <http://vit.com>.
- [JCG<sup>+</sup>12] Adam Jacobs, Grzegorz Cieslewski, Alan D. George, Ann Gordon-Ross, and Herman Lam. Reconfigurable Fault Tolerance: A Comprehensive Framework for Reliable and Adaptive FPGA-Based Space Computing. *ACM Trans. Reconfigurable Technol. Syst.*, 5(4):21:1–21:30, December 2012.
- [JOH<sup>+</sup>15] W. R. Johnston, T. P. O’Brien, S. L. Huston, T. B. Guild, and G. P. Ginet. Recent Updates to the AE9/AP9/SPM Radiation Belt and Space Plasma Specification Model. *IEEE Transactions on Nuclear Science*, 62(6):2760–2766, Dec 2015.

- [JSS10] G Jovanovic, M Stojcev, and Zoran Stamenkovic. A CMOS voltage controlled ring oscillator with improved frequency stability. *Scientific Publications of the State University of Novi Pazar, Series A: Applied Mathematics, Informatics and mechanics*, 2(1):1–9, 2010.
- [KAKAK03] Adnan Kabbani, Dhamin Al-Khalili, and Asim J Al-Khalili. Technology-portable analytical model for dsm cmos inverter transition-time estimation. *IEEE Transactions on Computer-Aided Design of Integrated Circuits and Systems*, 22(9):1177–1187, 2003.
- [KC06] Jonathan E Knudsen and Lawrence T Clark. An area and power efficient radiation hardened by design flip-flop. *Nuclear Science, IEEE Transactions on*, 53(6):3392–3399, 2006.
- [KGM<sup>+</sup>08] Sandeep S Kumar, Jorge Guajardo, Roel Maes, Geert-Jan Schrijen, and Pim Tuyls. The butterfly PUF protecting IP on every FPGA. In *Hardware-Oriented Security and Trust, 2008. HOST 2008. IEEE International Workshop on*, pages 67–70. IEEE, 2008.
- [KHZS07] Aman Kansal, Jason Hsu, Sadaf Zahedi, and Mani B Srivastava. Power management in energy harvesting sensor networks. *ACM Transactions on Embedded Computing Systems (TECS)*, 6(4):32, 2007.
- [KLA96] A Kelleher, W. Lane, and Leonard Adams. Investigation of on-chip high temperature annealing of PMOS dosimeters. *Nuclear Science, IEEE Transactions on*, 43(3):997–1001, Jun 1996.
- [KLR<sup>+</sup>11] Jae-Joon Kim, Barry P Linder, Rahul M Rao, Tae-Hyoung Kim, Pong-Fei Lu, Keith Jenkins, Chris H Kim, Aditya Bansal, Saibal Mukhopadhyay, Ching-Te Chuang, et al. Reliability monitoring ring oscillator structures for isolated/combined NBTI and PBTI measurement in high-k metal gate technologies. In *Reliability Physics Symposium (IRPS), 2011 IEEE International*, pages 2B–4. IEEE, 2011.
- [KPCC97] R Koga, SH Penzin, KB Crawford, and WR Crain. Single event functional interrupt (SEFI) sensitivity in microcircuits. In *Radiation and Its Effects on Components and Systems, 1997. RADECS 97. Fourth European Conference on*, pages 311–318. IEEE, 1997.
- [KPnS15] Merlin Kole, Mark Pearce, and Maria Mu noz Salinas. A model of the cosmic ray induced atmospheric neutron environment. *Astroparticle Physics*, 62:230 – 240, 2015.
- [KT03] Kenneth R Knowles and Nandor G Thoma. Ring oscillator providing single event transient immunity, November 4 2003. US Patent 6,642,802.
- [Lac08] Ronald C Lacoe. Improving integrated circuit performance through the application of hardness-by-design methodology. *IEEE transactions on Nuclear Science*, 55(4):1903–1925, 2008.
- [LCS<sup>+</sup>16] T. Lin, K. S. Chong, W. Shu, N. K. Z. Lwin, J. Jiang, and J. S. Chang. Experimental investigation into radiation-hardening-by-design (RHBD) flip-flop designs in a 65nm CMOS process. In *2016 IEEE International Symposium on Circuits and Systems (ISCAS)*, pages 966–969, May 2016.
- [LKJ<sup>+</sup>12] T. D. Loveless, J. S. Kauppila, S. Jagannathan, D. R. Ball, J. D. Rowe, N. J. Gaspard, N. M. Atkinson, R. W. Blaine, T. R. Reece, J. R. Ahlbin, T. D. Haeffner, M. L. Alles, W. T. Holman, B. L. Bhuvan, and L. W. Massengill. On-chip measurement of single-event transients in a 45 nm silicon-on-insulator technology. *IEEE Transactions on Nuclear Science*, 59(6):2748–2755, Dec 2012.
- [LKL97] Seog-Jun Lee, Beomsup Kim, and Kwyro Lee. A novel high-speed ring oscillator for multiphase clock generation using negative skewed delay scheme. *IEEE Journal of Solid-State Circuits*, 32(2):289–291, Feb 1997.
- [LLZH16] Yang Liu, Lin Liu, Yuchen Zhou, and Shiyan Hu. Leveraging carbon nanotube technologies in developing Physically Unclonable Function for cyber-physical system authentication. In *Computer Communications Workshops (INFOCOM WKSHPS), 2016 IEEE Conference on*, pages 176–180. IEEE, 2016.
- [LOM<sup>+</sup>98] R. C. Lacoe, J. V. Osborn, D. C. Mayer, S. Brown, and D. R. Hunt. Total-dose radiation tolerance of a commercial 0.35  $\mu\text{m}$  CMOS process. In *Radiation Effects Data Workshop, 1998. IEEE*, pages 104–110, Jul 1998.

- [LOM<sup>+</sup>01] RC Lacoe, JV Osborn, DC Mayer, S Brown, and J Gambles. Total-dose tolerance of the commercial taiwan semiconductor manufacturing company (TSMC) 0.35- $\mu$ m CMOS process. In *Radiation Effects Data Workshop, 2001 IEEE*, pages 72–76. IEEE, 2001.
- [May90] Donald C Mayer. Modes of operation and radiation sensitivity of ultrathin SOI transistors. *IEEE Transactions on Electron Devices*, 37(5):1280–1288, 1990.
- [MBH<sup>+</sup>07] M. McLain, H. J. Barnaby, K. E. Holbert, R. D. Schrimpf, H. Shah, A. Amort, M. Baze, and J. Wert. Enhanced TID Susceptibility in Sub-100 nm Bulk CMOS I/O Transistors and Circuits. *IEEE Transactions on Nuclear Science*, 54(6):2210–2217, Dec 2007.
- [McL88] F Barry McLean. Generic impulse response function for MOS systems and its application to linear response analysis. *IEEE Transactions on Nuclear Science*, 35(6):1178–1185, 1988.
- [MDA<sup>+</sup>12] M Meguelliati, F Djeffal, D Arar, F Douak, and L Khettache. New RADFET dosimeter design for radioactive environment monitoring applications. *tC*, 10:4, 2012.
- [MDE97] Jean-Paul Meyer, Luke O’C Drury, and Donald C Ellison. Galactic cosmic rays from supernova remnants. I. A cosmic-ray composition controlled by volatility and mass-to-charge ratio. *The Astrophysical Journal*, 487(1):182, 1997.
- [MF10] BH Mauk and NJ Fox. Electron radiation belts of the solar system. *Journal of Geophysical Research: Space Physics*, 115(A12), 2010.
- [MGJ<sup>+</sup>13] N. N. Mahatme, N. J. Gaspard, S. Jagannathan, T. D. Loveless, B. L. Bhava, W. H. Robinson, L. W. Massengill, S. J. Wen, and R. Wong. Impact of supply voltage and frequency on the soft error rate of logic circuits. *IEEE Transactions on Nuclear Science*, 60(6):4200–4206, Dec 2013.
- [MGS13] Abhranil Maiti, Vikash Gunreddy, and Patrick Schaumont. A systematic method to evaluate and compare the performance of physical unclonable functions. In *Embedded systems design with FPGAs*, pages 245–267. Springer, 2013.
- [MKS12] A. Maiti, I. Kim, and P. Schaumont. A Robust Physical Unclonable Function With Enhanced Challenge-Response Set. *IEEE Transactions on Information Forensics and Security*, 7(1):333–345, Feb 2012.
- [MKY<sup>+</sup>13] Masaki Masuda, Kanto Kubota, Ryosuke Yamamoto, Jun Furuta, Kazutoshi Kobayashi, and Hidetoshi Ono-dera. A 65 nm low-power adaptive-coupling redundant flip-flop. *IEEE Transactions on Nuclear Science*, 60(4):2750–2755, 2013.
- [MM15] H Mondal and MK Mandal. PLL-based clock recovery circuit using ring oscillator. *International Journal of Electronics Letters*, pages 1–6, 2015.
- [MMCK10] B. I. Matush, T. J. Mozdzen, L. T. Clark, and J. E. Knudsen. Area-Efficient Temporally Hardened by Design Flip-Flop Circuits. *IEEE Transactions on Nuclear Science*, 57(6):3588–3595, Dec 2010.
- [MO87] F Barry McLean and Timothy R Oldham. Basic mechanisms of radiation effects in electronic materials and devices. Technical report, DTIC Document, 1987.
- [MRFA15] Anas Mazady, Md Tauhidur Rahman, Domenic Forte, and Mehdi Anwar. Memristor puf-a security primitive: Theory and experiment. *IEEE Journal on Emerging and Selected Topics in Circuits and Systems*, 5(2):222–229, 2015.
- [MRMK13] Ahmed Mahmoud, Ulrich Rührmair, Mehrdad Majzoobi, and Farinaz Koushanfar. Combined Modeling and Side Channel Attacks on Strong PUFs. *IACR Cryptology ePrint Archive*, 2013:632, 2013.
- [MRV<sup>+</sup>12a] R. Maes, V. Rozic, I. Verbauwhede, P. Koeberl, E. van der Sluis, and V. van der Leest. Experimental evaluation of physically unclonable functions in 65 nm cmos. In *ESSCIRC (ESSCIRC), 2012 Proceedings of the*, pages 486–489, Sept 2012.

- [MRV<sup>+</sup>12b] R. Maes, V. Rozic, I. Verbauwheide, P. Koeberl, E. van der Sluis, and V. van der Leest. Experimental evaluation of Physically Unclonable Functions in 65 nm CMOS. In *ESSCIRC (ESSCIRC), 2012 Proceedings of the*, pages 486–489, Sept 2012.
- [MS09] A. Maiti and P. Schaumont. Improving the quality of a Physical Unclonable Function using configurable Ring Oscillators. In *Field Programmable Logic and Applications, 2009. FPL 2009. International Conference on*, pages 703–707, Aug 2009.
- [MS10] MK Mandal and BC Sarkar. Ring oscillators: Characteristics and applications. *Indian journal of pure & applied physics*, 48:136–145, 2010.
- [MS11] Abhranil Maiti and Patrick Schaumont. Improved ring oscillator PUF: an FPGA-friendly secure primitive. *Journal of cryptology*, 24(2):375–397, 2011.
- [MS14] Abhranil Maiti and Patrick Schaumont. The impact of aging on a physical unclonable function. *IEEE Transactions on Very Large Scale Integration (VLSI) Systems*, 22(9):1854–1864, 2014.
- [MSHL01] Ronald L Moore, Alphonse C Sterling, Hugh S Hudson, and James R Lemen. Onset of the magnetic explosion in solar flares and coronal mass ejections. *The Astrophysical Journal*, 552(2):833, 2001.
- [MSP<sup>+</sup>13] A Masi, G Spiezzi, P Peronnard, M Donze, M Brugger, and R Losito. The new generation of the CERN accelerator radiation monitoring system for electronics. *Nuclear Science, IEEE Transactions on*, 60(5):3475–3482, 2013.
- [MSSS11] Dominik Merli, Dieter Schuster, Frederic Stumpf, and Georg Sigl. Side-channel analysis of PUFs and fuzzy extractors. In *International Conference on Trust and Trustworthy Computing*, pages 33–47. Springer, 2011.
- [MT08] L. W. Massengill and P. W. Tuinenga. Single-Event Transient Pulse Propagation in Digital CMOS. *IEEE Transactions on Nuclear Science*, 55(6):2861–2871, Dec 2008.
- [MTV09] Roel Maes, Pim Tuyls, and Ingrid Verbauwheide. Low-overhead implementation of a soft decision helper data algorithm for SRAM PUFs. In *Cryptographic Hardware and Embedded Systems-CHES 2009*, pages 332–347. Springer, 2009.
- [MW78] T. C. May and M. H. Woods. A New Physical Mechanism for Soft Errors in Dynamic Memories. In *Reliability Physics Symposium, 1978. 16th Annual*, pages 33–40, April 1978.
- [Nar08] Balaji Narasimham. *Characterization of heavy-ion, neutron and alpha particle-induced single-event transient pulse widths in advanced CMOS technologies*. PhD thesis, Vanderbilt University, 2008.
- [NBS<sup>+</sup>07] B. Narasimham, B. L. Bhuva, R. D. Schrimpf, L. W. Massengill, M. J. Gadlage, O. A. Amusan, W. T. Holman, A. F. Witulski, W. H. Robinson, J. D. Black, J. M. Benedetto, and P. H. Eaton. Characterization of Digital Single Event Transient Pulse-Widths in 130-nm and 90-nm CMOS Technologies. *IEEE Transactions on Nuclear Science*, 54(6):2506–2511, Dec 2007.
- [NBTA04] Nathan Nowlin, John Bailey, Bob Turfler, and Dave Alexander. A total-dose hardening-by-design approach for high-speed mixed-signal CMOS integrated circuits. *International journal of high speed electronics and systems*, 14(02):367–378, 2004.
- [NSHB13] Dmitry Nedospasov, Jean-Pierre Seifert, Clemens Helfmeier, and Christian Boit. Invasive PUF analysis. In *Fault Diagnosis and Tolerance in Cryptography (FDTC), 2013 Workshop on*, pages 30–38. IEEE, 2013.
- [Nym06] R Nymnik. Initial conditions for radiation analysis: Models of galactic cosmic rays and solar particle events. *Advances in Space Research*, 38(6):1182–1190, 2006.
- [NZS<sup>+</sup>15] K. Ni, E. X. Zhang, I. K. Samsel, R. D. Schrimpf, R. A. Reed, D. M. Fleetwood, A. L. Sternberg, M. W. McCurdy, S. Ren, T. P. Ma, L. Dong, J. Y. Zhang, and P. D. Ye. Charge Collection Mechanisms in GaAs MOSFETs. *IEEE Transactions on Nuclear Science*, 62(6):2752–2759, Dec 2015.

- [OILV13] Carlos Gómez Osuna, Pablo Ituero, and Marisa López-Vallejo. A Self-Timed Multipurpose Delay Sensor for Field Programmable Gate Arrays (FPGAs). *Sensors*, 14(1):129–143, 2013.
- [OLMY98] JV Osborn, RC Lacoe, DC Mayer, and G Yabiku. Total dose hardness of three commercial CMOS microelectronics foundries. *IEEE Transactions on Nuclear Science*, 45(3):1458–1463, 1998.
- [OM03a] Timothy R Oldham and FB McLean. Total ionizing dose effects in MOS oxides and devices. 2003.
- [OM03b] T.R. Oldham and F.B. McLean. Total ionizing dose effects in MOS oxides and devices. *Nuclear Science, IEEE Transactions on*, 50(3):483–499, June 2003.
- [PAH14] L. Palkuti, M. Alles, and H. Hughes. The role of radiation effects in SOI technology development. In *2014 SOI-3D-Subthreshold Microelectronics Technology Unified Conference (S3S)*, pages 1–2, Oct 2014.
- [PBS<sup>+</sup>16] Roberta Pilia, Guillaume Bascoul, Kevin Sanchez, Giovanna Mura, and Fulvio Infante. Single event transient acquisition and mapping for space device characterization. *Microelectronics Reliability*, pages –, 2016.
- [PK15] Vladimir Petrovic and Milo Krstic. Design Flow for Radhard TMR Flip-Flops. In *Design and Diagnostics of Electronic Circuits & Systems (DDECS), 2015 IEEE 18th International Symposium on*, pages 203–208. IEEE, 2015.
- [PKPS13] Georgios Pouiklis, George Kottaras, Athanasios Psomoulis, and Emmanuel Sarris. A CMOS oscillator for radiation-hardened, low-power space electronics. *International Journal of Electronics*, 100(7):913–927, 2013.
- [PM15] Rainer Plaga and Dominik Merli. A new Definition and Classification of Physical Unclonable Functions. In *Proceedings of the Second Workshop on Cryptography and Security in Computing Systems*, page 7. ACM, 2015.
- [PPZM03] Benjamin J Patella, Aleksandar Prodić, Art Zirger, and Dragan Maksimović. High-frequency digital PWM controller IC for DC-DC converters. *Power Electronics, IEEE Transactions on*, 18(1):438–446, 2003.
- [PRTG02] Ravikanth Pappu, Ben Recht, Jason Taylor, and Neil Gershenfeld. Physical One-Way Functions. *Science*, 297(5589):2026–2030, Sept 2002.
- [PXS<sup>+</sup>10] J. A. Pellish, M. A. Xapsos, C. A. Stauffer, T. M. Jordan, A. B. Sanders, R. L. Ladbury, T. R. Oldham, P. W. Marshall, D. F. Heidel, and K. P. Rodbell. Impact of Spacecraft Shielding on Direct Ionization Soft Error Rates for Sub-130 nm Technologies. *IEEE Transactions on Nuclear Science*, 57(6):3183–3189, Dec 2010.
- [QXW<sup>+</sup>16] C. Qi, L. Xiao, T. Wang, J. Li, and L. Li. A highly reliable memory cell design combined with layout-level approach to tolerant single-event upsets. *IEEE Transactions on Device and Materials Reliability*, 16(3):388–395, Sept 2016.
- [RAGM] P. Roche, J. L. Autran, G. Gasiot, and D. Munteanu. Technology downscaling worsening radiation effects in bulk: SOI to the rescue, year=2013, pages=31.1.1-31.1.4, keywords=MOSFET;radiation hardening (electronics);silicon-on-insulator;CMOS technology;FinFET;IC reliability;PDSOI;SER;SOI technology;UTBB FDSOI;atmospheric radiation;failure rate;high soft error rate;radiation effect;size 28 nm;technology downscaling;FinFETs;Latches;Logic gates;Mesons;Neutrons;Radiation effects;Silicon, doi=10.1109/IEDM.2013.6724728, issn=0163-1918, month=Dec,. In *2013 IEEE International Electron Devices Meeting*.
- [Raz96] B. Razavi. A study of phase noise in CMOS oscillators. *IEEE Journal of Solid-State Circuits*, 31(3):331–343, Mar 1996.
- [RBH14] Abbas Ramazani, Sadegh Biabani, and Gholamreza Hadidi. CMOS ring oscillator with combined delay stages. *AEU-International Journal of Electronics and Communications*, 68(6):515–519, 2014.
- [RCN02] Jan M Rabaey, Anantha P Chandrakasan, and Borivoje Nikolic. *Digital integrated circuits*, volume 2. Prentice hall Englewood Cliffs, 2002.
- [RCW14] Ricardo Reis, Yu Cao, and Gilson Wirth. *Circuit design for reliability*. Springer, 2014.

- [RDK12] Ulrich Rührmair, Srinivas Devadas, and Farinaz Koushanfar. Security based on physical unclonability and disorder. In *Introduction to Hardware Security and Trust*, pages 65–102. Springer, 2012.
- [RFFT14] Tauhidur Rahman, Domenic Forte, Jim Fahny, and Mohammad Tehranipoor. ARO-PUF: An aging-resistant ring oscillator PUF design. In *Proceedings of the conference on Design, Automation & Test in Europe*, page 69. European Design and Automation Association, 2014.
- [RG05] P. Roche and G. Gasiot. Impacts of front-end and middle-end process modifications on terrestrial soft error rate. *IEEE Transactions on Device and Materials Reliability*, 5(3):382–396, Sept 2005.
- [RGM05] F Ravotti, M Glaser, and M Moll. Sensor catalogue data compilation of solid-state sensors for radiation monitoring. Technical report, 2005.
- [Rhe10] Randall W Rhea. *Discrete oscillator design: linear, nonlinear, transient, and noise domains*. Artech House, 2010.
- [RP02] Robert Reed and Chris Palor. Single Event Latchup Test Results IBM 5HP CMOS Ring Oscillator, 2002.
- [RS04] José Luis Rosselló and Jaume Segura. An analytical charge-based compact delay model for submicrometer cmos inverters. *IEEE Transactions on Circuits and Systems I: Regular Papers*, 51(7):1301–1311, 2004.
- [RSN<sup>+</sup>01] Andrew Rukhin, Juan Soto, James Nechvatal, Miles Smid, and Elaine Barker. A statistical test suite for random and pseudorandom number generators for cryptographic applications. Technical report, DTIC Document, 2001.
- [RSS<sup>+</sup>13] Ulrich Rührmair, Jan Sölder, Frank Sehnke, Xiaolin Xu, Ahmed Mahmoud, Vera Stoyanova, Gideon Dror, Jürgen Schmidhuber, Wayne Burleson, and Srinivas Devadas. PUF modeling attacks on simulated and silicon data. *IEEE Transactions on Information Forensics and Security*, 8(11):1876–1891, 2013.
- [RvD13] U. Rührmair and M. van Dijk. PUFs in Security Protocols: Attack Models and Security Evaluations. In *Security and Privacy (SP), 2013 IEEE Symposium on*, pages 286–300, May 2013.
- [RZB<sup>+</sup>12] N Rezzak, EX Zhang, DR Ball, ML Alles, TD Loveless, RD Schrimpf, and KP Rodbell. Total-ionizing-dose radiation response of 32 nm partially and 45 nm fully-depleted SOI devices. In *SOI Conference (SOI), 2012 IEEE International*, pages 1–2. IEEE, 2012.
- [SBN05] E. Socher, S. M. Beer, and Y. Nemirovsky. Temperature sensitivity of SOI-CMOS transistors for use in uncooled thermal sensing. *IEEE Transactions on Electron Devices*, 52(12):2784–2790, Dec 2005.
- [SBPS04] G Sarrabayrouse, D Buchdahl, V Polischuk, and S Siskos. Stacked-MOS ionizing radiation dosimeters: potentials and limitations. *Radiation Physics and Chemistry*, 71(3):737–739, 2004.
- [SBW<sup>+</sup>13] G. J. Schlenvoigt, H. J. Barnaby, J. Wilkinson, S. Morrison, and L. Tyler. Simulation of TID Effects in a High Voltage Ring Oscillator. *IEEE Transactions on Nuclear Science*, 60(6):4547–4554, Dec 2013.
- [SCEGV15] A. Sanchez-Clemente, L. Entrena, and M. Garcia-Valderas. Partial TMR in FPGAs Using Approximate Logic Circuits. In *2015 15th European Conference on Radiation and Its Effects on Components and Systems (RADECS)*, pages 1–4, Sept 2015.
- [SCM<sup>+</sup>11] S. Shambhulingaiah, L. T. Clark, T. J. Mozdzen, N. D. Hindman, S. Chella, and K. E. Holbert. Temporal sequential logic hardening by design with a low power delay element. In *Radiation and Its Effects on Components and Systems (RADECS), 2011 12th European Conference on*, pages 144–149, Sept 2011.
- [SD07] G Edward Suh and Srinivas Devadas. Physical unclonable functions for device authentication and secret key generation. In *Proceedings of the 44th annual Design Automation Conference*, pages 9–14. ACM, 2007.
- [SDDF98] MR Shaneyfelt, PE Dodd, BL Draper, and RS Flores. Challenges in hardening technologies using shallow-trench isolation. *IEEE Transactions on Nuclear Science*, 45(6):2584–2592, 1998.

- [SFB<sup>+</sup>00] W. Snoeys, F. Faccio, M. Burns, M. Campbell, E. Cantatore, N. Carrer, L. Casagrande, A. Cavagnoli, C. Dachs, S. Di Liberto, F. Formenti, A. Giraldo, E.H.M. Heijne, P. Jarron, M. Letheren, A. Marchioro, P. Martinengo, F. Meddi, B. Mikulec, M. Morando, M. Morel, E. Noah, A. Paccagnella, I. Ropotor, S. Saladino, W. Sansen, F. Santopietro, F. Scarlassara, G.F. Segato, P.M. Signe, F. Soramel, L. Vannucci, and K. Vleugels. Layout techniques to enhance the radiation tolerance of standard CMOS technologies demonstrated on a pixel detector readout chip . *Nuclear Instruments and Methods in Physics Research Section A: Accelerators, Spectrometers, Detectors and Associated Equipment*, 439(2-3):349 – 360, 2000.
- [SFW<sup>+</sup>16] Yabin Sun, Jun Fu, Yudong Wang, Wei Zhou, Zhihong Liu, Xiaojin Li, and Yanling Shi. Experimental study of bias dependence of pulsed laser-induced single-event transient in SiGe HBT. *Microelectronics Reliability*, pages –, 2016.
- [SGA02] W. J. Snoeys, T. A. P. Gutierrez, and G. Anelli. A new NMOS layout structure for radiation tolerance. *IEEE Transactions on Nuclear Science*, 49(4):1829–1833, Aug 2002.
- [SH13] J.F. Salzman and C.C. Hadsell. Extending Radiation Tolerance By Localized Temperature Annealing Of Semiconductor Devices, May 23 2013. US Patent App. 13/309,393.
- [Sko05] Sergei Skorobogatov. Data remanence in flash memory devices. In *International Workshop on Cryptographic Hardware and Embedded Systems*, pages 339–353. Springer, 2005.
- [SMM03] J. R. Srour, C. J. Marshall, and P. W. Marshall. Review of displacement damage effects in silicon devices. *IEEE Transactions on Nuclear Science*, 50(3):653–670, June 2003.
- [SMT94] G. R. Srinivasan, P. C. Murley, and H. K. Tang. Accurate, predictive modeling of soft error rate due to cosmic rays and chip alpha radiation. In *Reliability Physics Symposium, 1994. 32nd Annual Proceedings., IEEE International*, pages 12–16, April 1994.
- [SP13] J. R. Srour and J. W. Palko. Displacement Damage Effects in Irradiated Semiconductor Devices. *IEEE Transactions on Nuclear Science*, 60(3):1740–1766, June 2013.
- [SPM<sup>+</sup>97] A Scarpa, A Paccagnella, F Montera, G Ghibaudo, G Pananakakis, G Ghidini, and PG Fuochi. Ionizing radiation induced leakage current on ultra-thin gate oxides. *IEEE Transactions on Nuclear Science*, 44(6):1818–1825, 1997.
- [SRB<sup>+</sup>13] H. E. Spence, G. D. Reeves, D. N. Baker, J. B. Blake, M. Bolton, S. Bourdarie, A. A. Chan, S. G. Claudepierre, J. H. Clemmons, J. P. Cravens, S. R. Elkington, J. F. Fennell, R. H. W. Friedel, H. O. Funsten, J. Goldstein, J. C. Green, A. Guthrie, M. G. Henderson, R. B. Horne, M. K. Hudson, J.-M. Jahn, V. K. Jordanova, S. G. Kanekal, B. W. Klatt, B. A. Larsen, X. Li, E. A. MacDonald, I. R. Mann, J. Niehof, T. P. O’Brien, T. G. Onsager, D. Salvaggio, R. M. Skoug, S. S. Smith, L. L. Suther, M. F. Thomsen, and R. M. Thorne. Science goals and overview of the radiation belt storm probes (rbsp) energetic particle, composition, and thermal plasma (ect) suite on nasa’s van allen probes mission. *Space Science Reviews*, 179(1):311–336, 2013.
- [SRM<sup>+</sup>11] Brian D Sierawski, Robert A Reed, Marcus H Mendenhall, Robert A Weller, Ronald D Schrimpf, Shi-Jie Wen, Richard Wong, Nelson Tam, and Robert C Baumann. Effects of scaling on muon-induced soft errors. In *International Reliability Physics Symposium*, 2011.
- [SSDF08] Marty R Shaneyfelt, James R Schwank, Paul E Dodd, and James A Felix. Total ionizing dose and single event effects hardness assurance qualification issues for microelectronics. *Nuclear Science, IEEE Transactions on*, 55(4):1926–1946, 2008.
- [SSF<sup>+</sup>08] James R Schwank, Marty R Shaneyfelt, Daniel M Fleetwood, James A Felix, Paul E Dodd, Philippe Paillet, and Véronique Ferlet-Cavrois. Radiation effects in MOS oxides. *IEEE Transactions on Nuclear Science*, 55(4):1833–1853, 2008.
- [ŠTO05] Boris Škorić, Pim Tuyls, and Wil Ophey. Robust key extraction from physical uncloneable functions. In *Applied Cryptography and Network Security*, pages 407–422. Springer, 2005.
- [STP08] Dries Schellekens, Pim Tuyls, and Bart Preneel. Embedded trusted computing with authenticated non-volatile memory. In *International Conference on Trusted Computing*, pages 60–74. Springer, 2008.

- [SVIE15] Felix Siegle, Tanya Vladimirova, Jørgen Istad, and Omar Emam. Mitigation of radiation effects in SRAM-based FPGAs for space applications. *ACM Computing Surveys (CSUR)*, 47(2):37, 2015.
- [SY08] U. Seckin and C. K. K. Yang. A Comprehensive Delay Model for CMOS CML Circuits. *IEEE Transactions on Circuits and Systems I: Regular Papers*, 55(9):2608–2618, Oct 2008.
- [SYW13] Selahattin Sayil, Sumanth R Yeddula, and Juyu Wang. Single-event coupling soft errors in nanoscale cmos circuits. *IEEE Design & Test*, 30(6):89–97, 2013.
- [Tit13] Jeffrey L Titus. An updated perspective of single event gate rupture and single event burnout in power MOSFETs. *IEEE Transactions on Nuclear Science*, 60(3):1912–1928, 2013.
- [TPR<sup>+</sup>06] Alan D Tipton, Jonathan A Pellish, Robert A Reed, Ronald D Schrimpf, Robert A Weller, Marcus H Mendenhall, Brian Sierawski, Akil K Sutton, Ryan M Diestelhorst, Gustavo Espinel, et al. Multiple-bit upset in 130 nm CMOS technology. *IEEE Transactions on Nuclear Science*, 53(6):3259–3264, 2006.
- [TŠ07] Pim Tuyls and Boris Škorić. *Security, Privacy, and Trust in Modern Data Management*, chapter Strong Authentication with Physical Unclonable Functions, pages 133–148. Springer Berlin Heidelberg, Berlin, Heidelberg, 2007.
- [VAF59a] James Alfred Van Allen and Louis A Frank. Radiation around the Earth to a radial distance of 107,400 km. *Nature*, 183, 1959.
- [VAF59b] James Alfred Van Allen and Louis A Frank. Radiation measurements to 658,300 km. with Pioneer IV. *Nature*, 184, 1959.
- [VAFK14] I. Vaisband, M. Azhar, E. G. Friedman, and S. Kose. Digitally Controlled Pulse Width Modulator for On-Chip Power Management. *IEEE Transactions on Very Large Scale Integration (VLSI) Systems*, 22(12):2527–2534, Dec 2014.
- [VGB07] Christopher M Vigorito, Deepak Ganesan, and Andrew G Barto. Adaptive control of duty cycling in energy-harvesting wireless sensor networks. In *IEEE Communications Society Conference on Sensor, Mesh and Ad Hoc Communications and Networks (SECON)*, 2007., pages 21–30. IEEE, 2007.
- [VLPB98] S. Villa, A. L. Lacaita, L. M. Perron, and R. Bez. A physically-based model of the effective mobility in heavily-doped n-MOSFETs. *IEEE Transactions on Electron Devices*, 45(1):110–115, Jan 1998.
- [VN09] V. Vivekraja and L. Nazhandali. Circuit-level techniques for reliable Physically Uncloneable Functions. In *2009 IEEE International Workshop on Hardware-Oriented Security and Trust*, pages 30–35, July 2009.
- [WBB<sup>+</sup>15] M. Wind, J. V. Bagalkote, P. Beck, M. Latocha, and M. Poizat. TID and SEGR Radiation Characterisation of European COTS Power MOSFETs with Respect to Space Application Electronics. In *2015 15th European Conference on Radiation and Its Effects on Components and Systems (RADECS)*, pages 1–3, Sept 2015.
- [WFK<sup>+</sup>13] Neil E Wood, Patrick Fleming, Andrew T Kelly, Bin Li, and Daniel M Pirkl. Single-event upset hardened ring oscillator, October 1 2013. US Patent 8,547,178.
- [WH11] N.H.E. Weste and D.M. Harris. *CMOS VLSI Design: A Circuits and Systems Perspective*. ADDISON WESLEY Publishing Company Incorporated, 2011.
- [WH16] Michael Wirthlin and Alex Harding. Hybrid Configuration Scrubbing for Xilinx 7-Series FPGAs. In *FPGAs and Parallel Architectures for Aerospace Applications*, pages 91–101. Springer, 2016.
- [Win89] PS Winokur. Basic mechanisms of radiation effects on electronic materials and devices. *Transactions of the American Nuclear Society;(USA)*, 59(CONF-890604-), 1989.
- [WKH83] PS Winokur, KG Kerris, and L Harper. Predicting CMOS inverter response in nuclear and space environments. *IEEE Transactions on Nuclear Science*, 30(6):4326–4332, 1983.

- [WL88] WR Webber and JA Lockwood. Characteristics of the 22-year modulation of cosmic rays as seen by neutron monitors. *Journal of Geophysical Research: Space Physics*, 93(A8):8735–8740, 1988.
- [WM62] JT Wallmark and SM Marcus. Minimum size and maximum packing density of nonredundant semiconductor devices. *Proceedings of the IRE*, 50(3):286–298, 1962.
- [WVK07] G. I. Wirth, M. G. Vieira, and F. G. L. Kastensmidt. Accurate and computer efficient modelling of single event transients in cmos circuits. *IET Circuits, Devices Systems*, 1(2):137–142, April 2007.
- [WVNK08] Gilson I. Wirth, Michele G. Vieira, Egas H. Neto, and Fernanda Lima Kastensmidt. Modeling the sensitivity of CMOS circuits to radiation induced single event transients. *Microelectronics Reliability*, 48(1):29 – 36, 2008.
- [XBS<sup>+</sup>99] Michael Anthony Xapsos, JL Barth, EG Stassinopoulos, Edward A Burke, and GB Gee. Space environment effects: model for emission of solar protons (ESP): cumulative and worst case event fluences. 1999.
- [XDH<sup>+</sup>03] X Xi, Mohan Dunga, Jin He, Weidong Liu, Kanyu M Cao, Xiaodong Jin, Jeff J Ou, Mansun Chan, Ali M Niknejad, Chenming Hu, et al. Bsim4. 3.0 mosfet model. *UC Berkley*, 2003.
- [XIS14] Zhao Xinyuan, Wang liang, and Yue Suge. Impact of gate shapes on single event transients. In *Electron Devices and Solid-State Circuits (EDSSC), 2014 IEEE International Conference on*, pages 1–2, June 2014.
- [XOO12] Michael A Xapsos, Patrick M O'Neill, and T Paul O'Brien. Near-Earth space radiation models. 2012.
- [XSB<sup>+</sup>00] MA Xapsos, GP Summers, JL Barth, EG Stassinopoulos, and EA Burke. Probability model for cumulative solar proton event fluences. *IEEE Transactions on Nuclear Science*, 47(3):486–490, 2000.
- [YHC<sup>+</sup>14] Yang You, D Huang, J Chen, D Gong, Tiankuan Liu, and Jingbo Ye. Radiation-hardened-by-design clocking circuits in 0.13- $\mu$ m CMOS technology. *Journal of Instrumentation*, 9(01):C01029, 2014.
- [YQ09] Chi-En Yin and Gang Qu. Temperature-aware cooperative ring oscillator PUF. In *Hardware-Oriented Security and Trust, 2009. HOST'09. IEEE International Workshop on*, pages 36–42. IEEE, 2009.
- [YSX<sup>+</sup>15] Zhao Yuanfu, Yue Suge, Zhao Xinyuan, Lu Shijin, Bian Qiang, Wang Liang, and Sun Yongshu. Single event soft error in advanced integrated circuit. *Journal of Semiconductors*, 36(11):111001, 2015.
- [YYCS14] W. Ying, C. H. Yu, F. Cao, and M. G. Shan. Simulation study of single event effects for split-gate enhanced power u-shape metal-oxide semiconductor field-effect transistor. *IET Power Electronics*, 7(12):2895–2901, 2014.
- [ZFC<sup>+</sup>14] Le Zhang, Xuanyao Fong, Chip-Hong Chang, Zhi Hui Kong, and Kaushik Roy. Highly reliable memory-based physical unclonable function using spin-transfer torque MRAM. In *2014 IEEE International Symposium on Circuits and Systems (ISCAS)*, pages 2169–2172. IEEE, 2014.
- [ZJA<sup>+</sup>16] H. Zhang, H. Jiang, T. R. Assis, D. R. Ball, K. Ni, J. S. Kauppila, R. D. Schrimpf, L. W. Massengill, B. L. Bhuvu, B. Narasimham, S. Hatami, A. Anvar, A. Lin, and J. K. Wang. Temperature dependence of soft-error rates for ff designs in 20-nm bulk planar and 16-nm bulk finfet technologies. In *2016 IEEE International Reliability Physics Symposium (IRPS)*, pages 5C–3–1–5C–3–5, April 2016.
- [ZLQ15] Jiliang Zhang, Yaping Lin, and Gang Qu. Reconfigurable binding against FPGA replay attacks. *ACM Transactions on Design Automation of Electronic Systems (TODAES)*, 20(2):33, 2015.
- [ZM04] Quming Zhou and Kartik Mohanram. Transistor sizing for radiation hardening. In *Reliability Physics Symposium Proceedings, 2004. 42nd Annual. 2004 IEEE International*, pages 310–315. IEEE, 2004.
- [ZM06] Quming Zhou and Kartik Mohanram. Gate sizing to radiation harden combinational logic. *IEEE Transactions on Computer-Aided Design of Integrated Circuits and Systems*, 25(1):155–166, 2006.
- [ZMG12] Omid Zeynali, Daryoush Masti, and Saeed Gandomkar. Shielding protection of electronic circuits against radiation effects of space high energy particles. *Advances in Applied Science Research*, 3(1):446–451, 2012.

- [ZQLZ14] Ji-Liang Zhang, Gang Qu, Yong-Qiang Lv, and Qiang Zhou. A survey on silicon pufs and recent advances in ring oscillator pufs. *Journal of Computer Science and Technology*, 29(4):664–678, 2014.
- [ZVR<sup>+</sup>09] R. Zheng, J. Velamala, V. Reddy, V. Balakrishnan, E. Mintarno, S. Mitra, S. Krishnan, and Y. Cao. Circuit aging prediction for low-power operation. In *2009 IEEE Custom Integrated Circuits Conference*, pages 427–430, Sept 2009.





this page is intentionally left blank